Title	γp→π+n, π0p反応における偏極ターゲット非対称度の測定
Author(s)	徳田, 登
Citation	大阪大学, 1978, 博士論文
Version Type	VoR
URL	https://hdl.handle.net/11094/1529
rights	
Note	

Measurement of the Polarized Target Asymmetry for $\gamma p \to \pi^+ n$ and $\pi^o p$ Processes

Noboru Tokuda

February 1978

Department of Applied Mathematics

Faculty of Engineering Science

Osaka University

Contents

§1. Introduction

Single pion photoproduction process in the resonance region plays an important role in the investigation of electromagnetic properties of nucleon resonances. Study of resonances provides informations on the structure of particles and the interaction machanisms between them. The accumulation of various kinds of experimental data, spin parameters as well as differential cross section, has enabled phenomenological analyses, by which photocouplings of well-known resonances have been extracted. In the theoretical field the quark model has succeeded in classification of resonances and prediction of photocouplings of low mass resonances qualitatively. The model deserves further check and improvement by experiments.

1 - 1. πN scattering and pion photoproduction

Phase shift analyses on πN scattering ($\pi N \to N^* \to \pi N$) have confirmed a number of nucleon resonances and determined couplings for $N^* \to \pi N$ decay, at least in the lower energies below the socond resonance region. For higher energies above the third resonance region, however, some of resonances are clear and some are not [1]. The phase shift analysis determines amplitudes for $N^* \to \pi N$ decay in magnitude and relative sign. The signs can be fixed by analysis of $\pi N \to N^* \to \pi\Delta$.

Analysis of $\gamma N \to N^* \to \pi N$ process is interesting to investigate whether resonances confirmed by πN scattering are excited in photon-nucleon interaction and to study their electromagnetic properties. The analysis determines photoamplitudes in magnitude and sign, relative

to the Born term. The study of πN scattering is complementary to photoproduction analysis. Firstly the analysis makes use of knowledge on $N^* \to \pi N$ obtained by the phase shift analysis of πN scattering; spin, parity, mass and decay width. Secondly Watson's theorem [2] is useful in the energy range below $E_\gamma \lesssim 0.5$ GeV (E_γ : lab. incident photon energy), where the effect of double pion photoproduction is negligibe. This theorem, based on unitarity and time reversal invariance, requires a photoproduction multipole amplitude to have the same phase as the corresponding partial wave amplitude for πN scattering.

1 - 2. Observables in pion photoproduction

Single pion photoproduction is described in terms of four independent complex amplitudes. The helicity amplitudes H_i introduced by Walker [3] are often used. Four experimental quantities, which so far have been measured, are given as follows.

The differential cross section

$$\frac{d\sigma}{d\Omega}(\theta) = \frac{1}{2}\frac{q}{k}\left(|H_1|^2 + |H_2|^2 + |H_3|^2 + |H_4|^2\right) , \qquad (1\text{-}1)$$

where k and q are the momenta of photon and pion in the c.m. system.

The recoil nucleon polarization

$$P(\theta) = \frac{d\sigma\uparrow - d\sigma\downarrow}{d\sigma\uparrow + d\sigma\downarrow} = -\frac{q}{k}\frac{1}{d\sigma/d\Omega}\,\mathrm{Im}(H_1H_3^* + H_2H_4^*) , \qquad (1\text{-}2)$$

where $d\sigma\uparrow$ and $d\sigma\downarrow$ are differential cross sections for the recoil nucleon polarization pointing up and down perpendicular to the production plane. The up direction is defined by $\vec{k} \times \vec{q}$.

The polarized photon asymmetry

$$\Sigma(\theta) = \frac{d\sigma_{\parallel} - d\sigma_{\perp}}{d\sigma_{\parallel} + d\sigma_{\perp}} = \frac{q}{k}\frac{1}{d\sigma/d\Omega}\,\mathrm{Re}(H_1H_4^* - H_2H_3^*) \ , \qquad (1\text{-}3)$$

where $d\sigma_{\parallel}$ and $d\sigma_{\perp}$ are differential cross sections for linear photon polarizations parallel and perpendicular to the production plane.

The polarized target asymmetry

$$T(\theta) = \frac{\uparrow d\sigma - \downarrow d\sigma}{\uparrow d\sigma + \downarrow d\sigma} = \frac{q}{k}\frac{1}{d\sigma/d\Omega}\,\mathrm{Im}(H_1H_2^* + H_3H_4^*) \ , \qquad (1\text{-}4)$$

where $\uparrow d\sigma$ and $\downarrow d\sigma$ are differential cross sections for targets polarized upward and downward perpendicular to the production plane.

There are seven independent real quantities in the four helicity amplitudes, excluding the overall pahse. Therefore seven experimental quantities are necessary to determine the amplitudes at each incident photon energy and c.m. pion production angle. Although further three quantities concerning spins [4] are needed, they have not been measured yet because of difficulties in experimental techniques.

1 - 3. Present situation of the study

The situation of photoproduction is not so good as that of πN scattering because of difficulties in experiments and analyses. Experimental difficulties are due to

1. small cross sections, in the order of $\alpha = 1/137$ as small as those of πN scattering,
2. continueous energy spectrum of the bremsstrahlung photon beam, which requires that the energy of the incident photon have to

be determined from the momentum vectors of the scattered particles,

3. electron-positron background produced by the photon beam, which is serious particularly in experiments with a polarized target, because the e^+e^- pair are spread by a polarized target magnet.

The analysis is complicated, because

1. photon has a spin of 1 and nucleon of 1/2, which requires four independent amplitudes,
2. photon is a mixed state of isospin of 0 and 1: Four electromagnetic couplings are necessary for resonances with an isospin of 3/2, and two couplings for those with 1/2.

Figures 1(a) - (c) show the data accumulation up to the SLAC conference in 1975 [5], for three processes; $\gamma p \to \pi^+ n$, $\pi^o p$ and $\gamma n \to \pi^- p$. In order to improve the situation of photoproduction systematic and precise measurements, particularly of the three spin parameters, have been performed in these few years.

In the lower energy region below 0.5 GeV, precise data of $\Sigma(\theta)$, using polarized gamma beam by means of Ueberall effect, were presented by INS, Tokyo [6], and the Kharkov group [7]. The Tokyo group measured for $\gamma n \to \pi^- p$, and the Kharkov group for the three processes.

The Bonn group measured angular distribution of $T(\theta)$ for $\pi^+ n$ and $\pi^- p$ at 0.7 GeV [8,9] and 0.85 GeV [10,11], and for $\pi^o p$ at 1.0 and 1.1 GeV at forward angles [12]. Experiments on $\Sigma(\theta)$ for the three processes were performed in the energy range of 0.6 - 0.9 GeV at SLAC [13] using

laser beam scattered backward by polarized electorns and the 82-inch bubble chamber.

The Liverpool group at Daresbury Laboratory carried out a series of measurements in the energy range from the second resonance region to the intermediate region. For $\pi^{o}p$ angular distributions of $\Sigma(\theta)$ at 1.2 - 2.8 GeV [14] and $T(\theta)$ at 0.7 - 1.45 GeV [15] were measured. Simultaneous measurements of $P(\theta)$, $\Sigma(\theta)$ and $T(\theta)$ were performed by polarizing both of beam and target for $\pi^{+}n$ at 0.5 - 2.3 GeV [16] and for $\pi^{o}p$ at 1.15 - 2.25 GeV [17].

In the theoretical field Chew-Goldberger-Low-Nambu (CGLN) [18] discussed the electromagnetic coupling of the first resonance using dispersion relations and unitarity imposed via Watson's theorem. Their work was improved by Berends-Donnachie-Weaver (BDW) [19] and Schwela [20].

Accumulation of experimental data of cross section and spin parameters has enables χ^{2}-fitting of experimental data using a computer, and advanced phenomenological analysis, by which the photocouplings of resonances have been determined (table 1).

In the lower energy region below 0.5 GeV several authors [21-25] have tried energy independent analysis using Watson's theorem without further dynamical assumptions. Berends-Donnachie (BD) [26] extended this analysis to the second resonance region.

Walker [3] proposed an isobar model analysis, where an amplitude is composed of simple Breit-Wigner resonance term, the electric Born term and an additional background term. He performed his analysis

from threshold to 1.2 GeV. This analysis was improved by Metcalf-Walker (MW) [27] and the Nagoya group [28]. Fixed-t dispersion relations (FTDR's) are now a powerful tool for phenomenological analyses. The imaginary parts of amplitudes are assumed to be saturated with Breit-Wigner resonances. The real part is calculated from the imaginary part using the dispersion relations. Devenish-Lyth-Rankin (DLR) [29] applied first this method to the analysis of the second resonance region. Moorhouse-Oberlack-Rosenfeld (MOR) [30] extended the analysis to the third resonance region. They added small backgrounds to the imaginary parts for a good data fitting. Their analysis was improved by Knies-Moorhouse-Oberlack (KMO) [31] and Knies-Moorhouse-Oberlack-Rittenberg-Rosenfeld (KMORR) [32]. Crawford (C) [33] extended the analysis to the higher energy region.

Noelle [34] improved the FTDR analysis by imposing unitarity explicitly on amplitudes, considering the effect of other processes, $\gamma N \to \pi\Delta$, ηN, ρN and εN. Barbour-Crawford (BC) [35] extended the FTDR analysis to the intermediate energy region, where the imaginary parts are parametrized in terms of Regge pole exchanges.

1 - 4. The quark model and pion photoproduction

In the quark model a nucleon is considered as a composite system of three quarks, and a resonance as an excited states of the three quarks, assuming an interaction between them, e.g. a harmonic oscillator interaction. Then resonances are successfully classified into irreducible representations of $SU(6) \times O(3)$ [36]. A radiative decay

matrix element can be calculated by assuming an interaction between a quark and a photon [37]. The selection rules [38] derived from vanishing matrix elements are good criterions for the test of a model. When a forbidden phototransition is found experimentally, a model is improved by changing the type of the quark-photon interaction or introducing a new algebra, for instance, $SU(6)_W$.

Photocouplings have been predicted by several authors (table 1). In the non-relativistic quark model [37,39,27] the interaction between a quark and the photon is assumed to be

$$H_{\gamma q} = -\vec{\mu}_q \cdot \vec{B} - \frac{Q_q}{M_q} \vec{P}_q \cdot \vec{A} \ , \qquad (1\text{-}5)$$

where M_q is the quark mass, Q_q its charge, $\vec{\mu}_q$ its magnetic moment, $\vec{P}_q$ its momentum, $\vec{A}$ a vector potential representing the photon, $\vec{B}$ a magnetic component of the photon. Sandwitching this hamiltonian by eigen functions of the harmonic oscillator interaction, one can obtain a radiative decay matrix element. Selection rules forbid transitions,

$$\gamma p \to S_{11}(1700),\ D_{13}(1700),\ D_{15}(1670) \qquad \{\underline{70},1^-\}$$

$$\gamma n \to P_{13}(1810),\ F_{15}(1690) \text{ with helicity of } 3/2 \qquad \{\underline{56},2^+\}$$

Phenomenological analyses give rather larger values for $\gamma p \to S_{11}(1700)$ and $\gamma n \to P_{13}(1810)$ (table 1).

Feynman-Kislinger-Ravndal (FKR) [40] made relativistic formalism, though not completely for simplicity, and calculated photocouplings. Moorhouse-Oberlack (MO) [41] performed recalculation using FKR's method. Their results were almost as the same as those of the non-relativistic

quark model.

Kubota-Ohta (KO) [42] added a relativistic correction term to the non-relativistic photon-quark hamiltonian. This model forbids transitions

$$\gamma p \to S_{11}(1700),\ D_{13}(1700),\ D_{15}(1670) \text{ with helicity of } 1/2.$$

Babcock-Rosner (BR) [43] calculated photocouplings using $SU(6)_W$. They expressed the transition matrix element in terms of the electromagnetic current, which has a simple transition properties with respect to the current quark algebra, $SU(6)_{W,currents}$. The Melosh transformation is helpful to obtain transformation properties of this operator with respect to the constituent quark algebra, $SU(6)_{W,constituents}$, which describes hadronic states of particles. These transformation properties are simple, though including some parameters. BR expressed the matrix elements in terms of multipoles and obtained the parameters by fitting their multipoles presented by DLR [29], KMORR [32] and MW [27]. Their result allows the transition $\gamma p \to S_{11}(1700)$, which is forbidden by above mentioned models.

It must be stressed that these quark models have succeeded in prediction of photocouplings of resonances only qualitatively but not quantitatively and deserve further study. Therefore accumulation of experimental data, cross section and spin parameters, covering the resonance region is much desired.

1 - 5. Outline of the present experiment

Following experiments on photon energy dependence of $T(\theta)$ in 1971

[44] and 1973 [45], the present experiment was proposed and carried out to present systematic and precise data of angular distributions of $T(\theta)$ for $\gamma p \to \pi^+ n$ and $\pi^o p$ processes for the purpose of the definitive determination of photocouplings of the first and the second resonances and the preparation for the extension of the resonance study to further high energy region.

The measurements were performed in the energy range from 0.4 to 1.0 GeV and in the angular range from 40° to 160° for $\pi^+ n$ and from 30° to 120° for $\pi^o p$. The measured regions are shown in fig. 2, where existing data points are also plotted by open marks.

The experiment was done measuring events from polarized proton target. The polarized target asymmetry is given by

$$T(\theta) = \frac{1}{P_T} \frac{n\uparrow - n\downarrow}{n\uparrow + n\downarrow} , \tag{1-6}$$

where P_T is a target polarization, $n\uparrow$ and $n\downarrow$ are event rates from targets polarized up and down. As butanol was used as a target material, there were contamination of events from nuclei of other than hydrogen. Observed enents $N\uparrow$ and $N\downarrow$ contain this contamination N_C,

$$N\uparrow,\downarrow = n\uparrow,\downarrow + N_C \tag{1-7}$$

The target asymmetry is then

$$T(\theta) = \frac{1}{P_T} \frac{1}{R} \frac{N\uparrow - N\downarrow}{N\uparrow + N\downarrow} , \tag{1-8}$$

where R is a hydrogen yield ratio, defined by

$$R = \frac{n_o}{N_o} , \tag{1-9}$$

n_o and N_o are event rates from unpolarized targets,

$$n_o = \frac{n\uparrow + n\downarrow}{2} , \tag{1-10}$$

$$N_o = \frac{N\uparrow + N\downarrow}{2} , \tag{1-11}$$

which were obtained experimentally as mentioned later.

§2. Apparatases

2 - 1. Outline

The experiment was carried out at the INS (Institute for Nuclear Study, University of Tokyo) 1.3 GeV electron synchrotorn, using a bremsstrahlung gamma beam. An averaged intensity of the beam was 1.2×10^9 eq.q./sec.

Polarized target was 12 g n-butanol-water mixture doped with porphyrexide. The target was cooled by a ^{3}He cryostat with a cooling power of 200 mW at 0.5 K, and polarized in a magnetic field of 2.5 T by means of the dynamic nuclear orientation. Target polarization was measured by an NMR detection system with a mini-computer PDP-11/40. The averaged polarization during the experiment was about 65%.

An experimental layout is shown in fig. 3. For the $\gamma p \to \pi^+ n$ process, positive pions were detected and their momentum vectors were determined by a spectrometer with a focusing-type momentum analyzing magnet. For the $\pi^o p$ process with $\theta_\pi^{cm} = 30°$, double photons from the decay of the neutral pions were detected by a π^o counter, consisting of two identical gamma counters. For $\theta_\pi^{cm} = 80°$, 105° and 120° protons and single photons from the neutral pions were detected in coincidence by the magnetic spectrometer and a gamma counter, respectively.

Data were collected and processed by an on-line data acquisition system installed with a terminal computer TOSBAC-40C and a central computer TOSBAC-3400. The later analysis was performed by the central computer.

2 - 2. Beam

The synchrotron accelerated about 5×10^{10} electrons/pulse, with a frequency of 20.5 Hz. Colliding on an internal radiator of 50 μm thick platinum, the electrons produced a bremsstralhung gamma beam. The beam was collimated by a collimator with a hole of 5.5×5.5 mm^2 and 190 mm long, set at distance 5.2 m from the radiator. A beam cross section on the target, 12.8 m far from the collimator, was a square of 19×19 mm^2.

Contaminations of charged particles in the beam were swept by a magnet positioned at the downstream of the collimator. A vacuum was maintained between the collimator and the target to reduce electron-positron pair creations.

The beam intensity was determined by a thick-walled ionization chamber [46] located at the end of the beam line. The gamma beam produced an e^+e^- shower in a copper converter, 40 mm thick or 2.74 radiation lengths. They ionized the gas in the chamber, 95 vol% Ar + 5 vol% CO_2, and the total ion charge q was measured in monitor unit, 1 M.U. = 3.00×10^{-8} coul. The total energy U of the beam was given by

$$U = \alpha(E_\gamma^{max}) \cdot q \ , \qquad (2\text{-}1)$$

where $\alpha(E_\gamma^{max})$ is a conversion coefficient of the chamber, which varies with the end-point energy E_γ^{max} of the bremsstrahlung beam. The coefficient had been calibrated to the accuracy of 3% [47]. The beam intensity Q in equivalent quanta (eq.q.) is given by

$$Q = \frac{U}{E_\gamma^{max}} \ , \qquad (2\text{-}2)$$

A thin walled ionization chamber was also used as a sub-monitor. This chamber converted the beam into electrons and positrons in a four fold layer of aluminized mylar, 0.005 radiation lengths. The performance of the chamber was so sensitive to charged particles in the beam that a counting rate depended on the kind of target, i.e. butanol, polyethylene, carbon etc.. The performance was stable within ±1% for a certain kind of target.

The intensity of the gamma beam was defined by the size of the collimator, and was 0.5 - 1.3 × 10^9 eq.q./sec, dependent on the end-point energy of the beam. The averaged intensity during the experiment was 1.2 × 10^9 eq.q./sec. The spill width of the gamma beam was 3 - 7 msec, and the averaged duty factor was about 8%.

2 - 3. Polarized target

2 - 3 - 1. Outline

A polarized target system for this experiment consisted of two main parts (fig. 4). One is to polarize target material, and is composed of

(1) a polarized target (PT) magnet with a magnetic field of 2.5 T,

(2) a ^{3}He cryostat for a low temperature of 0.5 K,

(3) a microwave supplying system with 70 GHz klystrons for polarizing the target by meams of the dynamic nuclear orientation method (appendix 1).

The other is an NMR detection system for the measurement of target polarization.

The polarized target system used in the previous experiment [45]

had been improved, and the present system had following characteristics;

(1) a large target volume of 12 g, 3 - 4 times as large as that in the previous experiment,

(2) rapid calculation of target polarizations using a mini-computer PDP-11/40.

Apparatuses with underlines in fig. 4 are those used anew in this experiment.

The aim of the present experiment was to measure systematically and accurately the target asymmetries over the wide range of energy and angle. Therefore an efficient data acquisition with a large volume of target was required for the success in this experiment. A new PT magnet with a pole gap distance of 74.5 mm (48 mm for the magnet used previously) was constructed to hold target of a large volume. A new ^{3}He cryostat was designed and constructed for the purpose of keeping the target at a low temerature of 0.5 K under sufficient supply of microwave power and maintaining a high target polarization.

In the previous experiment the target polarization was obtained by integrating manually NMR signals recorded on a pen-recorder chart. This procedure costed a long time and much personal labor. To solve this problem a mini-computer was used. The process by a computer is also essential for the calculation of correction factors for a target polarization, e.g. contribution of the dispersion term, and for the fast-sweep method, which is useful for the polarized deuteron target.

2 - 3 - 2. Target material

A target material was n-butanol-water mixture ($C_4H_{10}O$ + 5 wt% H_2O) doped with 1 - 1.5 wt% porphyrexide [48] (fig. 5). The target was frozen into beads ∿1 mm in diameter to be cooled sufficiently in the presence of microwave heating.

A device [49] was prepared for quickly producing large quantities of small and uniform frozen beads (fig. 6). The diameter of the drops was adjusted by high voltage, 12 kV for 1 mm. The electric charge on drops, drifting on the surface of liquid nitrogen before freezed, prevented them from colliding one another into a large drop.

About 12 g beads were contained in a vessel mounted in the cavity. The vessel was made of 25 μm thick FEP foil into a size of 27 × 27 × 36 mm^3. The packing factor was about 60%.

The target was changed after irradiation of 0.5×10^{14} eq.q./cm^2, after about 3 days, to reduce the effect of radiation damage.

2 - 3 - 3. PT magnet

The views of the PT magnet are shown in fig. 7. The characteristics of the magnet were as follows:

maximum magnetic field	2.6 T,
maximum current	800 A,
uniformity (within 40 mm in radius)	$\pm\sim10^{-4}$,
pole gap distance	74.5 mm,
weight	∿15 ton.

Figures 8 and 9 show the distribution and the homogeneity of the mag-

netic field, respectively. The magnetic field was measured by means of a Hall probe calibrated with the NMR method.

The side view of the yoke is in the shape of C, and the beam irradiates the target through a hole penetrating the yoke. Therefore a wide range of scattering angle was acceptable, which was essential for the measurement of the angular distributions of the target asymmetry. The opening angle of the coils was ±25°, which enabled to detect particles off the scattering plane, e.g. double photons from the decay of the neutral pions.

The cryostat was firmly fixed to the yoke in order to reduce vibration caused by the ^{3}He pumping system (mentioned later), because the vibration at the nose part of the cryostat, where the target is settled, induced noises on NMR signals.

2 - 3 - 4. Cryostat

Details of the cryostat [50] are described in appendix 2. Figures 10 and 11 show the schematic diagram of the cooling mechanism and the scaled drawing of the cryostat. To obtain a large cooling power, the cryostat was designed so that ^{3}He and ^{4}He system were combined into a complex for a good heat contact between them. The whole cooling complex can be easily pulled out from the vacuum jacket for the convenience of the change of targets.

This cryostat had following characteristics:

(1) ^{4}He cooling system was enclosed in the vaporized ^{3}He atmosphere. Two tanks for liquid ^{4}He, i.e. a separator ($\sim$4 K) and

an evaporator (∿2 K) were installed.

(2) A tube-in-tube type counter flow heat exchanger was used for the cooling of ^{3}He gas from the room temperature to 4 K by ^{4}He gas pumped from the separator.

(3) Helices of a fine tube mounted in the separator and the evaporator were used for the cooling of ^{3}He and the condensation.

(4) Vaporized ^{3}He was pumped out through the full cross section of the cryostat to gain a high pumping speed.

Liquid ^{4}He was led to the separator from an external dewar through a transfer tube, then to the evaporator. ^{3}He was cooled and liquefied through heat exchange with the ^{4}He system. Liquid ^{3}He flowed into the target vessel and evaporated. Gaseous ^{3}He was pumped out by a 2000 m^3/h cascade pumping system. The pressure at the cavity was maintained at ∿0.1 torr, corresponding to ∿0.5 K. ^{3}He gas was refreshed through a purifier with charcoal cooled by liquid nitrogen, and fed back to the cryostat.

Figure 10 shows also the typical temperature distribtuion in the cryostat at a stable operation. Temperatures were monitored with platinum resistors (Okazaki 100Ω), germanium resistors (Scientific Instruments model N1G) and carbon resistors (Allen-Bradley 1/8W 10Ω). A pen-recorder, monitoring the change of temperatures, was useful for the operation of the cryostat. A McLeod gauge was used for the determination of the temperature at the cavity.

The performances of the cryostat are summarized in table 2, where those of the cryostat used in the previous experiment are also listed

for comparison. The cooling power, which was measured by a heating resistor fixed at the bottom of the cavity, achieved 200 mW at 0.5 K, and 400 mW at 0.6 K. It took 1.5 - 2 hours to reach a stable operation at 0.5 K from the precooling with liquid nitrogen. The consumption rate of liquid ^{4}He during the experiment was 3.5 ℓ/h: 2 ℓ/h was pumped out from the separator and 1.5 ℓ/h from the evaporator. The cryostat was operated with surplus liquid ^{4}He for a stable operation. The total amount of ^{3}He gas in the system was 13 - 16 ℓ STP.

2 - 3 - 5. Cavity and its surroundings

The cavity and its surroundings were made of thin materials (fig. 12) to reduce the electron-positron pair creations by the incident gamma beam and the multiple scattering and the energy loss of the particles. The cavity was made of thin phosphor bronze, 0.1 mm thick. Two windows of thin aluminum foils, 0.05 mm thick, were cut for the incident gamma beam. The cavity was plated with gold to keep good electric conductivity on the surface and reduce the conversion of the microwave power into heat. A mesh was used for the lid so that evaporated ^{3}He might be pumped out efficiently. The target vessel, filled with about 12 g frozen butanol beads, was mounted in the cavity with an NMR coil and a carbon resistor for the monitor of temperature, which were set avoiding the incident beam.

The cavity was surrounded by three coaxial cylindrical walls. The inner wall was made of 0.3 mm thick stainless steel, and 0.05 mm thick stainless foil were soldered for the beam window. The radiation shield

II was made of 0.5 mm thick copper cylinder plated with gold, where 0.05 mm aluminum foil windows were used for the beam and recoil protons. The external vacuum jacket was made of 1 mm thick aluminum, and the beam windows with 0.1 mm thick mylar were prepared.

2 - 3 - 6. Microwave circuit

Figure 13 shows a circuit for the supply of 70 GHz microwave.

Oscillators were kylstorns, OKI KA701 or KA701A, with a frequency range of 68 - 72 GHz and the maximum power of 300 - 500 mW. Two klystrons tuned to oscillate microwaves of frequencies for up and down polarizations were prepared for quick reverse of the polarization polarity. It took 15 - 20 minutes for the reverse.

The system was simplified as much as possible and a double-size (35 GHz) wave guide, plated with gold, was used between the circuit and the cavity, so that a sufficient power might be supplied to the target without a large power loss in the path.

2 - 3 - 7. NMR detection system

In the NMR detection system with a mini-computer PDP-11/40 both of the fast and the slow sweep method were acceptable (fig. 14). The slow sweep method was used in this experiment. The block diagram for the slow sweep method is shown in fig. 15.

The rf source was an EMF Inc. type VTN-1E generator/sweeper. The frequency was sweeped around 104.85 MHz with a sweep width of 400 kHz every 50 sec.

The tuning box contained an LC series resonant circuit and an

attenuator for the control of the current supplied to the NMR coil. The current was regulated to be ∿0.8 mA, so that the rf magnetic field induced by the NMR coil might not reduce the difference of the spin populations in the two Zeeman energy levels. The capacitor in the tuning box and the NMR coil was connected by a coaxial copper cable, Fujikura 1.5D-QEV or Malco 250-3947, with one wave length, ∿190 cm.

The NMR coil was made of double 2-turn coils (0.3 mmϕ copper) connected in parallel for a good filling factor and homogeneity of the rf magnetic field (fig. 16). The end point of the coil was grounded to the cavity.

The NMR signal was amplified by a two stage amplifier with VHF-band hybrid IC's, NEC MC-5120 and MC-5108. The gain of the amplifiers was ∿40 dB. The input voltage was about 10 mV (peak-to-peak). The dependence of the gain on the frequency was ∿0.05 dB (∿0.58%) in a frequency range of 106 ± 4 MHz. The gain drifted ±0.3 %/°C with a change of temperature, which was reduced to ±0.9°C by a control circuit.

A lock-in-amplifier, PAR model 116, was used to improve the S/N ratio of the NMR signal. The output of the lock-in-amplifier, a differential of the NMR signal, was fed to the computer PDP-11/40 and digitized into 256 ch (frequency) × 4096 ch (voltage) by an ADC (analog-to-digital converter). The computer has following functions:

(1) calculation of the target polarization in an on-line process,

(2) display of the NMR signal and the value of polarization on a CRT (cathode ray tube) for monitoring (fig. 17),

(3) recording of the input signal, differentiated NMR signal,

onto a magnetic tape for the later analysis, where the precise calculation of the polarization was performed considering the effects of radiation damage and contribution of the dispersion term (§5 - 1).

2 - 4. Particle detectors

2 - 4 - 1. Magnetic spectrometer

A spectrometer, constucted on a rotating table with a focusing-type magnet, was used to determine productin angles and momenta of positive pions and protons for the $\gamma p \to \pi^+ n$ and $\pi^o p$ processes, repectively. The spectrometer (fig. 3) consisted of

(1) three scintillation counters for triggering (T_1, T_2, T_3),

(2) two 8-bin and 12-bin scintillation counter hodoscopes(H_1, H_2), defining the production angles and momenta,

(3) a lucite Cerenkov counter (C_L),

(4) a gas Cerenkov counter (C_G).

The characteristics of the spectrometer and specification of the counters are shown in tables 3 and 4.

The geometrical acceptance, defined by the T_1, was 2.04 mstr. The T_1 counter was protected against the spray of electrons and positrons spread by the PT magnet by lead shields, which were constructed carefully along the path of aimed particles, positive pions or protons. A fan-shaped table of duralumin was set surrounding the target for the construction of the shielding.

The production angles and momenta for the particles were deter-

mined according to firing patterns in the two hodoscopes. The detail of the determination will be discussed later. The resolution of production angles was 1.1 %/(ch in H_2), and the total momentum acceptance was 15%.

The deflection angle of the momentum analyzing magnet was 49.3°, and the curvature radius was 1195 mm. The magnet was able to analyze momenta up to 700 MeV/c. The magnetic field distribution of the magnet was calibrated by the hot wire method and the rotating coil method calibrated by the NMR method.

The Cerenkov counter C_L made of 44 mm thick lucite was used for the discrimination between positive pions and protons. The efficiency was measured with momentum analyzed negative pions, and turned out to be about 96% for pions with momenta higher than 350 MeV/c (fig. 18). The gas Cerenkov counter C_G fulled with 4.6 kg/cm^2 freon 12 gas suppressed positron background. The threshold velocity was $\beta \simeq 0.995$, and the efficiency of this counter was 99% for positrons with momenta $\geq$200 MeV/c.

2 - 4 - 2. Gamma counter

Single photons from the decay of the neutral pions were detected in coincidence with the protons by the gamma counter (fig. 19) set on a rotating table. The counter consisted of

(1) a hardener of 8.3 g/cm^2 thick lithiumhydride against soft gamma rays,

(2) a veto scintillation counter against charged particles (V_C),

(3) a total absorption type lead glass Cerenkov counter (C_C). The acceptance of the counter was 62 mstr defined by a lead collimator, 27 × 27 cm^2 and 50 mm thick. The Cerenkov counter was made of SF-2 lead glass (Ohara Optical Glass Mfg. Co. Ltd.) with a size of 30 × 30 × 30 cm^3 (10.5 radiation lengths).

This counter determined the energies of photons, detecting Cerenkov lights emitted by the shower of electrons and positrons created in the lead glass. The glass was viewed by 9 photobutes (Hamamatsu TV, R329). The output signals from the phototubes were added and converted by an ADC into digitized signals.

An absolute energy calibration of the counter was carried out by using electrons of energies analyzed by a magnet, produced in a solder target by the photon beam. The energy scale and the FWHM resolution were shown in fig. 20. The resolution was 24% for 600 MeV/c electrons.

This counter was set off the scattering plane as shown in fig. 19 in order to avoid photons produced in the proton Compton process and the spray of electrons and positrons by the gamma beam.

2 - 4 - 3. π^o counter

Double photons from the decay of neutral pions were detected by the π^o counter (fig. 21) consisting of two identical counters. Each counter consisted of

(1) a polyethylene hardener against soft gamma rays,

(2) a veto counter consisted of two scintillation counters, rejecting charged particles ($V_{A,B}$),

(3) a ∿5 mm thick (0.9 radiation lengths) lead converter,

(4) a two-dimensional hodoscope, 5 bin × 21 bin, consisting of 3 and 11 scintillation counters, respectively ($HX_{A,B}$, $HY_{A,B}$),

(5) a total absorption type lead glass Cerenkov counter ($C_{A,B}$).

The photons were converted into electron-positron pairs in the lead converter. The production angle of the neutral pions and the opening angle between the two photons were determined by the hodoscopes. The energy of a photon was measured by the Cerenkov counter with a SF-2 lead glass block (Ohara Optical Glass Mfg. Co. Ltd.) of 25 × 25 × 25 cm^3 (8.8 radiation lengths) viewed by 9 phototubes (RCA, 6655A).

An absolute energy calibration of the counters were performed in the same way as the gamma counter, and the similar results to the gamma counter were obtained.

This counter was set at 17° from the beam line, corresponding θ_π^{cm} ≃ 30°. The opening angle between the two counters was defined by the minimum opening angle of double photons.

2 - 5. Fast logic system

Figures 22(a) - (c) show block diagrams of a fast logic system, which was composed of electronics of standard NIM (Nuclear Instruments Module). Signals from phototubes were fed to the discriminator and then to the selection logics. Output signals from detectors viewed by more than two phototubes, C_A, C_B, C_C, C_G and C_L, were added at first and sent to the discriminator. Delays and attenuators adjusted pulses in timing and pulse height in accordance with momenta of particles to be detected. Discriminators produced clear-shaped logic pulses, -1 V in

height and ∿10 nsec in width. The system discriminated requisite events by means of the coincidence and the anti-coincidence methods, and generated master trigger pulses for switching on a data acquisition system.

Aimed events were defined as follows:

$$PI^{+} = (T \cdot C_L) \cdot \overline{(T \cdot (T \cdot C_G))} \qquad \text{for } \gamma p \to \pi^{+} n,$$

$$PG = P \cdot \gamma_C \qquad \text{for } \gamma p \to \pi^{o} p \ (p \cdot \gamma),$$

$$GG = \gamma_A \cdot \gamma_B \qquad \text{for } \gamma p \to \pi^{o} p \ (\gamma \cdot \gamma),$$

where

$$T = T_1 \cdot T_2 \cdot T_3 \ ,$$

$$P = T \cdot \overline{(T \cdot C_G)} \cdot \overline{(T \cdot C_L)} \ ,$$

$$\gamma_C = C_C \cdot \overline{(C_C \cdot V_C)} \ ,$$

$$\gamma_n = (C_n \cdot H_n) \cdot \overline{(C_n \cdot H_n \cdot V_n)} \ ,$$

$$H_n = \sum_{i=1}^{3} HX_{ni} \cdot \sum_{i=1}^{11} HY_{ni} \ ,$$

n = A or B.

M·N means a coincidence between detectors M and N, and $M \cdot \overline{(M \cdot N)}$ an anti-coincidence, where firing in the detector N is rejected.

Anti-coincidences in this logic system were defined as $M \cdot \overline{(M \cdot N)}$ but not as M·N in order to reduce accidental vetoing by the background particles. A pulse width for the anti-coincidence was about 30 nsec (FWHM), wide enough to cover partner pulses, which had flactuations of 5 nsec at most in coincidence timing due to the momentum acceptance of

the magnetic spectrometer.

Signals from detectors, C_A, C_B, C_C, C_L and T_2, were digitized through ADC's to obtain energies or energy losses of particles from pulse heights. For measurements of TOF's (time-of-flight) between T_1-T_3 and T_3-C_C signals from detectors were differentiated for a better time resolution and fed to zero-crossing discriminators, which supplied logic pulses to TDC's (time-to-digital converter). A resolution of the TOF was about ±1.5 nsec.

Delayed coincidence events were counted to investigate accidental coincidence rates,

$$T_{1d}\cdot T_2\cdot T_3\cdot\overline{(T\cdot C_G)}\ ,\quad T_1\cdot T_2\cdot T_{3d}\cdot\overline{(T\cdot C_G)} \qquad \text{for } \pi^+n\ ,$$

$$P_d\cdot\gamma_C\ ,\quad P\cdot\gamma_{Cd} \qquad \text{for } p\cdot\gamma\ ,$$

$$\gamma_{Ad}\cdot\gamma_B\ ,\quad \gamma_A\cdot\gamma_{Bd} \qquad \text{for } \gamma\cdot\gamma\ .$$

M_d means that signals from a detector M are delayed. Timings were shifted about 100 nsec from timings of prompt coincidence.

The aimed events and delayed coincidences were used as master triggers, which switched on counters for data collection, e.g. ADC, TDC, strobed coincidence etc..

2 - 6. Data acquisition system

Figure 23 shows the block diagram of the data acquisition system, installed with a terminal computer TOSBAC-40C (12kW) and a central computer TOSBAC-3400 (112 kW).

For each event following informations were collected by TOSBAC-40C

through the CAMAC system;

(1) firing patterns in the hodoscopes H_1, H_2, $HX_{A,B}$ and $HY_{A,B}$,

(2) pulse heights in the detectors, C_A, C_B, C_C, C_G C_L and T_2,

(3) TOF's between T_1-T_3, T_3-C_C and C_A-C_B,

(4) triggering logics, aimed events or delayed coincidences.

Besides them,

(5) target polarization,

(6) beam monitor count in the thick-walled ionization chamber,

(7) current through the momentum analyzer magnet

were also collected. TOSBAC-40C made several histograms and displayed them on a CRT for the monitor of particle detectors. Every 140 events the raw data were transferred to TOSBAC-3400 and recorded on a magnetic disk. This computer made several histograms, including two-dimensional ones, e.g. $H_1 \times H_2$, (pulse height in T_2) $\times$ TOF(T_1-T_3) etc.. These histograms and the raw data were transferred back to TOSBAC-40C at the end of a data taking. The raw data were copied onto magnetic tapes in the both computers.

§3. Experimental procedure

3 - 1. Data taking

Measured regions were divided into data sets,

51 for $\pi^+ n$

12 for $p \cdot \gamma$,

14 for $\gamma \cdot \gamma$.

At each data set target asymmetries for several data points, 2 - 6, with nearly the same θ_π^{cm}'s and different E_γ's ($\Delta E_\gamma \simeq 40$ MeV), were measured simultaneously (fig. 24(a) - (c)). Measurements for the $\pi^+ n$ process and the $\pi^o p$ process ($p \cdot \gamma$) were carried out separately. Measurements for the $\pi^o p$ process ($\gamma \cdot \gamma$) were performed simultaneously with one of the above two measurements, so long as paths of double photons were not obstructed by the gamma counter. The end-point energy of the bremsstrahlung beam was set 20 - 50 MeV higher than the maximum of the photon energy range to be measured.

A data set was completed by measurements with seven kinds of targets. Data taking for each target was continued for about an hour. The unit of the measurement was called a 'run'. Runs were accumulated until sufficiently small statistical errors were obtained.

For the polarized targets directions of polarization were reversed every three or four runs to reduce systematic errors owing to some drift in performances of particle detectors and the polarized target during the measurements.

Normalization of the target volume (N_o in eq. 5-14) was evaluated by measurements in which the cryostat was operated so that ^{3}He was not

liquefied ('without He' run). Events from walls of the cryostat and the cavity were evaluated by measurements without butanol targets nor/but the cavity ('empty' and 'empty cavity' runs).

The hydrogen yield ratio R was evaluated according to yields from polyethylene target and graphite target ('CH_2' and 'C' runs). These two runs, as well as 'empty' and 'empty cavity' runs, were performed separately from measurements with butanol targets. Experimental conditions, i.e. the gamma beam, construction of lead shields around the target, megnetic field of the momentum analyzer magnet etc., were carefully set as the same as in measurements with butanol targets.

Targets and their components are summarized in table 5, and the specifications of butanol, polyethylene and graphite targets are in table 6.

3 - 2. Event selection and corrections

3 - 2 - 1. Discrimination of particles in the magnetic spectrometer

Discrimination between positive pions, protons and positrons was the problem.

Positrons were discriminated from positive pions and protons by the gas Cerenkov counter C_G.

The discrimination between positive pions and protons was done by three methods;

(1) the lucite Cerenkov counter C_L,

(2) TOF between the counters T_1 and T_3,

(3) energy loss (dE/dx) in the counter T_2.

The discrimination was mainly performed by the lucite Cerenkov counter in the fast logic stage. This counter was used as a trigger counter in the pion detection for $\gamma p \rightarrow \pi^+ n$ and as a veto counter in the proton detection for $\gamma p \rightarrow \pi^o p$. Thus events of positive pions and protons were defined respectively by PI^+ and P in §2 - 5. For positive pions with momenta less than 350 MeV/c this counter was not used because of its low efficiency (fig. 18). The TOF and dE/dx methods were employed supplementarily in the off-line analyses. Figure 25 shows good discriminations by the two methods.

3 - 2 - 2. Pulse heights in the gamma counter

In the measurement of $\gamma p \rightarrow \pi^o p$ $(p \cdot \gamma)$ event selection by pulse heights in the lead glass C_C was useful to reduce

(1) accidental coincidences owing to background photons of low energies,

(2) background events from complex nuclei in the butanol target and the surroundings of the target,

(3) photons originating from multi-pion photoproduction processes.

Figure 26 shows the measured pulse heights for butanol target and carbon target, and proves that pulse heights of events from carbon nuclei were distributes in the lower energy region than those from hydrogen nuclei. Figure 27 shows the simulated pulse heights for single pion and double pion photoproduction processes. It is apparent that photons from the double pion process are distributed in lower energies.

For the better quality of events coincidenced events with photons

of lower energies than a threshold were rejected. The threshold energies were set at 150 - 260 MeV. 61 - 76% coincidenced events survived after this event selection.

3 - 2 - 3. Firing patterns in hodoscopes

(a) Magnetic spectrometer

In the measurement of $\pi^+ n$ and $\pi^o p$ $(p \cdot \gamma)$ a firing pattern in the hodoscopes H_1 and H_2 was examined for each event whether it was normal or abnormal. In the normal firing a bin in each of the two hodoscopes is fired. Abnormal events had a non-firing or a multi-firing pattern in either of the hodoscopes.

The non-firing event was such that any bin in a hodoscope was not fired. That was due to particles flying through the gap between the bins. The ratio of the non-firing events to the normal firing events was almost constant, $\sim$5%, independently of the kind of targets. These events were rejected, since they have no effects on the value of the target asymmetry.

The multi-firing event was such that more than two bins were fired. This was caused by an accidental firing of bins coincidenced with a normal event. The ratio of the multi-firing events to the normal events varied, 2 - 7%, with the kind of targets and the condition of the beam. These events were not rejected but counted as good events in the way mentioned later (§3 - 2 - 5(a,b)).

(b) π^o counter

As the hodoscopes $HX_{A,B}$ and $HY_{A,B}$ in the π^o counter detected e^+e^- showers spread spacially, normal firing was defined by following criterions: For $HX_{A,B}$ one or adjacent two scintillators should be fired, and for $HY_{A,B}$ less than adjacent three scintillators should be fired.

Abnormal firing patterns were non-firing and multi-firing. The non-firing was considered to be due to some incomplete performance of the electronics in the data acquisition system, because the scintillation counters in the hodoscopes were overlapped and no particles flew through the gap between them. Multi-firing were caused in the same way as in the hodoscopes H_1 and H_2. The respective event ratios to the normal firing events were 20% and 10%. These bad events were added to the normal events in the fashion mentioned later (§3 - 2 - 5(c)).

3 - 2 - 4. π^o events

For the $\gamma \cdot \gamma$ detection π^o events were selected by following conditions,

(1) the two photon events (γ_A, γ_B in §2 - 5) must be coincidenced within 6 nsec,

(2) firing patterns in $HX_{A,B}$ and $HY_{A,B}$ must be normal ones,

(3) the value of

$$\frac{(k_A - k_A')^2}{k_A} + \frac{(k_B - k_B')^2}{k_B}$$

must be smaller than a threshold, which was settled so that events with effective mass of the two photons below 100 MeV

might be reduced (fig. 28). k_A and k_B are energies of photons, and k_A' and k_B' are measureed photon enrgies, which differ from k_A and k_B because of bad energy resolutions of lead glass Cerenkov counters (§4 - 2).

3 - 2 - 5. Correction for accidental coincidences

Triggered events were composed of prompt coincidences and accidental coincidences. The amount of accidental coincidences was evaluated according to couting numbers of delayed coincidence.

(a) $\gamma p \to \pi^+ n$

Events in accidental coincidence were subtracted from those in prompt coincidence,

$$PI^+_{Ni} - PI^+_{di} \cdot \left(1 - \frac{PI^+_Z}{PI^+_{Ni}}\right) , \qquad (3\text{-}1)$$

where

$$PI^+_d = T_{1d} \cdot T_2 \cdot T_3 \cdot \overline{(T \cdot C_G)} + T_1 \cdot T_2 \cdot T_{3d} \cdot \overline{(T \cdot C_G)} ,$$

The meanings of subscipts are

i : number of data point,

N : normal firing events,

Z: non-firing events.

For delayed coincidence events the signals in hodoscopes were not fed to the fast logic system in a normal timing. Therefore the recorded firing pattern was the non-firing. In order to get rid of 'true' non-

firing events (§3 - 2 - 3(a)) the ratio of the non-firing events to the normal firing events in delayed coincidence was assumed to be equal to that in prompt coincidence.

Multi-firing events were added to normal firing ones by multiplying

$$1 + \frac{PI^{+}_{M}}{PI^{+}_{N}} ,$$

where M means multi-firing events. The resultant counting number was

$$N_i = PI^{+}_{Ni} \cdot (1 - \eta_d) \cdot (1 + \eta_M) , \qquad (3\text{-}2)$$

where

$$\eta_d = \frac{PI^{+}_{d}}{PI^{+}_{N}} \cdot \left(1 - \frac{PI^{+}_{Z}}{PI^{+}_{N}} \right) , \qquad (3\text{-}3)$$

$$\eta_M = \frac{PI^{+}_{M}}{PI^{+}_{N}} . \qquad (3\text{-}4)$$

(b) $\gamma p \rightarrow \pi^{o} p \ (p \cdot \gamma)$

Counting rates of accidental coincidences $P \cdot \gamma_{Cd}$ and $P_d \cdot \gamma_C$ to that of $P \cdot \gamma_C$ was 10 - 30%. These accidental coincidences were mainly due to background photons below 100 MeV detected in the gamma counter, and were reduced to 1 - 9% in the off-line analysis by setting the threshold on pulse heights in the counter C_C.

The corrections were performed considering abnormal firing patterns in the hodoscopes H_1 and H_2, because the ratio of abnormal firing events to normal firing ones was larger in delayed coincidence than in prompt

coincidence; 37% at maximum for the former and 18% at maximum for the latter. For the delayed coincidence $P\cdot\gamma_{Cd}$ the firing pattern of the hodoscopes was fed to the fast logic system in a normal timing but the pulse height in the Cerenkov counter C_C was not. For $P_d\cdot\gamma_C$ the pulse height was fed in a normal timing but the firing pattern was not. Therefore the counting number was corrected, considering the multi-firing events as follows,

$$N_i = (P\cdot\gamma_C)_{Ni}\cdot(1 + \eta_M) - (P\cdot\gamma_{Cd})_{Ni}\cdot\eta_{dT}\cdot(1 + \eta_{dM}) \qquad (3\text{-}5)$$

where N_i : corrected counting number,

$$\eta_M = \frac{(P\cdot\gamma_C)_{MT}}{(P\cdot\gamma_C)_T} , \qquad (3\text{-}6)$$

$$\eta_{dM} = \frac{(P\cdot\gamma_{Cd})_M}{(P\cdot\gamma_{Cd})} , \qquad (3\text{-}7)$$

$$\eta_{dT} = \frac{(P_d\cdot\gamma_C)_T}{(P_d\cdot\gamma_C)} . \qquad (3\text{-}8)$$

The meanings of subscripts are

N : normal firing events,

M : multi-firing events,

T : events with pulse heights in C_C above the threshold.

Two subscripts mean a logical product. Numerical values of correction factors were

η_M, η_{dM} 2 - 13% ,

η_{dT} 11 - 31% .

The rate of accidental coincidence, (the 2nd term)/(the 1st term) in

eq. 3-1, was 1 - 9%.

(c) $\gamma p \to \pi^{o} p$ $(\gamma \cdot \gamma)$

Accidental coincidence events should be subtracted as follows,

$$N_i = (\gamma \cdot \gamma)_{Ni} \cdot (1 + \eta_B) - (\gamma \cdot \gamma)_{di} \cdot (1 + \eta_B) \ , \tag{3-9}$$

where

$$(\gamma \cdot \gamma)_N = \gamma_A \cdot \gamma_B \ , \tag{3-10}$$

$$(\gamma \cdot \gamma)_d = \frac{1}{2} (\gamma_{Ad} \cdot \gamma_B + \gamma_A \cdot \gamma_{Bd}) \ , \tag{3-11}$$

$$\eta_B = \frac{(\gamma \cdot \gamma)_B}{(\gamma \cdot \gamma)} \ , \tag{3-12}$$

B : bad firing events.

For delayed coincidence events, however, neither the event selection according to the effective mass distribution of two photons nor reconstruction of kinematical quantitites could not be performed, since neither firing patterns of hodoscopes nor pulse heights of the Cerenkov counters were not recorded by the computer. As $(\gamma \cdot \gamma)_{di}$ could not obtained directly, it was estimated by assuming that the distribution of kinematical quantitites of $(\gamma \cdot \gamma)_d$, e.g. effective mass, are similar to that of $(C \cdot C)_d$, where $(C \cdot C)$ means coincidenced events of charged particles (electrons or positrons) detected in the two gamma counters.

$$(\gamma \cdot \gamma)_{di} \to (\gamma \cdot \gamma)_{dT} \frac{(C \cdot C)_{Ni}}{(C \cdot C)_T} \ , \tag{3-13}$$

where T means a total counts including normal and bad events. Consequently

$$N_i = (\gamma\cdot\gamma)_{Ni}\cdot(1+\eta_B) - (C\cdot C)_{Ni}\cdot\eta_{dC}\cdot(1+\eta_{CB}) \ , \quad (3\text{-}14)$$

$$\eta_{dC} = \frac{(\gamma\cdot\gamma)_{dT}}{(C\cdot C)_T} \ , \quad (3\text{-}15)$$

$$\eta_{CB} = \frac{(C\cdot C)_B}{(C\cdot C)} \ , \quad (3\text{-}16)$$

The accidental rates was 2 - 10%, and the averaged value was 5%.

3 - 2 - 6. Correction for beam doze

There was a loss of incident photons because of their conversion into electron-positron pairs in the target and walls of the cryostat. These pairs were deflected in the field of the PT magnet and did not inject into the thick-walled ionization chamber. To obtain a beam intensity at the target point, a measured beam monitor count was corrected by conversion rates, which were evaluated to be 7.4% with a target, and 0.6% without a target. Though these values have uncertainties originated from those in the density of the target and effect on the target asymmetry was negligibly small.

3 - 3. Rejection of competing process

In order to reduce systematic errors of the target asymmetries the single pion photoproduction processes were discriminated from their competing processes:

(1) multi-pion photoproduction processes,

$\gamma p \to \pi^+\pi^o n$, $\pi^+\pi^- p$, $\pi^+\pi^o\pi^o n$, etc. for $\pi^+ n$,

$\gamma p \rightarrow \pi^o\pi^o p$, $\pi^o\pi^+\pi^- p$, $\pi^o\pi^o\pi^o p$, etc. for $p\cdot\gamma$,

$\gamma p \rightarrow \pi^o\pi^o p$, $\pi^o\pi^+ n$, $\pi^o\pi^+\pi^- p$, $\pi^o\pi^o\pi^+ n$, etc. for $\gamma\cdot\gamma$,

(2) eta meson photoproduction process,

$\gamma p \rightarrow \eta p$ for $p\cdot\gamma$ and $\gamma\cdot\gamma$,

(3) proton Compton process,

$\gamma p \rightarrow \gamma p$ for $p\cdot\gamma$.

(a) $\gamma p \rightarrow \pi^+ n$

The multi-pion processes were rejected completely by choosing the end-point energy of the bremsstrahlung gamma beam. When production angles and momenta of pions are measured, the threshold energy of the photon beam for the multi-pion (n pions, $n \geq 2$) processes is

$$E_\gamma^{th} = \frac{M_N E_\pi + (n-1)M_\pi M_N + (n^2/2 - n)M_\pi^2}{P_\pi \cos\theta_\pi - E_\pi + M_N}, \qquad (3\text{-}17)$$

where M_N : mass of nucleon,

M_π : mass of pion,

θ_π : lab. production angle of pion,

P_π : lab. momentum of pion,

E_π : lab. kinetic energy of pion.

The energy of the incident photon for the single pion photoproduction process is

$$E_\gamma = \frac{M_N E_\pi - M^2/2}{P_\pi \cos\theta_\pi - E_\pi + M_N}. \qquad (3\text{-}18)$$

The relation between the pion momentum and the two photon energies E_γ^{th} and E_γ are illustrated in fig. 29(a). As is apparent in the figure, there are no contaminations of the multi-pion processes, so far as one chooses the end-point energy of the photon beam between E_γ^{th} and the maximum of E_γ, defined by the momentum acceptance of the magnetic spectrometer. Actually the end-point energy was set 30 - 40 MeV above the photon energy range to be measured.

(b) $\gamma p \rightarrow \pi^o p$ $(p \cdot \gamma)$

The multi-pion processes were discriminated completely for about half of the data points by the choice of the end-point energy of the beam. For the other data points there were some contaminations.

The threshold energy of the multi-pion (n pions) or eta meson photoproduction processes is

$$E_\gamma^{th} = \frac{M_p E_p - M_p^2 + M_x^2/2}{P_p \cos\theta_p - E_p + M_p} , \qquad (3\text{-}19)$$

where $M_x = nM_\pi$ or M_η (mass of η meson). The photon energy for the single pion process is

$$E_\gamma = \frac{M_p E_p - M_p^2 + M_\pi^2/2}{P_p \cos\theta_p - E_p + M_p} , \qquad (3\text{-}20)$$

where θ_p : lab. production angle of proton,

P_p : lab. momentum of proton,

E_p : lab. kinetic energy of proton.

As is apparent in fig. 29(b), only the $\pi^o\pi^o p$ process was the problem, and the rejection of this process was not complete. For the data points with contaminations, the influence of the multi-pion processes on the target asymmetry was estimated by means of the Monte-Carlo method, as will be discussed later (§5 - 5 - 3).

The contamination of the proton Compton process was eliminated completely by setting the gamma detector off the scattering plane (fig. 19).

§4. Determination of kinematical quantities

The values of the target asymmetry are given in terms of lab. incident photon enrgies and c.m. pion production angles, which were obtained from momentum vectors of pions for $\gamma p \to \pi^+ n$ and $\pi^o p$ ($\gamma \cdot \gamma$), or protons for $\gamma p \to \pi^o p$ ($p \cdot \gamma$). Lab. photon energies are given by momentum vectors of pions as eq. 3-7, and by those of protons as eq. 3-8. The production angles of pions in the c.m. system are

$$\theta_\pi^{cm} = \tan^{-1} \frac{P_\pi \cos\theta_\pi}{\gamma(P_\pi \cos\theta_\pi - \beta E_\pi)} \qquad \text{for pion detection,} \quad (4\text{-}1)$$

$$\theta_\pi^{cm} = -\tan^{-1} \frac{P_p \cos\theta_p}{\gamma(P_p \cos\theta_p - \beta E_p)} \qquad \text{for proton detection,} \quad (4\text{-}2)$$

where

$$\beta = \frac{E_\gamma}{E_\gamma + M_p}, \qquad \gamma = 1/\sqrt{1 - \beta^2}\ . \qquad (4\text{-}3)$$

4 - 1. Detection in the magnetic spectrometer ($\pi^+ n$ and $p \cdot \gamma$)

Momentum vectors of positive pions or protons were determined from firing patterns in the hodoscopes H_1 and H_2. Simulations using the Monte-Carlo method were performed in the determination, because

(1) lab. production angles could not be determined only by the hodoscope H_1, because the trajectires of particles were deflected in the magneitc field of the PT magnet,

(2) lab. momenta could not be determined only by the hodoscope H_2, because it was not set on the focal plane of the momen-

tum analyzing magnet,

(3) target and its surroundings, i.e. complex-shaped walls of the cryostat, were so thick that energy losses and multiple scattering of particles in them were not negligible.

In the simulations particles with certain values of momenta and production angles were produced at random. In order to investigate firing patterns in the hodoscopes H_1 and H_2, trajectries of particles were calculated taking account of

(1) deflections in magnetic fields of the PT magnet and the momentum analyzing magnet,

(2) energy losses,

(3) Coulomb multiple scattering in the target and its surroundings.

These events were accumulated, and distributions of momenta and production angles, as well as their resolutions, were determined. Details on the simulation are described in appendix 4.

For sufficient small statistical errors and suitable spacing of data points, some combinations of channels in the hodoscopes were added to compose a data point. Additons were performed so that resolutions of incident photon energies might be smallest and steps of incident photon energies might be 20 - 50 MeV for $\pi^+ n$, and $\sim$40 MeV for $\pi^o p$. Resolutions of incident photon energy and pion production angle for each data point are summarized in tables 10(a) - (c). Typical resolutions of the kinematical quantities in the $p \cdot \gamma$ measurement are shown in table 7. Figures 30(a) - (c) show the distributions of E_γ and θ_π^{cm} for data points, and fig. 31 the range of kinematical quantities mea-

sured in a data set.

4 - 2. Detection in the π^o counter

Lab. production angles of the neutral pions were determined by the hodoscopes $HX_{A,B}$ and $HY_{A,B}$. The momenta were calculated according to energies and opening angle of the both photons from the decay of the neutral pions. As the uncertainty of the photon energies were larger than 20%, the momentum should be calculated making use of the opening angle between the two photons, which was determined to the accuracy of ±1%.

There is a following relation among the three values,

$$k_1 \cdot k_2 = \frac{M_\pi^2}{2(1 - \cos\psi)} = A \ , \qquad (4\text{-}4)$$

where k_1, k_2 : energies of the photons,

ψ : opening angle,

M_π : mass of the neutral pions.

k_1 and k_2 are on a hyperbola defined by A determined by ψ (fig. 32). For observed photon energies k_1' and k_2', however, this equation does not hold because of bad resolutions of the photon energies, i.e. k_1' and k_2' are off the hyperbola. The most probable values of photon energies k_1 and k_2, on the hyperbola, are presumed to minimize

$$\frac{(k_1 - k_1')^2}{[\sigma(k_1)]^2} + \frac{(k_2 - k_2')^2}{[\sigma(k_2)]^2} \ , \qquad (4\text{-}5)$$

where $\sigma(k_i)$ is the resolution of photon energies, approximated as

$$\sigma(k_i) \propto 1/\sqrt{k_i} \ . \tag{4-6}$$

Then k_1 and k_2 are given by

$$k_1 = \sqrt{\frac{k_1'^2 + A}{k_2'^2 + A}}\, A \ , \quad k_2 = \sqrt{\frac{k_2'^2 + A}{k_1'^2 + A}}\, A \ . \tag{4-7}$$

The momentum is obtained by

$$P_\pi = \sqrt{k_1^2 + k_2^2 + 2k_1k_2 \cos\psi} \ . \tag{4-8}$$

The resolutions of the production angle and momentum were less than ±0.7% and ±2.2%, respectively.

§5. Data reduction

5 - 1. Target polarization

Target polarization P_T (appendix 3) is given by

$$P_T = \frac{S}{S_{TE}} P_{TE} \eta_r \eta_d , \qquad (5\text{-}1)$$

with two correction factors,

η_r : depolarization due to radiation damage,

η_d : contribution of the dispersion term.

(1) S

The base line of the NMR signal was determined by fitting a line to the straight part of the signal. The integrated value S depended slightly on the number of channel used in the fit. Its deviation was smaller than ±0.5%.

(2) S_{TE}

As the S/N ratio of a thermal equilibrium signal was small, the integration was performed carefully. The thermal equilibrium state of the spin system was confirmed by the saturated values of S_{TE}. It took about an hour for the system to reach the thermal equilibrium at a temperatures of 0.8 - 0.9 K. Signals without a big noise nor distortion were selected among those saturated completely. The values of S_{TE} deviated within ±2% around the average value. The value S_{TE} of a signal changed about ±2% with the number of channels used in the determination of a base line. Therefore uncertainty of S_{TE} was estimated to be ±3%.

(3) P_{TE}

The polarization P_{TE} at the thermal equilibrium was obtained by magnetic field and temperature,

$$P_{TE} = \tanh \frac{\mu H}{kT} , \qquad (5\text{-}2)$$

where μ : magnetic moment of proton,

k : the Boltzmann constant.

The magnetic field was determined by measuring the NMR frequency with a negligibly small uncertainty. The typical frequency was 104.85 MHz (2.46 T). The temperature was obtained from the ^{3}He vapor pressure measured with a McLeod gauge. The typical value of the temperature was 0.86 K (4.1 torr). Since the error of the temperature was ±0.5%, that of P_{TE} was also ±0.5%.

(4) η_r

A target polarization decreases due to the radiation damage. The polarization after the irradiation of a radiation doze of ϕ is

$$P_{rad} = P_{int} \exp(-\phi/\phi_o) , \qquad (5\text{-}3)$$

where P_{int} is the initial polarization, and ϕ_o is a damping factor. As the beam cross section was smaller than that of the target, the observed polarization P_{obs} is

$$P_{obs} = (1 - \eta_b) P_{int} + \eta_b P_{rad} \qquad (5\text{-}4)$$

$$= [(1 - \eta_b) \exp(\phi/\phi_o) + \eta_b] P_{rad} , \qquad (5\text{-}5)$$

where η_b is defined as

$$\eta_b = \int_{V_b} H'^2(\vec{r})\, d\vec{r} \;/\; \int_{V_t} H'^2(\vec{r})\, d\vec{r} \;, \tag{5-6}$$

with V_b : target volume irradiated by the beam,

V_t : total target volume,

H' : rf magnetic field induced by the NMR coil.

Define η_r as

$$\eta_r = 1/[(1 - \eta_b)\, \exp(\phi/\phi_o) + \eta_b] \;. \tag{5-7}$$

Then

$$P_{rad} = \eta_r\, P_{obs} \;. \tag{5-8}$$

The value of ϕ_o was calculated to be $(5.9 \pm 1.7) \times 10^{14}$ eq.q./cm^2 from that presented by the Bonn group [51], taking into account the difference of target lengths. η_b was estimated to be 0.3 ± 0.1 according to a numerical integration of eq. (5-6).

The error of η_r is originated from ambiguities of ϕ_o and η_b, and grows large as ϕ increases. Therefore the target was changed after irradiation of 0.5×10^{14} eq.q./cm^2. With this irradiation the error of η_r was $\pm 2\%$.

(5) η_d

The NMR signal detected by the Q-meter circuit contains a small contribution of the dispersion part χ' of an rf susceptibility and the higher order of the absorption part χ'' (appendix 3, eq. A3-8). This effect is appreciable for the enhanced signal, but not for the thermal

equilibrium signal. This contribution was calculated to obtain a correct target polarization.

The dispersion term χ' was calculated from χ'' by means of the dispersion relation

$$\chi'(\omega) = \frac{P}{\pi} \int_0^\infty \frac{\chi''(\omega')}{\omega' - \omega} d\omega' \quad . \tag{5-9}$$

$\chi''(\omega')$ was approximated by the observed NMR signal, a integration of the signal recorded on a magnetic tape. The intergration was carried out by a computer program. Putting $\chi'(\omega)$ and $\chi''(\omega)$ into eq. A3-8 in appendix 3 and setting the values of r and Q from the characteristic curve of the Q-meter circuit, the intergration of $|Z|$ was evaluated. Comparing this value with the integration of the observed NMR signal, the value of η_d turned out to be 1 ± 0.044. (+/- is for positive/negative polarization, where the positive direction is defined by that of polarization at thermal equilibrium.)

The error of η_d was originated from uncertainties of R and Q, and estimeated to be $\Delta\eta_d/\eta_d = \pm 2\%$.

The averaged polarization during the experiment was 65%, and the maximum was 73%. The error $\Delta P_T/P_T$ was ±4%. The error of each term is listed in table 8.

5 - 2. Polarized target asymmetry

Experimental data for one data set were collected through many runs. Target polarizations (absolute values and polarities) and irra-

diations of the gamma beam differed in runs. Therefore the target asymmetry was caluculated by means of the least square method, instead of using event rates and target polarizations averaged over runs.

Let x_i be an element of a population, the distribution of which is a Gaussian type with a central value x and a standard deviation Δx_i. A probability of a sampling $\{x_i : i = 1, \ldots, N\}$ is

$$P(x) = \prod_{i=1}^{N} \frac{1}{\Delta x_i \sqrt{2\pi}} \exp\left\{-\frac{1}{2}\left(\frac{x_i - x}{\Delta x_i}\right)^2\right\} \quad . \tag{5-10}$$

P(x) takes the maximum value for such x that

$$\frac{d}{dx} \sum_{i=1}^{N} \left(\frac{x_i - x}{\Delta x_i}\right)^2 = 0 \quad . \tag{5-11}$$

Then

$$x = \frac{\sum_{i=1}^{N} x_i/(\Delta x_i)^2}{\sum_{i=1}^{N} 1/(\Delta x_i)^2} \quad , \tag{5-12}$$

$$(\Delta x)^2 = \sum_{i=1}^{N} \left(\frac{\partial x}{\partial x_i}\right)^2 (\Delta x_i)^2 \tag{5-13}$$

$$= \frac{1}{\sum_{i=1}^{N} 1/(\Delta x_i)^2} \tag{5-14}$$

Using above equations, target asymmetry T and its error ΔT were calculated from T_i's and ΔT_i's obtained from data collected in a run. As is clear from eqs. 5-12 and 5-14,

$$T_i = \frac{1}{N_o\ R\ P_i}\left(\frac{N_i}{M_i} - N_{NE} - N_o\right) \quad , \tag{5-15}$$

$$(\Delta T_i)^2 = \left(\frac{1}{N_o\ R\ P_i}\right)^2 \left\{\left(\frac{\Delta N_i}{M_i}\right)^2 + (\Delta N_{HE})^2 + \left(\frac{N_i/M_i - N_{HE}}{N_o}\Delta N_o\right)^2\right\}$$

$$+ \left(T_i \frac{\Delta R}{R}\right)^2 \quad , \tag{5-16}$$

where N_i : yields from polarized targets (contribution of liquid ^{3}He is included),

M_i : irradiation of the gamma beam,

N_{HE} : yields from liquid ^{3}He per unit beam irradiation,

N_o : counting from unpolarized target per unit beam irradiation (contribution of liquid ^{3}He is not included),

R : hydrogen yield ratio,

P_i : target polarization.

ΔN_i etc. mean statistical errors,

$$\Delta N_i \simeq \sqrt{N_i} \propto \sqrt{M_i} \quad . \tag{5-17}$$

As the main term of eq. 5-16 was the first term,

$$(\Delta T_i)^2 \simeq \left(\frac{N_i}{N_o\ R\ P_i\ M_i}\right)^2 \propto \frac{1}{P_i^2\ M_i} \quad . \tag{5-18}$$

Therefore T was given from eq. 5-12 by

$$T = \frac{\sum_{i=1}^{N} P_i N_i - (N_o + N_{HE}) \sum_{i=1}^{N} P_i M_i}{N_o\ R \sum_{i=1}^{N} P_i^2\ M_i} \quad . \tag{5-19}$$

Deviation of T, R and N_{HE} will be discussed later.

For the case target polarization varied appreciablby during a run, the run was divided further into mini-runs, so that variation of target polarization during a mini-run might be smaller than 0.1. For a data set where target were changed T's and ΔT's for each target were averaged in the fashion of eqs. 5-12 and 5-14.

5 - 3. Hydrogen yield ratio

The hydrogen yield ratio R was obtained from R_o,

$$R_o = \frac{N_P - N_G}{N_P} , \tag{5-20}$$

where N_P : yields from polyethylene target (CH_2),

N_G : yields from graphite target (C),

(The numbers of carbon atoms in the both targets were normalized to be equal.)

N_P and N_G were measured as mentioned above. R was evaluated by making correction for R_o, considering of contributions of oxgen and nitrogen nuclei, contained in butanol-water mixture and porphyrexide. The target was assumed to be X_5H_{10}. X is a assumed nucleus with a mass number of A_{eff} = 13.0, which was calculated considering the composition of the target material. The dependence of a cross section from nucleus on its mass number was assumed to be proportional to $A^{2/3}$. Then R was given by

$$R = R_o \, \eta_R , \tag{5-21}$$

$$\eta_R = \{1 + \{(\frac{A_{eff}}{A_C})^{2/3} - 1\}(1 - R_o)^{-1}\}, \qquad (5\text{-}22)$$

$$A_C = 12 \ . \qquad (5\text{-}23)$$

The respective averaged values of R_o's and η_R's were

0.4 ,	0.968	for $\pi^+ n$,
0.8 ,	0.989	for $p \cdot \gamma$,
0.15,	0.955	for $\gamma \cdot \gamma$.

The values of R's are shown in figs. 33(a) - (c).

5 - 4. Events from liquid ^{3}He

N_{HE} is given by

$$N_{HE} = \frac{\sum_{i=1}^{N} N_i - N_o R T \sum_{i=1}^{N} M_i P_i}{\sum_{i=1}^{N} M_i} \ . \qquad (5\text{-}24)$$

N_{HE} cannot be evaluated unless T is known, and vice versa. Therefore the iteration method was used. In the first step T was calculated setting $N_{HE} = 0$. Then N_{HE} was evaluated with this T. This procedure was repeated until these values converged:

$$N_{HE}^{(0)} = 0 \rightarrow T^{(0)} \rightarrow N_{HE}^{(1)} \rightarrow T^{(1)} \rightarrow \cdots\cdots$$

Since $T^{(n)}$ $(n \geq 2)$ was almost constant, $T^{(2)}$ was taken as the final value. Yields from liquid ^{3}He was about 3% of those from the whole of target materials.

5 - 5. Errors of the polarized target asymmetry

5 - 5 - 1. Statistical error

The statistical error was obtained by differentiating eq. 5-19 by counting numbers,

$$(\Delta T_S)^2 = (\Delta T_1)^2 + (\Delta T_2)^2 + (\Delta T_3)^2 + (\Delta T_4)^2 , \qquad (5\text{-}25)$$

$$(\Delta T_1)^2 = \sum_{i=1}^{N} \left(\frac{P_i}{N_o R \sum_{j=1}^{N} P_j M_j} \right)^2 (\Delta N_i)^2 , \qquad (5\text{-}26)$$

$$(\Delta T_2)^2 = \left(\frac{\sum_{i=1}^{N} P_i N_i - N_{HE} \sum_{i=1}^{N} P_i M_i}{N_o^2 R \sum_{i=1}^{N} P_i^2 M_i} \right)^2 (\Delta N_o)^2 , \qquad (5\text{-}27)$$

$$(\Delta T_3)^2 = \left(\frac{\sum_{i=1}^{N} P_i N_i - N_o \sum_{i=1}^{N} P_i M_i}{N_o R^2 \sum_{i=1}^{N} P_i^2 M_i} \right)^2 (\Delta R)^2 = T^2 \left(\frac{\Delta R}{R} \right)^2 \qquad (5\text{-}28)$$

$$(\Delta T_4)^2 = \left(\frac{\sum_{i=1}^{N} P_i M_i}{N_o R \sum_{i=1}^{N} P_i^2 M_i} \right)^2 (\Delta N_{HE})^2 . \qquad (5\text{-}29)$$

The statistical errors of T are given in tables 9 - 11.

5 - 5 - 2. Error from that of target polarization

Target polarizations for up and down are assumed to be equal in

magnitude for brevity. Then

$$T = \frac{\varepsilon}{P_T} , \tag{5-30}$$

where

$$\varepsilon = \frac{\sum_{i=1}^{N} \xi_i \left[N_i - (N_o + N_{HE}) M_i \right]}{N_o R \sum_{i=1}^{N} M_i} , \tag{5-31}$$

where ξ_i = 1/-1 for up/down polarization,

P_T : target polarization > 0.

The error of T is

$$(\Delta T)^2 = \left(T \frac{\Delta \varepsilon}{\varepsilon} \right)^2 + \left(T \frac{\Delta P_T}{P_T} \right)^2 . \tag{5-32}$$

The first term is the statistical error evaluated above, and the second term, $(\Delta T_p)^2$, is an error from that of target polarization. As $\Delta P_T/P_T$ = ±4%, ΔT_p was less than ±4%.

$\Delta P_T/P_T$ was evaluated including the error originated from the correction for the effect of the dispersion term. The effect of the contribution of the dispersion term to the target asymmetry was a second-order correction, i.e. about 0.4% for η_d = 1.04, because the measurements with up and down polarizations were performed in the same weight in the beam irradiation. Therefore the effect of the error of η_d, $\Delta\eta_d/\eta_d$ = ±1.5%, on the target asymmetry was less than ±0.2%, and was negligible.

5 - 5 - 3. Error due to competing processes

In the measurement for $\pi p \to \pi^o p$ there was a contamination of protons produced in $\pi^o\pi^o p$ process. The effect on the target asymmetry was numerically evaluated.

Define a contamiantion ratio C,

$$C = \frac{Y_{2\pi}}{Y_{\pi}} , \tag{5-33}$$

where Y_{π} and $Y_{2\pi}$ are respective event rates for $\gamma p \to \pi^o p$ and $\pi^o\pi^o p$. Then an observed target asymmetry T_{obs} is

$$T_{obs} \simeq T - C(T - T_D) , \tag{5-34}$$

where T_D is a target asymmetry for $\pi^o\pi^o p$. ΔT_D, the error of the target asymmetry due to the contamination of the double pion process, was defined as the maximum value of $C|T \pm 1|$, assuming $T_D = \pm 1$ as the worst case.

The contamination ratio C was calculated from

$$Y_{\pi} = n\ell \frac{Q}{E_{\gamma}^{\pi}} B(E_{\gamma}^{\pi}) \Delta E_{\gamma}^{\pi} \frac{d\sigma_{\pi}}{d\sigma^*} \Delta\Omega \eta_{\pi} , \tag{5-35}$$

$$Y_{2\pi} = n\ell \frac{Q}{E_{\gamma}^{2\pi}} B(E_{\gamma}^{2\pi}) \Delta E_{\gamma}^{2\pi} \frac{\sigma_{2\pi}}{4\pi} \frac{R_S}{R_T} \Delta\Omega \eta_{2\pi} , \tag{5-36}$$

where
- n : density of the target (protons/cm^3),
- ℓ : length of the target (cm),
- Q : beam intensity (eq.q./sec),
- $E_{\gamma}^{\pi,2\pi}$: incident photon energies,
- $B(E_{\gamma}^{\pi,2\pi})$: spectrum function of bremsstrahlung photon beam,

$\Delta E_{\gamma}^{\pi,2\pi}$: ranges of $E_{\gamma}^{\pi,2\pi}$, defined by the momentum acceptance of the magnetic spectrometer,

$d\sigma_{\pi}/d\sigma^*$: differential cross section for $\gamma p \to \pi^o p$,

$\sigma_{2\pi}$: total cross section for $\gamma p \to \pi^o \pi^o p$,

$\partial\Omega^*/\partial\Omega$: Jacobian for a transformation from the c.m. to the lab. system,

$\Delta\Omega$: solid angle of the magnetic spectrometer,

$4\pi R_T$: total invariant phase volume for three bodies,

$\Delta\Omega R_S$: invariant phase volume defined by the acceptance of the magnetic spectrometer,

$\eta_{\pi,2\pi}$: detection efficiencies of the gamma counter.

Calculation of Y_{π} was no problem. For double-pion process, however, accumulation of experimental data is so poor that the total cross section $\sigma_{2\pi}$ was assumed to be 10 μbarn independently of incident photon energy. The distribution of momentum vectors of the three particles was assumed to be uniform in the invariant phase space. Detection efficiencies $\eta_{\pi,2\pi}$ were defined by the ratio of the numbers of photons detected in the gamma detector to those of produced neutral pions. They were obtained by means of the Monte-Carlo method.

(a) $p \cdot \gamma$

The respective values of η_{π} and $\eta_{2\pi}$ were 10 - 20% and 2 - 15%.

The double pion process was rejected, though not completely, making use of the difference of pulse heights in the gamma counter, because pulse heights originating from the double-pion process distri-

bute in the lower energy reange. The difference of distributions of pulse heights in the $\pi^o p$ and $\pi^o \pi^o p$ processes are shown in fig. 27. ΔT_D was less than ±2%.

Though the estimation was based on several assumptions, this evaluation seemed correct, because

(1) two kinds of target asymmetries, one was derived from data free from the double pion process and the other was not, did not differ from each other systematically,

(2) calculated differential cross sections (appendix 5) were not prominently larger than existing data.

(b) $\gamma \cdot \gamma$

The respective values of $\Delta\Omega\eta_\pi$ and $\Delta\Omega\eta_{2\pi}$ were $2 - 3 \times 10^{-7}$ and $1 - 9 \times 10^{-9}$. ΔT_D was less than ±6%.

6. Results and discussion

Resulting values of the target asymmetry and its statistical error are listed in tables 9 - 11.

Statistical errors were reduced less than ±7% at most of the data points, except at $\theta_\pi^{cm} = 30°$ for $\gamma p \to \pi^o p$ detecting double photons from the decay of neutral pions. Systematic errors due to competing processes and the error of target polarization were examined as mentioned above, and turned out to be small enough. The reliability of these data were confirmed by calculating differential cross sections for $\gamma p \to \pi^+ n$ and $\pi^o p$ processes using data with polyethylene and carbon targets by the subtraction method (appendix 5).

(a) $\gamma p \to \pi^+ n$

Angular distributions are shown in figs. 34(a) - (r), and energy dependences are in figs. 35(a) - (i). Existing data of Nagoya-Osaka [44,45], Bonn [8,51,52] and Daresbury [16] are also plotted. The data by the Bonn group on the angular distribution at $E_\gamma = 0.7$ GeV, with small statistical errors, agree well with the present results (fig. 34 (k)). The Daresbury data at 75°, 90° and 150° are also consistent (figs. 34(k) - (m)). The previous data of Nagoya-Osaka at 90° and 130° are consistent except for two data points of 130° at energies 0.63 and 0.67 GeV, where they are slightly smaller than the present data.

Predicted curves by phenomenological analyses of Metcalf-Walker (MW) [27], Moorhouse-Oberlack-Rosenfeld (MOR) [30] and Nagoya [28] are plotted in the figures. As a whole the present data agree well with

the Nagoya analysis. In the lower energy region below 0.5 GeV these three analyses consist with one another and with the present results, except at forward angles of 0.41 and 0.47 GeV, where the experimental values are rather small (figs. 34(b) - (d)). From 0.53 to 0.71 GeV (figs. 34(f) - (k)) MW predicts larger asymmetries at backward angles than MOR and Nagoya. At higher energies above 0.75 GeV the Nagoya analysis gives smaller values at backward region and consists with experimental data. Particularly higher than 0.92 GeV it succeeds in reproducing the structures of the data (figs. 34(p) - (r)). The excellency of this analysis at backward angles are well shown in figs. 35(f) - (i).

A tentative analysis [53] using the present data was performed only for $\gamma p \to \pi^+ n$ process in the similar way to the Nagoya analysis. The resulting radiative decay matrix elements of resonances are listed in table 12 where the results of the Nagoya analysis are also listed for comparison. The results of the new anlaysis are almost the same as those of the Nagoya analysis, except for $S_{11}(1535)$ and $P_{11}(1470)$.

The photocoupling of $S_{11}(1535)$ was incresed 20%. This change improved the energy dependence at 160° above 0.75 GeV be suppressing of a bump around 0.8 GeV, which was produced in the Nagoya analysis by an interference between the Born term and $D_{13}(1520)$ (fig. 36). A flat energy dependence above 0.75 GeV at 80° was reproduced by this modification. Furthermore the data of the anglular distribution of $\Sigma(\theta)$ at 0.7 GeV presented by the Daresbury group was fitted by this increased photocoupling of $S_{11}(1535)$. A shallow dip around 0.6 GeV at 120° was obtained by slightly decreasing the photocoupling of $P_{11}(1470)$ (fig. 37).

(b) $\gamma p \rightarrow \pi^o p$

Resulting angular distributions at various photon energies are shown in figs. 38(a) - (n) with existing data and prediction curves by recent phenomenological analyses. The present data are consistent with existing data, and smooth continuities between them have been obtained. Below 0.8 GeV the analyses by Noelle and Nagoya succeed in reproducing the gross structure of experimental data, whereas MOR fails at backward angles, where it predicts too large negative values. Above 0.85 GeV the Nagoya analysis reproduces fairly well the behaviours of experimental data.

Figures 39(a) - (d) show E_γ-dependence at the four pion production angles. At 30° the present data are nearly 0 below 0.55 GeV and have a broad bump between 0.6 and 0.9 GeV. At the other angles of 80°, 105° and 120° the target asymmetry decreases monotonously from 0 to -0.8 in the photon energy range between 0.4 and 0.6 GeV. At 80°, where a wide energy range was covered by the measurement, a wide dip at 0.6 GeV and a bump at 0.85 GeV were observed. Also at 105° the dip at 0.6 GeV seemed to exist.

At 30° between 0.6 and 0.9 GeV prediction curves by MOR, MW and Nagoya show a large bump of $T \gtrsim 0.7$, which was caused by contributions of high partial waves. The present data, however, are rather small, $T \lesssim 0.5$. Only Noelle's prediction agrees well to the experimental data. Recent data of the differential cross section at forward angles for $\gamma p \rightarrow \pi^o p$ measured at INS [54] supports the superiority of Noelle's analysis to the others.

At 80° every analysis reproduces the gross structure of the present data, though not completely. Prediction curves of MOR and MW are higher than the data, particularly above 0.9 GeV. The Nagoya prediction is good above 0.7 GeV, though it is slightly too low below 0.6 GeV. Noelle's result is fairly good also at this angle. At 105° and 120° analyses by MOR, MW and Noelle reproduce well the data, and that by Nagoya gives too small values.

Let's investigate the effect of resonances on the target asymmetry at 30°. The dotted line in fig. 40 is a calculated curve only by the first and the second resonances given by MW, where the electric Born term was neglected because of its small contribution. The curve increases in the energy range between 0.3 and 0.6 GeV, where the experimental data are nearly 0. From 0.7 to 1.0 GeV it is almost constantly 0 and fails in reproduction of the bump. Then background term was added to the resonance terms. According to the isobar model analyses by MW and Nagoya the E_{0+} term is dominant among background amplitudes in the lower energy region. The dashed line in fig. 40 is a curve by the first and the second resonances and the imaginary part of the E_{0+} background term given by MW. The real part was neglected, because it is almost cancelled by the electric Born term. It is apparent that the E_{0+} background is important for the reproduction of experimental data below 0.55 GeV. At higher energies the curve is too low, so the third resonances are necessary for a fit of experimental data. The solid line in the figure is a curve by the first, the second and the third resonances; $D_{15}(1670)$, $F_{15}(1690)$, $S_{31}(1650)$, $D_{33}(1670)$, $S_{11}(1700)$ and $P_{11}(1780)$.

A big bump is produced at 0.8 GeV, though it is higher than the data. As is apparent in table 1 the photocoupling of $S_{31}(1650)$ by MW is larger than those by others. So this photocoupling was reduced to 0, then the bump became lower (—·— in fig. 40). For good fitting the center of the bump must be shifted to lower energies by 0.1 GeV. As this shift was impossible only by the manipulation of the third resonances, so a rigorous treatment of background terms corresponding higher partial waves are essential.

For 80° the $P_{33}(1232)$ resonance amplitude and the E_{0+} background amplitude are dominant in the lower energy region below 0.6 GeV. Therefore experimental data are expected to be reproduced by these two amplitudes. The dotted lines in figs. 41(a) - (c) are calculated curves by $P_{33}(1232)$ and the imaginary part of E_{0+} background amplitude. The decreasement of experimental data from 0.4 to 0.6 GeV are well reproduced. In order to investigate the effects of the second resonances on the target asymmetry each of them was added to the P_{33} + Im E_{0+} term (fig. 41). It is apparent that $S_{11}(k535)$ and $D_{13}(1520)$ are effective in reproducing the increasement of the asymmetry from 0.6 to 0.9 GeV. The solid lines in the figures are calculated curves by P_{33} + Im E_{0+} + (three second resonances). Though a good agreement with experimental data was obtained at 80°, the curves at 105° and 120° are too low. A good fitting at 105° and 120° can be obtained by P_{33} + (three second resonances) + E_{0+} + (electric Born), taking account of the real part of E_{0+} and the electric Born term (--- in fig. 41). The gross structure above 0.6 GeV at 80° is also reproduced by these terms. A better agree-

ment will be obtained by a complete analysis taking the third resonances into account.

From the above discussions the significance of the present data on $\gamma p \to \pi^o p$ are as follows.

(1) As experimental data below 0.6 GeV at 80°, 105° and 120° can be reproduced by the interference between $P_{33}(1232)$ resonance term and the imaginary part of E_{0+} background term, the E_{0+} background amplitude can be determined accurately based on M_{1+} amplitude of well established $P_{33}(1232)$. This is efficient to improve uncertainty of the coupling constant of $S_{11}(1535)$, which has the largest ambiguity among the second resonances.

(2) Any analyses succeed in fitting neither the experimental data at 30° in the energy region above 0.6 GeV nor those at 80° in the whole energy region from 0.4 to 0.95 GeV. A good fit will be obtained by a treatment of the third resonances and background amplitudes. Therefore the present data are helpful for the determination of these amplitudes.

The accumulation of experimental data of the target asymmetry for $\gamma p \to \pi^+ n$ and $\pi^o p$ processes below 1 GeV has been much improved by the present measurement both in quantity and in quality. The set of data for the $\pi^+ n$ process, in particular, is so complete that further measurement in this energy region is not necessary. Definite photocouplings of the second resonances will be obtained by a phenomenological analysis

using the present data, as is expected form the fact that resulting values of these photocouplings by the tentative analysis for the $\pi^+ n$ process did not differ much from those by the Nagoya analysis. Therefore it is desired to perform a complete analysis for $\gamma p \to \pi^+ n$, $\pi^o p$ and $\gamma n \to \pi^- p$ processes.

The future subject of the pion photoproduction study are as follows.

(1) It is necessary to enrich experimental data of spin parameters for $\gamma n \to \pi^- p$ process, which are poor compared with $\gamma p \to \pi^+ n$ and $\pi^o p$ processes. These data are essential for the improvement of uncertainties in photocouplings of $N^* \to \gamma n$ and for isospin decomposition of resonance amplitudes.

(2) The determination of photocouplings must be developed to the third resonance region. In this energy region it is difficult to extract the photocoupling of each resonance, because there exists many small resonances and the contribution of background grows large. Therefore a complete set of experimental data of differential cross sections and spin parameters for the three processes is much desired.

(3) Background amplitude must be studied. They are essential for a good fit to experimental data. It is necessary to investigate the physical meaning of background terms or what processes contribute to background amplitudes. Properties of amplitudes derived from background processes, for instance energy dependence, must be investigated, and the hypothesis

by Walker that background amplitudes should vary smoothly with energy must be checked. Because photocouplings cannot be extracted accurately without the knowledge on properties of background amplitudes.

Appendix 1. Mechanism of the dynamic nuclear orientation

1. Introduction

When particles with a spin 1/2 are brought into magnetic field, they stay in the two Zeeman energy levels accoring to the Boltzmann distribution. The polarization is

$$P = \tanh(\mu H/kT) ,$$

where μ : magnetic moment of the particle,

k : the Boltzmann constant,

H : magnetic field,

T : temperature.

It takes values for electrons 99.8% and for protons only 0.5% under a condition of $H = 2.5$ T and $T = 0.5$ K.

It is necessary to obtain a high proton polarization for the practical use in high energy physics experiments. A high electron polarization can be transfered to proton spins by making use of a dipole-dopole interaction between proton spins and electron spins. When one applies an rf field of a particular frequency to a spin system of protons and electrons, proton spins pointing, say, upward flip through the interaction with electron spins and point downward. As proton spins interact weakly with the lattice, they have a long relaxation time. Therefore the spins pointing down are accumulated, and a high polarization is attained. This method is called 'dynamic nuclear orientation', and several machanisms have been discussed [55]

2. Solid state effect

When the spins of protons couple to those of electrons through the dipole-dipole interaction, a hyperfine separation is caused in the two Zeeman energy levels of electrons (fig. 42). The resonance width of the electron spins are considered to be narrow with respect to the proton Larmor frequency ν_p. For the case of H = 2.5 T Larmor frequencies of electrons and protons are ν_e = 70 GHz and ν_p = 106 MHz. When microwaves of a frequency $\nu_e - \nu_p$ are irradiated to the spin system, a double-flip transitions $\downarrow\uparrow \rightarrow \uparrow\uparrow$ are induced. ($\uparrow,\downarrow$: electron spins, $\uparrow,\uparrow$: proton spins) Electrons, with a stronger spin-lattice interaction of a relaxation time in the order 1 msec at 1 K, soon fall down their initial energy level. Protons, however, stay their new level, with a long relaxation time of several minutes (fig. 43). This means transitions $\uparrow\uparrow \rightarrow \downarrow\uparrow$. In summary application of microwaves induces transitions,

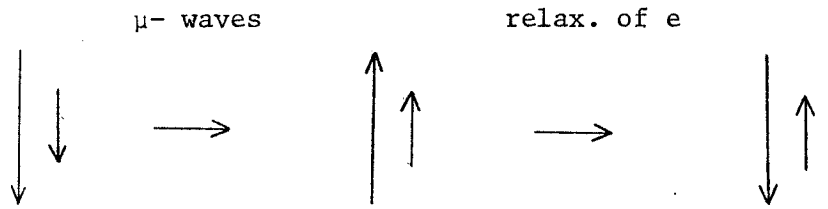

Induced populations in the four energy levels are shown in fig. 42, and the resultant polarization of proton spins P_p is

$$P_p = P_e \simeq 100\%,$$

where P_e is the elelctron polarization. Similarly for the frequency of $\nu_e + \nu_p$,

$$P_p = - P_e \simeq -100\%.$$

3. Cross effect

Consider two electron spin systems S' and S". A particular relationship is assumed between their respective resonance frequencies, ν_e' and ν_e'', which differ precisely by ν_p:

$$\nu_e' - \nu_e'' = \nu_p$$

where electron resonance lines are narrow with respect to ν_p. Cross-relaxation transitions involving one spin in S', one spin in S" and one proton spin

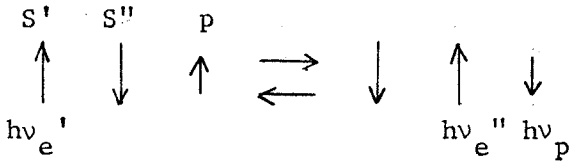

are important, as they conserve the total Zeeman energy.

When one applies an rf field with the frequency ν_e', the spin system S' is saturated, i.e. half of the spins in S' are pointing down, and the rest pointing up. All the spins in S", however, are pointing down. When the spins in S' pointing up, the cross-relaxation transitions in which the proton spin flips from up to down are induced.

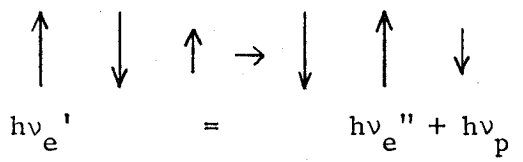

But transitions through which proton spins flip from down to up are forbidden. When a spin in S' is pointing down, transitions with a spin in S" are forbidden, because of angular momentum conservation.

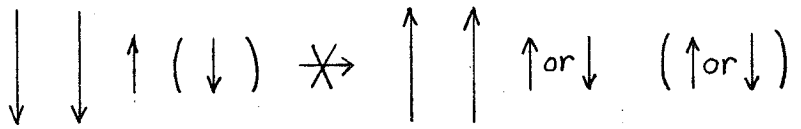

After the cross-relaxation transitions the electron spins in S" go back to down state, and the proton spins stay in the down state, according to their respective short and long relaxation times. Thus this process accumulates the proton spins into the down state, and the proton polarization of -100% is obtained. Similarly with an rf field of a frequency ν_e", the proton spins acquire a polarization of 100%.

4. DONKEY effect

The basis of 'dynamic orientation of nuclei by cooling of electron spin-spin interaction' is the possibility of cooling the electron spin-spin interaction (ESSI) reservoir.

Consider an ESSI reservoir consisting of three eelctron spins, for example. Two different configurationa are available for the case that two of the three spins are pointing up and the other is pointing down.

(1) (2)

The potential energies are

$$V = -\frac{a}{r^3} + \frac{a}{8r^3} - \frac{a}{r^3} = -\frac{15a}{8r^3} \qquad \text{for (1)},$$

$$V = +\frac{a}{r^3} - \frac{a}{8r^3} - \frac{a}{r^3} = -\frac{a}{8r^3} \qquad \text{for (2)},$$

where V : potential energy,

r : distance between the spins,

a : constant.

It is evident that the ESSI reservoir can be cooled or warmed by the rearrangement of the electron spin configuration, where the polarization is conserved. For the description on the energy state of a spin system, a 'spin temerature T_s' is introduced. When the interaction between the spins is negligible, e.g. proton spins, the distribution of the spins are given by the Boltzmann factor, $n_2/n_1 = \exp[-(E_2 - E_1)/kT_s]$.

In the DONKEY effect the ESR line is supposed broad.

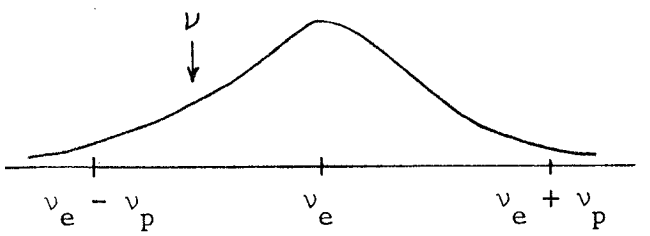

If one applies an rf field of $\nu = \nu_e - \Delta$ ($\Delta > 0$) to the electron spin system the following transitions are induced.

$$h\nu + (ESSI)_I = h\nu_e + (ESSI)_F$$

where ⦚ : irradiated photon,

↑ : electron spins,

Ⓘ, Ⓕ : ESSI reservoir in the initial and the final states.

With this irradiation the energy in the ESSI reservoir is changed:

$$(ESSI)_F - (ESSI)_I = h\nu - h\nu_e$$

$$= - h\nu < 0 .$$

This means the reservoir is cooled through the transitions induced by the irradiation of an rf field. Similarly with $\nu = \nu_e + \Delta$, the reservoir is warmed, that leads to a 'negative' spin temperature.

Introduce the proton spin now. The proton polarization is given by a spin temperature,

$$P_p = \tanh (\mu_p H/kT_s).$$

The spin temperature is determined through heat contact between the proton Zeeman energy (PZE) reservoir and the ESSI reservoir. The mechanism of the heat contact will be discussed later. As mentioned above, with an rf field of $\nu = \nu_e - \Delta$ ($\Delta > 0$), the ESSI reservoir is cooled and kept at a low spin temperature $T_s > 0$, so the proton spin system has a high positive poalrization, where spins pointing up exceed those pointing down. With $\nu = \nu_e + \Delta$, the ESSI reservoir is warmed and the spin temperaure is negative, that leads a negative proton polarization.

The heat exchange between the two reservoirs is induced by an rf field $\nu = \nu_e - \Delta$,

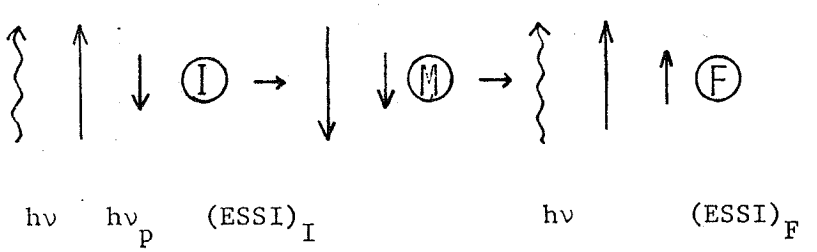

In the first step the spin of the electron flips through the rf field, but that of the proton stays in its initial states. In the second step the electron spin flips back to its initial state, because of the short relaxation time, emitting a photon of ν. Simultaneously the proton spin flips through the dipole-dipole interaction with the electron spin, and stays pointing up are accumulated. The energy difference in the ESSI reservoir is

$$(ESSI)_F - (ESSI)_I = h\nu_p \ .$$

This means the ESSI reservoir is warmed and the PZE reservoir is cooled. As a spin temperature of the both reservoir, after the heat contact, is higher than that of the initial ESSI reservoir, the proton polarization does not attain +100%, in contrast with the solid state effect and the cross effect.

Appendix 2. Details of the cryostat

1. Introduction

A cryostat for high energy physics experiments is required to have a large cooling power for absorbing microwave heating at the target. A sufficient supply of microwave power is necessary for high target polarization and quick reverse of polarization polarity, which are essential for reducing systematic errors of experimental data of the target asymmetry.

A cryostat with a large cooling power can reach a stable operation from room temperature within a short time. This is important for the experiments with a gamma or electron beam, where the target depolarization owing to the radiation damage is a severe problem. Depolarized target must be changed or annealed, at 120 - 130 K for the case of butanol target. For an efficient data acquisition a warmed cryostat must be cooled rapidly to a stable operation.

In a ^{3}He cryostat, ^{3}He gas is cooled and liquefied by liquid and vaporized ^{4}He. Liquid ^{3}He maintains target at low temperatures $\sim$0.5 K. For a large cooling power the Roubeau-type cryostat used in the previous experiment [45] was improved, and a new type cryostat was designed so that ^{3}He and ^{4}He system have a wide contact area for an efficient heat exchange between them.

2. Cooling mechanism

Figure 10 shows the schematic diagram of the cooling machanism of the cryostat, and fig. 44 the flow diagram of ^{3}He and ^{4}He.

Liquid ^{4}He was led to the separator through a transfer tube (fig. 45) from an external dewar. Gaseous ^{4}He in the separator was pumped out by a 15 m^3/h rotary pump (DAIA CRP-250), and liquid ^{4}He flowed into the evaporator through the heat exchanger I, in which the liquid ^{4}He was cooled from 3.5 K to 2.0 K. (In the stage of precooling liquid ^{4}He was led to the evaporator directly through a bypass for rapid cooling.) A 150 m^3/h rotary pump (ULVAC PKS-030) reduced the pressure at the evaporator by pumping out vaporized ^{4}He through the heat exchanger I and a baffled pumping line. In a normal operation the temperature at the evaporator was regulated to be 1.7 - 1.9 K by controling a flow rate of liquid ^{4}He into the evaporator by a needle valve. The flow rate of liquid ^{4}He from the dewar to the separator was regulated by a needle valve in the pumping line between the cryostat and the 15 m^3/h rotary pump.

^{3}He flowed through the inner tube of the tublar heat exchanger, the helix in the separator, the heat exchanger I, the condenser helix, the heat exchanger II and the cavity. The ^{3}He condensed in the condenser helix is cooled from 1.5 K to 1.0 K through the heat exchanger II. The flow rate of the ^{3}He and the vapor pressure at the cavity was regulated by an expansion valve. (A bypass of the heat exchanger II was efficient for the fast cooling of the nose part of the cryostat in the stage of precooling.) The vaporized ^{3}He was pumped out by a 2000 m^3/h cascade pumping system consiting of 2000 m^3/h and 600 m^3/h roots pumps (ULVAC PMB-020A and 006) and a 54 m^3/h rotary pump (Alcatel 2060H) (fig. 44). ^{3}He gas was refreshed by a purifier with charcoal (fig. 46)

operated at the liquid nitrogen temperature, and fed back to the cryostat.

3. Construction of the cryostat

The insulation vacuum was maintained at 10^{-6} - 10^{-7} torr by a 15 m^3/h rotary pump, Alcatel type 2012, in order to reduce heat flow into the cryostat. For this purpose radiation shields I and II, made of copper plated with gold, were installed.

The inner tube of the tublar heat exchanger was made of a stainless steel tube 3 mm in diameter and 1175 cm long. For the outer tube two copper tubes were connected, 4 mm in diameter and 655 cm long, and 5 mm and 520 cm, considering the expansion of the outgoing ^{4}He gas. The tublar heat exchanger was wound about twenty times and fitted to the inner wall of the vacuum jacket. At the middle of the heat exchanger a thermal anchor, normally kept 10 - 20 K, was provided for the cooling of the radiation shield I. Inside the coil of the tube-in-tube heat exchanger five baffles were installed with a distance of 4.5 cm for the Joule-Thomson cooling by the flow of vaporized ^{3}He gas. The tapered pumping line of ^{4}He gas from the evaporator was also connected to these baffles. Twenty small baffles were installed in this line to cool the five baffles by outgoing ^{4}He gas.

The separator contained a helix of stainless steel tube 2 mm in diameter and 300 cm long, where the ^{3}He gas was cooled from 10 K to 4 K. The ^{3}He condenser mounted in the evaporator was a helix made of stainless steel tube of 1.5 mm in diameter and 165 cm long.

In addition to the thermal anchor for the radiation shield I, two thermal anchors were installed near the separator and the evaporator for the cooling of the radiation shield II and the inner wall of the vacuum jacket.

The heat exchanger I consisted of five baffeles. Each of them was made of 1 mm thick copper plate with holes of various diameters as indicated in fig. 47. On each baffle three one-turn stainless steel tubes were soldered. One was for incoming ^{3}He (2 mmϕ), another was for incoming liquid ^{4}He (2 mmϕ) and the other was for outgoing ^{4}He gas (4 mmϕ).

The heat exchanger II consisted of ten 0.8 mm thick copper baffles with the hole patterns shown in fig. 47. On each baffle a one-turn coil of stainless steel tube (1.5 mmϕ) was soldered for the incoming liquid ^{3}He. These baffles were plated with silver to prevent stains and keep good thermal contact with the ^{3}He gas pumped out from the cavity.

4. Operations

Figure 48 shows a typical cooling process of the cryostat. The internal complex was cooled with liquid nitrogen and the target container was packed with target beads. Then the internal complex was mounted in the vacuum jacket. Liquid nitrogen was poured to the nose part through a transfer line for 15 - 20 minutes to cool down the whole complex about 80 K. Liquid nitrogen remaining in the target vessel was vaporized by a heating resistor at the bottom of the cavity, and the gaseous nitrogen was exhausted within 10 - 20 minutes by the 2000 m^3/h

pumping system. After that the supply of liquid ^{4}He and the circulation of ^{3}He were started at the same time. About one hour later the evaporator was filled with liquid ^{4}He, then the bypass was closed and the flow rate of liquid ^{4}He was regulated by the needle valve to keep the evaporator about 1.7 K. The ^{3}He bypass was closed, and the expansion valve was adjusted to the operation temperature of 0.5 K. It took about 1.5 hours to reach a stable operation at 0.5 K from the room temperature.

5. Performances of the cryostat

5 - 1. Cooling power

The maximum cooling power achieved about 200 mW at 0.5 K, and 400 mW at 0.6 K.

The limitation of the cooling power of 200 mW at 0.5 K was defined only by the ^{3}He pumping speed, because no breakdown of the heat exchange was observed. For cooling powers larger than 200 mW the pumping system could not maintain the vapor pressure at the cavity to be 0.1 torr, corresponding to 0.5 K (fig. 49), because of increased vaporization of ^{3}He.

For 400 mW at 0.6 K the limitation was set by the structure of the sealing in the pumping and circulation system of ^{3}He, which was not complete for the pressure higher than 1 atm. For 400 mW the inlet pressure of ^{3}He at the entrance of the cryostat was about 600 torr and the output pressure of the 54 m^3/h rotary pump reached nearly 1 atm. So a further higher power test had not been performed.

5 - 2. Consumption rate of liquid ^{4}He

The minimum consumption rate without a microwave power was 1.6 ℓ/h; 1.3 ℓ/h from the separator and 0.3 ℓ/h from the evaporator. The consumption rate from the separator hardly depended on the flow rate of ^{3}He or a cooling power. The required heat to warm 0.045 g/sec (1.3 ℓ/h in liquid) ^{4}He gas from 4 K to 300 K is 70 W, and the emitted heat by ^{3}He gas of 0.04 g/sec (corresponding to a cooling power of 400 mW) in cooling down from 300 K to 4 K is 83 W. An agreement of the two values means that the incoming ^{3}He gas was cooled efficiently by the outgoing ^{4}He gas through the tube-in-tube heat exchanger, and that little liquid ^{4}He in the separator was vaporized by the incoming ^{3}He gas. The reason why the consumption rate did not decrease for a small flow rate of ^{3}He is supposed that most of liquid ^{4}He vaporized in the transfer tube between the dewar and the separator. A good trasfer tube is essential for a small consumption rate.

The consumption rate from the evaporator was almost proportional to the flow rate of ^{3}He as shown in fig. 50. The dashed line in the figure is an estimated value obtained by the calculation of heats exchanged in the evaporator.

5 - 3. Amount of ^{3}He gas

The total amount of ^{3}He gas in the system was 13 ℓ STP for the cooling power of 200 mW, and 16 ℓ STP for 400 mW. For a large cooling power the amount of ^{3}He gas must be increased to obtain a high inlet pressure, so that the flow rate of ^{3}He increases (fig. 51). As the

evaporator was operated below 2 K, ^{3}He condensed at low pressures (fig. 52) so the amount of ^{3}He gas was smaller than the Bonn group [56], who used 30 ℓ STP.

Appendix 3. Principle of measuring target polarization

A target polarization is proportional to the absorption term $\chi''(\omega)$ of an rf magnetic susceptibility $\chi(\omega) = \chi'(\omega) - i\,\chi''(\omega)$ [55],

$$\text{polarization} \propto \int_0^\infty \chi''(\omega)\, d\omega \ . \tag{A3-1}$$

$\chi''(\omega)$ is observed by menas of a series circuit Q-meter (fig. 53). The inductance of an NMR coil containing the target material with $\chi(\omega)$ is

$$L = L_o\ (1 + 4\pi\eta\ \chi(\omega)) \ , \tag{A3-2}$$

where η is the filling factor of the coil. The impedance of the circuit is

$$Z = r + \frac{1}{\omega C} + i\ \omega L_o(1 + X(\omega)) \tag{A3-3}$$

$$= r\ \left(1 + \frac{\omega}{\omega_o} Q\ X''(\omega) + i\ Q\ \{\frac{\omega}{\omega_o} - \frac{\omega_o}{\omega} + \frac{\omega}{\omega_o} X'(\omega)\}\right) \ , \tag{A3-4}$$

where

$$X(\omega) \equiv 4\pi\eta\ \chi(\omega) = X'(\omega) - i\ X''(\omega) \ , \tag{A3-5}$$

$$\omega_o = 1/\sqrt{LC} \qquad \text{(central NMR frequency)} \tag{A3-6}$$

$$Q = \omega_o L_o / r \qquad \text{(Q-factor)} \tag{A3-7}$$

When a constant current is supplied to the coil, the NMR signal is proportional to $|Z|$,

$$|Z| = r\sqrt{(1 + \frac{\omega}{\omega_o} Q\ X'')^2 + Q^2\ (\frac{\omega}{\omega_o} - \frac{\omega_o}{\omega} + \frac{\omega}{\omega_o} X')^2} \ . \tag{A3-8}$$

With

$$Q\ X','' \ll 1 \qquad \text{and} \qquad \frac{\omega}{\omega_o} \simeq 1 \ , \tag{A3-9}$$

$|Z|$ is approximated to $|Z|_1$,

$$|Z|_1 = r\ (1 + Q\ X'')\ . \tag{A3-10}$$

Therefore the observed NMR signal is proportional to the absorption term χ'', subtracting the constant term.

Define S and S_{TE} as

$$S = \int_0^\infty \text{(enhanced NMR signal)}\ d\omega\ ,$$

$$S_{TE} = \int_0^\infty \text{(thermal equilibrium NMR signal)}\ d\omega\ .$$

Then the enhanced polarization P is given by

$$P = \frac{S}{S_{TE}} P_{TE}\ , \tag{A3-11}$$

where P_{TE} is the polarization at a thermal equilibrium. The value of P_{TE} is obtained by measureing a magnetic field H and a temperature T. Assuming the Boltzmann distribution,

$$P_{TE} = \tanh \frac{\mu H}{kT}\ , \tag{A3-12}$$

where μ : magnetic moment of the proton.

k : the Boltzmann constat.

Appendix 4. Simulation for determination of kinematical quantities in the magnetic spectrometer

1. Generation of events

Incident photon energies E_γ and c.m. pion production angles θ_π^{cm} were sampled on following assumptions;

(1) A spectrum of a bremsstrahlung gamma beam was proportional to $1/E_\gamma$.

(2) A differential cross section was isotropic in an angular range to be simulated.

(3) Production points distributed uniformly in the irradiated part of the target.

2. Deflection in the magnetic fields

The magnetic field of the PT magnet was cylindrically symmetric and digitized into 24 bins with respect to radius. The field distribution of the momentum analyzer magnet was approximated to be square shaped with effective edges. Horizontal components of the magnetic fields were neglected.

3. Energy loss

Values of the energy loss were sampled assuming a Gaussian distribution. The central value was the stopping power,

$$S = \frac{0.307}{\beta^2}\frac{Z}{A}\left\{\ln\left(\frac{0.511 \times 10^6}{I_{av}}\frac{\beta^2}{1-\beta^2}\right) - \beta^2\right\} \quad (\mathrm{MeV}\cdot\mathrm{cm}^2/\mathrm{g}) \quad \text{(A4-1)}$$

where I_{av} is an averaged ionization potential energy. The value of I_{av} was refered from [58]. The values of S in the measured region were 4 - 12 MeV/g·cm^2. The standard deviation [59] is

$$\sigma_E = \sqrt{\frac{0.1569\ Z\ z^2}{A}\ \frac{1 - \beta^2/2}{1 - \beta^2}\ s} \qquad \text{(A4-2)}$$

$$= 0.05 - 0.15 \quad (\text{MeV}\cdot\text{cm}^2/\text{g})$$

where s is the thickness of the absorber in g/cm^2. The energy loss between the target and the counter T_3 were 12 - 28 MeV: 50 - 60% was due to detectors, and 40 - 50% was the target and wall of the cryostat.

4. Coulomb mutiple scattering

Deflection angles due to the Coulomb multiple scattering were assumed to be given by a Gaussian distribution [60] with a central value of 0° and a standard deviation of

$$\theta_o = \frac{E_s}{p\beta c}\left(\frac{L}{LR}\right)^{1/2}(1 - \varepsilon(L))\ (1 + \frac{M^2}{E\ m_t}), \qquad \text{(A4-3)}$$

where E : kinetic energy of the particle,

E_s = 17.5 MeV,

m_t : mass of nucleus of the matter.

The two correction factors $\varepsilon(L)$ and M^2/Em_t were 0.1 or so in the measured region. Respective values of θ_o for the target and walls of the cryostat were 0.4° and 0.7°.

Appendix 5. Differential cross sections

Differential cross sections for $\gamma p \to \pi^+ n$ and $\pi^o p$ were calculated from the experimental data with polyethylene and graphite targets by means of the subtraction method. Comparison of the caculated values with existing data, presented by experiments with ordinary hydrogen targets, is a good check of the detection system. Furthermore a good agreement between them would assure reliability of the data on the target asymmetry.

Differential cross section $d\sigma/d\Omega^*$ is calculated from

$$Y = n\ell \frac{Q}{E_\gamma} B(E_\gamma)\ \Delta E_\gamma \frac{d\sigma}{d\Omega^*} \frac{\partial\Omega^*}{\partial\Omega}\ \Delta\Omega\ \eta\ , \qquad \text{(A5-1)}$$

The meaning of symbols are the same as in §5 - 5 - 3. The acceptances ΔE_γ and $\Delta\Omega$ were obtained by the Monte-Carlo calculation. The detection efficiencies were

$$\eta = \eta_\pi^{dcy}\ \eta_\pi^{abs}\ \eta_{NF} \qquad \text{for } \pi^+ n \qquad \text{(A5-2)}$$

$\eta^{dcy} = 0.65 - 0.85$: due to the decay of $\pi^+ \to \mu^+ \nu$,

$\eta^{abs} = 0.89 - 0.94$: due to nuclear absorption of π^+ in the target, its surroundings and detectors,

$\eta_{NF} = 0.95$: due to non-firing in the hodoscopes.

$$\eta = \eta_\pi^{\Omega}\ \eta_\pi^{abs}\ \eta_p^{abs}\ \eta_{NF} \qquad \text{for } p\cdot\gamma, \qquad \text{(A5-3)}$$

$\eta_\pi^{\Omega} = 0.10 - 0.20$: due to the solid angle acceptance of the gamma counter,

$\eta_{\pi}^{abs} = 0.10 - 0.20$: due to absorption of photons from π^{o} in the target, its surroundings and and the photon hardner,

$\eta_{p}^{abs} = 0.97 - 0.99$: due to nuclear absorption of protons in the target, its surroundings and detectors,

$\eta_{NF} = 0.95$: due to non-firing in the hodoscopes.

$$\eta = \eta_{\pi}^{\Omega} \eta_{\pi}^{abs} \eta_{NF} \qquad \text{for } \gamma\cdot\gamma, \tag{A5-3}$$

$\Delta\Omega\ \eta_{\pi}^{\Omega} = 2 - 3 \times 10^{-7}$: due to the solid angle acceptance of the π^{o} counter,

$\eta_{\pi}^{abs} = 0.10 - 0.20$: due to absorption of pnotons from π^{o} in the target, its surroundings and the photon hardner,

$\eta_{NF} = 0.8$: due to non-firing in the hodoscopes.

Results of the differential cross sections are shown in figs. 54 - 56, where existing data are also plotted for comparison. As a whole above calculated differential cross sections are consistent with existing data [54,61-64].

Acknowledgements

The author tanks Prof. S. Takagi for his encouragement in the study. Thanks are due to my collaborators in the experiment; Mr. M. Daigo, Dr. M. Fukushima, Prof. N. Horikawa, Prof. R. Kajikawa, Dr. H. Kobayakawa, Dr. T. Matsuda, Dr. K. Mori, Dr. T. Nakanishi, Dr. T. Ohshima, Dr. C. O. Pak and Dr. S. Suzuki.

Mr. S. Okumi was my good coworker in the construction of the Polarized target system. Mr. Y. Ohhashi and Mr. T. Tauchi made the device for target beads. Mr. K. Watanabe performed the tentative analysis on $\gamma p \to \pi^+ n$ process using the present data.

He thanks Dr. H. Herr for his kind discussion on the cryostat, and Dr. P. Noelle for his instructive discussion on the results of the measurement.

Rererences

[1] Particle Data Group, Review of Modern Physics 48 No. 2 part II (1976).

[2] K. M. Watson, Phys. Rev. 95 (1954) 228.

[3] R. L. Walker, Phys. Rev. 182 (1969) 1729.

[4] I. S. Barker et al., Daresbury preprint DL/P 232 (1975).

[5] H. M. Fischer, Proceedings of the 7th International Symposium on Lepton and Photon Interactions at High Energies, Stanford, 1975.

[6] K. Kondo et al., Phys. Rev. D9 (1974) 529.

[7] V. B. Ganenko et al., Sov. J. Nucl. Phys. 23 (1976) 52, 162, 511.

[8] K. H. Althoff et al., Phys. Letters 63B (1976) 107.

[9] K. H. Althoff et al., Nucl. Phys. B116 (1976) 253.

[10] K. H. Althoff et al., Bonn University preprint BONN-HE-77-11 (1977).

[11] K. H. Althoff et al., Proceedings of the 8th International Symposium on Lepton and Photon Interactions at High Energies, Hamburg, 1977.

[12] H. Herr et al., Bonn University preprint BONN-HE-77-3 (1977).

[13] G. Knies et al., Phys. Rev. D10 (1974) 2778.

[14] P. J. Bussey et al., Nucl. Phys. B104 (1976) 253.

[15] P. S. L. Booth et al., Nucl. Phys. B121 (1977) 45.

[16] P. J. Bussey et al., Proceedings of the 7th International Symposium on Lepton and Photon Interactions at High Energies, Stanford, 1975, paper 125.

[17] P. J. Bussey et al., ibid., paper 126.

[18] G. F. Chew, M. L. Goldberger, F. E. Low and Y. Nambu, Phys. Rev. 106 (1957) 1345.

[19] F. A. Berends, A. Donnachie and D. L. Weaver, Nucl. Phys. B4 (1967) 1, 54.

[20] D. Schwela, Bonn University preprint BONN-PI-2-86 (1970).

[21] P. Noelle, W. Pfeil and D. Schwela, Nucl. Phys. B26 (1971) 461.
P. Noelle and W. Pfeil, Nucl. Phys. B31 (1971) 1.
P. Noelle, Bonn University preprint BONN-PI-2-92 (1971).

[22] F. A. Berends and D. L. Weaver, Nucl. Phys. B30 (1971) 575.

[23] S. Suzuki et al., Nucl. Phys. B68 (1974) 413.

[24] M. Nigro et al., Nucl. Phys. B84 (1975) 201.

[25] F. A. Berends and A. Donnachie, Nucl. Phys. B84 (1975) 342.

[26] F. A. Berends and A. Donnachie, Proceedings of the 7th International Symposium on Lepton and Photon Interactions at High Energies, Stanford, 1975, paper 214.

[27] W. J. Metcalf and R. L. Walker, Nucl. Phys. B76 (1974) 253.

[28] P. Feller et al., Nucl. Phys. B104 (1976) 219.

[29] R. C. E. Devenish, D. H. Lyth and W. A. Rankin, Phys. Letters 36B (1971) 394, Daresbury preprints DNPL/P 109 (1971), DNPL/P 150 (1973), Phys. Letters 52B (1974) 227.

[30] R. G. Moorhouse, H. Oberlack and A. H. Rosenfeld, Phys. Rev. D9 (1974) 1.

[31] G. Knies, R. G. Moorhouse and H. Oberlack, Phys. Rev. D9 (1974) 2680.

[32] G. Knies, R. G. Moorhouse, H. Oberlack, A. Rittenberg and A. H. Rosenfeld, Proceedings of the 17th International Conference on High

Energy Physics, London, 1974, paper 957.

[33] R. L. Crawford, Nucl. Phys. B97 (1975) 125.

[34] P. Noelle, Bonn University thesis BONN-IR-75-20 (1976), Nagoya University preprints DPNU-15, 16-77 (1977).

[35] I. Barbour and R. L. Crawford, University of Glasgow preprint (1975).

[36] D. Faiman and A. W. Hendry, Phys. Rev. 173 (1968) 1720.

[37] R. L. Walker, Proceedings of the 4th International Symposium on Electron and Photon Interactions at High Energies, Liverpool, 1969.

[38] B. H. Bransden and R. G. Moorhouse, The Pion-Nucleon System, Princeton University Press, 1973.

[39] D. Faiman and A. W. Hendry, Phys. Rev. 180 (1969) 1572.

[40] R. P. Feynman, M. Kislinger and F. Ravndal, Phys. Rev. D3 (1971) 2706.

[41] R. G. Moorhouse and H. Oberlack, Phys. Letters 43B (1973) 44.

[42] T. Kubota and K. Ohta, Phys. Letters 65B (1976) 374.

[43] J. Babcock and J. L. Rosner, California Institute of Technology preprint CALT-68-485 (1975).

[44] S. Arai et al., Phys. Letters 40B (1972) 426, Nucl. Phys. B48 (1972) 397.

[45] P. Feller et al., Phys. Letters 52B (1974) 105, 55B (1975) 241, Nucl. Phys. B102 (1976) 207, B110 (1976) 397.

[46] Y. Murata and S. Watanabe, INS report (in Japanese) INS-TH-53 (1966).

[47] Y. Akino et al., INS report (in Japanese) INS-TH-66 (1970).

[48] S. Mango et al., Nucl. Instr. Meth. 72 (1969) 45.

[49] M. Fukushima et al., Genshikaku Kenkyu (in Japanese) 21 (1976) 939.

[50] M. Fukushima et al., Nucl. Instr. Meth. 140 (1977) 275.

[51] K. H. Althoff et al., Nucl. Phys. B53 (1973) 9.

[52] K. H. Althoff et al., Phys. Letters 59B (1975) 93.

[53] K. Watanabe, Nagoya University master thesis (in Japanese), 1977.

[54] M. Yoshioka et al., INS report INS-report-281 (1977).

[55] C. D. Jeffries, Dynamic Nuclear Orientation, Interscience Publishers, 1963.

M. Borghini, Proceedings of the 2nd International Conference on Polarized Targets, Berkeley, 1971.

W. de Boer, CERN report CERN 74-11, 1974.

[56] H. Herr and V. Kadansky, Nucl. Instr. Meth. 121 (1974) 1.

[57] A. Abragam, The Principles of Nuclear Magnetism, Oxford, 1961.

[58] H. Bichsel, Passage of Charged Particles through Matter, American Institute of Physics Handbook (3rd edition), McGraw-Hill, 1972.

U. Fano, Ann. Rev. of Nucl. Sci. 13 (1963) 1.

[59] P. V. Vavilov, Sov. Phys. - JETP 5 (1957) 749.

[60] V. L. Highland, Nucl. Instr. Meth. 129 (1975) 497.

[61] H. A. Thiessen, Phys. Rev. 155 (1967) 1488.

[62] C. Betourne et al., Phys. Rev. 172 (1968) 1343.

[63] S. D. Ecklund and R. L. Walker, Phys. Rev. 159 (1967) 1195.

[64] J. S. Barton et al., Nucl. Phys. B84 (1975) 449.

Table captions

Table 1. Radiative decay matrix elements given by phenomenological analyses (MW [27], Nagoya [28], DLR [29], KMORR [32], C [33], and BC [35]) and quark models (MW [27], FKR [40], KO [42] and BR [43]). Units are 10^{-3} $GeV^{-1/2}$. Values of BR are from the fitting to KMORR's results.

Table 2. Performance of the ^{3}He cryostat. Those of the old cryostat (Roubeau-type) used in the previous experiment [45] are also shown for comparison.

Table 3. Characteristics of the magnetic spectrometer.

Table 4. Specification of the counters in the magnetic spectrometer.

Table 5. Targets and their compositions.

Table 6. Specifications of butanol, polyethylene and graphite targets.

Table 7. Resolutions of kinematical quantities in $p\cdot\gamma$ measurement for a combination of channels in the hodoscopes H_1 and H_2.

Table 8. Error of target polarization.

Table 9. Results of the target asymmetry for $\gamma p \to \pi^+ n$. Errors are statistical only.

Table 10. Results of the target asymmetry for $\gamma p \to \pi^o p$ $(\gamma\cdot\gamma)$. Errors are statistical only.

Table 11. Results of the target asymmetry for $\gamma p \to \pi^o p$ $(p\cdot\gamma)$. Errors are statistical only.

Table 12. Radiative decay matrix elements obtained by the tentative analysis on $\gamma p \to \pi^+ n$ [53], of which the method was the same

as the Nagoya analysis [28]. Results of the Nagoya analysis are slso listed for comparison.

Figure captions

Fig. 1. Summary of existing experimental data at SLAC conference, 1975. (a) $\gamma p \rightarrow \pi^{+} n$, (b) $\gamma p \rightarrow \pi^{o} p$, (c) $\gamma n \rightarrow \pi^{-} p$.

Fig. 2. Data points of the present experiment, indicated by closed dots. Existing data points are also shown with open marks, □ Daresbury. Δ Bonn, ○ INS.

Fig. 3. Experimental layout.

Fig. 4. Composition of the polarized target system.

Fig. 5. Structural formulae of butanol and porphyrexide.

Fig. 6. Device for producing target beads.

Fig. 7. Views of the PT magnet. Units are cm.

Fig. 8. Field distribution of the PT magnet.

Fig. 9. Homogeneity of the magnetic field of the PT magnet.

Fig. 10. Schematic diagram of the ^{3}He cryostat. Typical temperature distribution is also shown.

Fig. 11. Scaled figure of the ^{3}He cryostat.

Fig. 12. Construction of surroundings of the target.

Fig. 13. Microwave circuit.

Fig. 14. Construction of the NMR detection system acceptable for the both of the fast and slow sweep method.

Fig. 15. NMR detection system for the slow sweep method, used in the present experiment.

Fig. 16. NMR coil.

Fig. 17. Differentiated NMR signals, enhanced and at the thermal equi-

librium.

Fig. 18. Efficiency of the lucite Cerenkov counter.

Fig. 19. Construction of the gamma counter.

Fig. 20. The energy and the energy resolution of the lead glass Cerenkov counter C_C in the gamma counter.

Fig. 21. Construction of the π^o counter.

Fig. 22. Fast logic systems. (a) π^+n, (b) π^op $(p\cdot\gamma)$, (c) π^op $(\gamma\cdot\gamma)$.

Fig. 23. Data acquisition system.

Fig. 24. Data sets. (a) π^+n, (b) π^op $(p\cdot\gamma)$, (c) π^op $(\gamma\cdot\gamma)$.

Fig. 25. Discrimination between protons and positive pions by the TOF and dE/dx methods.

Fig. 26. Measured pulse heights of photons detected in the lead glass Cerenkov counter C_C from butanol target and carbon target.

Fig. 27. Simulated pulse height distributions of photons from $\gamma p \to \pi^o p$ and $\gamma p \to \pi^o\pi^o p$ (hatched) detected in C_C.

Fig. 28. Effective mass of the double photons from the decay of π^o.

Fig. 29. Relations between incident photon energy and momentum of particles detected in the magnetic spectrometer for single and double pion photoproduction processes. (a) $\gamma p \to \pi^+n$ (positive pions are detected), (b) $\gamma p \to \pi^o p$ (protons are detected).

Fig. 30. Resolutions of incident photon energy and c.m. pion production angle. (a) π^+n, (b) π^op $(p\cdot\gamma)$, (c) π^op $(\gamma\cdot\gamma)$.

Fig. 31. Phase volume measured by the magnetic spectrometer in the $p\cdot\gamma$ measurement.

Fig. 32. Kinematics of the double photons from the decay of neutral pions.

Fig. 33. Hydrogen yield ratio R.

Fig. 34. Resulting angular distributions of the polarized target asymmetry for $\gamma p \to \pi^+ n$. Existing data and prediction curves by phenomenological analyses are also shown. • Nagoya-Osaka [44, 45], × Bonn [8,51,52], Δ Daresbury [16], —— Nagoya [28], --- MW [27], —•— MOR [30].

Fig. 35. Resulting energy dependences of the polarized target asymmetry for $\gamma p \to \pi^+ n$. Symbols are the same as in fig. 35.

Fig. 36. The effect of $S_{11}(1700)$ on $T(\theta)$ at 160°. The photocoupling was increased 20% (thin line) than the Nagoya analysis (thick line).

Fig. 37. The effect of $P_{11}(1470)$ on $T(\theta)$ at 120°. The photocoupling was decreased 5% (thin line) than the Nagoya analysis (thick line).

Fig. 38. Resulting angular distribuions of the polarized target asymmetry for $\gamma p \to \pi^o p$. • this experiment, o Nagoya-Osaka [45], Δ Daresbury [15,17]. Prediction curves are also shown. —— Nagoya [28], —•— MOR [30], ••• Noelle [34].

Fig. 39. Resulting energy dependence of the polarized target asymmetry for $\gamma p \to \pi^o p$. Symbols are the same as in fig. 38.

Fig. 40. Contribution of resonance and background terms to the target asymmetry for $\gamma p \to \pi^o p$ at 30°.

··· 1st and 2nd resonances,

--- (1st and 2nd resonances) + Im E_{0+},

—— 1st, 2nd and 3rd resonances,

—·— photocoupling of $S_{31}(1650)$ is reduced to 0,

Values of photocouplings and the background amplitude are given by MW [27].

Fig. 41. Contribution of resonances and background terms to the target asymmetry for $\gamma p \to \pi^o p$ at 80°, 105° and 120°.

··· $P_{33}(1232)$ + Im E_{0+},

—·— P_{33} + Im E_{0+} + $S_{11}(1535)$,

—··— P_{33} + Im E_{0+} + $P_{11}(1470)$,

—···— P_{33} + Im E_{0+} + $D_{13}(1520)$,

—— P_{33} + Im E_{0+} + (three 2nd resonances),

--- P_{33} + E_{0+} + (three 2nd resonances) + (electric Born),

The photocouplings and the background amplitude are given by MW [27].

Fig. 42. Zeeman energy levels for an electron-proton spin system.

Fig. 43. Relaxation time of proton spins in butanol in the magnetic field of 2.5 T.

Fig. 44. Flow diagram of ^{3}He and ^{4}He.

Fig. 45. Transfer tube for liquid ^{4}He linking the dewar and the separator.

Fig. 46. Purifier for ^{3}He gas. The purifier was cooled in liquid nitrogen.

Fig. 47. Copper buffles in the heat exchanger I and II.

Fig. 48. Operation of the cryostat.

(1) precooling with liquid nitrogen,

(2) evaporation of liquid nitrogen in the target container,

(3) exhaustion of gaseous nitrogen,

(4) start of supply of liquid ^{4}He and circulation of ^{3}He,

(5) control of temperture at the evaporator by regulatiing the flow rate of liquid ^{4}He by the needle valve.

(6) close of the bypass needle valve for ^{3}He, and the control of temperature at the cavity by the main needle valve.

Fig. 49. ^{3}He vapor pressure and temperature.

Fig. 50. Flow rate of ^{3}He (cooling power of the cryostat) and the consumption rate of liquid ^{4}He at the evaporator. The dashed line is an expected line according to the calculation of the heat exchange at the evaporator.

Fig. 51. Flow rate of ^{3}He and the pressure difference of ^{3}He gas between the inlet and the condenser. The dashed line is an expected line based on the calculation of the conductance of the ^{3}He line.

Fig. 52. ^{3}He input pressure and the condensation temperature. •, ○, ▲, △ and □ correspond to cooling powers of 0, 100, 200, 300 and 400 mW.

Fig. 53. Series circuit Q-meter.

Fig. 54. Differential cross section for $\gamma p \to \pi^+ n$ calculated by the subtraction method. Existing data are also shown for comparison. • present data, ○ [61], △ [62], □ [63].

Fig. 55. Differential cross section for $\gamma p \to \pi^o p$ $(\gamma \cdot \gamma)$ at 30° calculated by the subtraction method. Existing data at 35° [54] are also shown for comparison. • present data, o [54].

Fig. 56. Differential cross section for $\gamma p \to \pi^o p$ $(p \cdot \gamma)$ at 80°, 105° and 120° calculated by the subtraction method. Existing data are also shown for comparison. • present data, o [54], □ [64].

		$A^p_{1/2}$	$A^p_{3/2}$	$A^n_{1/2}$	$A^n_{3/2}$
$P_{33}(1232)$	MW	−140 ± 6	−254 ± 7		
	Nagoya	−141 ± 4	−256 ± 3		
	DLR	———	———		
	KMORR	———	———		
	C	−130 ± 2	−248 ± 3		
	BC	−129 ±	−251		
	MW	−101	−175		
	FKR	−108	−187		
	KO	———	———		
	BR	———	———		
$S_{11}(1535)$	MW	63 ± 13		−51 ± 21	
	Nagoya	70 ± 4		———	
	DLR	78 ± 20		−37 ± 23	
	KMORR	89		−52	
	C	82 ± 7		−88 ± 10	
	BC	63		−109	
	MW	166		−116	
	FKR	156		−108	
	KO	97		−101	
	BR	72		−74	
$P_{11}(1470)$	MW	−70 ± 23		66 ± 13	
	Nagoya	−87 ± 6		———	
	DLR	−79 ± 12		41 ± 25	
	KMORR	−80		0	
	C	−70 ± 4		44 ± 8	
	BC	−53		58	
	MW	29		−19	
	FKR	27		−18	
	KO	−5		4	
	BR	−76		50	
$D_{13}(1520)$	MW	−6 ± 6	165 ± 11	−66 ± 10	−118 ± 13
	Nagoya	−5 ± 5	164 ± 8	———	———
	DLR	−8 ± 15	171 ± 12	−89 ± 19	−155 ± 19
	KMORR	−19	170	−70	−128
	C	−14 ± 4	162 ± 4	−66 ± 3	−133 ± 3
	BC	−12	158	−56	−136
	MW	−38	114	−31	−114
	FKR	−34	109	−31	−109
	KO	6	174	−52	−144
	BR	−36	165	−28	−125

TABLE 1(A)

		$A^p_{1/2}$	$A^p_{3/2}$	$A^n_{1/2}$	$A^n_{3/2}$
$D_{15}(1670)$	MW	10 ± 13	42 ± 24	4 ± 15	-9 ± 30
	Nagoya	34 ± 4	19 ± 9		
	DLR	19 ± 21	14 ± 4	-29 ± 23	-68 ± 20
	KMORR	7	17	-43	-90
	C	27 ± 9	15 ± 6	-52 ± 3	-83 ± 7
	BC	10	17	-62	-78
	MW	0	0	-39	-56
	FKR	0	0	-38	-53
	KO	0	0	-36	-51
	BR	0	0	-48	-68
$F_{15}(1690)$	MW	-8 ± 11	129 ± 16	8 ± 18	0 ± 30
	Nagoya	-9 ± 2	121 ± 10		
	DLR	27 ± 19	163 ± 11	31 ± 28	-21 ± 28
	KMORR	-25	96	33	-15
	C	-13 ± 2	135 ± 6	21 ± 1	-15 ± 4
	BC	-3	132	32	-30
	MW	-13	73	43	0
	FKR	-10	59	35	0
	KO	24	106	19	-21
	BR	-26	98	38	-36
$S_{31}(1650)$	MW	105 ± 38			
	Nagoya	-5 ± 16			
	DLR	-10 ± 17			
	KMORR	27			
	C	44 ± 27			
	BC	45			
	MW	46			
	FKR	47			
	KO	86			
	BR	99			
$D_{33}(1670)$	MW	0 ± 48	0 ± 41		
	Nagoya	72 ± 33	87 ± 23		
	DLR	54 ± 29	72 ± 14		
	KMORR	79	61		
	C	101 ± 11	116 ± 24		
	BC	119	102		
	MW	93	85		
	FKR	88	84		
	KO	90	91		
	BR	110	101		

TABLE 1(B)

		$A^p_{1/2}$	$A^p_{3/2}$	$A^n_{1/2}$	$A^n_{3/2}$
$S_{11}(1700)$	MW	12 ± 15		-19 ± 22	
	Nagoya	68 ± 9			
	DLR	29 ± 18		-6 ± 31	
	KMORR	52		-55	
	C	44 ± 18		-103 ± 10	
	BC	44		-22	
	MW	0		30	
	FKR	0		31	
	KO	0		4	
	BR	48		-53	
$P_{11}(1780)$	MW	-68 ± 24		-48 ± 45	
	Nagoya	53 ± 19			
	DLR	-14 ± 21		-60 ± 61	
	KMORR	18		18	
	C	62 ± 7		-20 ± 16	
	BC	5		-10	
	MW	-39		13	
	FKR	-40		10	
	KO	-7		2	
	BR				
$P_{13}(1810)$	MW	0 ± 25	0 ± 22	0 ± 50	0 ± 44
	Nagoya				
	DLR	25 ± 34	-87 ± 57	13 ± 45	-83 ± 90
	KMORR	26	-12	14	-23
	C	22 ± 12	-16 ± 16	-37 ± 22	-38 ± 15
	BC	105	-62	6	48
	MW	115	-37	-34	0
	FKR	100	-30	-30	0
	KO	42	-54	13	12
	BR	39	4	1	-18
$D_{13}(1700)$	MW	0 ± 34	0 ± 29	0 ± 34	0 ± 44
	Nagoya	-14 ± 25	0 ± 14		
	DLR	-48 ± 50	-6 ± 14	-21 ± 98	-26 ± 67
	KMORR	22	61	73	51
	C	-12 ± 10	-12 10	81 ± 15	107 ± 25
	BC	-4	-27	33	29
	MW	0	0	-14	-73
	FKR	0	0	-10	-40
	KO	0	0	15	-17
	BR	0	0	27	-11

TABLE 1(c)

	old	new
cooling power	20 mW	200 mW (at 0.5 K)
		400 mW (at 0.6 K)
precooling time	4 h	2 h
consumption rate of liq. ^{4}He	3 ℓ/h	3.5 ℓ/h
total amount of ^{3}He gas	10 ℓ	15 ℓ
weight of the target	3.7 g	12 g
averaged target polarization	61 %	65 %

TABLE 2

Characteristics of the Magnetic Spectrometer

solid angle acceptance	(T1)	2 mstr
angle resolution	(H1)	0.86°/ch
momentum resolution	(H2)	$\Delta P/P \simeq 1.1$ %/ch
		(total acceptance ≃ 14%)
maximum momentum		∿700 MeV
lucite Cerenkov counter	(C_L)	$\beta_{th} \simeq 0.67$
		{ 130 MeV/c for pion 830 MeV/c for proton }
		eff. ≃ 96% for ≳350 MeV/c π
gas Cerenkov counter	(C_G)	$\beta_{th} \simeq 0.995$
		eff. ≃ 99% for ≳200 MeV/c electron

TABLE 3

Specifications of the Counter

counter	material	dimension (mm) W × H × T	phototube	distance from the target*(cm)	note
H1	plastic scinti.	30 × 80 × 3	6655A	200	8ch hodoscope
T1	plastic scinti.	234 × 38 × 3	56AVP	209	
T2	plastic scinti.	368 × 150 × 3	56AVP	418	
H2	plastic scinti.	30 × 240 × 3	6655A	599	12ch hodoscope
T3	plastic scinti.	380 × 200 × 3	56AVP	614	
C_L	lucite	430 × 220 × 44	8575 × 2	629	threshold type Cerenkov counter refractive index ~ 1.49**
C_G	freon 12 4.6 kg/cm^2 (abs.)	effective aperture ~500 mmϕ	4522 × 2		threshold type Cerenkov counter refractive index ~ 1.0050**

* including the deflection by the PT magnet

** review of particle properties, 1976

TABLE 4

target	contribution				
	proton	nucleus	cryostat	cavity	liq. ^{3}He
polarized butanol (↑,↓)	◎	O	O	O	O
without He	O	O	O	O	X
CH_2 (polyethylene)	O	O	O	X	X
C (graphite)	X	O	O	X	X
empty	X	X	O	X	X
empty cavity	X	X	O	O	X

TABLE 5

Specifications of the Targets

material	composition	dimension (mm) W × H × L	density (g/cm^3)	thickness (g/cm^2)
polyethylene	CH_2	25.10 × 34.04 × 23.00	0.9536	2.193 ± 0.009
graphite	C	25.01 × 34.12 × 12.95	1.593	2.063 ± 0.008
butanol*	C_4H_9OH	25. × 25. × 36.	0.59	2.13 ± 0.18**

* polarized target in frozen 1 mmϕ sphere

** standard deviation between 8 targets

TABLE 6

Resolutions of P_p, θ_p, E_γ, θ^*_π (FWHM)

set	ΔP_p (%)	$\Delta\theta_p$ (deg)	ΔE_γ (MeV)	$\Delta\theta^*_\pi$ (deg)
#110	1.7	1.8	56	4.0
#111	2.0	2.0	51	4.3
#112	2.4	2.3	44	4.8
#113	3.6	2.6	39	5.4
#114	5.4	2.9	34	6.1
#120	1.7	1.9	27	4.1
#121	2.1	1.9	22	4.2
#122	2.5	2.2	22	4.8
#123	3.3	2.6	21	5.5
#130	2.6	2.3	29	5.0
#131	3.4	2.5	30	5.4
#132	4.0	3.0	31	6.3

TABLE 7

$\Delta S/S$	±0.5 %
$\Delta S_{TE}/S_{TE}$	±3 %
$\Delta P_{TE}/P_{TE}$	±0.5 %
$\Delta \eta_r/\eta_r$	±2 %
$\Delta \eta_d/\eta_d$	±1.5 %
NMR circuit	±1 %
$\Delta P/P$	±4%

TABLE 8

Photon Energy E_γ (GeV)	π^+ angle in c.m.s. θ (deg)	Asymmetry $T(\theta)$
0.541 ± 0.008	37.1 ± 2.5	-0.046 ± 0.122
0.560 ± 0.012	38.9 ± 2.8	-0.147 ± 0.045
0.594 ± 0.013	41.0 ± 2.8	-0.190 ± 0.037
0.631 ± 0.014	41.4 ± 3.8	-0.132 ± 0.042
0.671 ± 0.013	39.0 ± 2.8	-0.328 ± 0.048
0.713 ± 0.015	40.0 ± 3.2	-0.445 ± 0.043
0.748 ± 0.014	40.3 ± 3.4	-0.414 ± 0.051
0.792 ± 0.014	40.8 ± 3.0	-0.490 ± 0.083
0.829 ± 0.014	42.6 ± 2.8	-0.489 ± 0.105
0.473 ± 0.008	48.0 ± 2.5	0.069 ± 0.050
0.500 ± 0.011	50.3 ± 2.6	0.170 ± 0.052
0.532 ± 0.011	51.1 ± 3.0	-0.047 ± 0.051
0.566 ± 0.009	50.1 ± 2.7	-0.045 ± 0.086
0.597 ± 0.009	50.5 ± 3.2	-0.083 ± 0.055
0.631 ± 0.012	51.8 ± 3.4	-0.187 ± 0.062
0.675 ± 0.014	50.7 ± 3.1	-0.292 ± 0.057
0.713 ± 0.014	49.8 ± 2.7	-0.209 ± 0.043
0.753 ± 0.012	49.8 ± 3.4	-0.439 ± 0.051
0.790 ± 0.014	51.3 ± 3.5	-0.412 ± 0.053
0.830 ± 0.015	50.8 ± 2.9	-0.553 ± 0.094
0.391 ± 0.005	57.6 ± 2.3	0.572 ± 0.119
0.410 ± 0.010	59.3 ± 2.5	0.369 ± 0.054
0.441 ± 0.010	60.3 ± 3.1	0.301 ± 0.066
0.470 ± 0.011	60.8 ± 3.6	0.214 ± 0.043
0.499 ± 0.011	60.1 ± 3.0	0.182 ± 0.039
0.531 ± 0.011	60.2 ± 3.3	0.068 ± 0.046
0.561 ± 0.011	58.7 ± 2.5	0.035 ± 0.057
0.594 ± 0.013	59.8 ± 2.9	-0.074 ± 0.062
0.630 ± 0.014	60.0 ± 3.3	-0.090 ± 0.034
0.668 ± 0.014	60.5 ± 3.5	-0.174 ± 0.043
0.711 ± 0.015	58.3 ± 2.7	-0.311 ± 0.087
0.750 ± 0.014	59.8 ± 2.7	-0.301 ± 0.077
0.788 ± 0.015	61.5 ± 2.6	-0.311 ± 0.103
0.833 ± 0.015	60.7 ± 3.4	-0.300 ± 0.066
0.872 ± 0.018	60.4 ± 2.7	-0.324 ± 0.063
0.920 ± 0.019	63.3 ± 2.4	-0.179 ± 0.063
0.968 ± 0.018	66.2 ± 1.7	-0.042 ± 0.114

TABLE 9(A)

Photon Energy E_γ (GeV)	π^+ angle in c.m.s. θ (deg)	Asymmetry $T(\theta)$
0.414 ± 0.009	68.1 ± 2.3	0.494 ± 0.083
0.441 ± 0.010	70.1 ± 2.7	0.459 ± 0.070
0.468 ± 0.011	70.7 ± 3.2	0.244 ± 0.040
0.499 ± 0.012	71.2 ± 2.7	0.151 ± 0.050
0.529 ± 0.010	70.8 ± 3.0	0.162 ± 0.056
0.560 ± 0.012	69.6 ± 2.9	0.114 ± 0.052
0.591 ± 0.013	70.1 ± 3.1	0.008 ± 0.041
0.628 ± 0.015	71.3 ± 2.9	-0.073 ± 0.041
0.673 ± 0.014	70.7 ± 3.0	-0.070 ± 0.044
0.710 ± 0.015	70.0 ± 2.5	-0.070 ± 0.049
0.748 ± 0.016	69.3 ± 3.3	-0.123 ± 0.053
0.788 ± 0.017	70.9 ± 3.3	-0.150 ± 0.064
0.833 ± 0.016	67.5 ± 3.6	-0.202 ± 0.066
0.871 ± 0.018	68.6 ± 2.6	-0.114 ± 0.059
0.917 ± 0.020	70.4 ± 2.6	0.006 ± 0.052
0.968 ± 0.022	72.0 ± 2.5	0.042 ± 0.046
1.021 ± 0.023	75.1 ± 1.8	0.160 ± 0.176
0.386 ± 0.008	78.0 ± 2.1	0.687 ± 0.083
0.411 ± 0.011	80.6 ± 2.1	0.575 ± 0.063
0.439 ± 0.011	79.7 ± 2.9	0.499 ± 0.056
0.471 ± 0.010	80.7 ± 2.8	0.323 ± 0.052
0.498 ± 0.011	81.4 ± 3.1	0.340 ± 0.065
0.531 ± 0.012	79.8 ± 3.4	0.043 ± 0.046
0.560 ± 0.013	78.8 ± 2.3	0.174 ± 0.095
0.597 ± 0.013	79.1 ± 3.1	0.120 ± 0.059
0.630 ± 0.015	80.4 ± 3.1	0.012 ± 0.037
0.671 ± 0.016	80.4 ± 3.8	0.054 ± 0.043
0.711 ± 0.015	78.1 ± 2.4	0.024 ± 0.049
0.751 ± 0.016	79.6 ± 2.5	0.005 ± 0.067
0.797 ± 0.015	78.9 ± 2.7	0.074 ± 0.045
0.832 ± 0.015	79.0 ± 2.6	0.046 ± 0.040
0.878 ± 0.016	79.6 ± 2.9	0.079 ± 0.059
0.922 ± 0.018	79.8 ± 3.3	0.025 ± 0.036
0.970 ± 0.020	80.5 ± 3.1	0.044 ± 0.045

TABLE 9(B)

Photon Energy E_γ (GeV)	π^+ angle in c.m.s. θ (deg)	Asymmetry $T(\theta)$
0.410 ± 0.011	100.1 ± 2.3	0.598 ± 0.057
0.441 ± 0.010	100.1 ± 2.1	0.601 ± 0.076
0.469 ± 0.011	100.2 ± 2.3	0.336 ± 0.046
0.501 ± 0.011	99.9 ± 2.1	0.323 ± 0.062
0.529 ± 0.011	100.3 ± 2.3	0.196 ± 0.043
0.560 ± 0.012	100.0 ± 2.2	0.140 ± 0.045
0.591 ± 0.014	100.5 ± 2.2	0.146 ± 0.040
0.632 ± 0.015	100.0 ± 2.4	0.223 ± 0.044
0.671 ± 0.015	100.4 ± 2.2	0.195 ± 0.038
0.711 ± 0.015	100.1 ± 2.4	0.205 ± 0.053
0.752 ± 0.015	99.5 ± 2.4	0.158 ± 0.052
0.788 ± 0.016	100.3 ± 2.4	0.261 ± 0.052
0.830 ± 0.017	100.3 ± 2.5	0.266 ± 0.076
0.871 ± 0.018	100.4 ± 2.2	0.222 ± 0.095
0.921 ± 0.020	100.2 ± 2.4	0.144 ± 0.041
0.970 ± 0.020	100.0 ± 2.4	0.179 ± 0.054
1.021 ± 0.021	101.0 ± 2.3	0.076 ± 0.050
0.441 ± 0.011	120.2 ± 2.0	0.548 ± 0.063
0.471 ± 0.012	120.0 ± 2.0	0.628 ± 0.083
0.498 ± 0.011	120.2 ± 1.9	0.294 ± 0.054
0.529 ± 0.013	119.9 ± 2.0	0.361 ± 0.061
0.560 ± 0.013	120.2 ± 1.9	0.240 ± 0.051
0.591 ± 0.015	120.2 ± 2.0	0.222 ± 0.046
0.632 ± 0.016	120.2 ± 2.0	0.290 ± 0.048
0.668 ± 0.017	120.3 ± 2.0	0.279 ± 0.059
0.714 ± 0.016	119.4 ± 2.0	0.346 ± 0.048
0.750 ± 0.019	120.4 ± 2.0	0.311 ± 0.038
0.790 ± 0.019	120.2 ± 2.2	0.475 ± 0.070
0.831 ± 0.019	120.5 ± 2.0	0.321 ± 0.107
0.871 ± 0.021	120.0 ± 1.9	0.146 ± 0.045
0.918 ± 0.023	119.9 ± 2.0	0.161 ± 0.042
0.970 ± 0.024	120.4 ± 2.0	0.050 ± 0.046
1.016 ± 0.024	121.5 ± 1.7	0.060 ± 0.099

TABLE 9(c)

Photon Energy E_γ (GeV)	π^+ angle in c.m.s. θ (deg)	Asymmetry $T(\theta)$
0.529 ± 0.015	140.2 ± 1.7	0.335 ± 0.091
0.561 ± 0.014	140.1 ± 1.7	0.275 ± 0.091
0.596 ± 0.015	139.9 ± 1.6	0.027 ± 0.048
0.628 ± 0.018	140.3 ± 1.7	0.171 ± 0.050
0.668 ± 0.019	140.2 ± 1.7	0.267 ± 0.069
0.711 ± 0.019	140.0 ± 1.6	0.324 ± 0.049
0.748 ± 0.021	140.2 ± 1.8	0.467 ± 0.055
0.786 ± 0.022	140.4 ± 1.6	0.601 ± 0.093
0.873 ± 0.023	139.9 ± 1.6	0.498 ± 0.077
0.917 ± 0.027	139.8 ± 1.7	0.312 ± 0.050
0.970 ± 0.027	140.5 ± 1.6	0.158 ± 0.053
1.021 ± 0.029	140.6 ± 1.6	0.091 ± 0.071
0.500 ± 0.015	160.2 ± 1.5	0.177 ± 0.143
0.531 ± 0.017	160.0 ± 1.6	0.116 ± 0.122
0.562 ± 0.016	160.0 ± 1.5	0.297 ± 0.125
0.591 ± 0.017	160.0 ± 1.4	-0.049 ± 0.087
0.628 ± 0.019	160.1 ± 1.5	0.053 ± 0.097
0.673 ± 0.017	160.0 ± 1.4	0.238 ± 0.080
0.706 ± 0.022	160.2 ± 1.5	0.336 ± 0.047
0.750 ± 0.022	160.2 ± 1.4	0.523 ± 0.073
0.787 ± 0.022	159.9 ± 1.4	0.363 ± 0.097
0.828 ± 0.024	160.1 ± 1.4	0.388 ± 0.090
0.874 ± 0.026	160.3 ± 1.4	0.291 ± 0.074
0.917 ± 0.027	159.9 ± 1.4	0.238 ± 0.066
0.969 ± 0.031	160.2 ± 1.4	0.299 ± 0.138

TABLE 9(D)

Photon Energy E_γ (GeV)	π^o angle in c.m.s. θ (deg)	Asymmetry $T(\theta)$
0.404 ± 0.021	24.5 ± 3.1	0.015 ± 0.372
0.454 ± 0.025	24.8 ± 2.9	-0.029 ± 0.178
0.503 ± 0.027	25.5 ± 2.8	-0.106 ± 0.132
0.551 ± 0.028	26.0 ± 2.8	-0.016 ± 0.157
0.588 ± 0.026	26.7 ± 2.8	0.321 ± 0.191
0.652 ± 0.030	27.1 ± 2.7	0.385 ± 0.323
0.702 ± 0.028	27.3 ± 2.3	-0.231 ± 0.278
0.749 ± 0.030	27.8 ± 2.4	0.260 ± 0.146
0.799 ± 0.032	28.4 ± 2.6	0.420 ± 0.500
0.852 ± 0.031	28.8 ± 2.5	0.241 ± 0.236
0.897 ± 0.029	29.4 ± 2.5	0.110 ± 0.245
0.948 ± 0.033	29.9 ± 2.6	-0.107 ± 0.226
0.997 ± 0.033	30.5 ± 2.8	-0.096 ± 0.117

TABLE 10

Photon Energy E_γ (deg)	π^o angle in c.m.s. θ (deg)	Asymmetry $T(\theta)$
0.419 ± 0.025	82.9 ± 4.5	-0.258 ± 0.064
0.460 ± 0.030	78.2 ± 4.5	-0.370 ± 0.075
0.499 ± 0.028	74.6 ± 3.5	-0.412 ± 0.132
0.469 ± 0.020	85.3 ± 4.3	-0.216 ± 0.090
0.502 ± 0.025	82.3 ± 4.3	-0.378 ± 0.066
0.539 ± 0.025	79.0 ± 5.0	-0.596 ± 0.080
0.580 ± 0.028	76.2 ± 4.0	-0.923 ± 0.184
0.548 ± 0.023	85.4 ± 3.5	-0.614 ± 0.143
0.581 ± 0.028	82.7 ± 4.0	-0.695 ± 0.091
0.620 ± 0.025	79.9 ± 5.3	-0.830 ± 0.083
0.661 ± 0.035	77.8 ± 4.5	-0.644 ± 0.080
0.690 ± 0.025	76.4 ± 3.5	-0.654 ± 0.187
0.661 ± 0.028	84.5 ± 3.5	-0.730 ± 0.115
0.700 ± 0.028	81.7 ± 4.8	-0.575 ± 0.063
0.740 ± 0.033	80.0 ± 5.0	-0.452 ± 0.049
0.782 ± 0.043	77.8 ± 4.5	-0.356 ± 0.052
0.819 ± 0.025	76.2 ± 2.8	-0.311 ± 0.119
0.740 ± 0.025	87.0 ± 3.3	-0.463 ± 0.087
0.779 ± 0.035	84.1 ± 3.0	-0.338 ± 0.053
0.820 ± 0.035	82.0 ± 4.3	-0.240 ± 0.041
0.859 ± 0.035	80.8 ± 5.0	-0.086 ± 0.053
0.899 ± 0.048	79.2 ± 4.5	-0.268 ± 0.080
0.945 ± 0.048	77.4 ± 4.0	-0.442 ± 0.176
0.390 ± 0.013	109.1 ± 4.5	0.057 ± 0.094
0.419 ± 0.020	104.3 ± 6.3	-0.097 ± 0.042
0.458 ± 0.025	100.6 ± 4.5	-0.232 ± 0.072
0.459 ± 0.020	107.2 ± 5.3	-0.157 ± 0.060
0.500 ± 0.023	103.6 ± 5.5	-0.248 ± 0.070
0.531 ± 0.020	100.7 ± 4.0	-0.252 ± 0.173
0.507 ± 0.020	109.6 ± 4.3	-0.443 ± 0.070
0.542 ± 0.020	106.0 ± 6.0	-0.498 ± 0.053
0.583 ± 0.028	103.4 ± 5.8	-0.557 ± 0.062
0.582 ± 0.023	109.1 ± 4.8	-0.788 ± 0.079
0.621 ± 0.025	106.1 ± 5.5	-0.771 ± 0.053
0.662 ± 0.020	104.0 ± 6.0	-0.685 ± 0.050
0.423 ± 0.018	121.4 ± 6.0	-0.050 ± 0.078
0.459 ± 0.023	118.4 ± 6.0	-0.149 ± 0.091
0.469 ± 0.018	122.7 ± 5.5	-0.156 ± 0.095
0.500 ± 0.023	120.0 ± 7.3	-0.324 ± 0.057
0.542 ± 0.020	123.0 ± 5.8	-0.464 ± 0.063
0.579 ± 0.023	120.6 ± 7.3	-0.635 ± 0.070
0.619 ± 0.025	117.6 ± 4.3	-0.675 ± 0.103

TABLE 11

	helicity	present analysis	Nagoya
$P_{33}(1232)$	$A_{1/2}$	-141 ± 4	-141 ± 4
	$A_{3/2}$	-255 ± 3	-256 ± 3
$S_{11}(1535)$	$A_{1/2}$	84 ± 2	70 ± 4
$P_{11}(1470)$	$A_{1/2}$	-83 ± 5	-87 ± 6
$D_{13}(1520)$	$A_{1/2}$	-10 ± 4	-5 ± 5
	$A_{3/2}$	166 ± 11	164 ± 8
$S_{11}(1700)$	$A_{1/2}$	75 ± 8	68 ± 9
$P_{11}(1780)$	$A_{1/2}$	80 ± 17	53 ± 19
$D_{13}(1700)$	$A_{1/2}$	-19 ± 29	-14 ± 25
	$A_{3/2}$	0 ± 15	0 ± 14
$D_{15}(1670)$	$A_{1/2}$	25 ± 13	34 ± 4
	$A_{3/2}$	21 ± 6	19 ± 9
$F_{15}(1690)$	$A_{1/2}$	-9 ± 2	-9 ± 2
	$A_{3/2}$	122 ± 12	121 ± 10
$S_{31}(1650)$	$A_{1/2}$	-15 ± 16	-5 ± 16
$D_{33}(1670)$	$A_{1/2}$	89 ± 33	72 ± 33
	$A_{3/2}$	65 ± 23	87 ± 23

TABLE 12

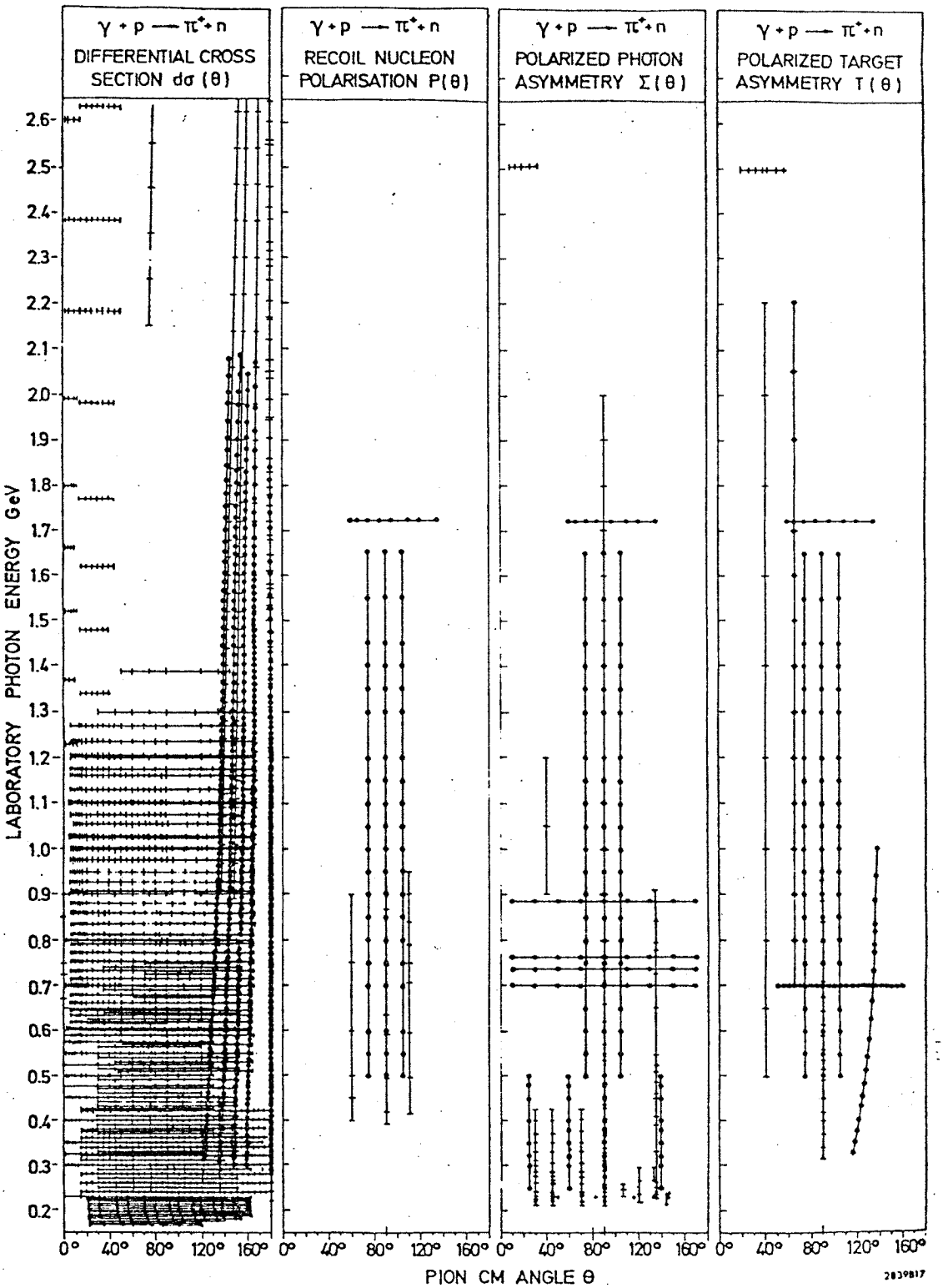
γ + p → π⁺ + n
DIFFERENTIAL CROSS SECTION dσ (θ)
γ + p → π⁺ + n
RECOIL NUCLEON POLARISATION P(θ)
γ + p → π⁺ + n
POLARIZED PHOTON ASYMMETRY Σ(θ)
γ + p → π⁺ + n
POLARIZED TARGET ASYMMETRY T(θ)
LABORATORY PHOTON ENERGY GeV
2.6
2.5
2.4
2.3
2.2
2.1
2.0
1.9
1.8
1.7
1.6
1.5
1.4
1.3
1.2
1.1
1.0
0.9
0.8
0.7
0.6
0.5
0.4
0.3
0.2
0° 40° 80° 120° 160°
PION CM ANGLE θ
2839817

FIG. 1(A)

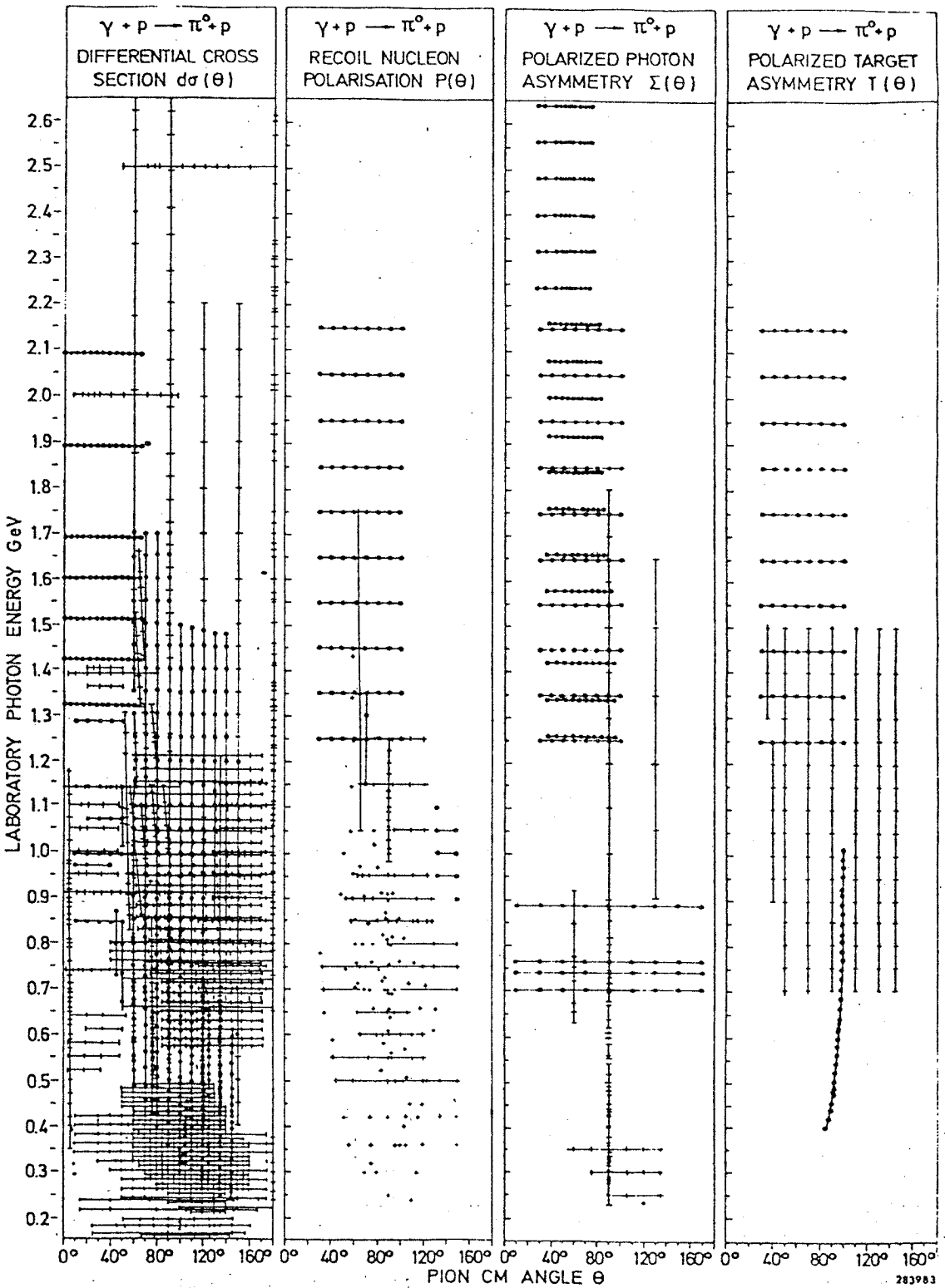
γ + p → π°+ p
DIFFERENTIAL CROSS SECTION dσ (θ)
γ + p → π°+ p
RECOIL NUCLEON POLARISATION P(θ)
γ + p → π°+ p
POLARIZED PHOTON ASYMMETRY Σ(θ)
γ + p → π°+ p
POLARIZED TARGET ASYMMETRY T (θ)
LABORATORY PHOTON ENERGY GeV
2.6
2.5
2.4
2.3
2.2
2.1
2.0
1.9
1.8
1.7
1.6
1.5
1.4
1.3
1.2
1.1
1.0
0.9
0.8
0.7
0.6
0.5
0.4
0.3
0.2
0° 40° 80° 120° 160°
PION CM ANGLE θ
283983

FIG. 1(B)

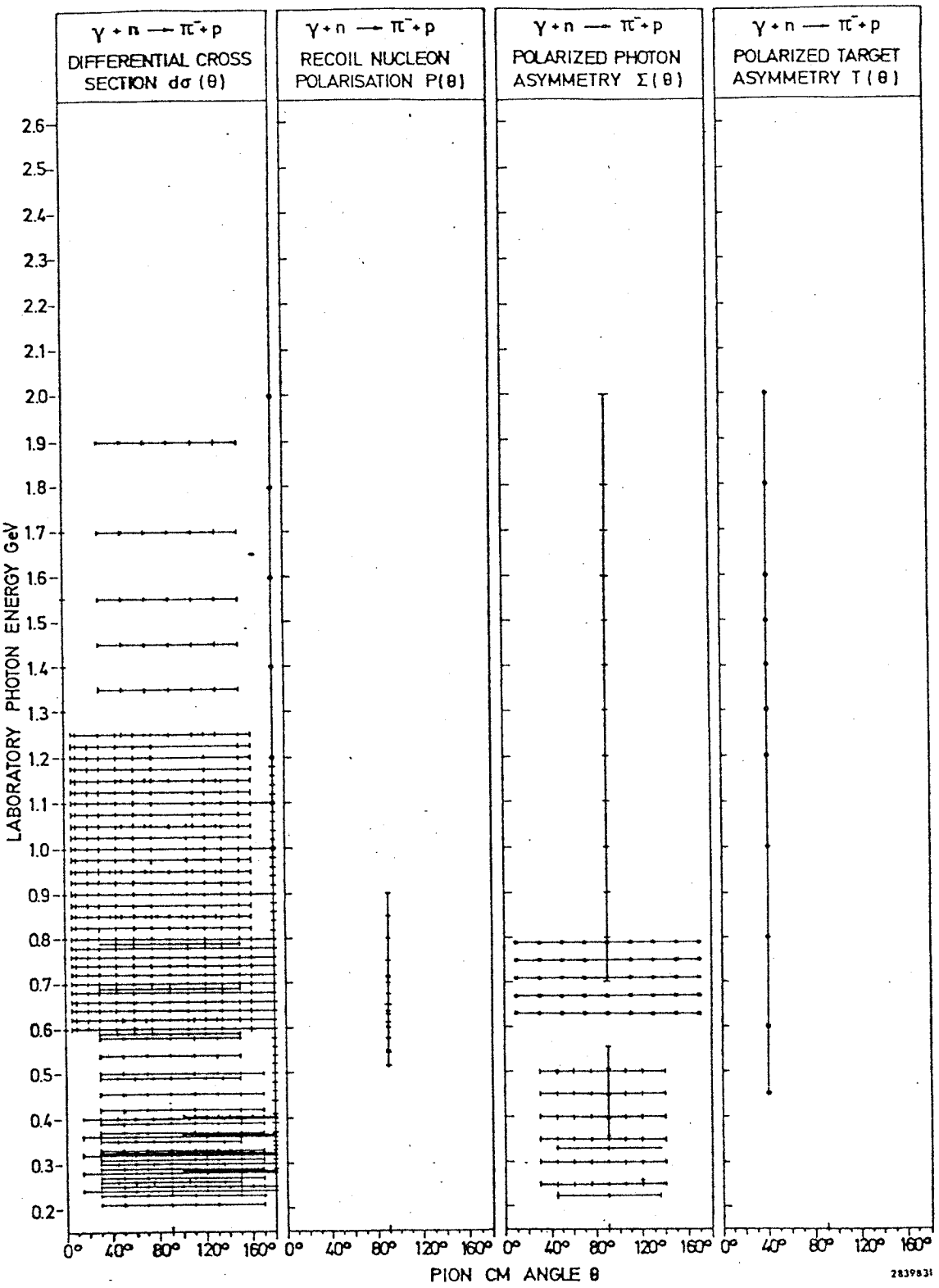
γ + n → π⁻ + p
DIFFERENTIAL CROSS SECTION dσ (θ)
γ + n → π⁻ + p
RECOIL NUCLEON POLARISATION P(θ)
γ + n → π⁻ + p
POLARIZED PHOTON ASYMMETRY Σ(θ)
γ + n → π⁻ + p
POLARIZED TARGET ASYMMETRY T(θ)
LABORATORY PHOTON ENERGY GeV
2.6
2.5
2.4
2.3
2.2
2.1
2.0
1.9
1.8
1.7
1.6
1.5
1.4
1.3
1.2
1.1
1.0
0.9
0.8
0.7
0.6
0.5
0.4
0.3
0.2
0° 40° 80° 120° 160°
PION CM ANGLE θ
2839831

FIG. 1(c)

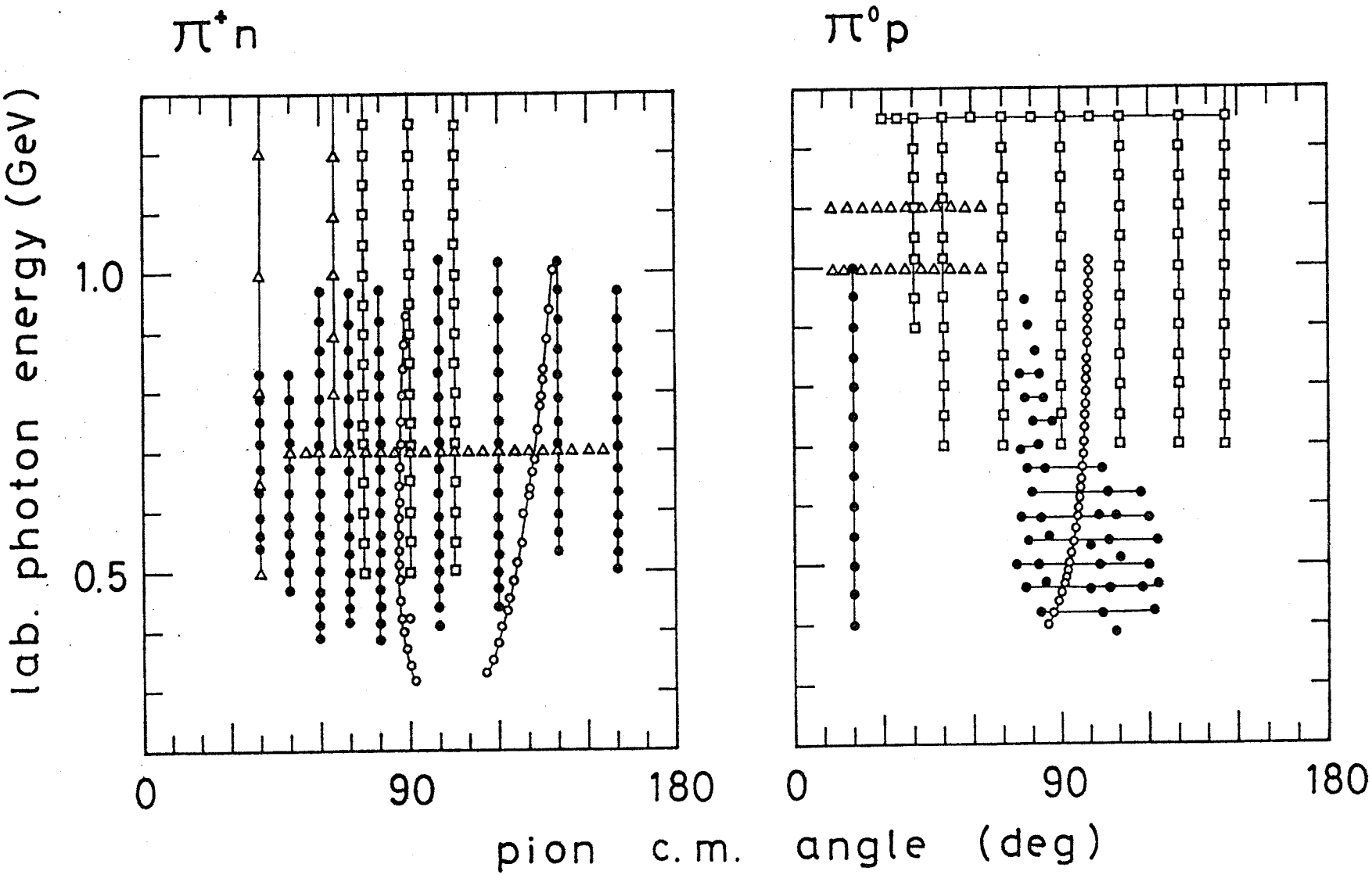
π⁺n
π⁰p
lab. photon energy (GeV)
1.0
0.5
0
90
180
0
90
180
pion c.m. angle (deg)

FIG. 2

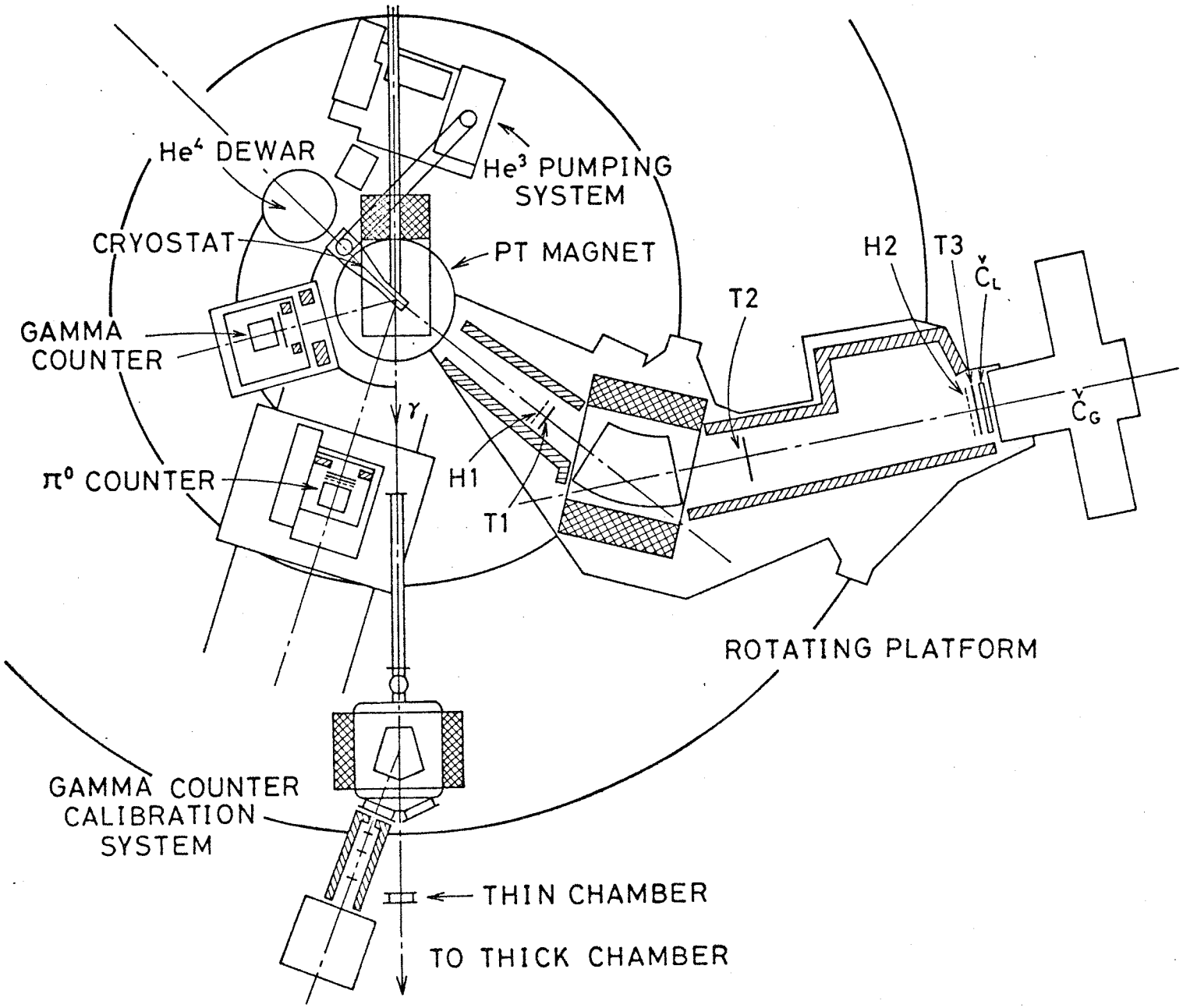
He⁴ DEWAR
He³ PUMPING SYSTEM
CRYOSTAT
PT MAGNET
H2
T3
$\check{C}_L$
T2
GAMMA COUNTER
γ
$\check{C}_G$
π⁰ COUNTER
H1
T1
ROTATING PLATFORM
GAMMA COUNTER CALIBRATION SYSTEM
THIN CHAMBER
TO THICK CHAMBER

FIG. 3

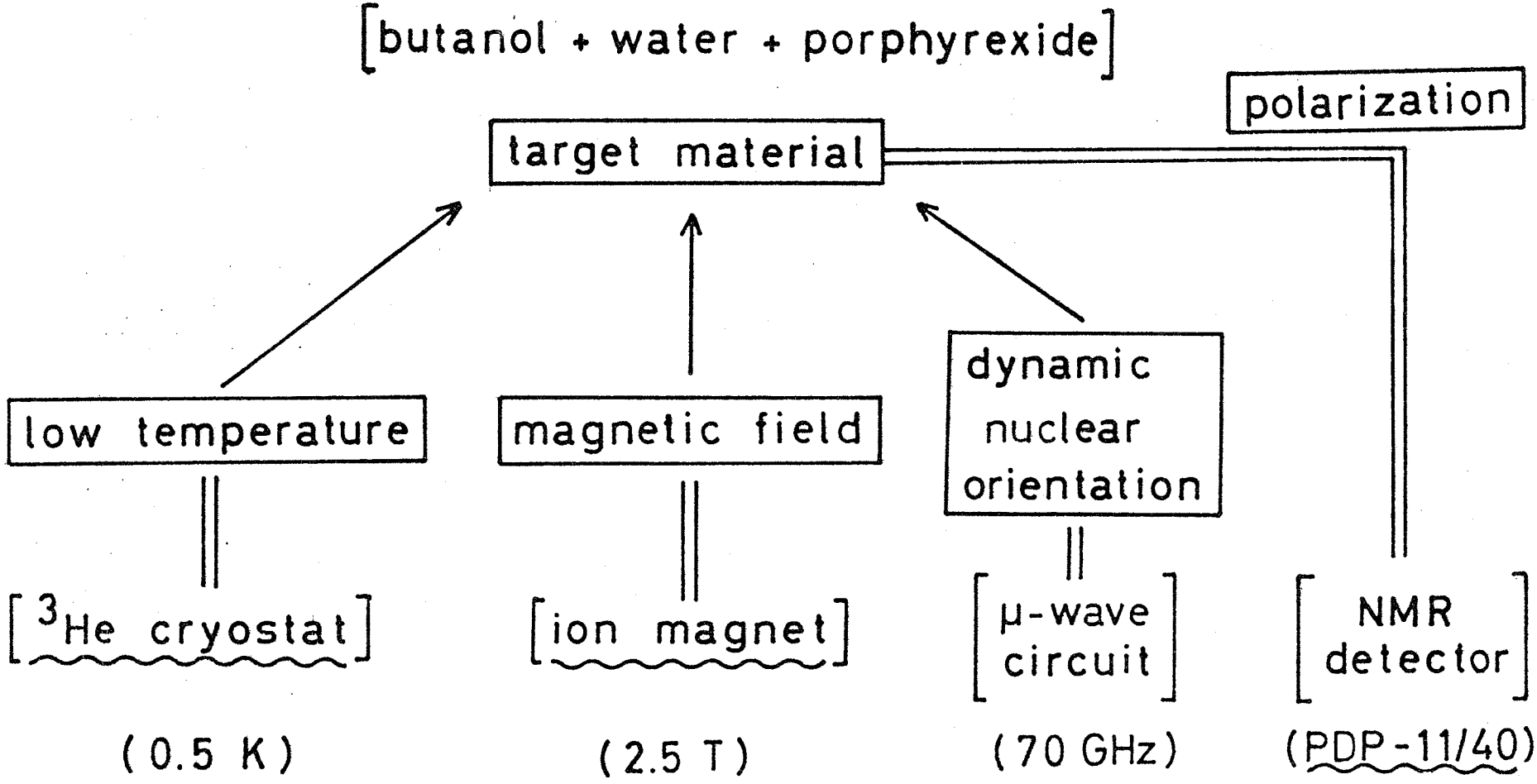
[butanol + water + porphyrexide]
target material
polarization
low temperature
magnetic field
dynamic nuclear orientation
[^{3}He cryostat]
[ion magnet]
[μ-wave circuit]
[NMR detector]
(0.5 K)
(2.5 T)
(70 GHz)
(PDP-11/40)

FIG. 4

butanol

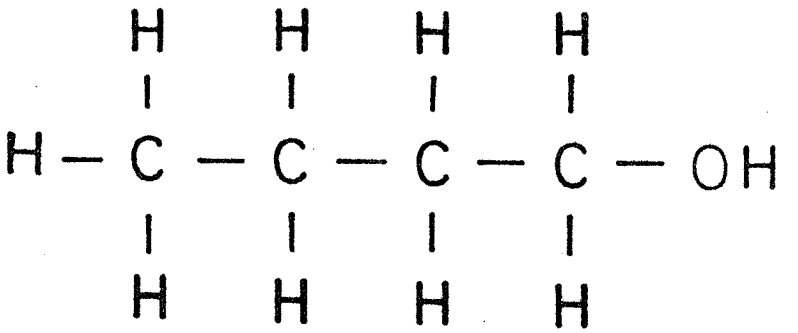

porphyrexide

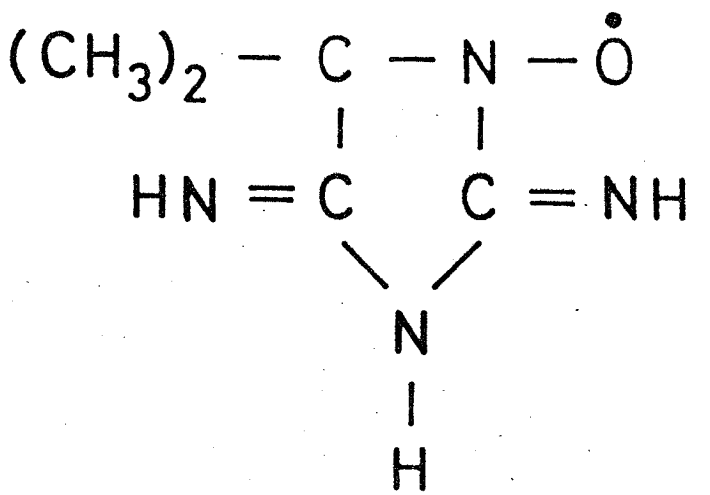

FIG. 5

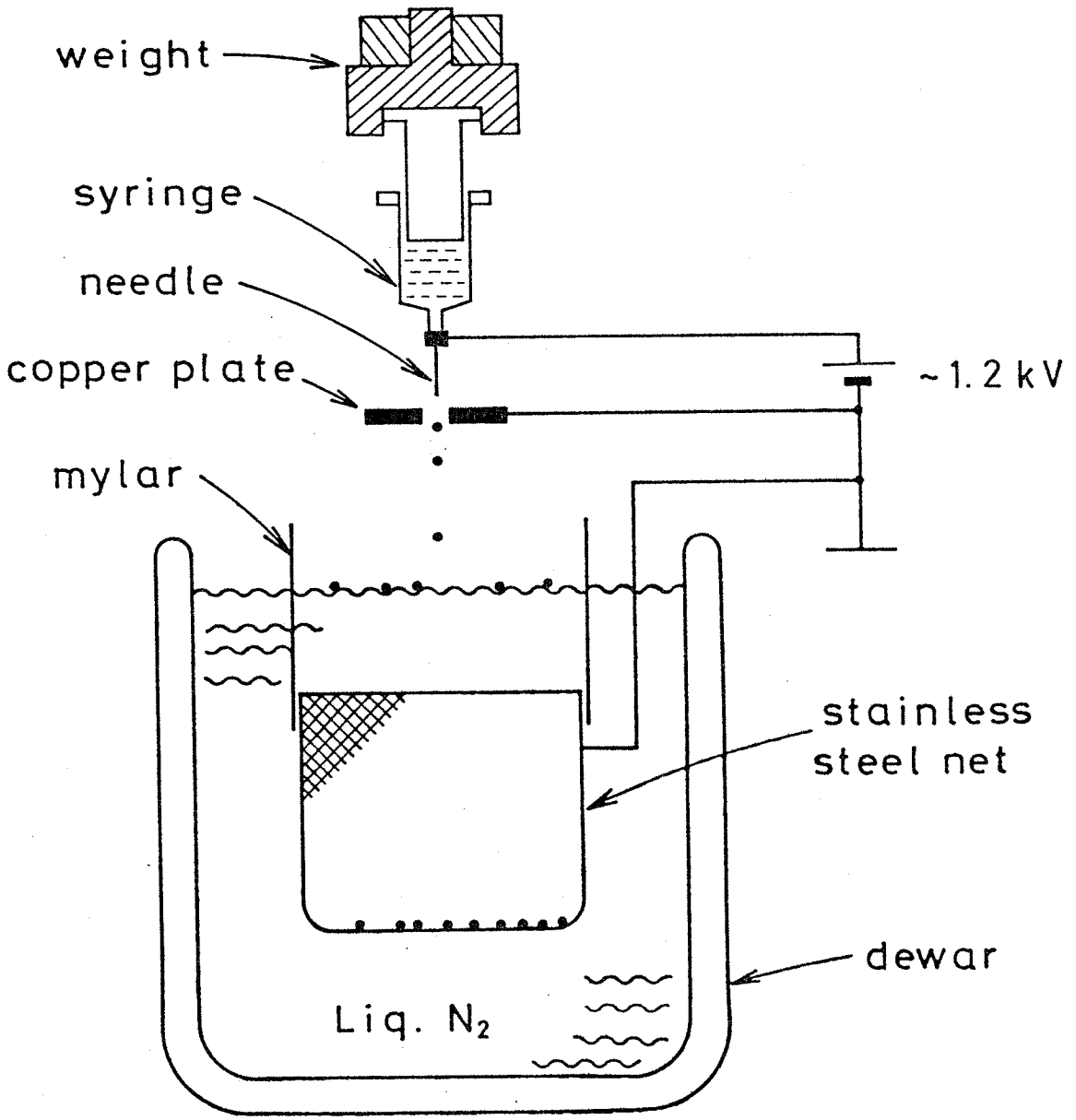
weight
syringe
needle
copper plate
~1.2 kV
mylar
stainless
steel net
dewar
Liq. N_2

FIG. 6

PT MAGNET

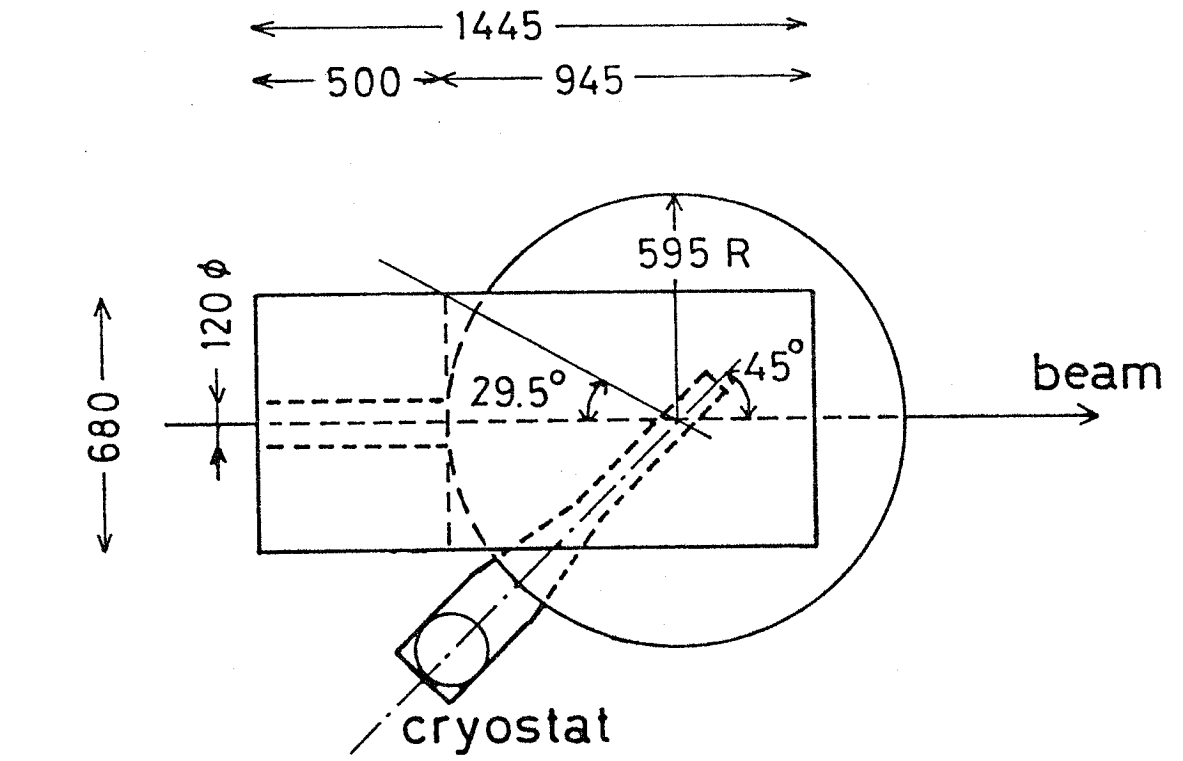

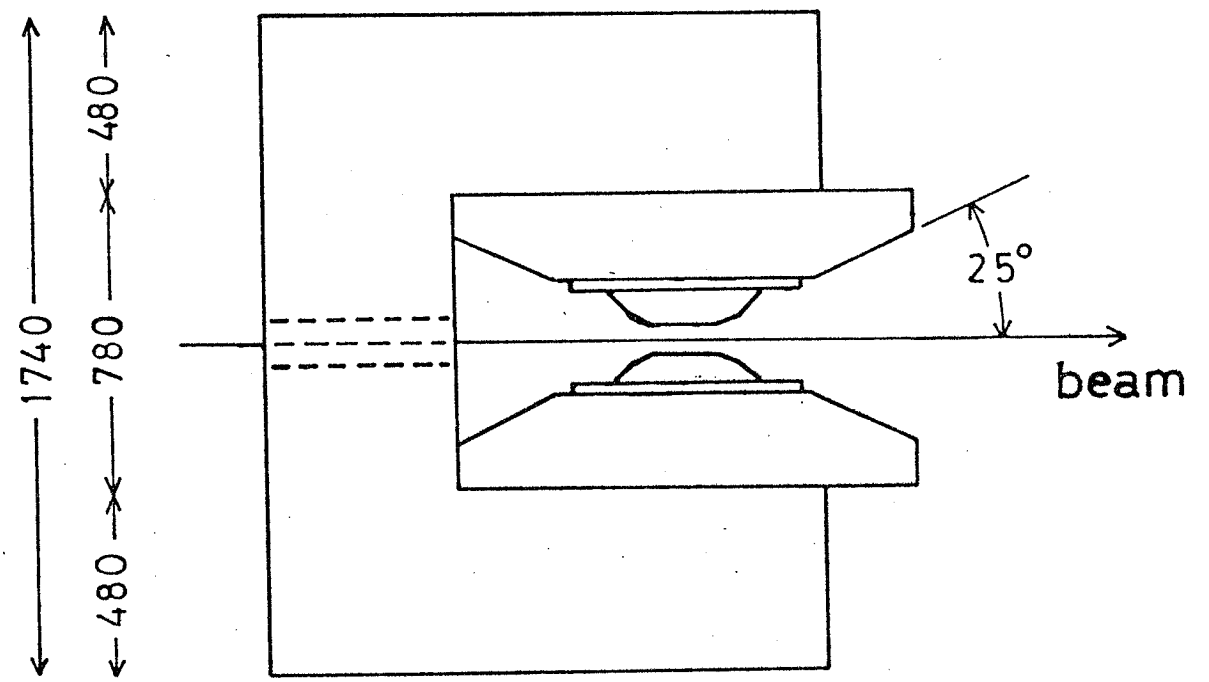

FIG. 7

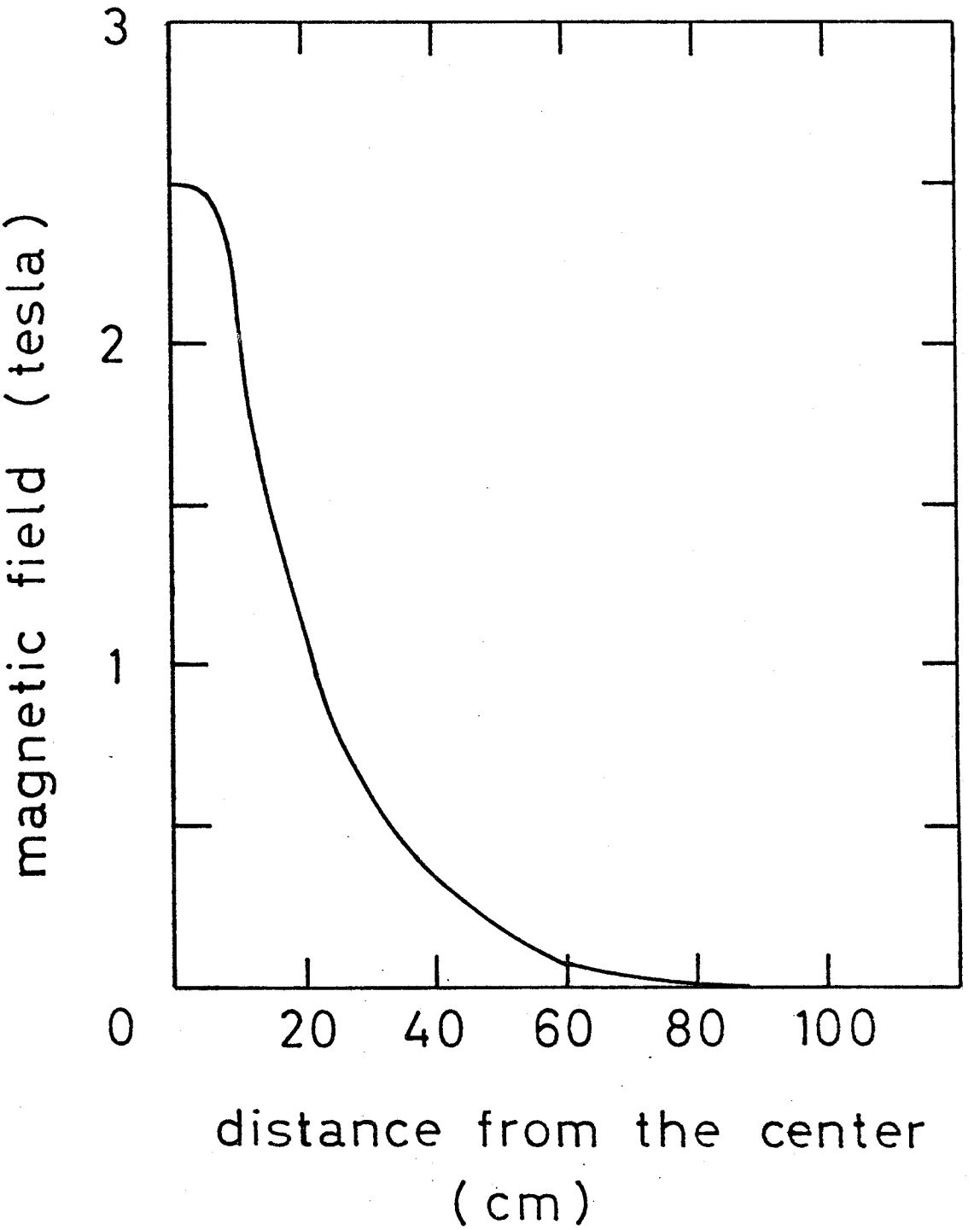
3
2
1
0
magnetic field (tesla)
20
40
60
80
100
distance from the center
(cm)

FIG. 8

homogeneity of the magnetic field

$H_0 = 2.5850$ T

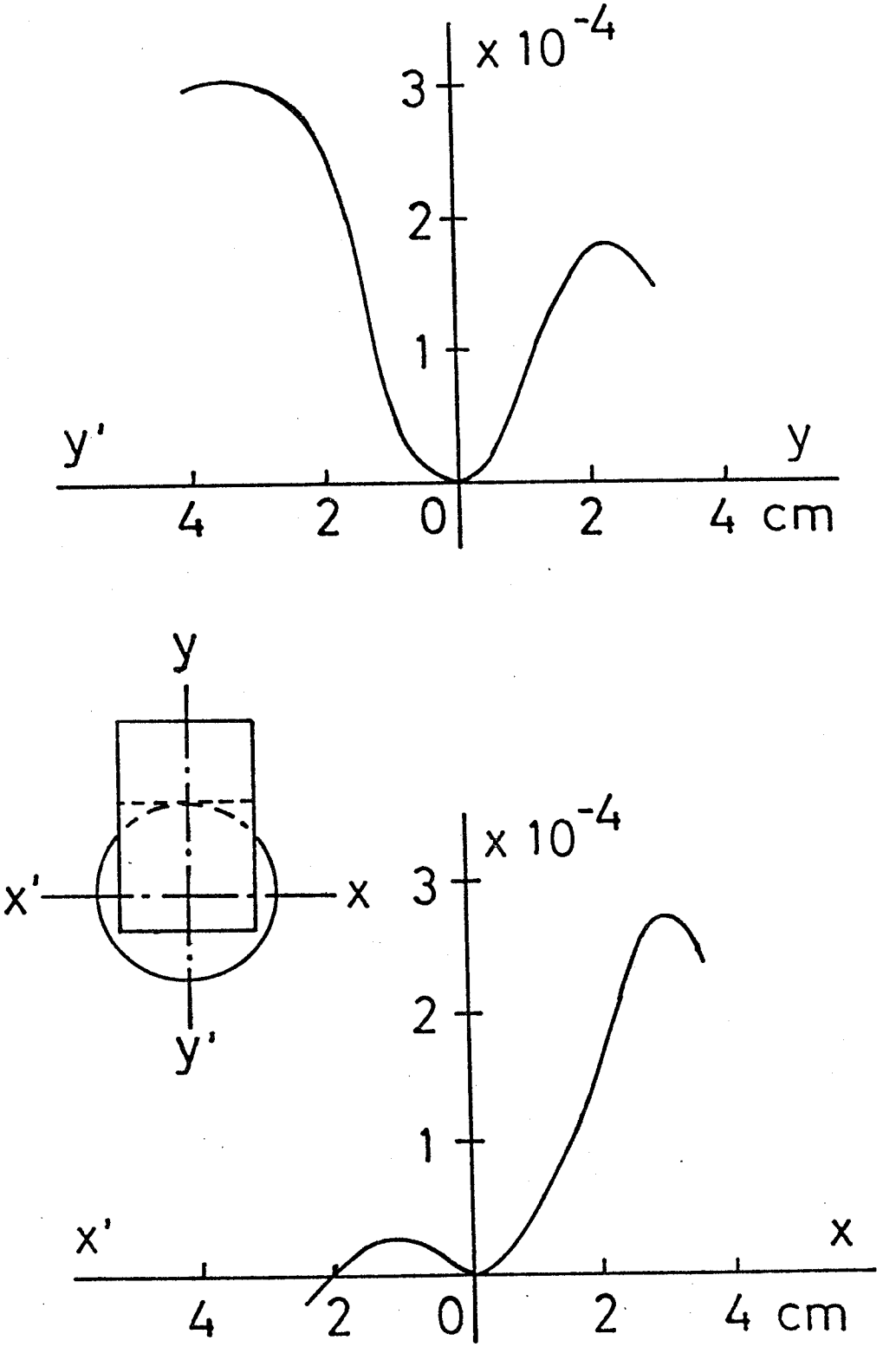

FIG. 9

1 cavity
2 heat exchanger II
3 evaporator & condenser
4 heat exchanger I
5 separator
6 tube-in-tube heat exchanger
7 thermal anchor I
8 " II
9 " III
10 radiation shield I
11 " II

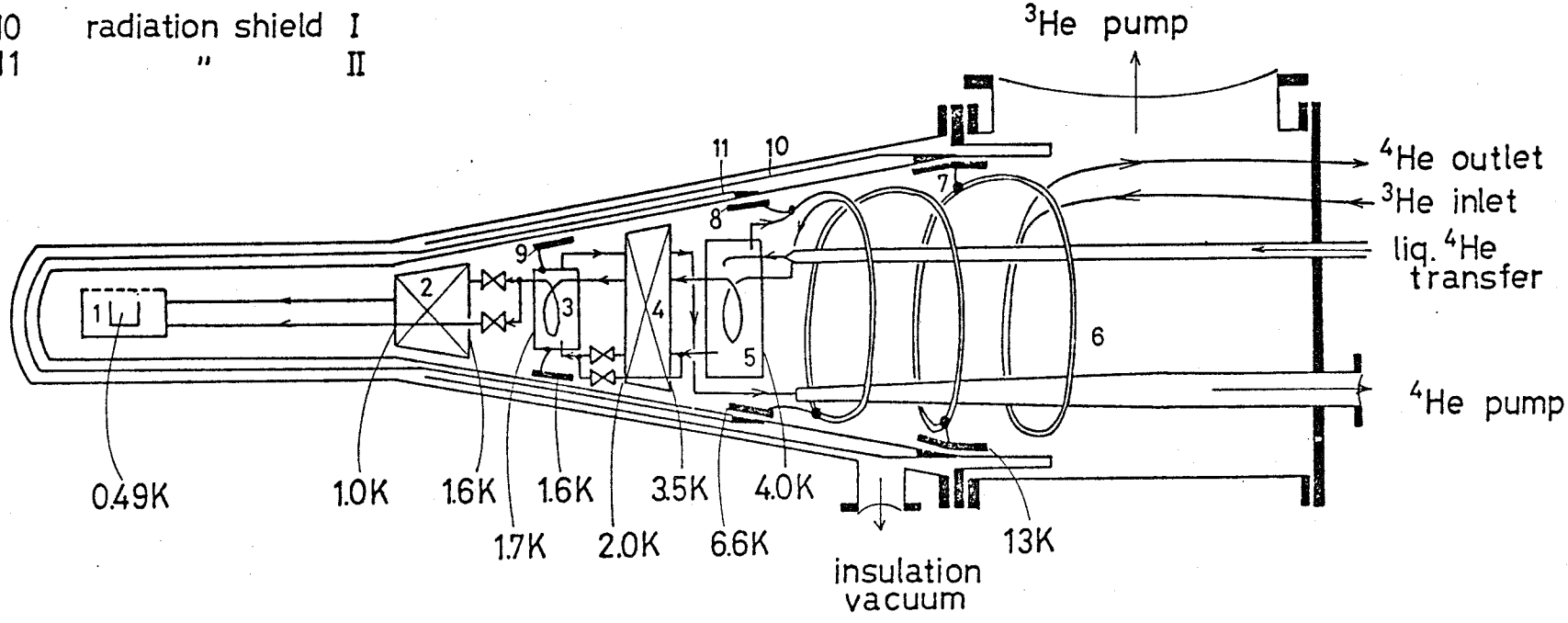

FIG. 10

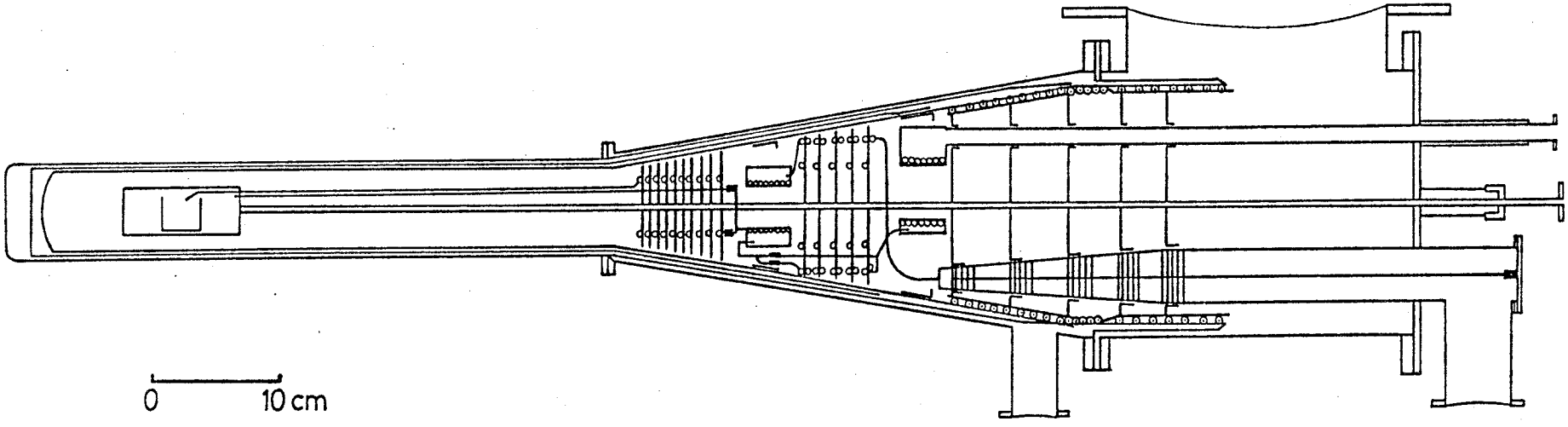

FIG. 11

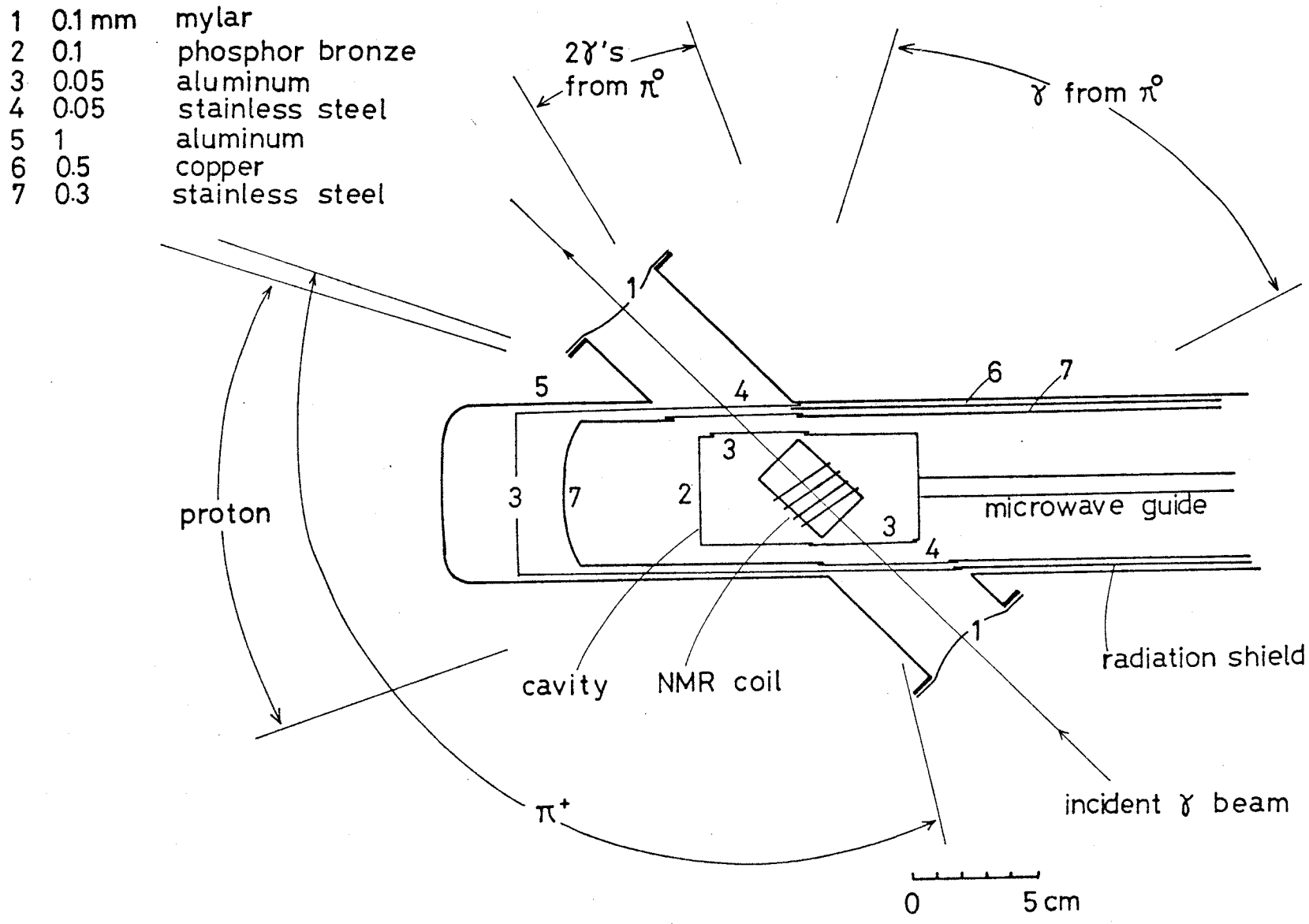
1 0.1 mm mylar
2 0.1 phosphor bronze
3 0.05 aluminum
4 0.05 stainless steel
5 1 aluminum
6 0.5 copper
7 0.3 stainless steel
2γ's from π°
γ from π°
proton
microwave guide
cavity
NMR coil
radiation shield
π+
incident γ beam
0
5 cm

FIG. 12

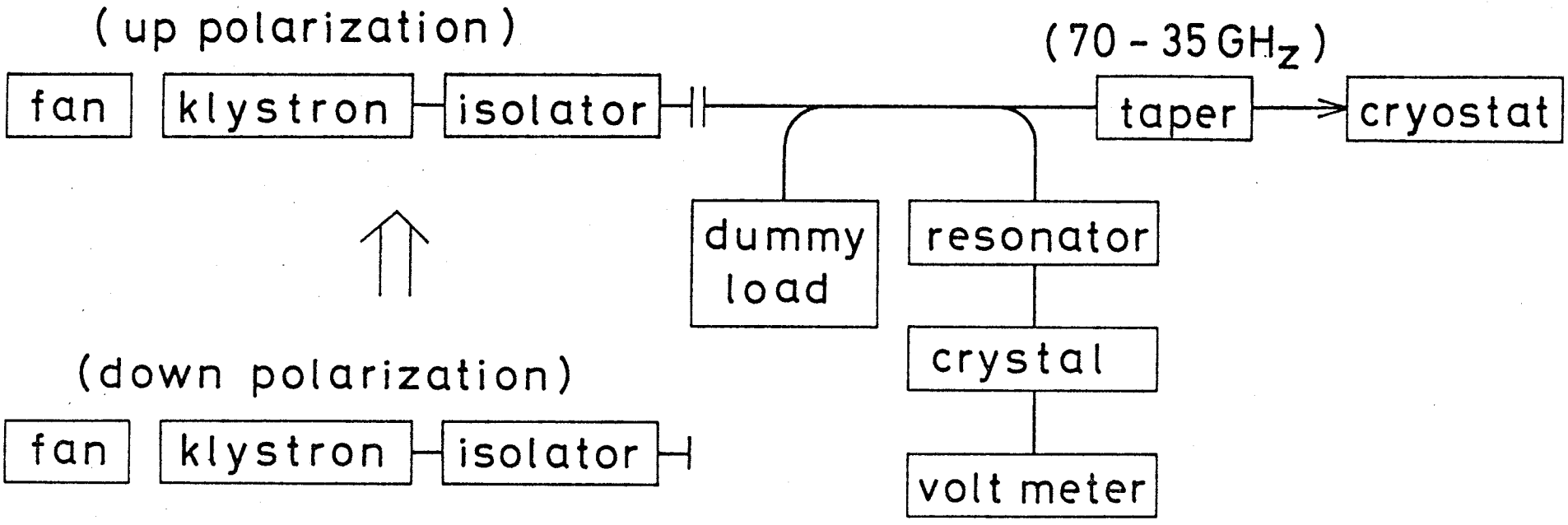
(up polarization)
fan
klystron
isolator
(70 - 35 GHz)
taper
cryostat
dummy load
resonator
crystal
volt meter
(down polarization)
fan
klystron
isolator

FIG. 13

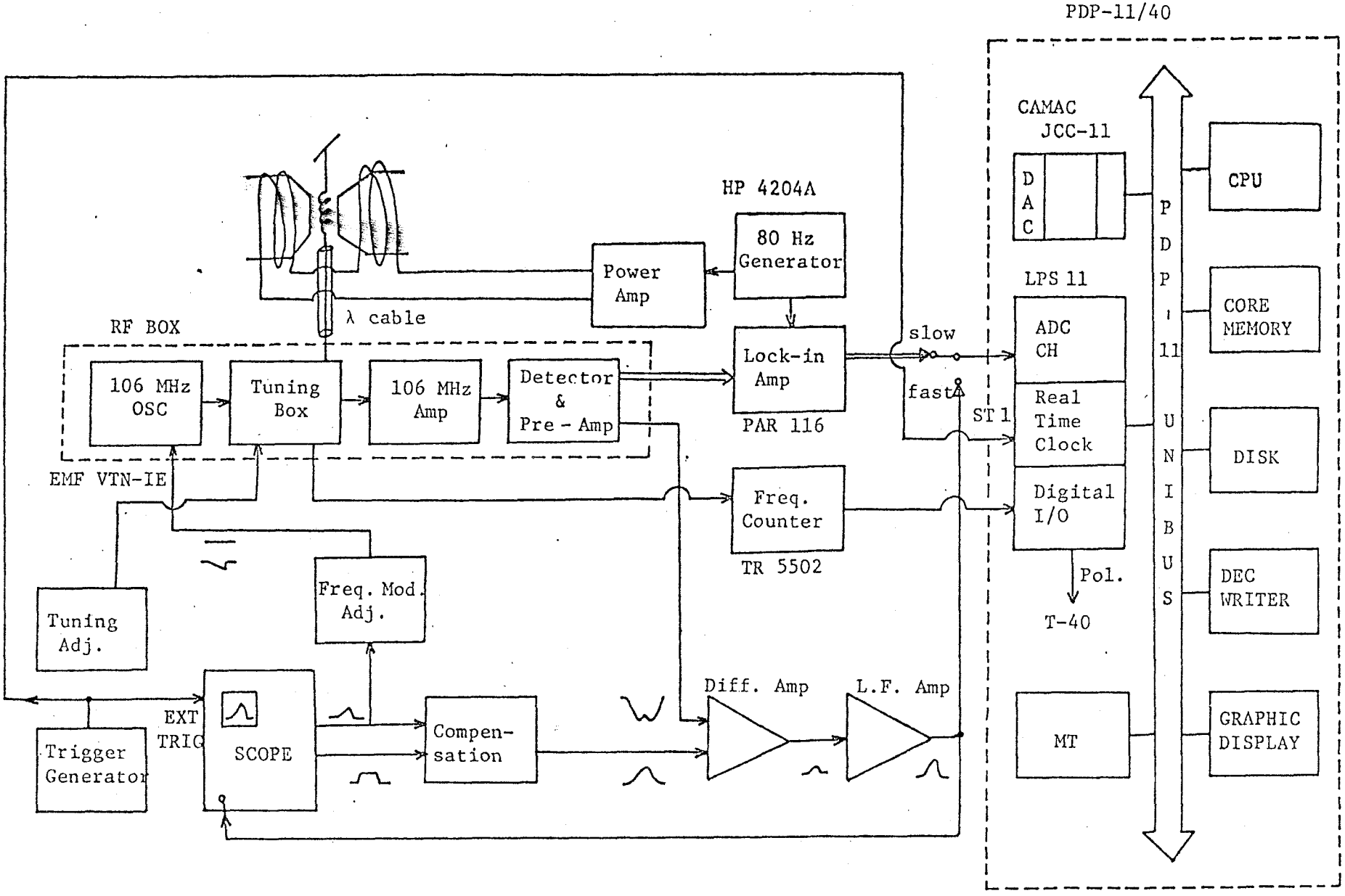
PDP-11/40
CAMAC
JCC-11
D
A
C
CPU
HP 4204A
80 Hz
Generator
Power
Amp
λ cable
RF BOX
106 MHz
OSC
Tuning
Box
106 MHz
Amp
Detector
&
Pre - Amp
Lock-in
Amp
PAR 116
slow
fast
ST 1
LPS 11
ADC
CH
Real
Time
Clock
Digital
I/O
CORE
MEMORY
DISK
DEC
WRITER
GRAPHIC
DISPLAY
MT
P
D
P
-
11
U
N
I
B
U
S
EMF VTN-IE
Freq.
Counter
TR 5502
Pol.
T-40
Tuning
Adj.
Freq. Mod.
Adj.
EXT
TRIG
SCOPE
Trigger
Generator
Compen-
sation
Diff. Amp
L.F. Amp

Fig. 14

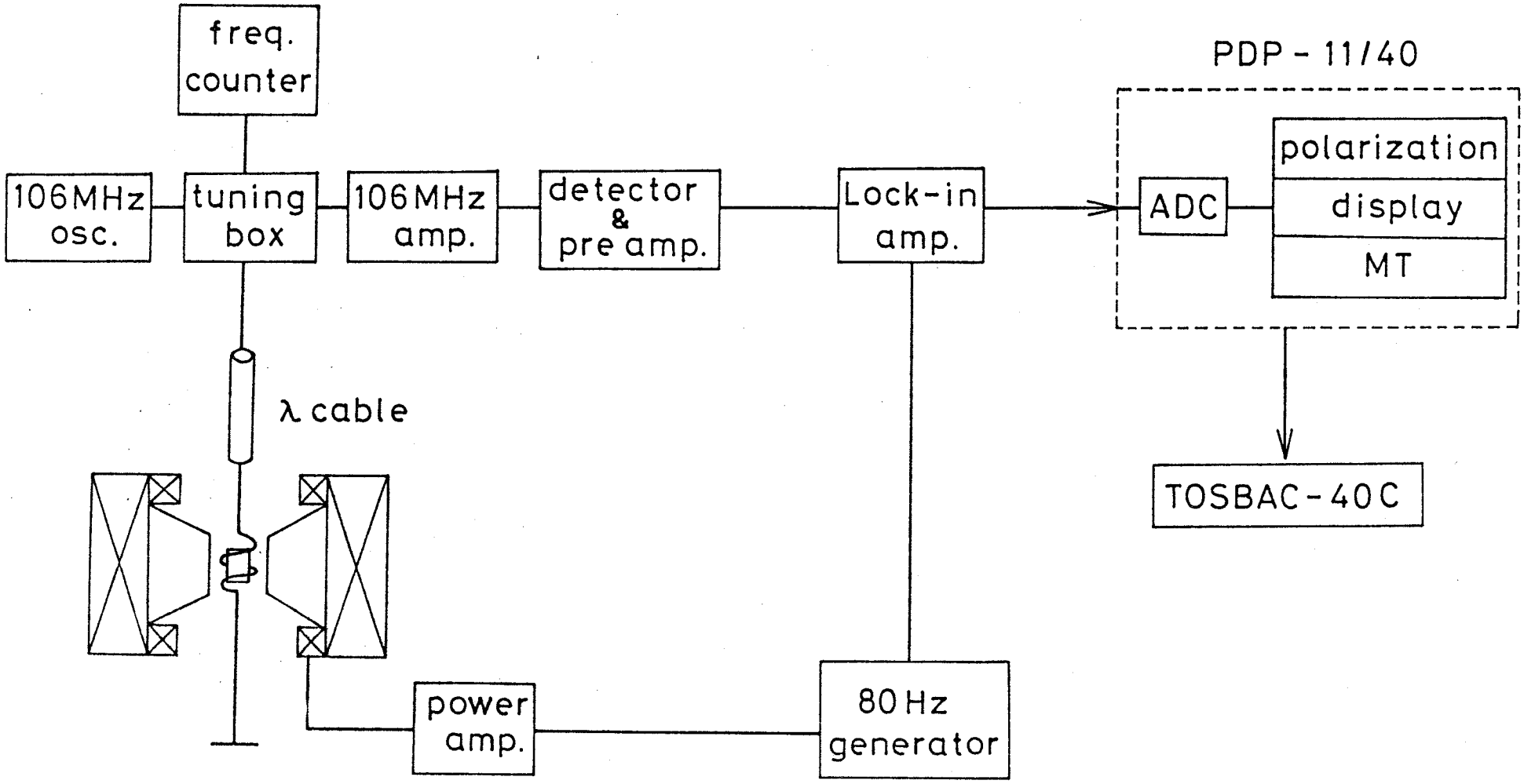
freq.
counter
106MHz
osc.
tuning
box
106MHz
amp.
detector
&
pre amp.
Lock-in
amp.
PDP - 11/40
ADC
polarization
display
MT
TOSBAC - 40C
λ cable
power
amp.
80 Hz
generator

FIG. 15

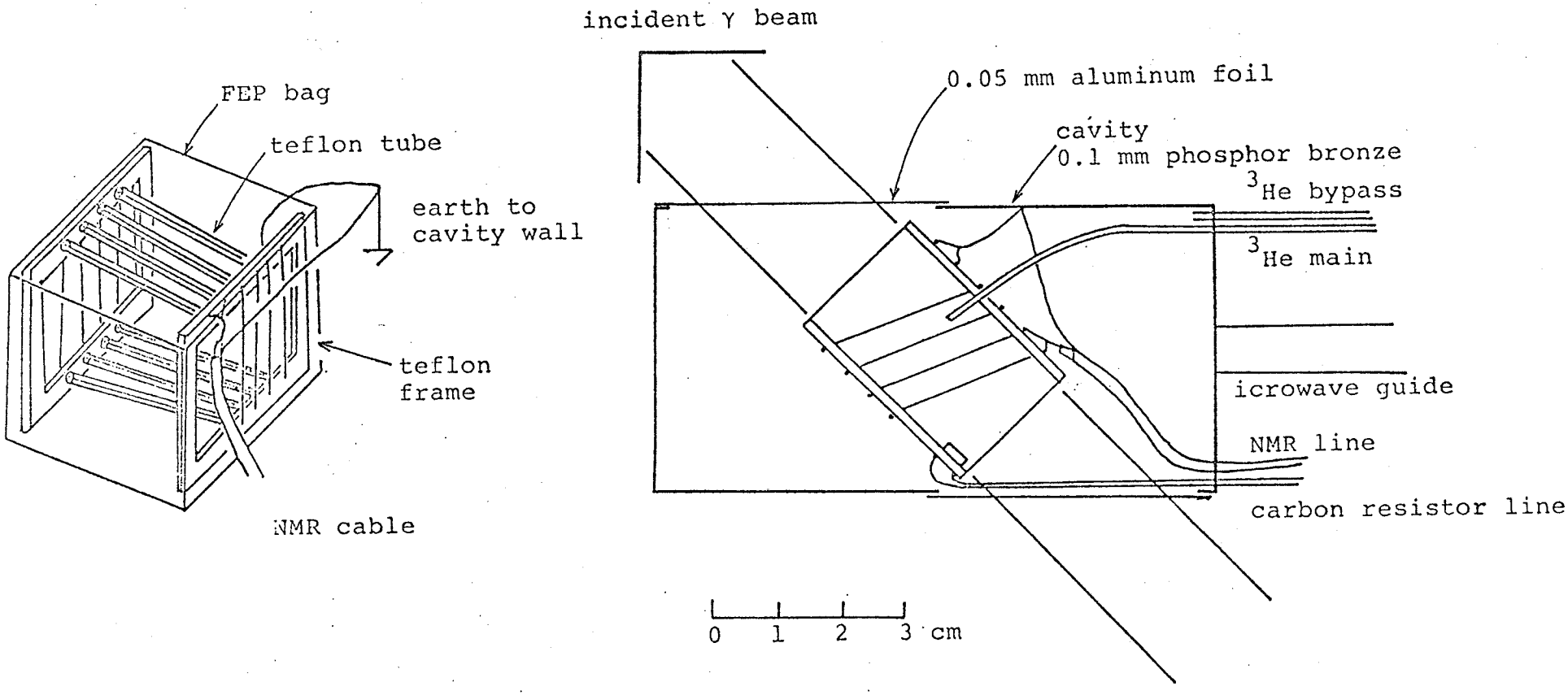

(a) NMR coil

(b) μ wave cavity

FIG. 16

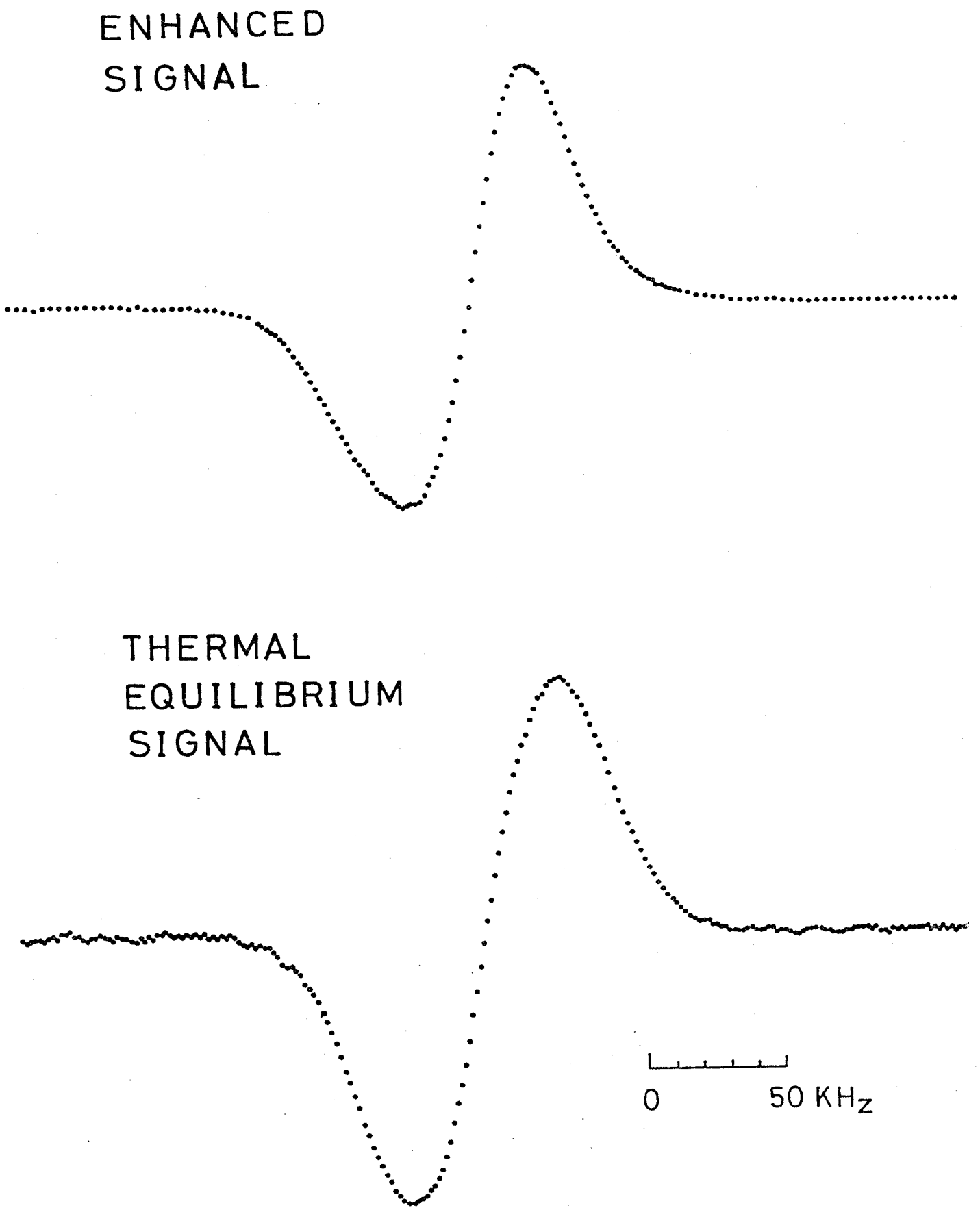

FIG. 17

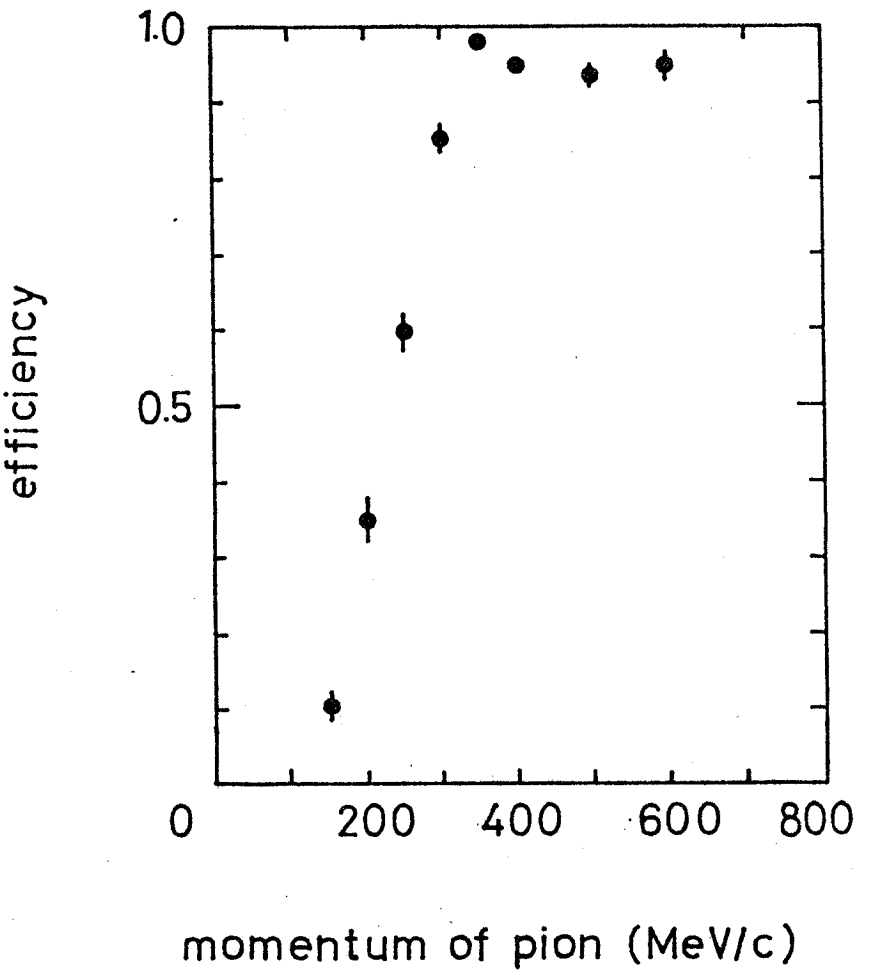

FIG. 18

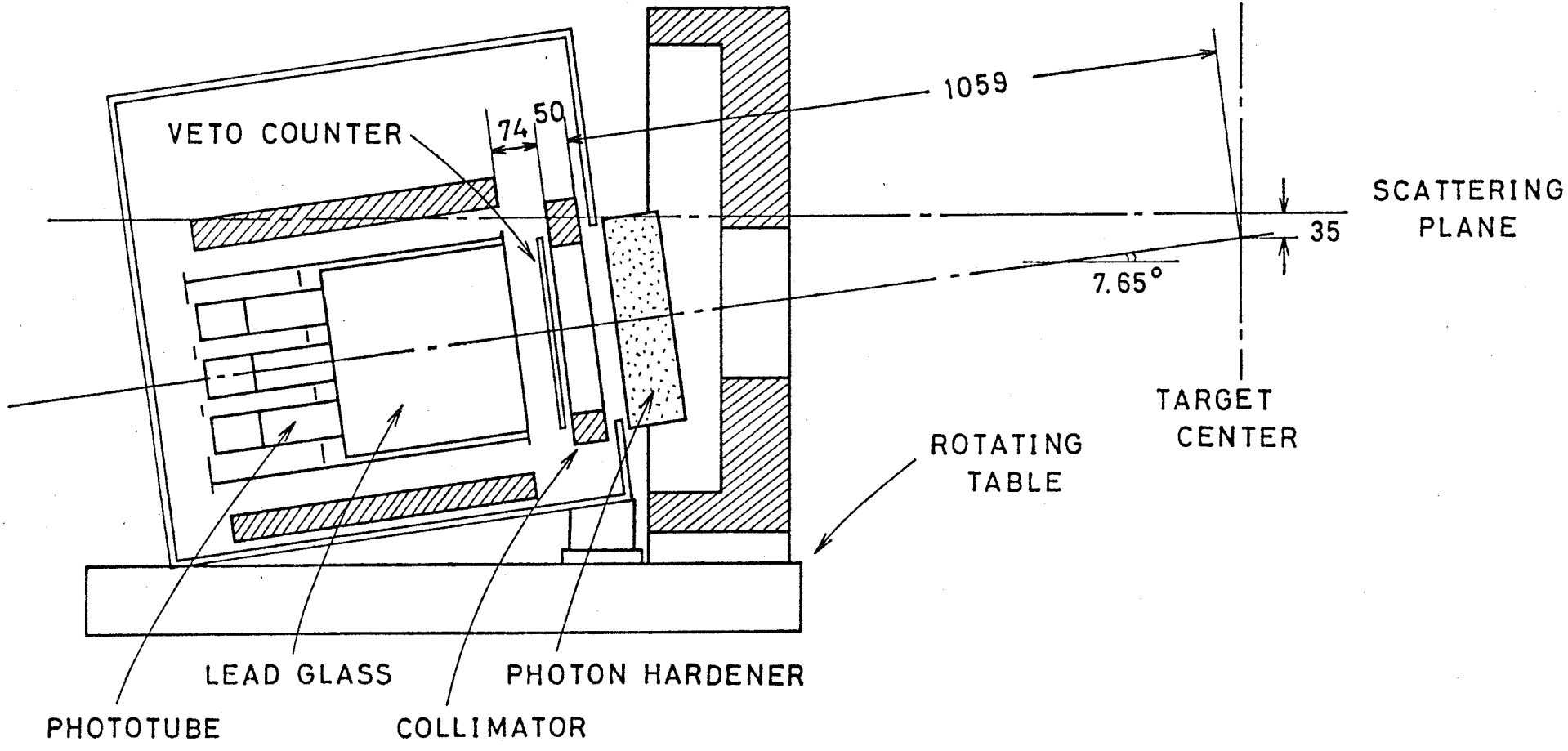
VETO COUNTER
74
50
1059
SCATTERING
PLANE
35
7.65°
TARGET
CENTER
ROTATING
TABLE
LEAD GLASS
PHOTON HARDENER
PHOTOTUBE
COLLIMATOR
LEAD
LiH

FIG. 19

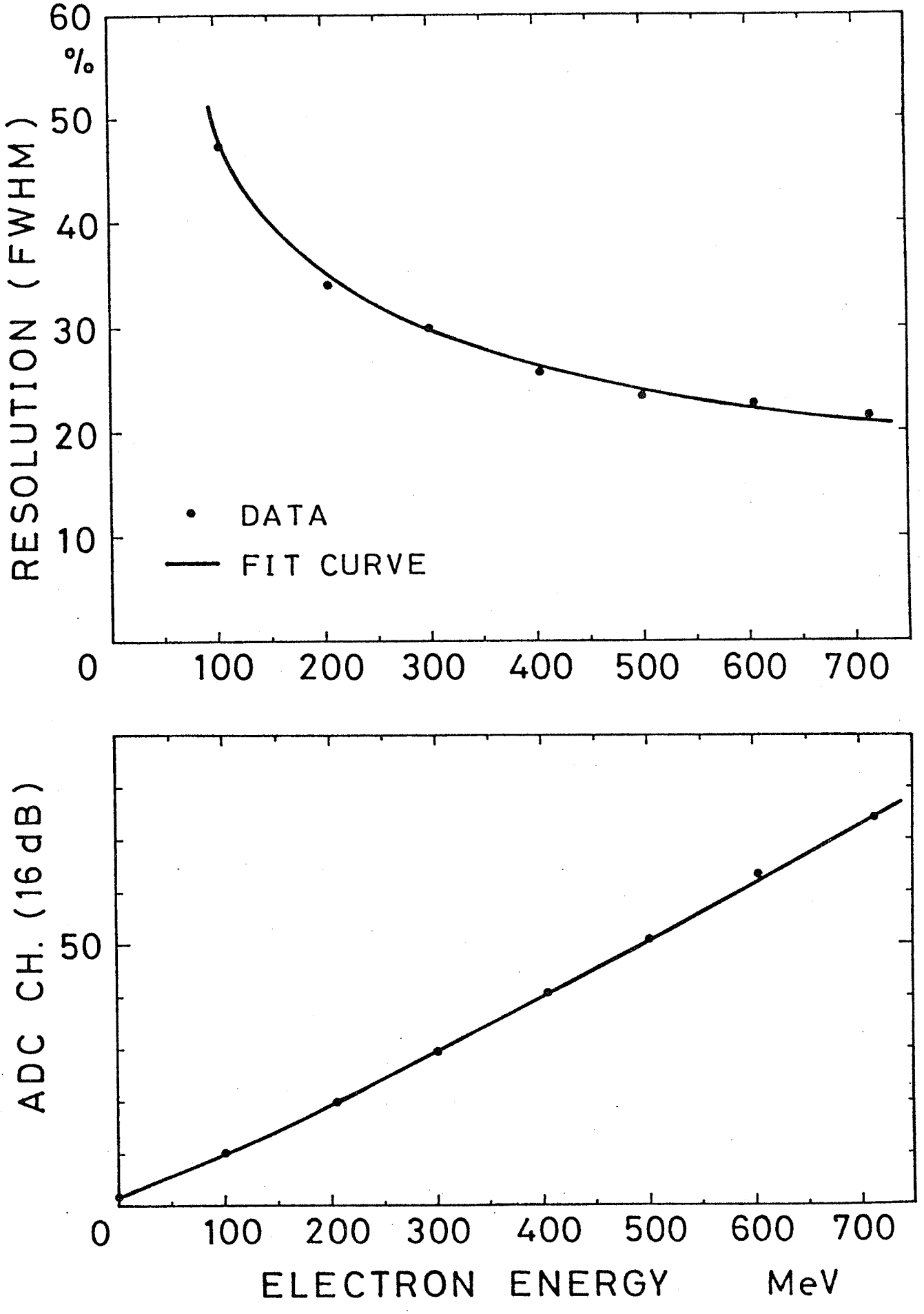
60
%
50
40
30
20
10
0
RESOLUTION (FWHM)
DATA
FIT CURVE
100
200
300
400
500
600
700
ADC CH. (16 dB)
50
0
100
200
300
400
500
600
700
ELECTRON ENERGY
MeV

FIG. 20

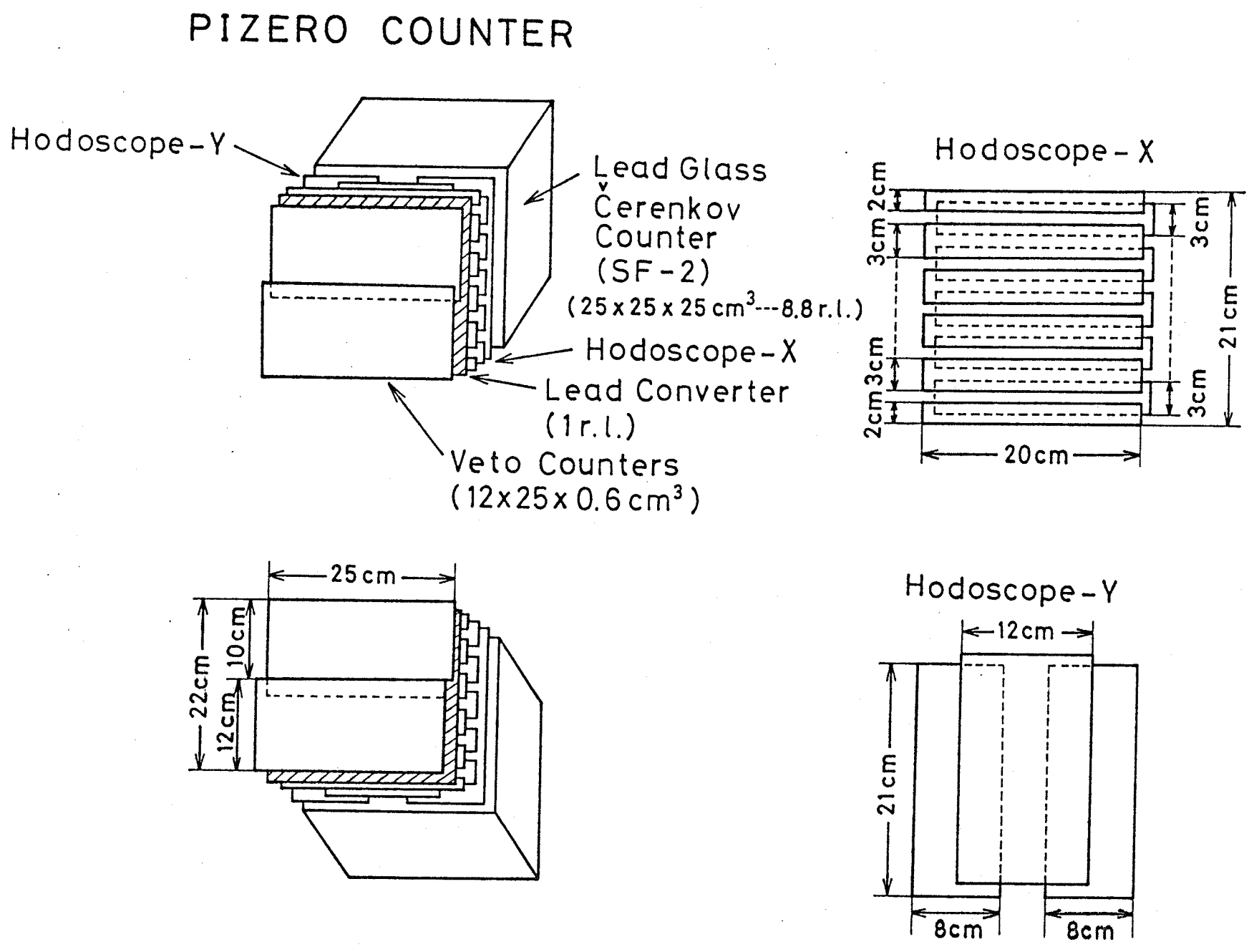
PIZERO COUNTER
Hodoscope-Y
Lead Glass
Cerenkov
Counter
(SF-2)
(25x25x25 cm³---8.8 r.l.)
Hodoscope-X
Lead Converter
(1 r.l.)
Veto Counters
(12x25x0.6 cm³)
Hodoscope-X
2cm
3cm
3cm
3cm
3cm
2cm
21cm
20cm
25cm
22cm
10cm
12cm
Hodoscope-Y
12cm
21cm
8cm
8cm

FIG. 21

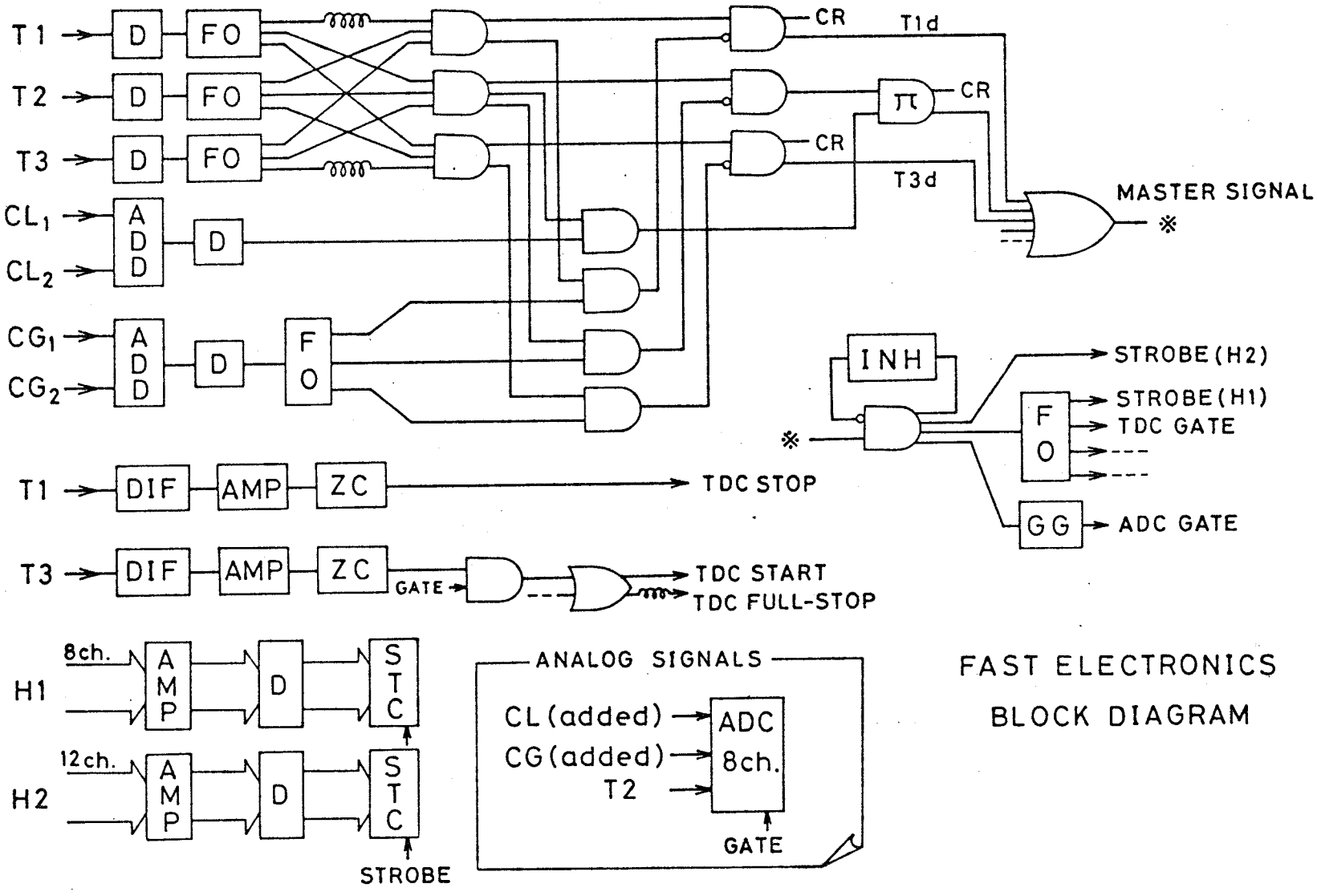
T1
T2
T3
CL1
CL2
CG1
CG2
D
FO
ADD
CR
T1d
T3d
MASTER SIGNAL
INH
STROBE(H2)
STROBE(H1)
TDC GATE
GG
ADC GATE
DIF
AMP
ZC
TDC STOP
GATE
TDC START
TDC FULL-STOP
8ch.
12ch.
H1
H2
STC
STROBE
ANALOG SIGNALS
CL(added)
CG(added)
ADC
8ch.
GATE
FAST ELECTRONICS
BLOCK DIAGRAM

FIG. 22(A)

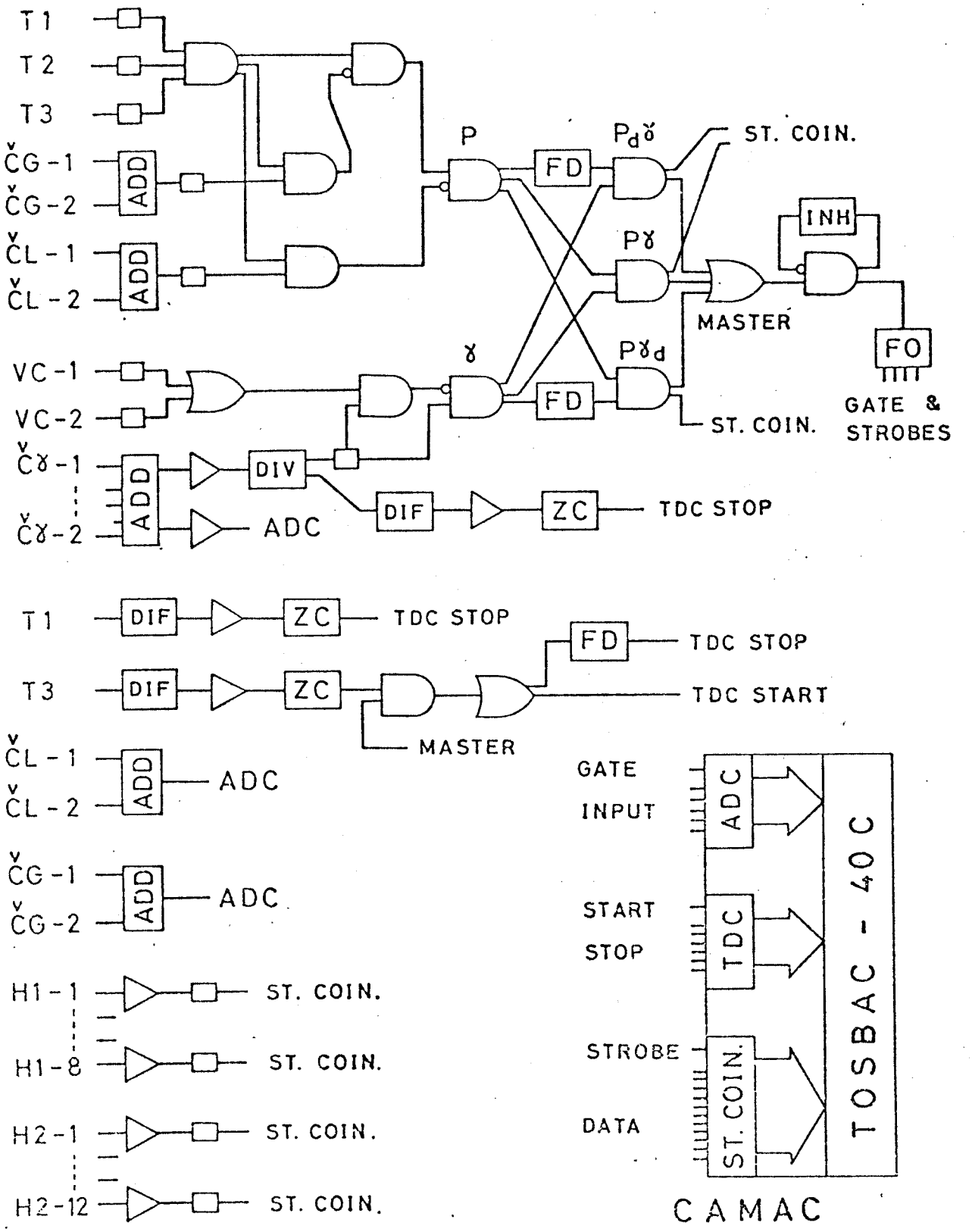
T1
T2
T3
CG-1
CG-2
CL-1
CL-2
ADD
P
FD
Pdδ
ST. COIN.
INH
Pγ
MASTER
FO
GATE & STROBES
VC-1
VC-2
γ
Pγd
Cγ-1
Cγ-2
DIV
DIF
ZC
TDC STOP
ADC
FD
TDC STOP
TDC START
MASTER
GATE
INPUT
START
STOP
STROBE
DATA
TDC
ST. COIN.
TOSBAC - 40 C
CAMAC
H1-1
H1-8
H2-1
H2-12
DISCRIMINATOR
AMPLIFIER
FIXED DELAY
COINCIDENCE
LIN. ADDER
INHIBITOR
FAN IN
DIFF. MODULE
ZERO CROSS. DISCRIM.
FAN OUT
DIVIDER

FIG. 22(B)

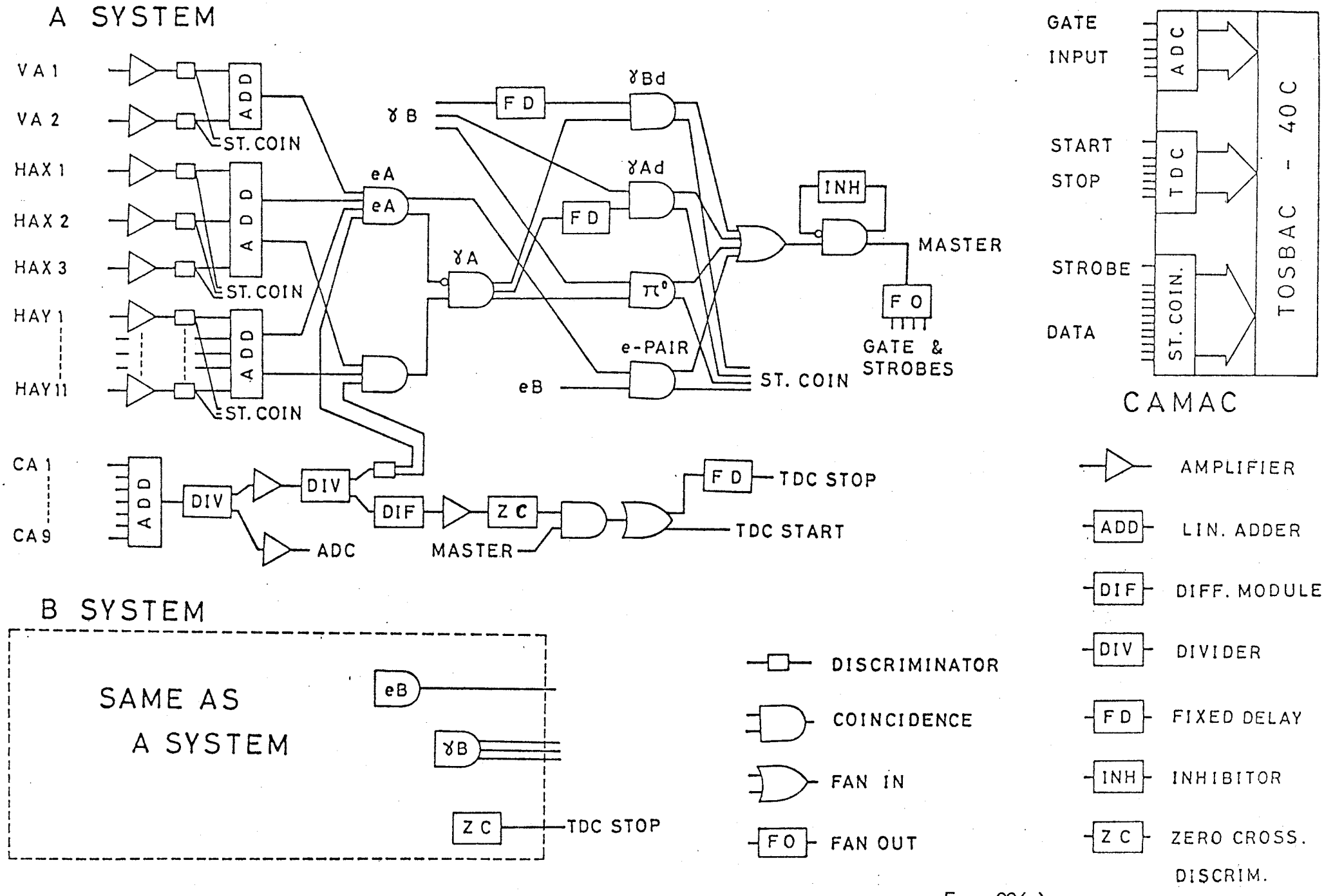
A SYSTEM
VA 1
VA 2
HAX 1
HAX 2
HAX 3
HAY 1
HAY 11
CA 1
CA 9
ADD
ST. COIN
eA
γ B
γ Bd
γ Ad
γ A
FD
INH
MASTER
FO
GATE & STROBES
e-PAIR
eB
ST. COIN
DIV
DIF
ZC
ADC
MASTER
FD
TDC STOP
TDC START
GATE
INPUT
START
STOP
STROBE
DATA
ADC
TDC
ST. COIN.
TOSBAC - 40C
CAMAC
B SYSTEM
SAME AS
A SYSTEM
eB
γB
ZC
TDC STOP
DISCRIMINATOR
COINCIDENCE
FAN IN
FO
FAN OUT
AMPLIFIER
ADD
LIN. ADDER
DIF
DIFF. MODULE
DIV
DIVIDER
FD
FIXED DELAY
INH
INHIBITOR
ZC
ZERO CROSS. DISCRIM.

FIG. 22(c)

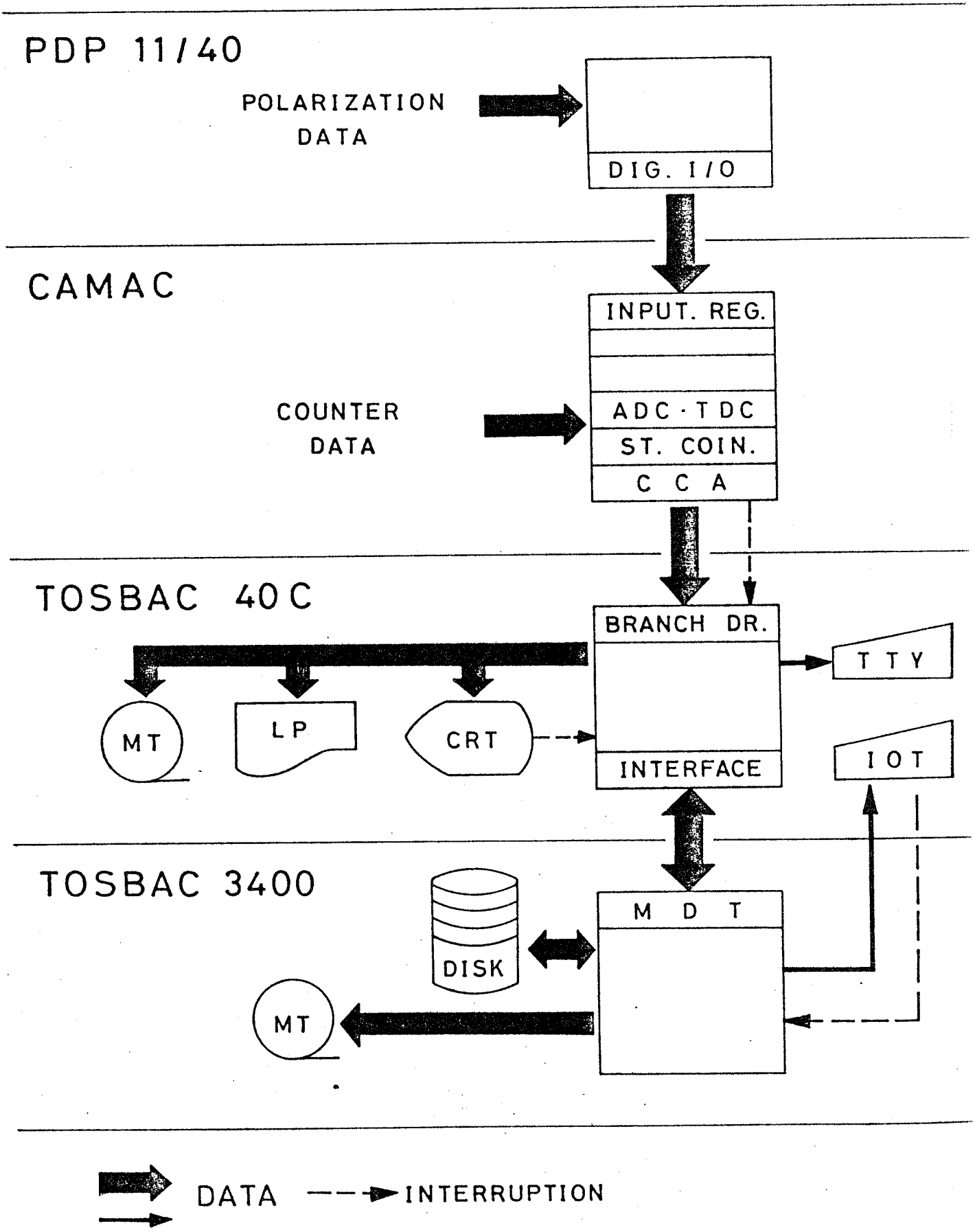
PDP 11/40
POLARIZATION DATA
DIG. I/O
CAMAC
INPUT. REG.
COUNTER DATA
ADC · TDC
ST. COIN.
C C A
TOSBAC 40C
BRANCH DR.
T T Y
MT
LP
CRT
INTERFACE
I O T
TOSBAC 3400
M D T
DISK
MT
DATA
INTERRUPTION

FIG. 23

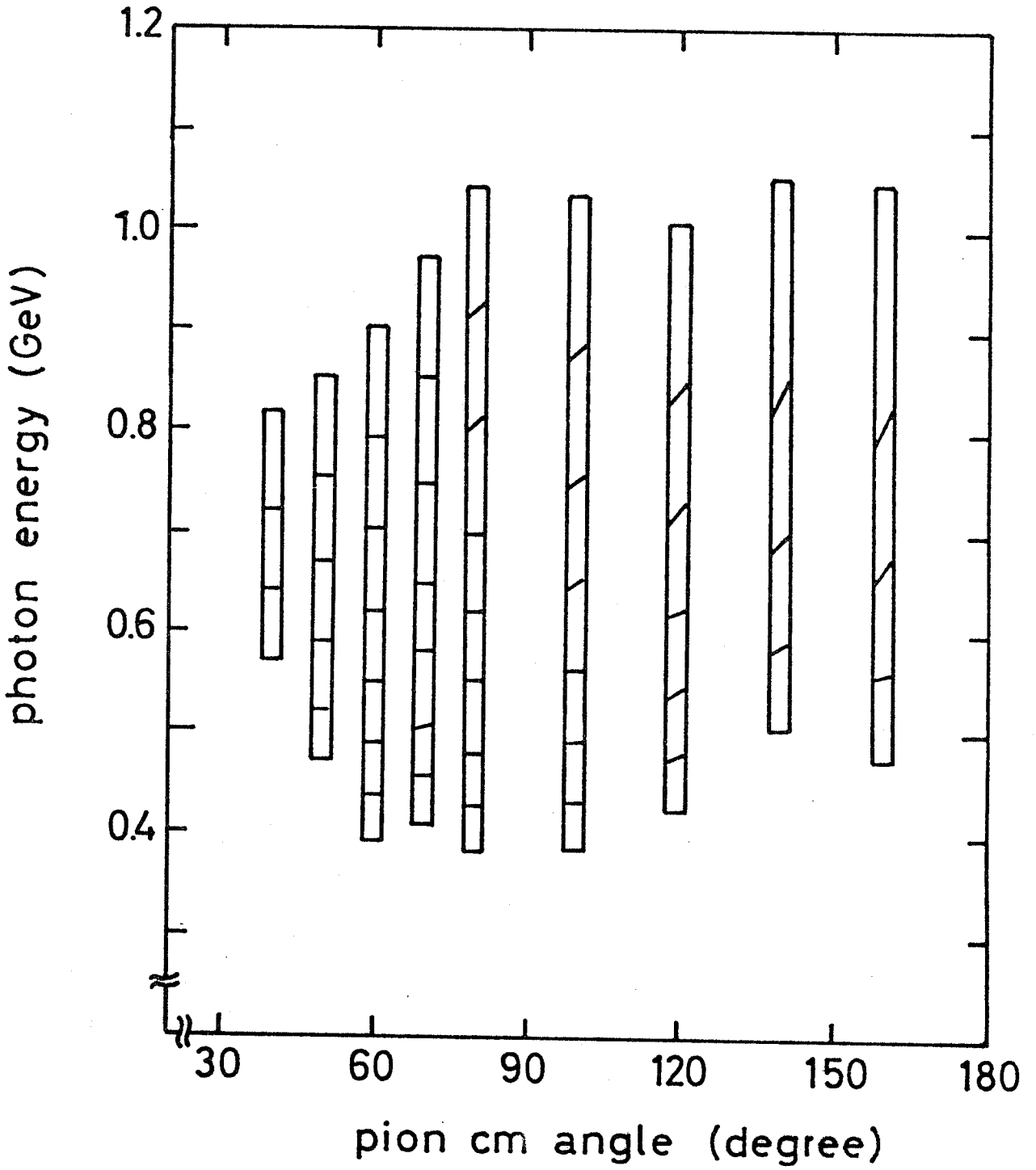
1.2
1.0
0.8
0.6
0.4
photon energy (GeV)
30
60
90
120
150
180
pion cm angle (degree)

FIG. 24(A)

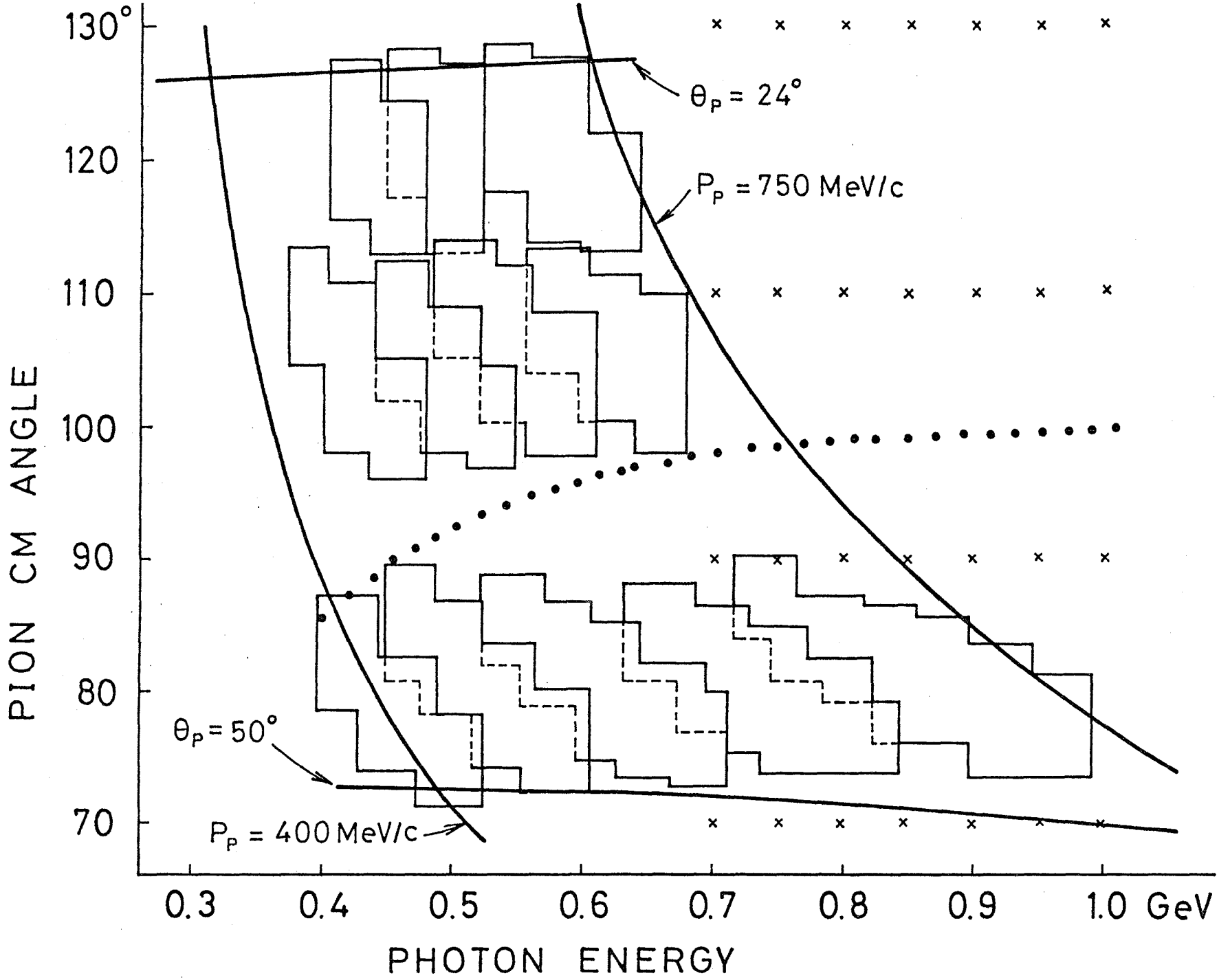
130°
120
110
100
90
80
70
PION CM ANGLE
θP = 24°
PP = 750 MeV/c
θP = 50°
PP = 400 MeV/c
0.3
0.4
0.5
0.6
0.7
0.8
0.9
1.0 GeV
PHOTON ENERGY

FIG. 24(B)

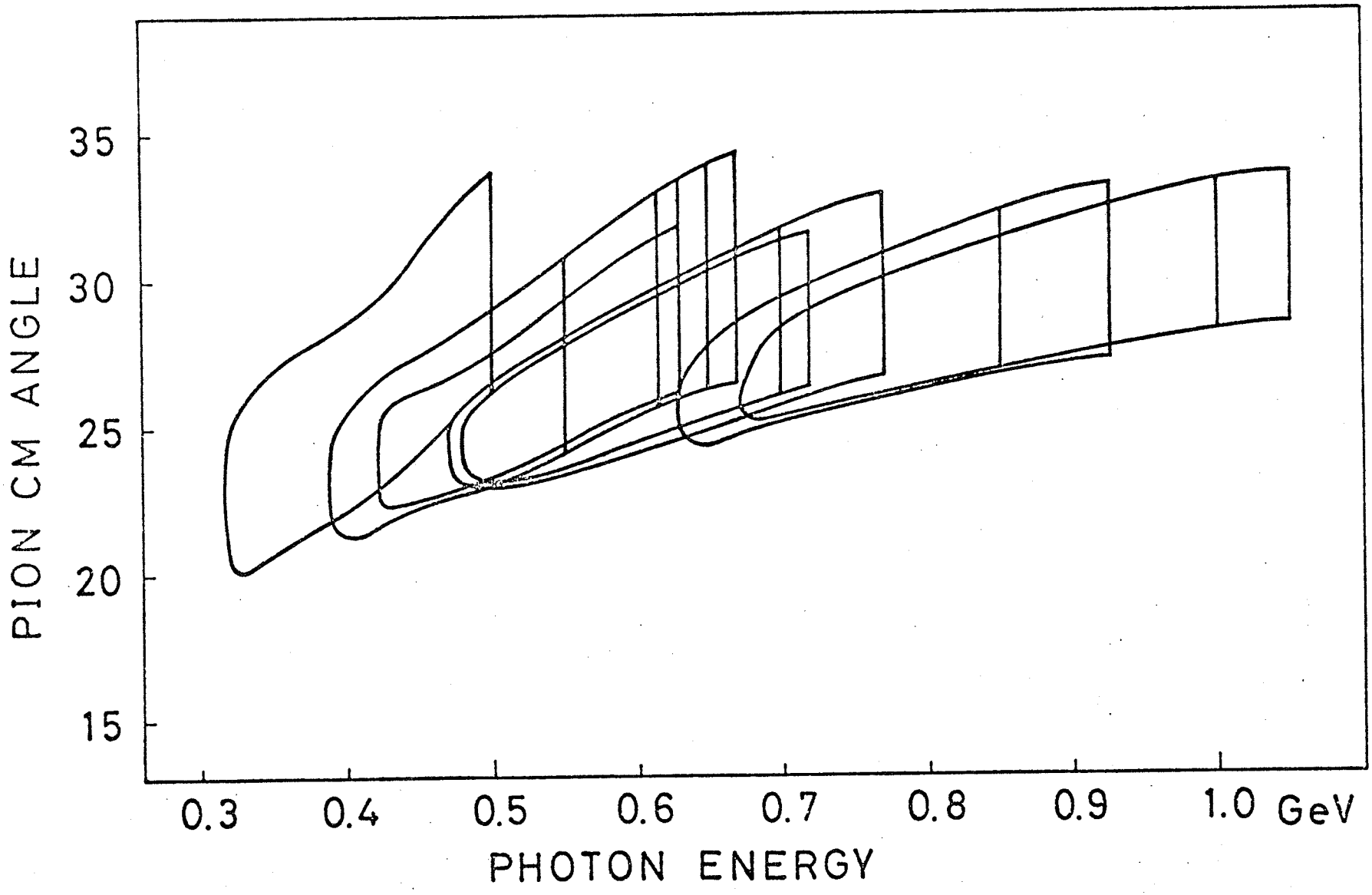
PION CM ANGLE
35
30
25
20
15
0.3
0.4
0.5
0.6
0.7
0.8
0.9
1.0 GeV
PHOTON ENERGY

FIG. 24(c)

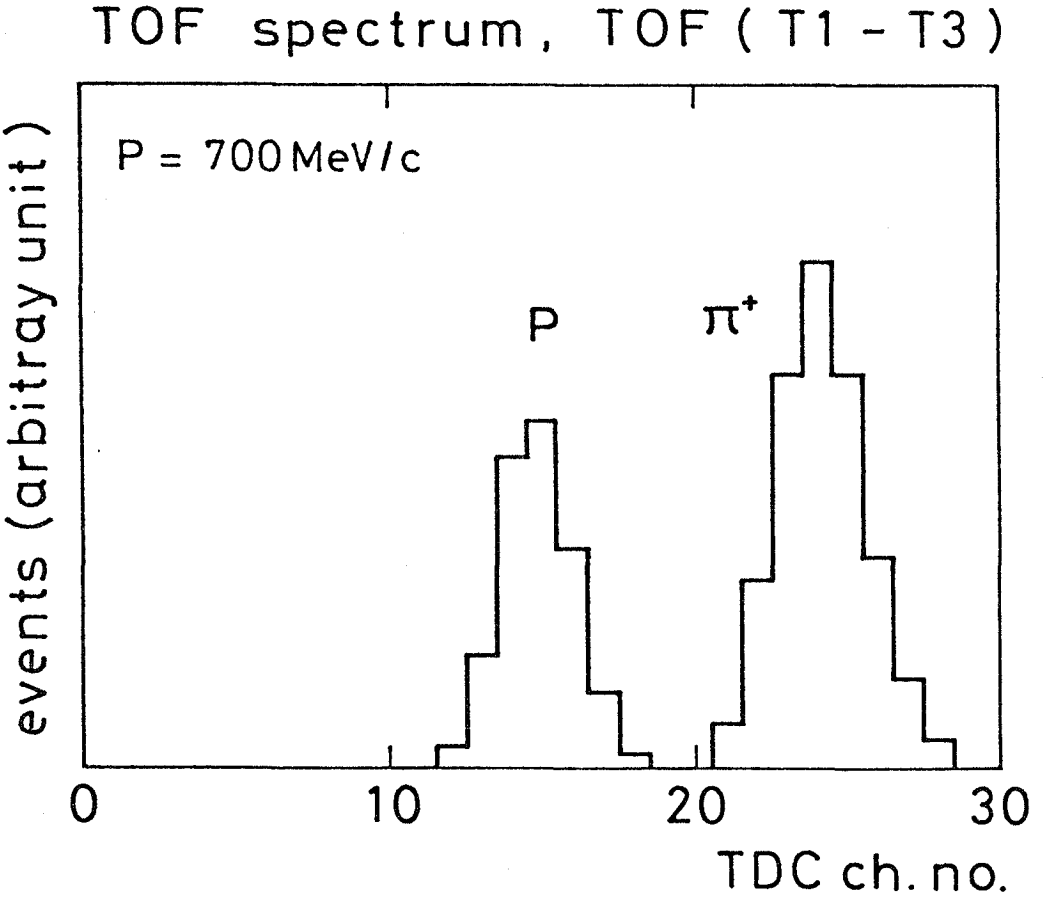
TOF spectrum, TOF (T1 - T3)
P = 700 MeV/c
P
π+
events (arbitray unit)
0
10
20
30
TDC ch. no.

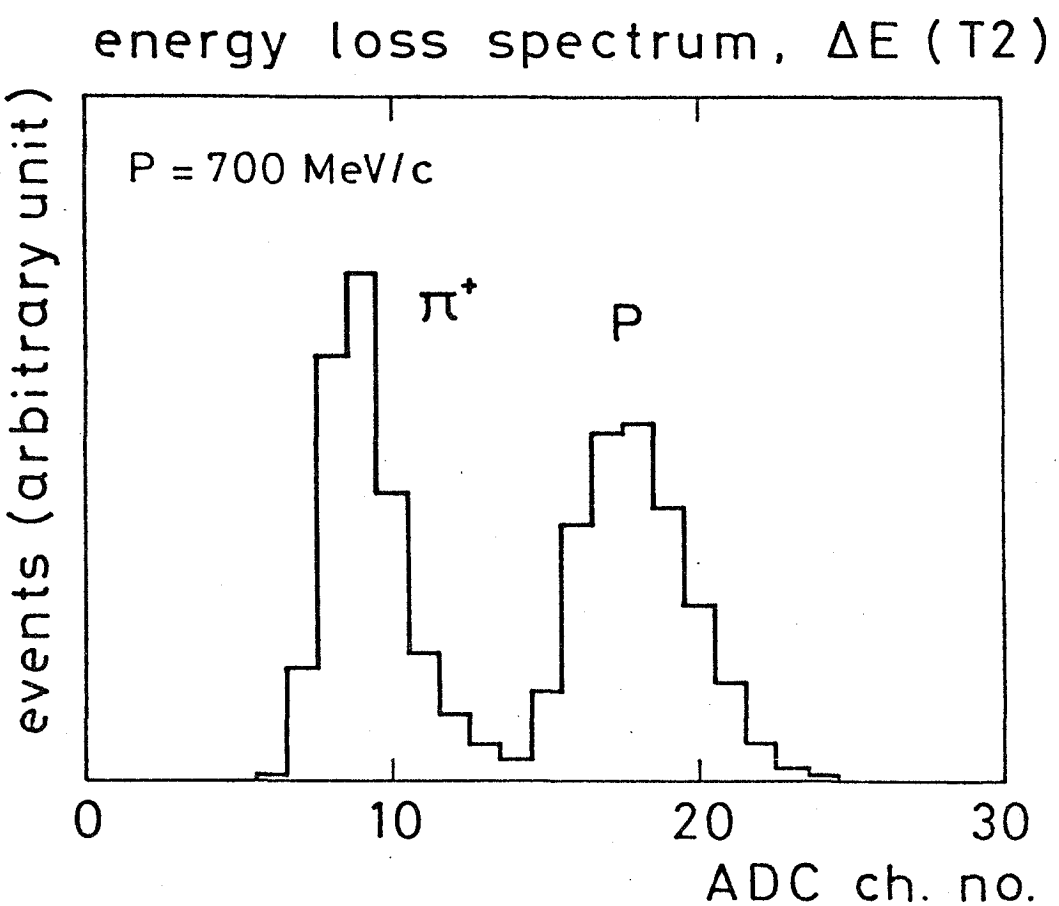
energy loss spectrum, ΔE (T2)
P = 700 MeV/c
π+
P
events (arbitrary unit)
0
10
20
30
ADC ch. no.

FIG. 25

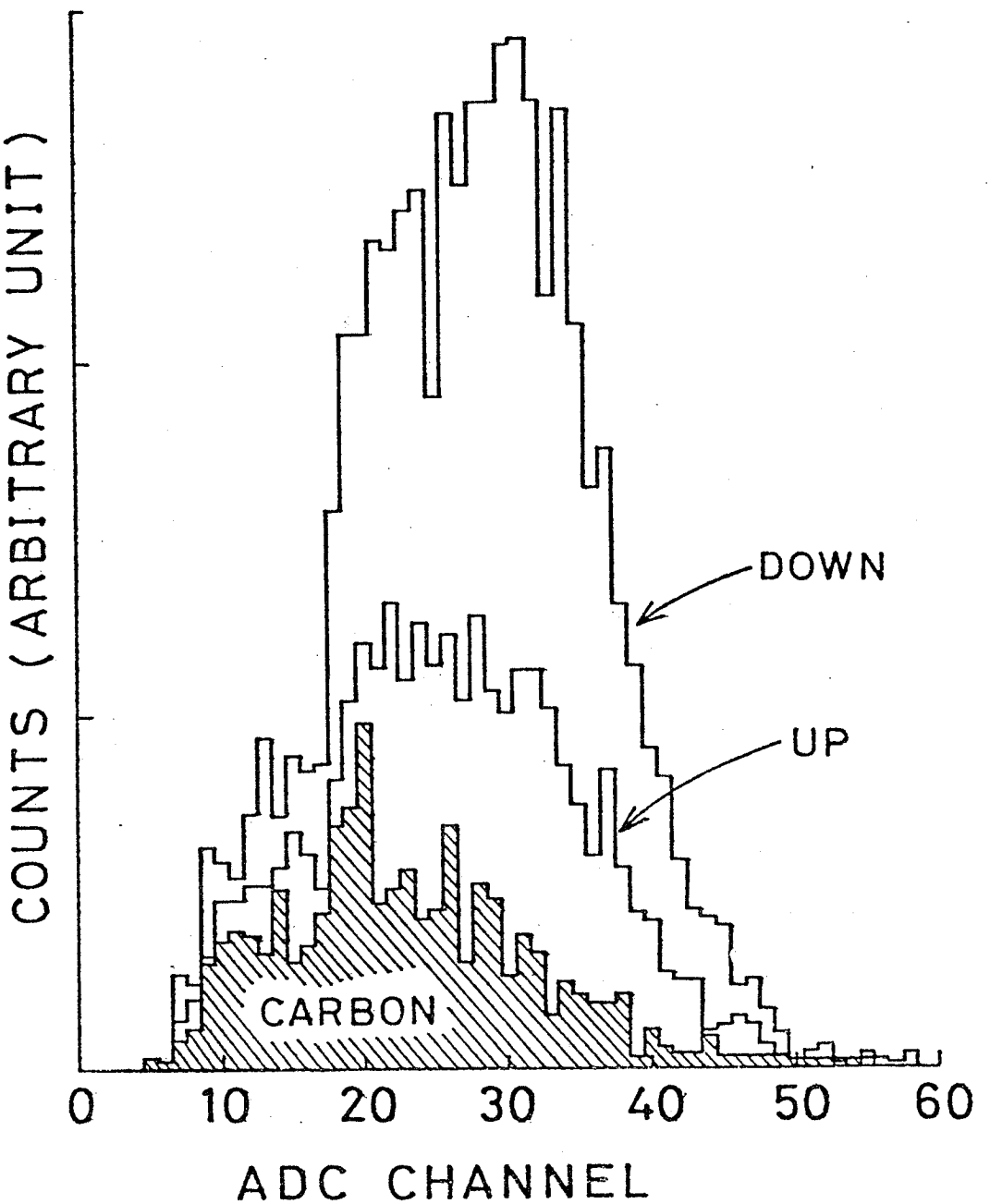
COUNTS (ARBITRARY UNIT)
DOWN
UP
CARBON
0
10
20
30
40
50
60
ADC CHANNEL

FIG. 26

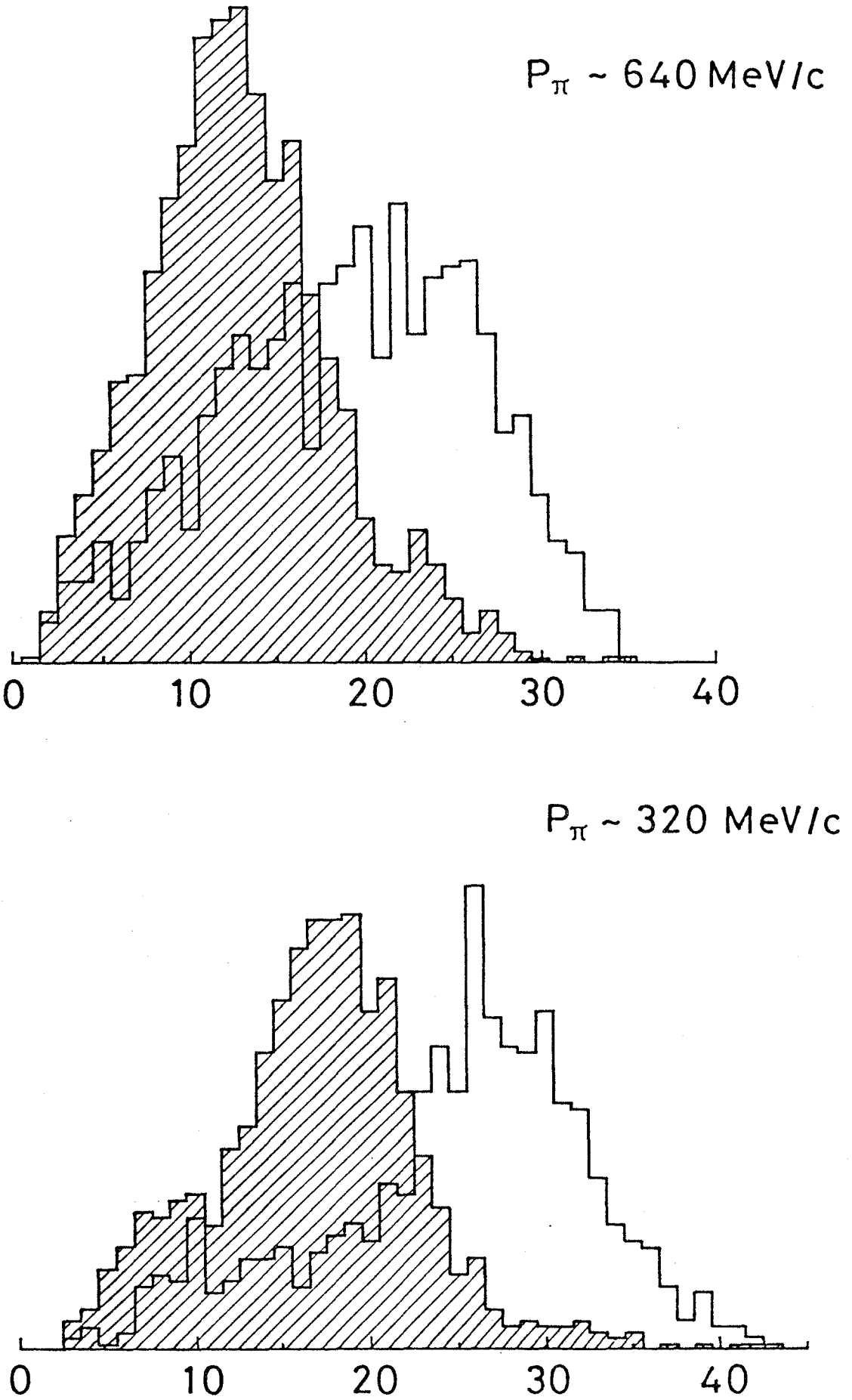

FIG 27

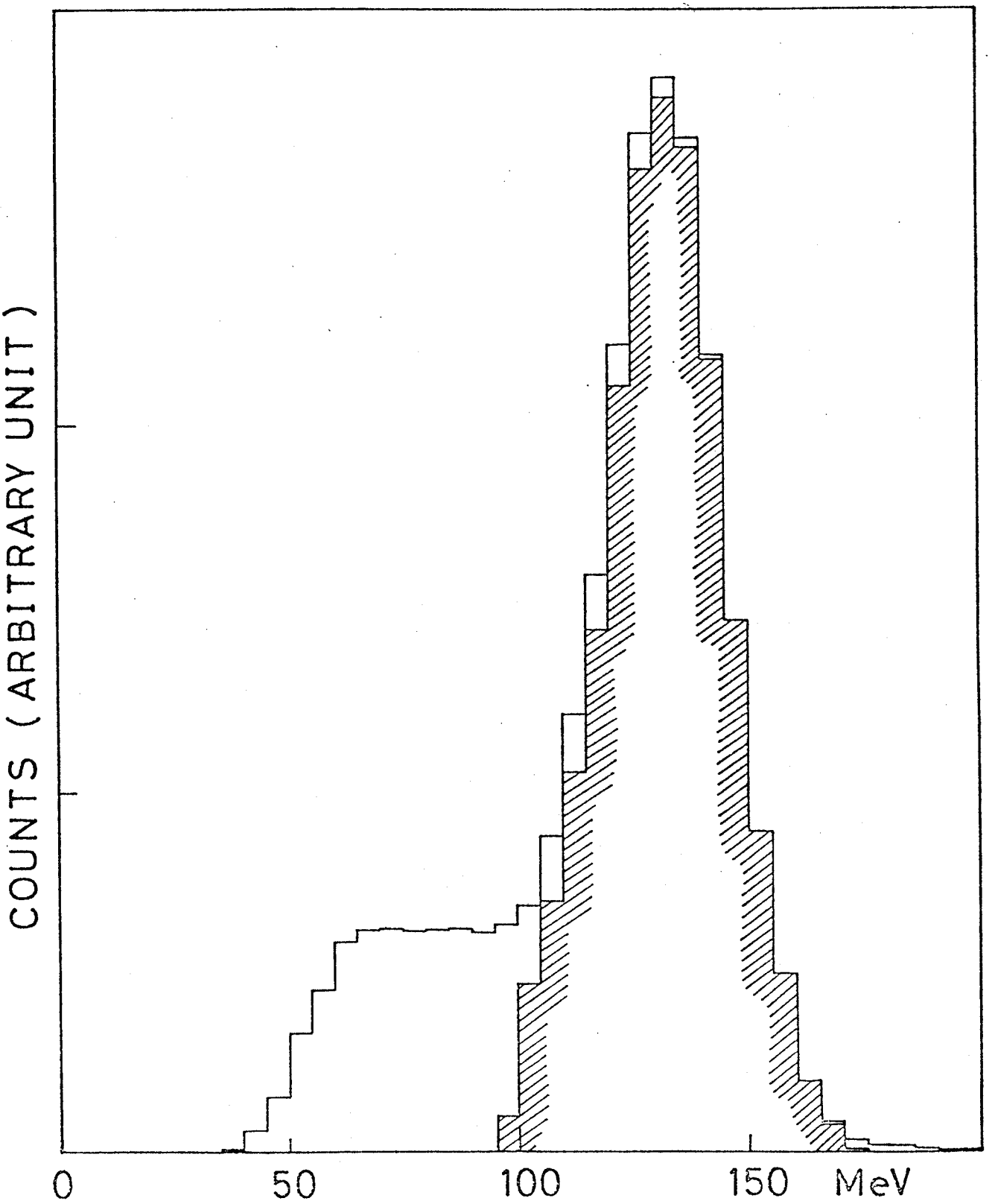

FIG. 28

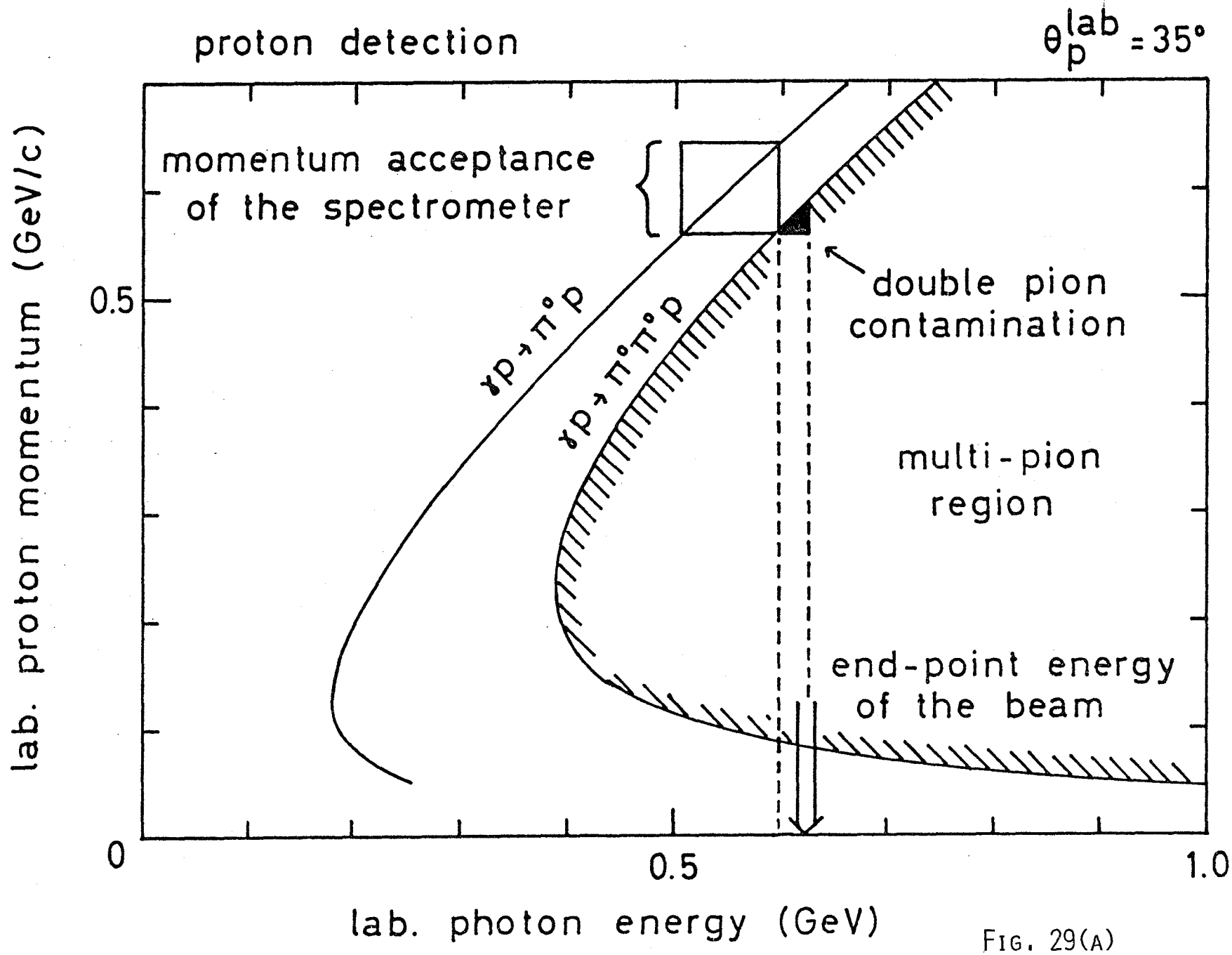
proton detection
$\theta_p^{lab} = 35°$
momentum acceptance
of the spectrometer
$\gamma p \to \pi^0 p$
$\gamma p \to \pi^0\pi^0 p$
double pion
contamination
multi-pion
region
end-point energy
of the beam
lab. proton momentum (GeV/c)
0.5
0
0.5
1.0
lab. photon energy (GeV)

FIG. 29(A)

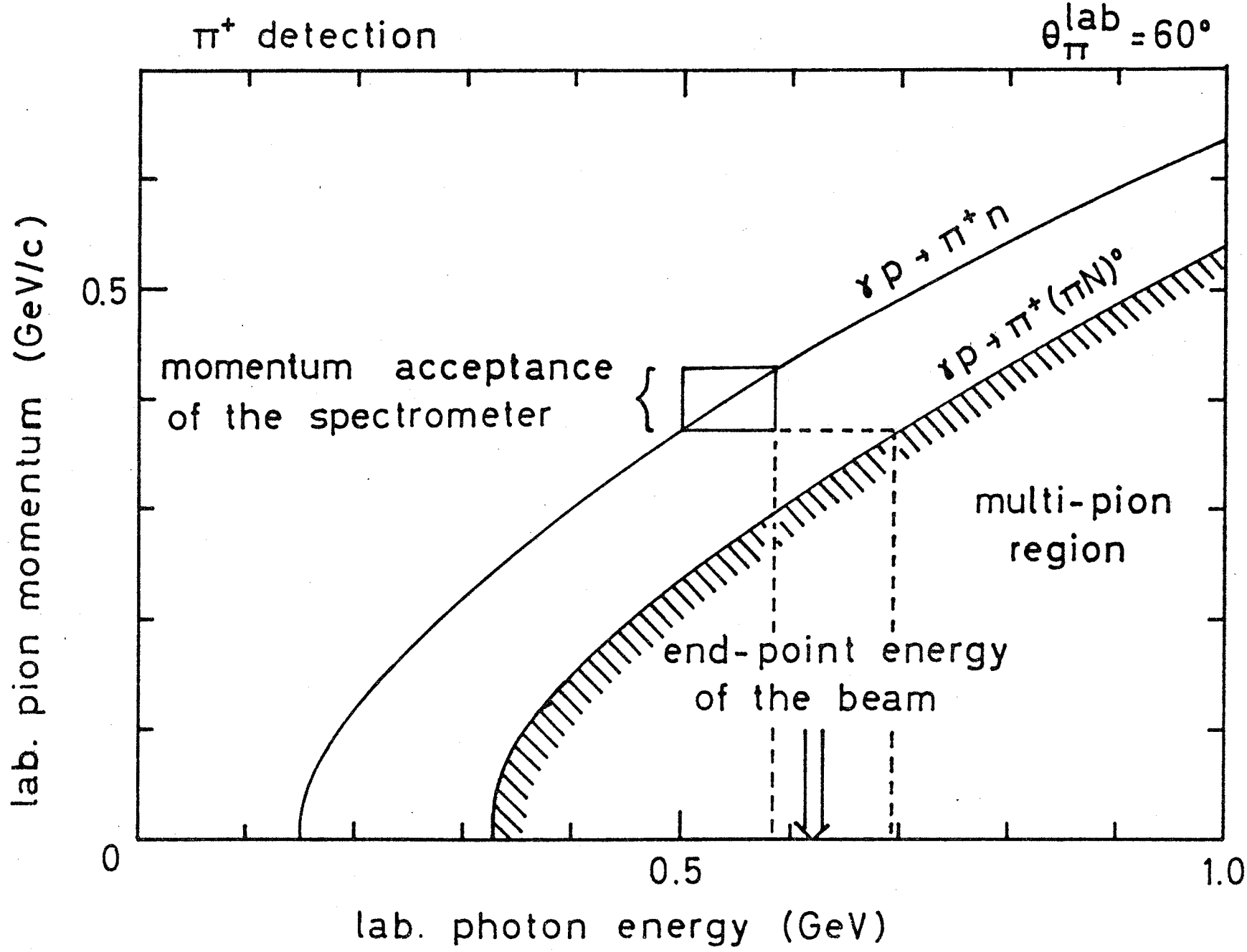
π+ detection
θπlab = 60°
lab. pion momentum (GeV/c)
0.5
0
momentum acceptance
of the spectrometer
γp → π+n
γp → π+(πN)°
multi-pion
region
end-point energy
of the beam
0.5
1.0
lab. photon energy (GeV)

FIG. 29(B)

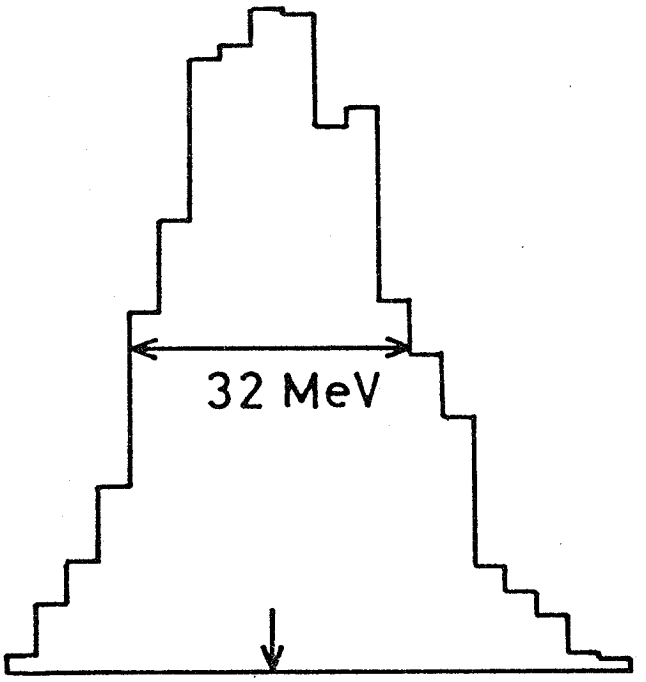

k_γ = 526 MeV

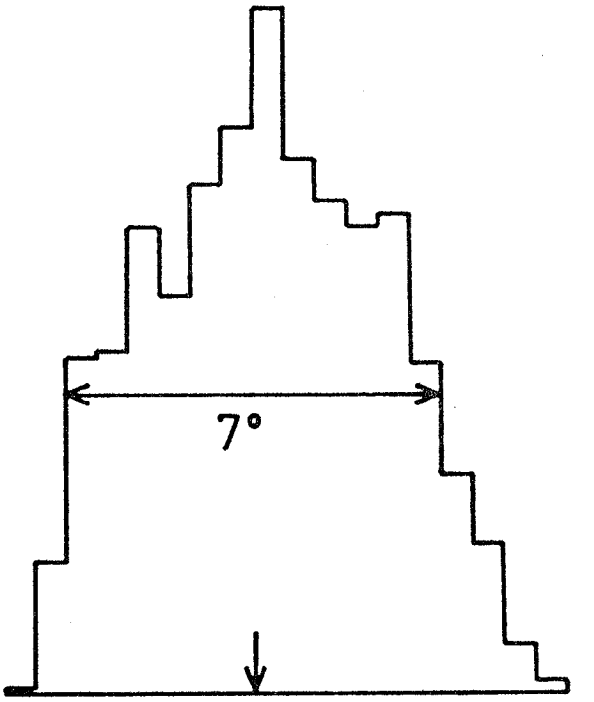

θ_π^* = 120°

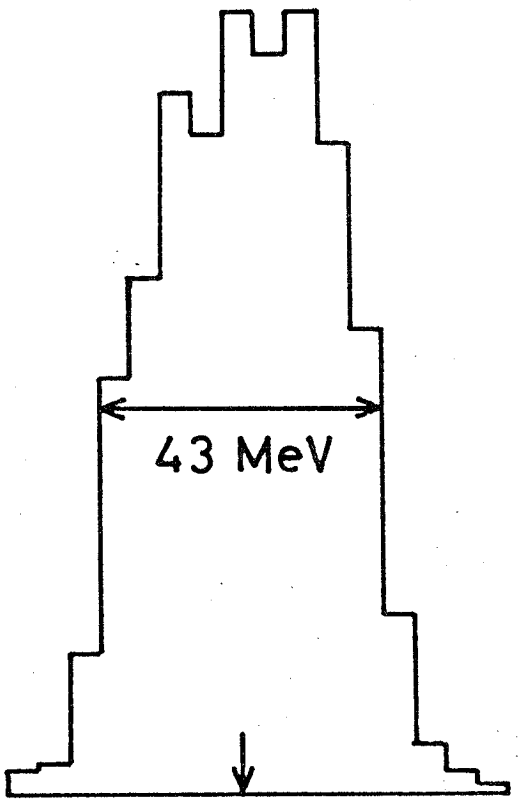

k_γ = 630 MeV

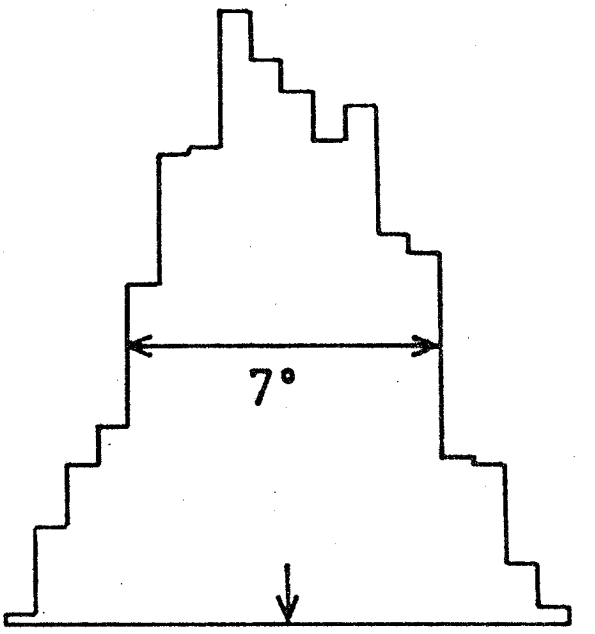

θ_π^* = 50°

FIG. 30(A)

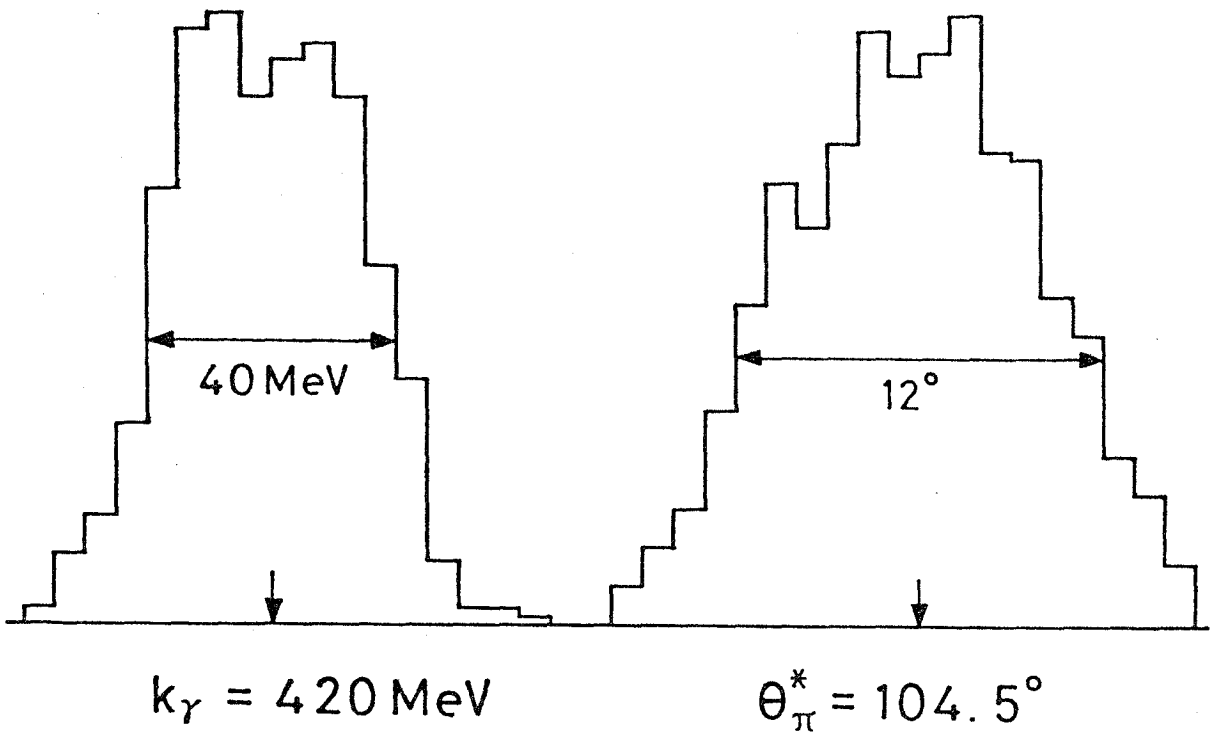
40 MeV
12°
k_γ = 420 MeV
θ^*_π = 104.5°

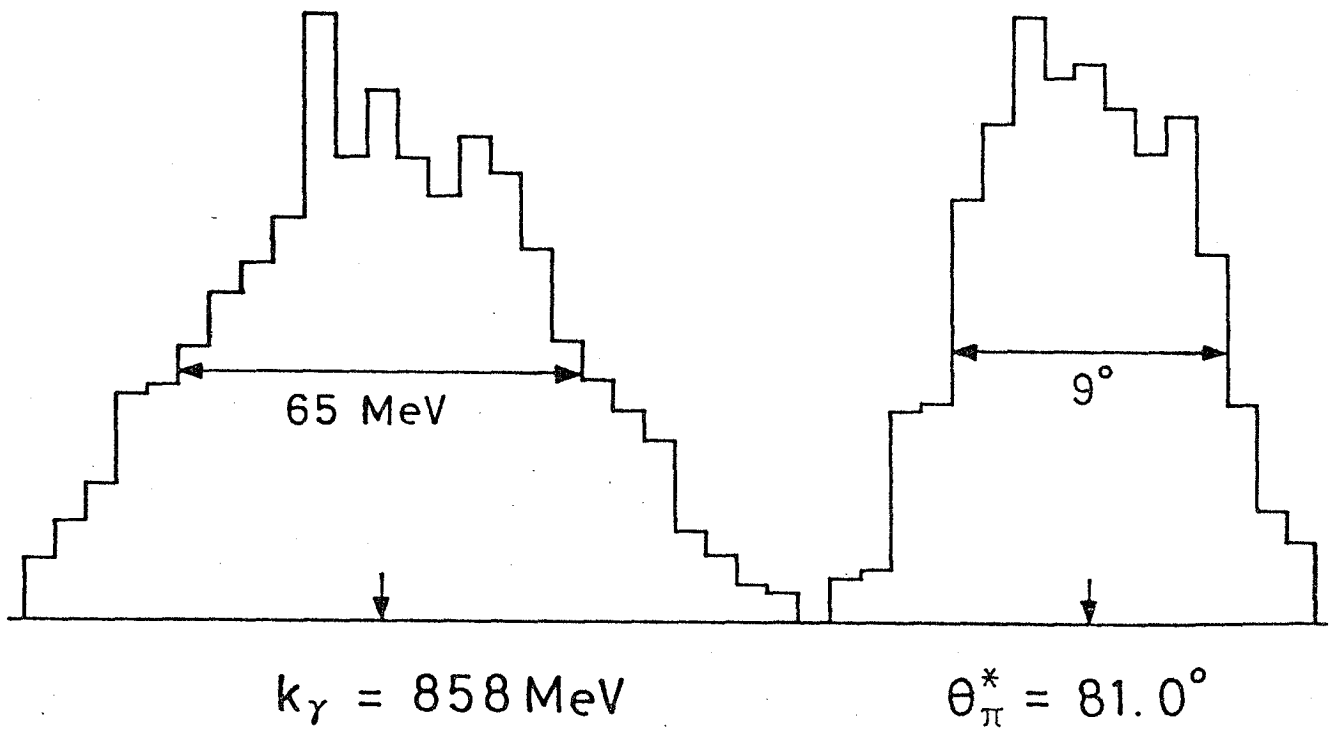
65 MeV
9°
k_γ = 858 MeV
θ^*_π = 81.0°

FIG. 30(B)

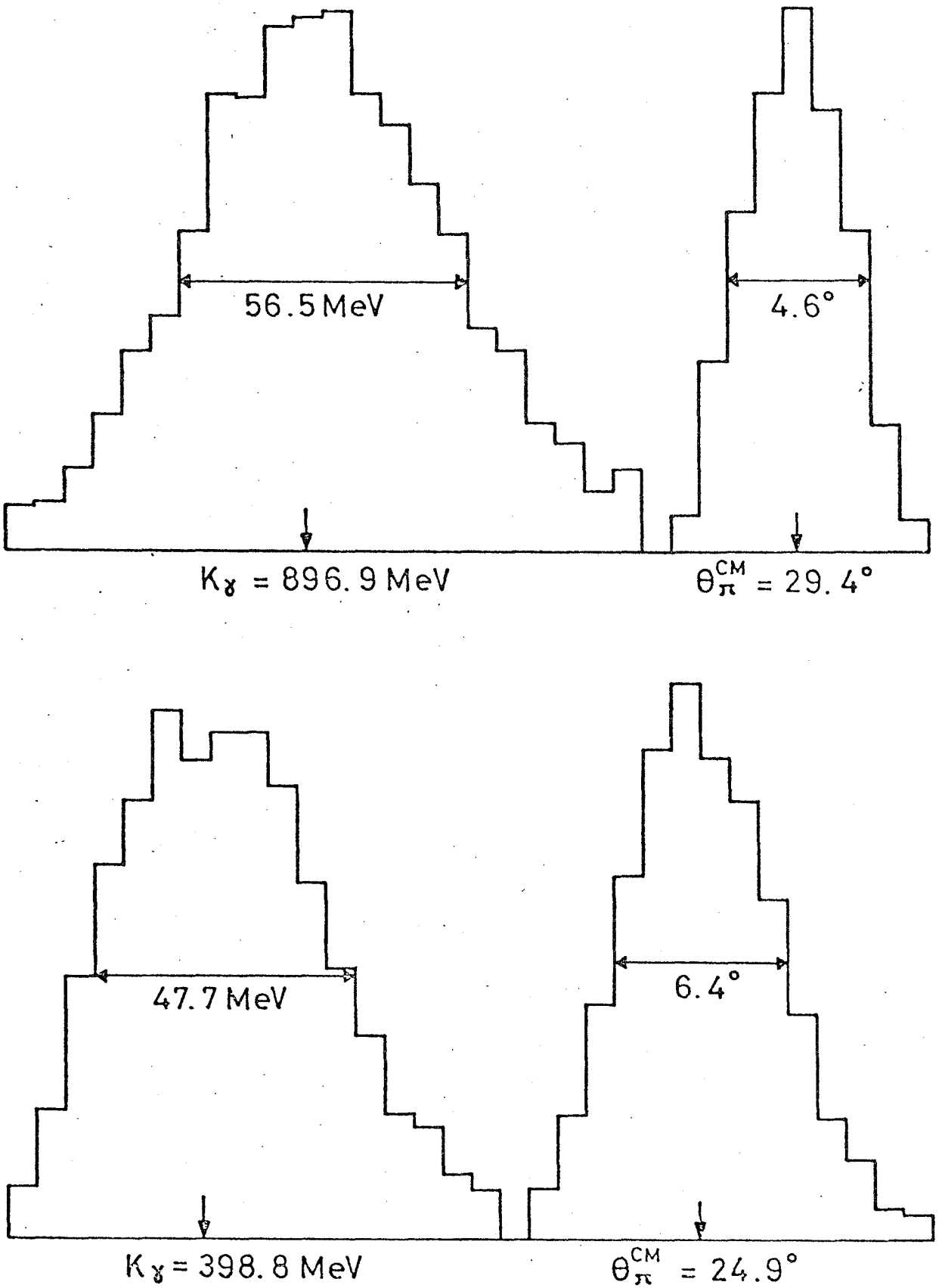
56.5 MeV
4.6°
K_γ = 896.9 MeV
θ_π^{CM} = 29.4°
47.7 MeV
6.4°
K_γ = 398.8 MeV
θ_π^{CM} = 24.9°

FIG. 30(c)

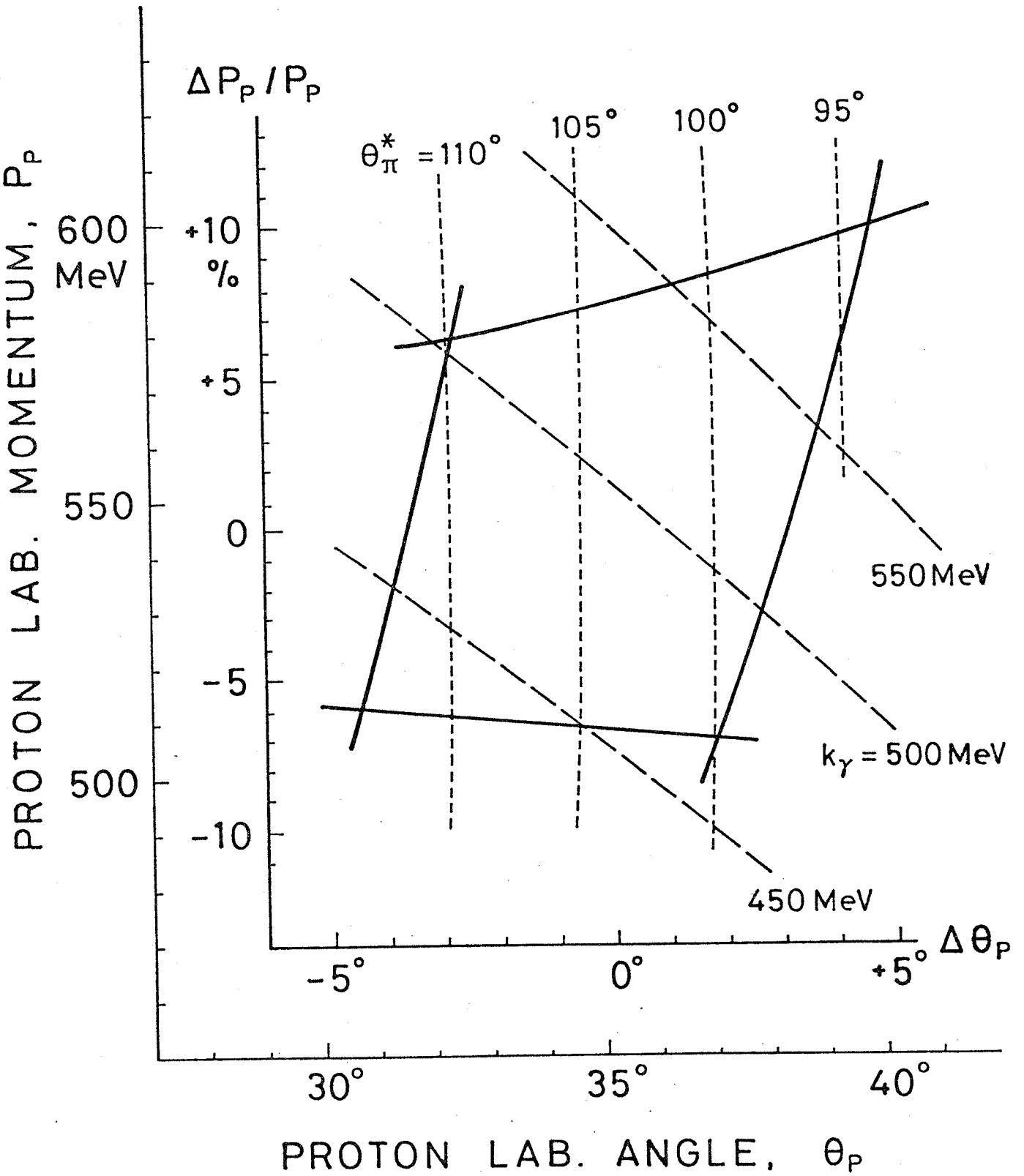
ΔP_P / P_P
θ*_π = 110°
105°
100°
95°
+10 %
+5
0
-5
-10
600 MeV
550
500
550 MeV
k_γ = 500 MeV
450 MeV
-5°
0°
+5°
Δθ_P
30°
35°
40°
PROTON LAB. MOMENTUM, P_P
PROTON LAB. ANGLE, θ_P

FIG. 31

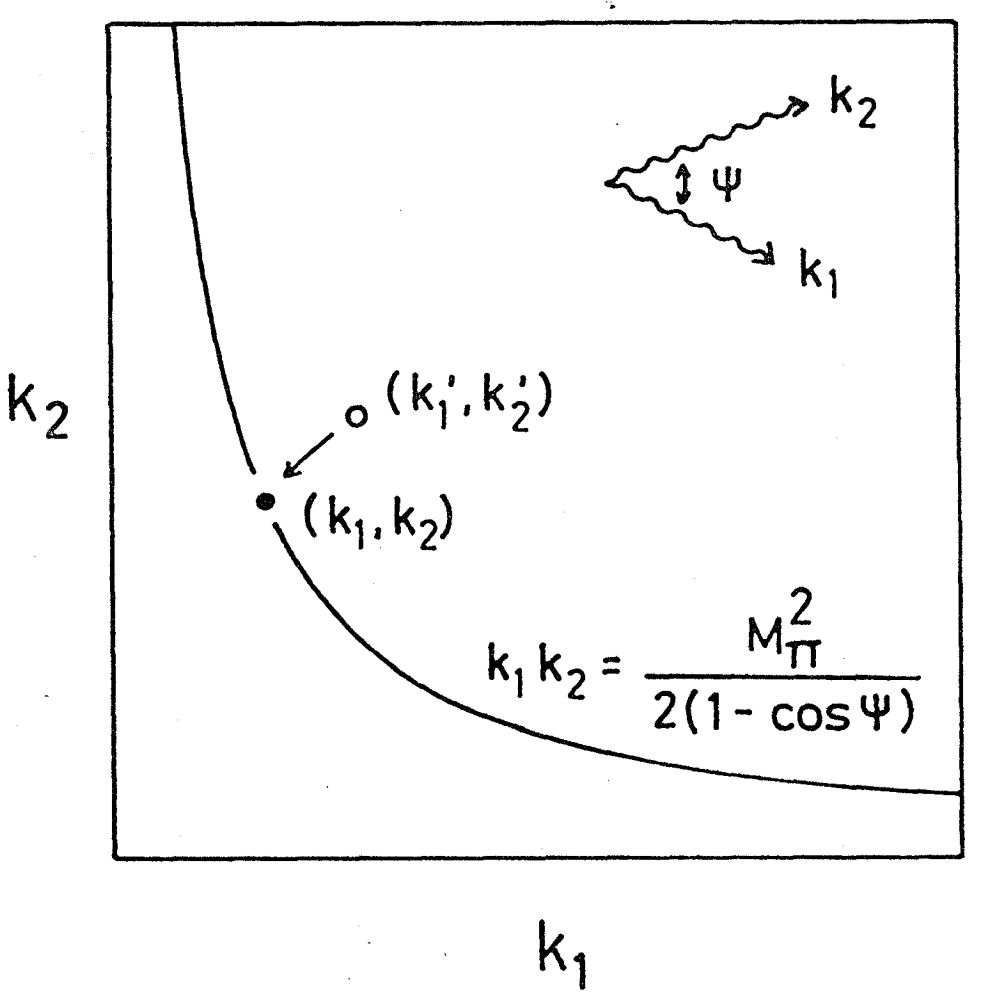

FIG. 32

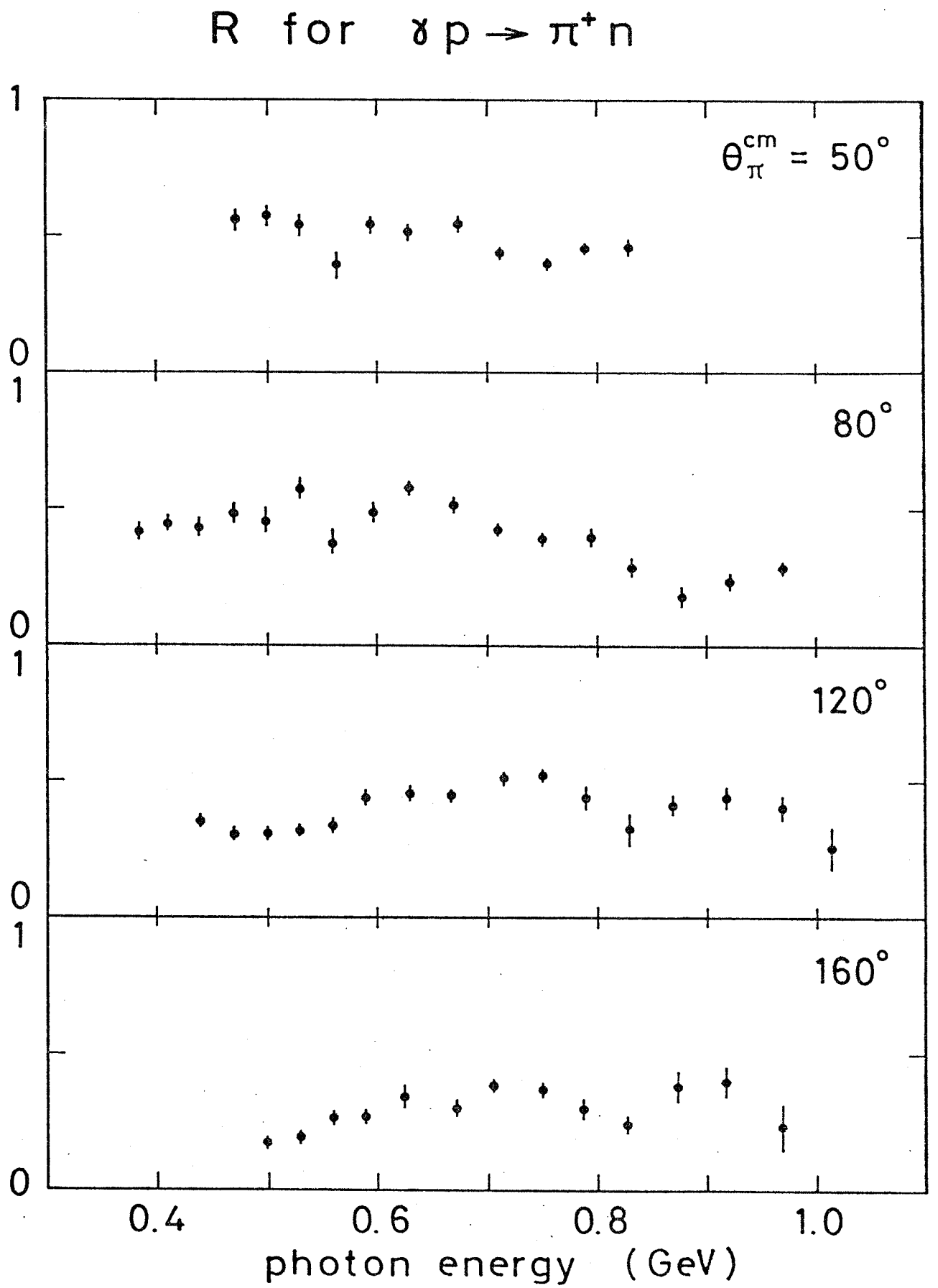
R for γp → π⁺n
1
0
θ_π^{cm} = 50°
1
0
80°
1
0
120°
1
0
160°
0.4
0.6
0.8
1.0
photon energy (GeV)

FIG. 33(A)

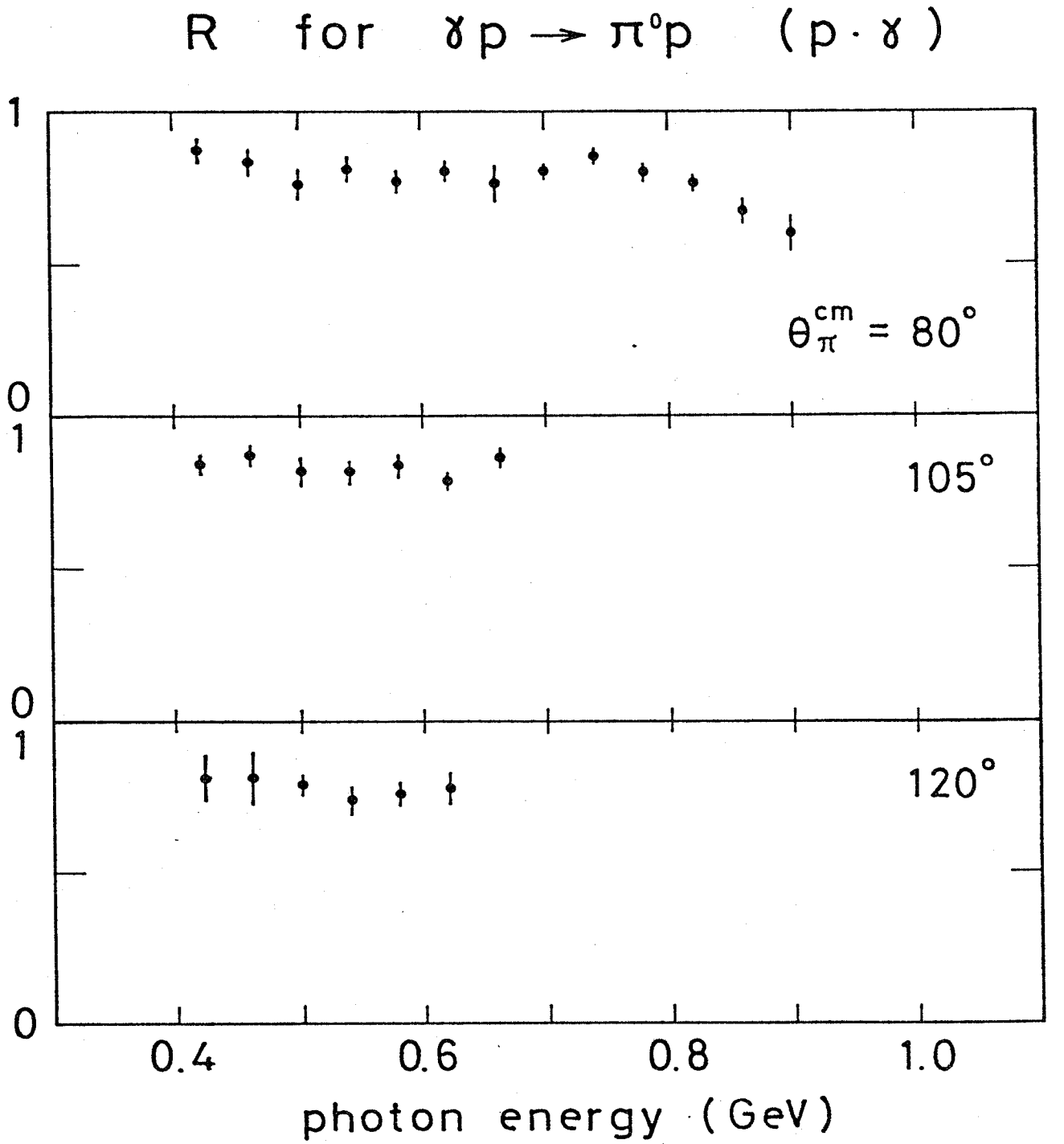
R for γp → π°p (p·γ)
1
0
1
0
1
0
θ_π^{cm} = 80°
105°
120°
0.4
0.6
0.8
1.0
photon energy (GeV)

FIG. 33(B)

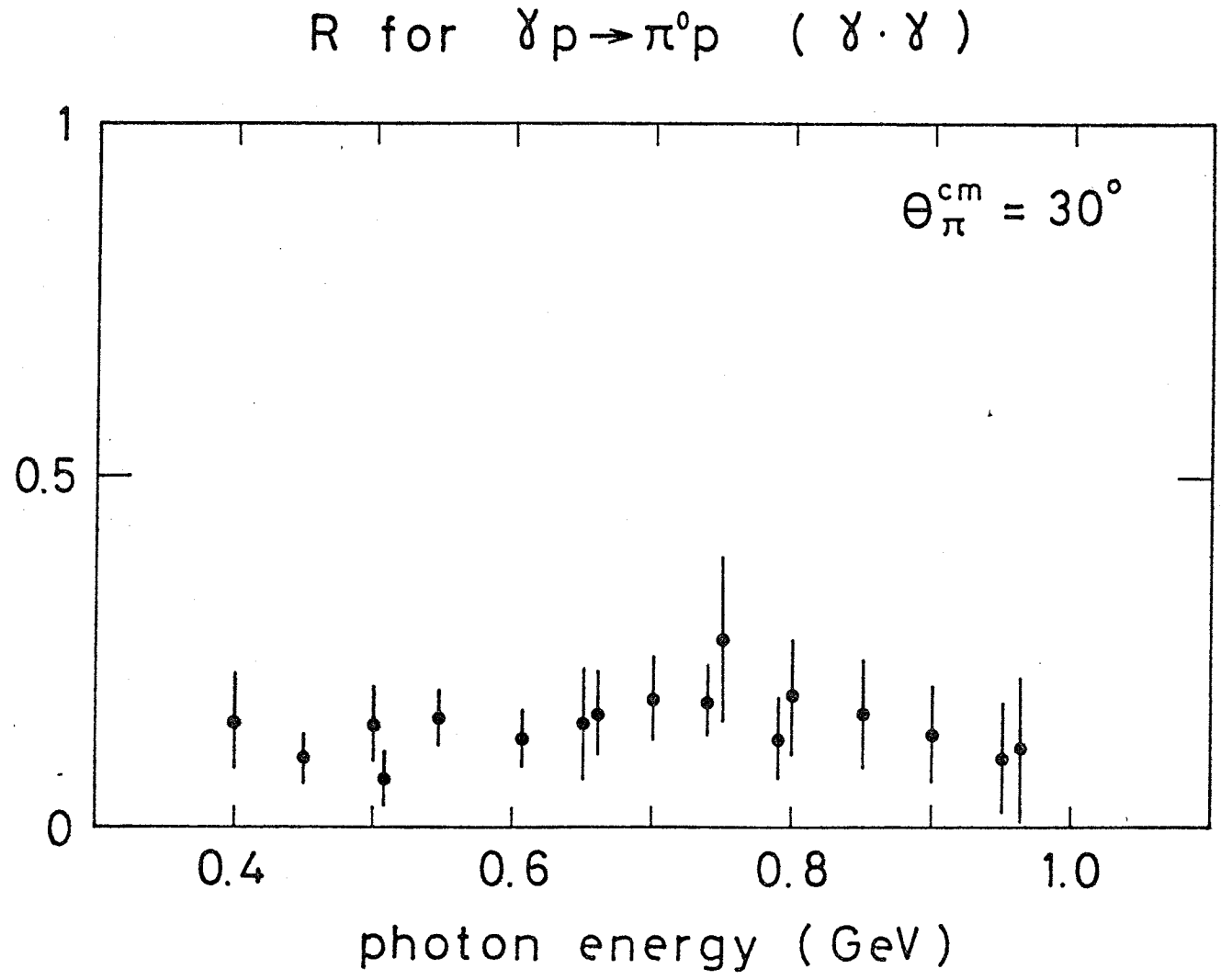

FIG. 33(c)

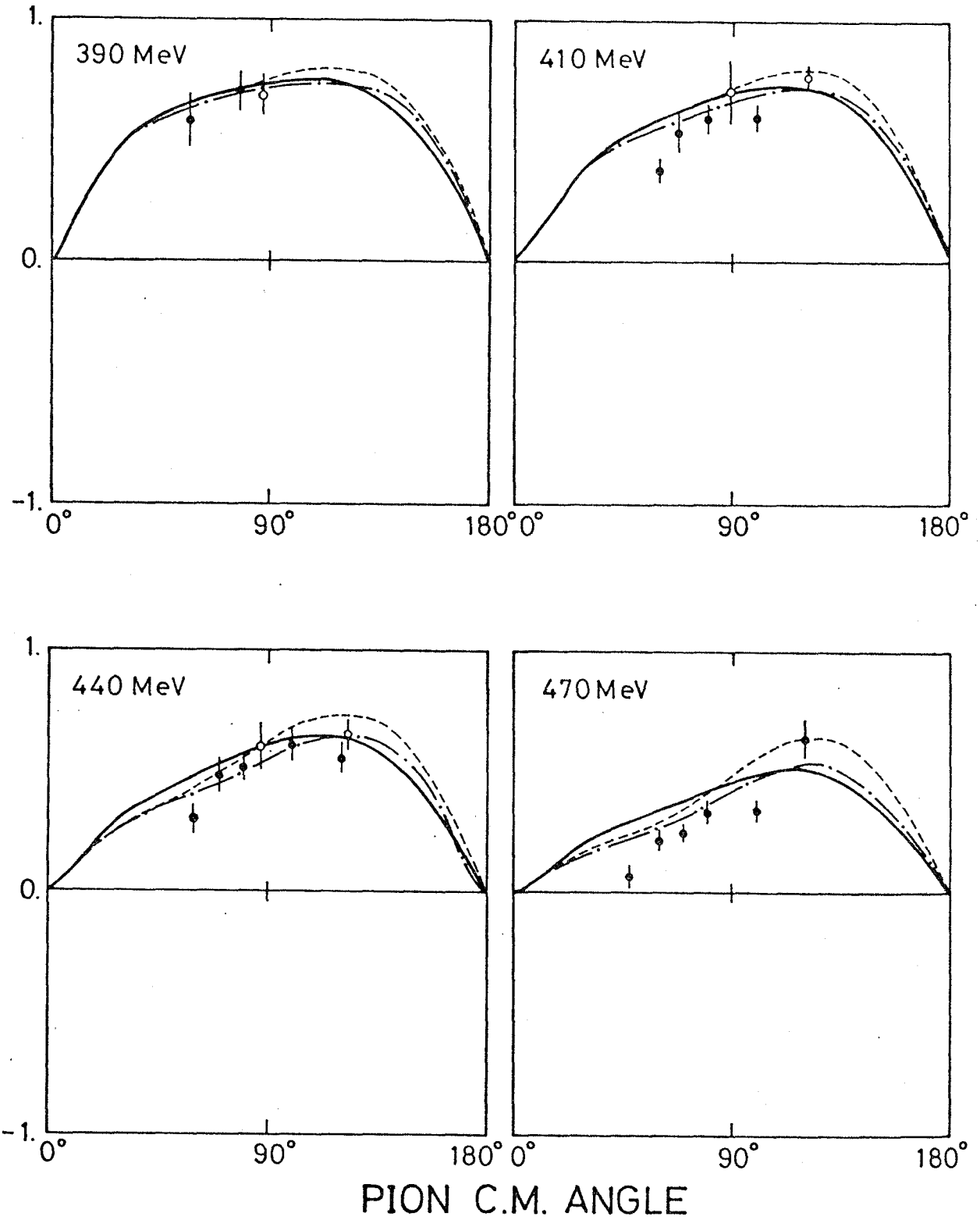

FIG. 34(A) - (D)

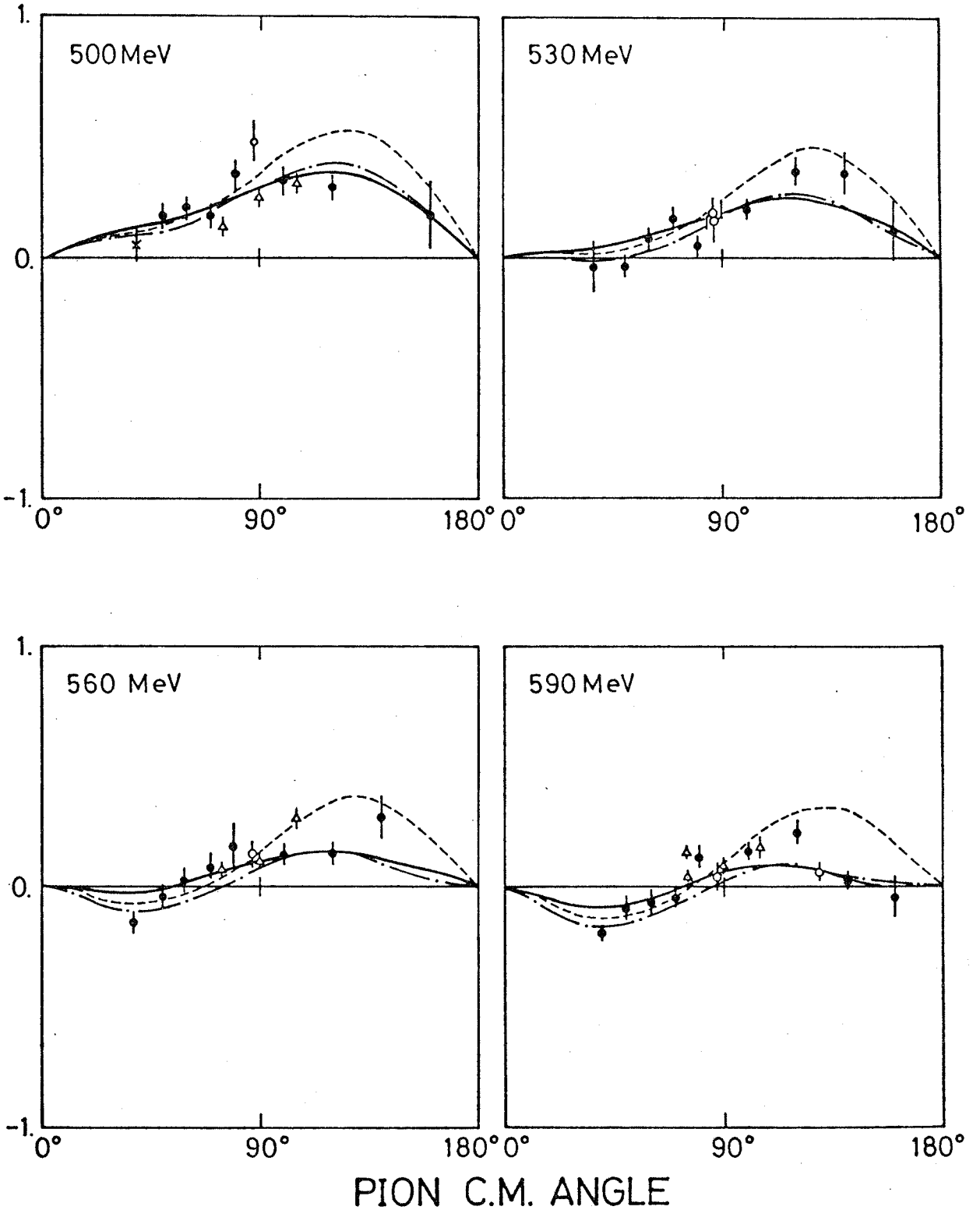

FIG. 34(E) -(H)

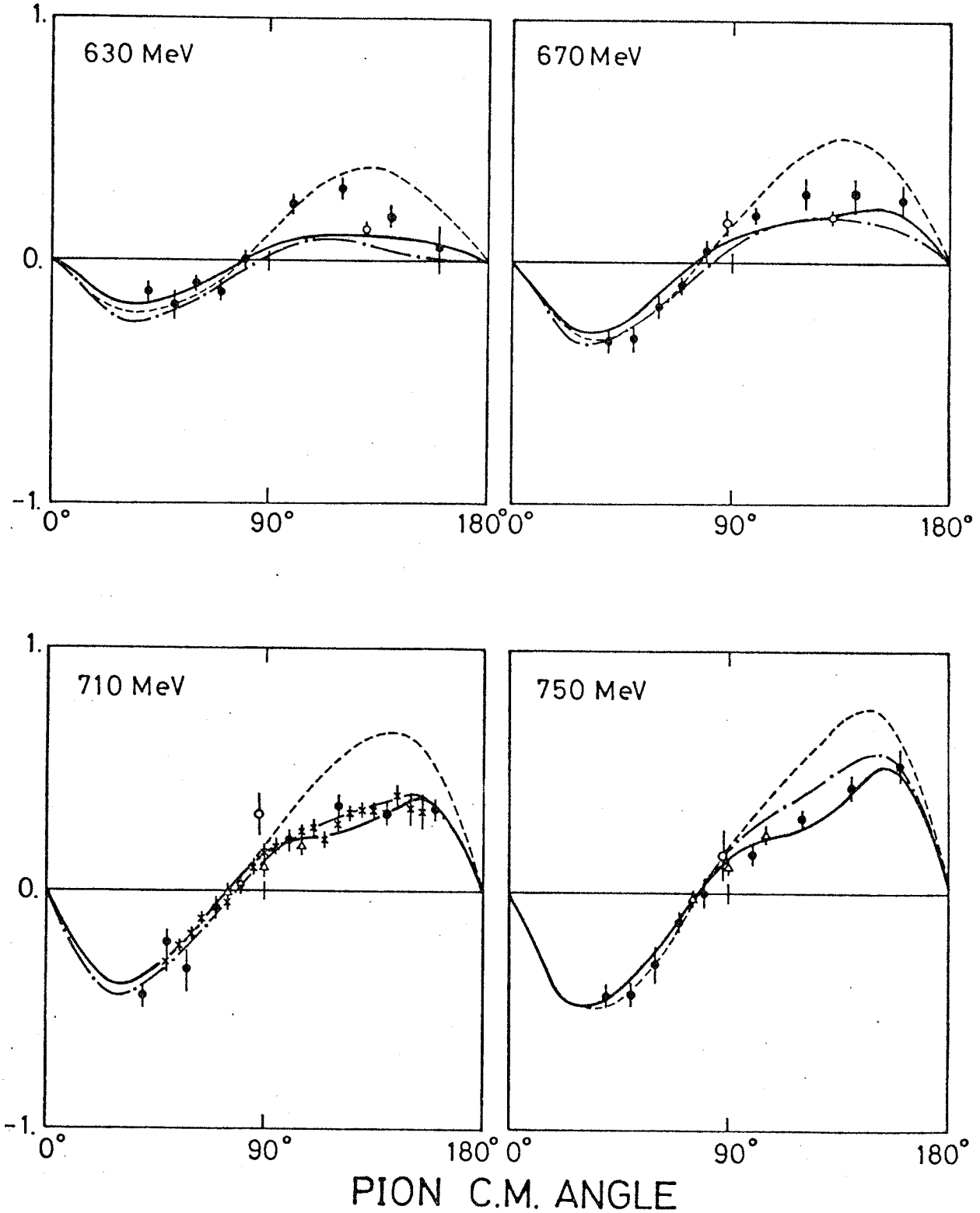

FIG. 34(I) - (L)

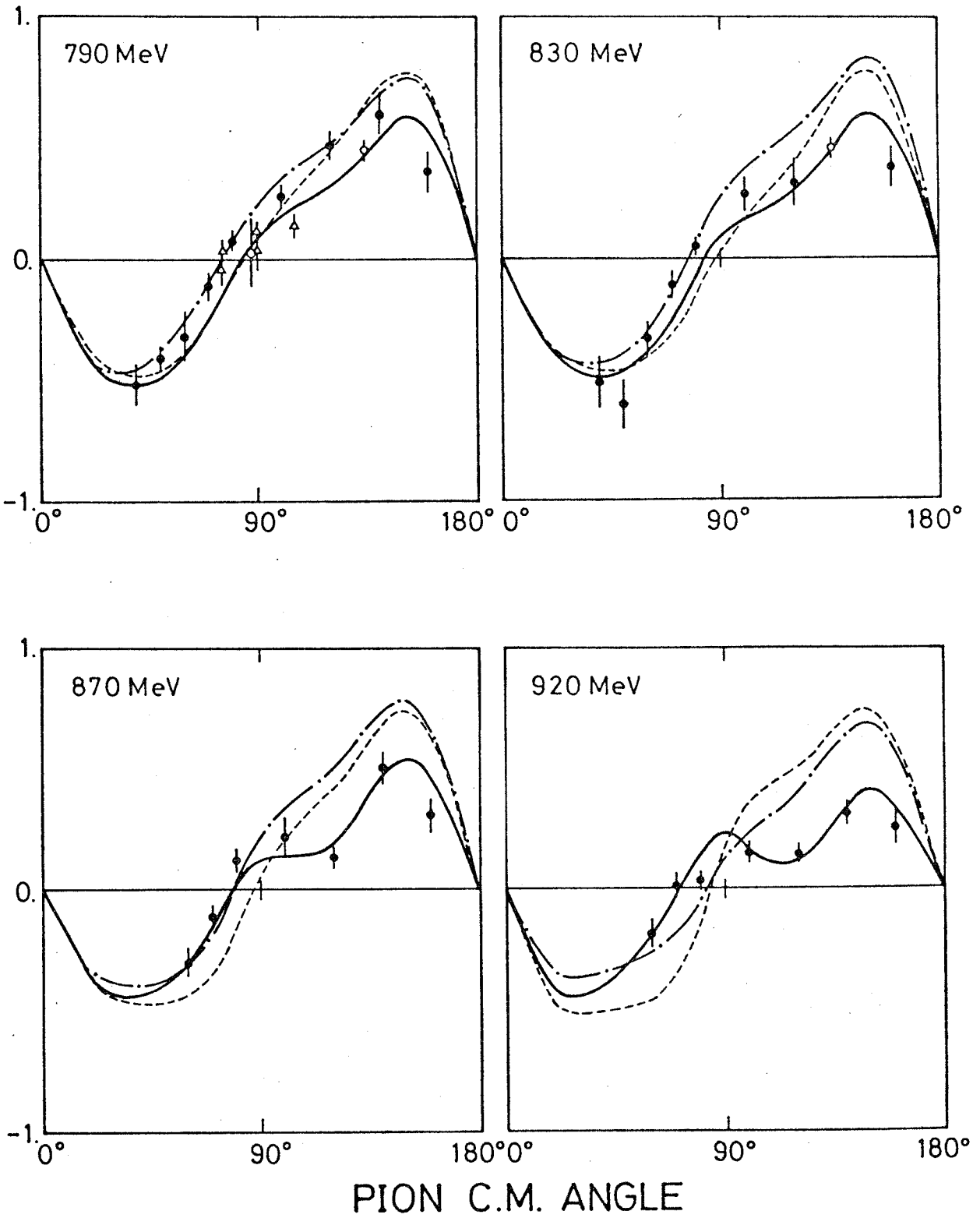

FIG. 34(M) - (P)

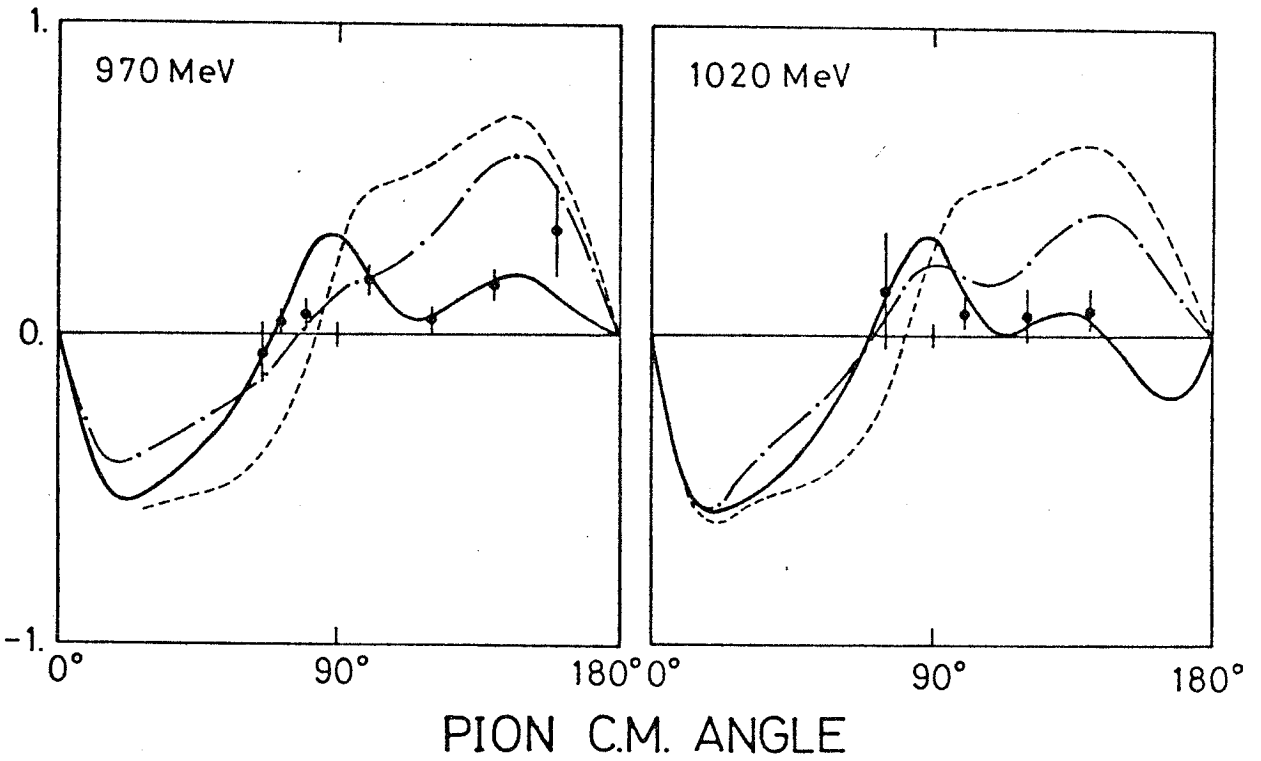

FIG. 34(Q) - (R)

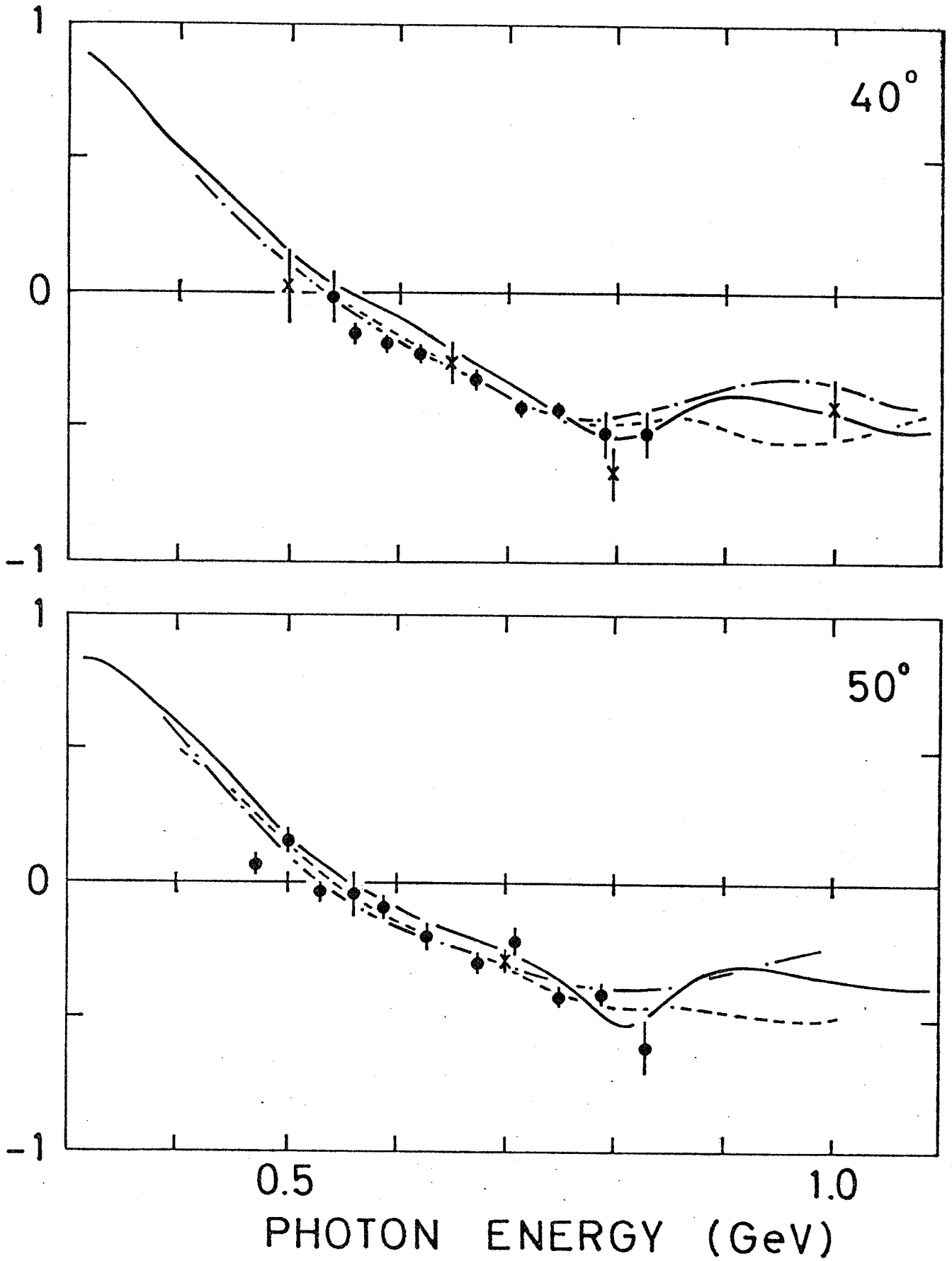

FIG. 35(A), (B)

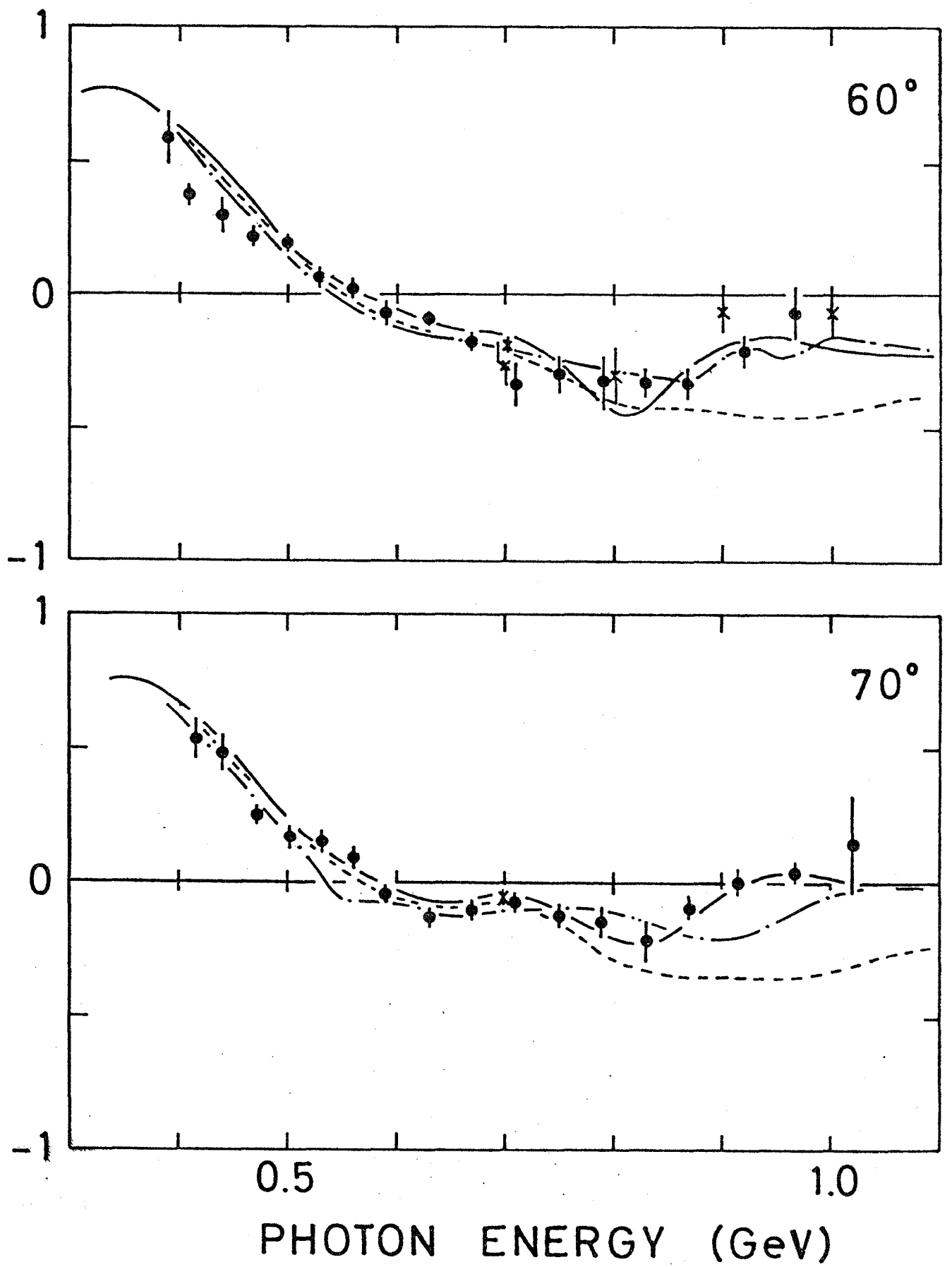

FIG. 35(C), (D)

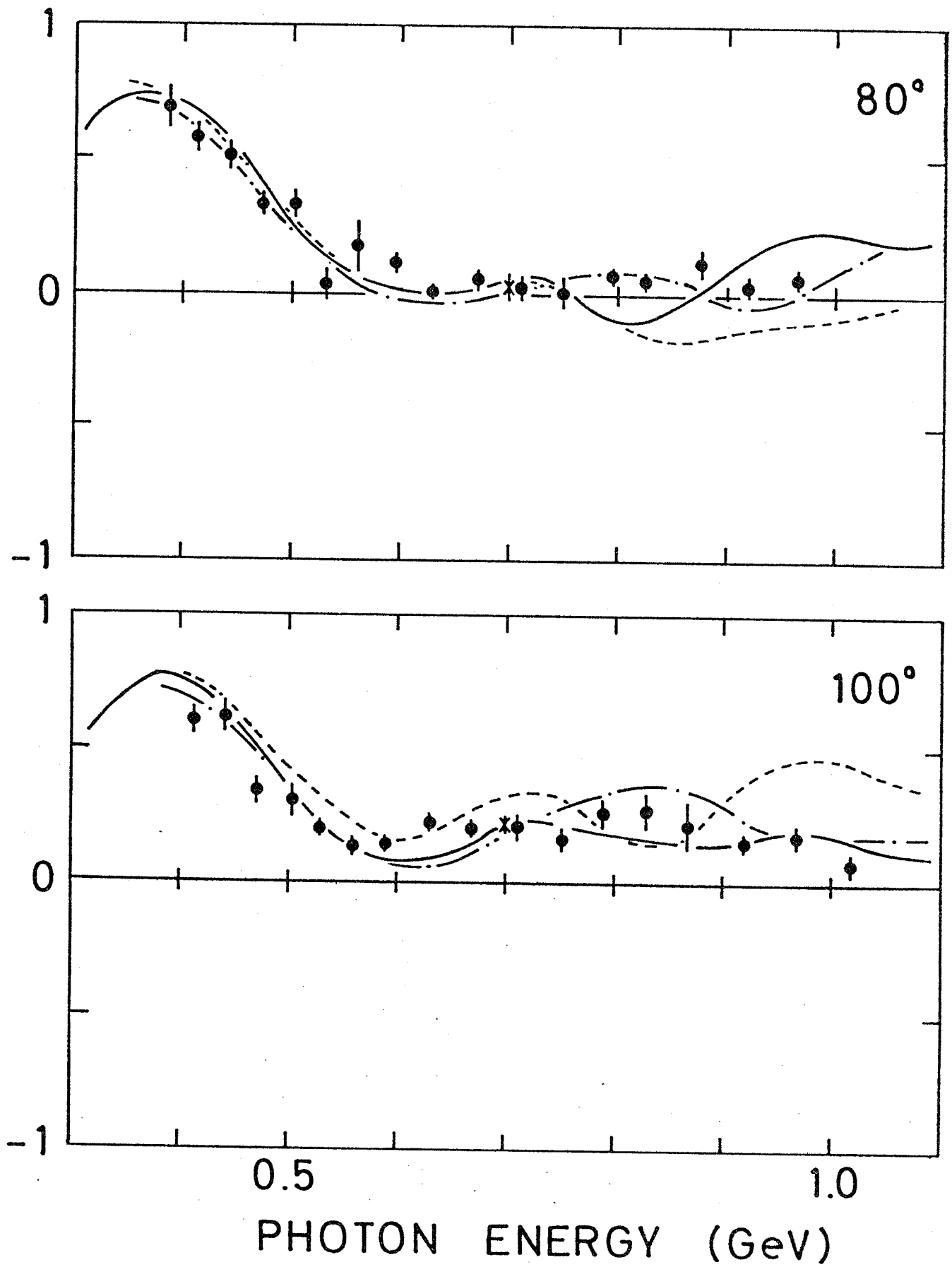

FIG. 35(E), (F)

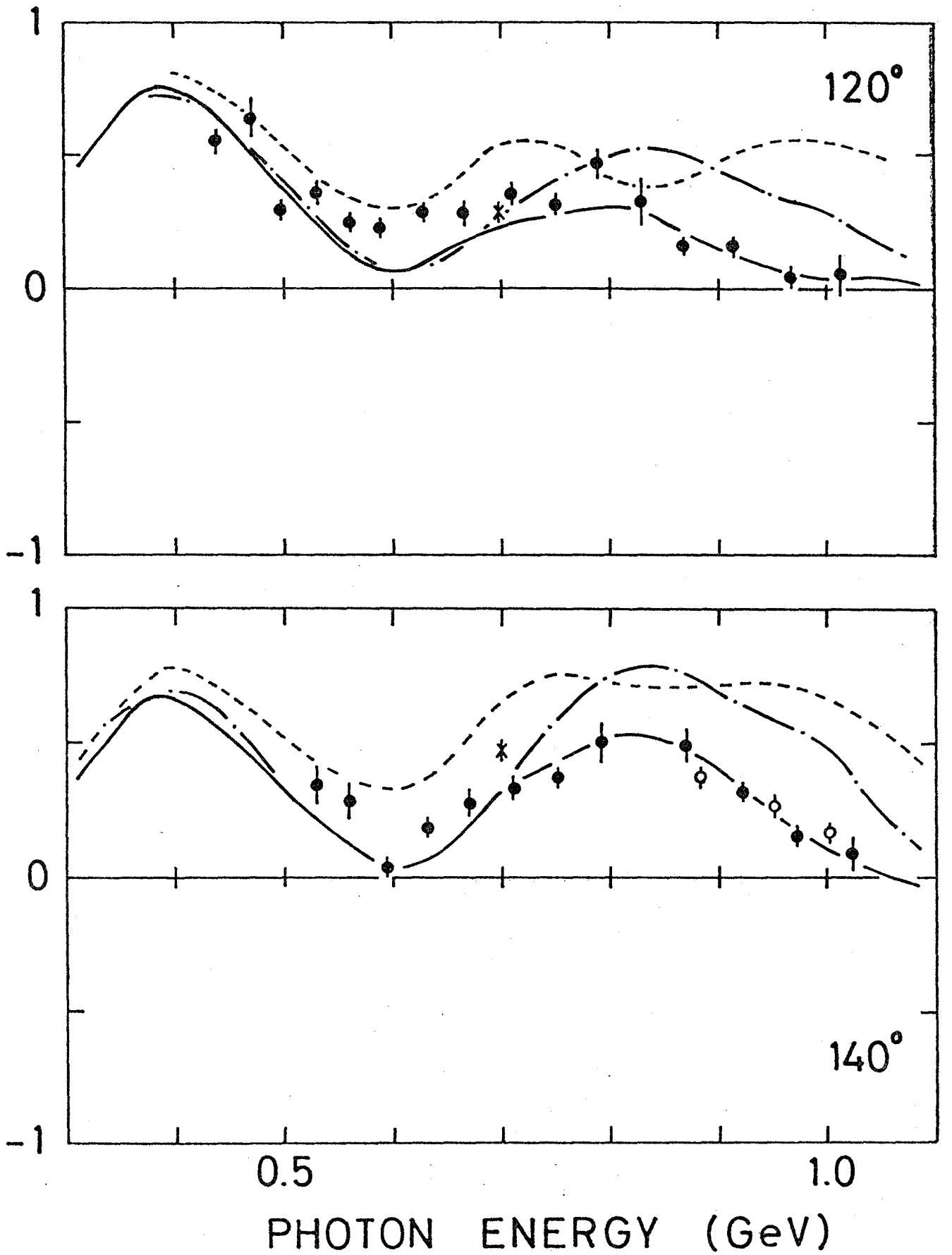

FIG. 35(G), (H)

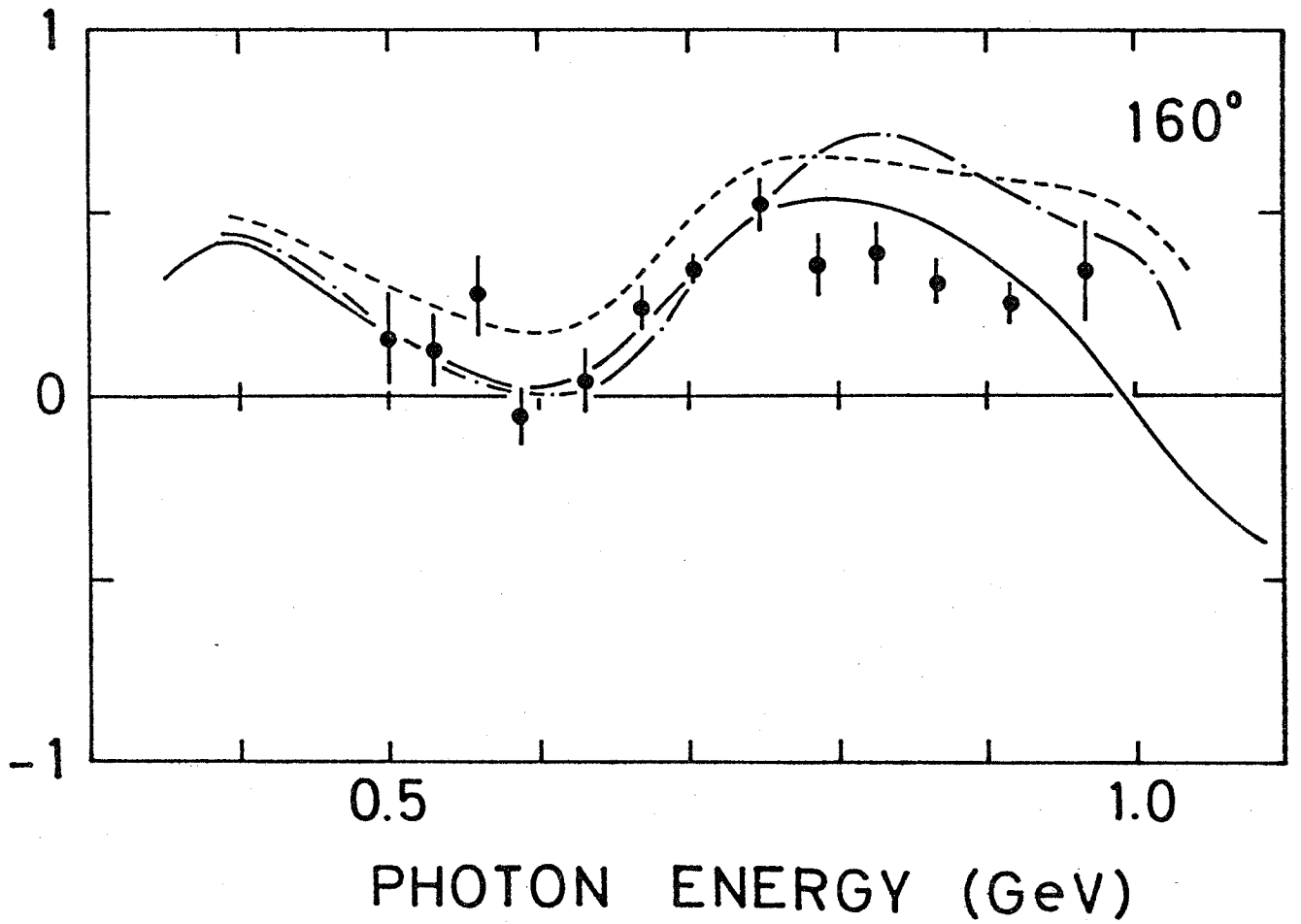

FIG. 35(I)

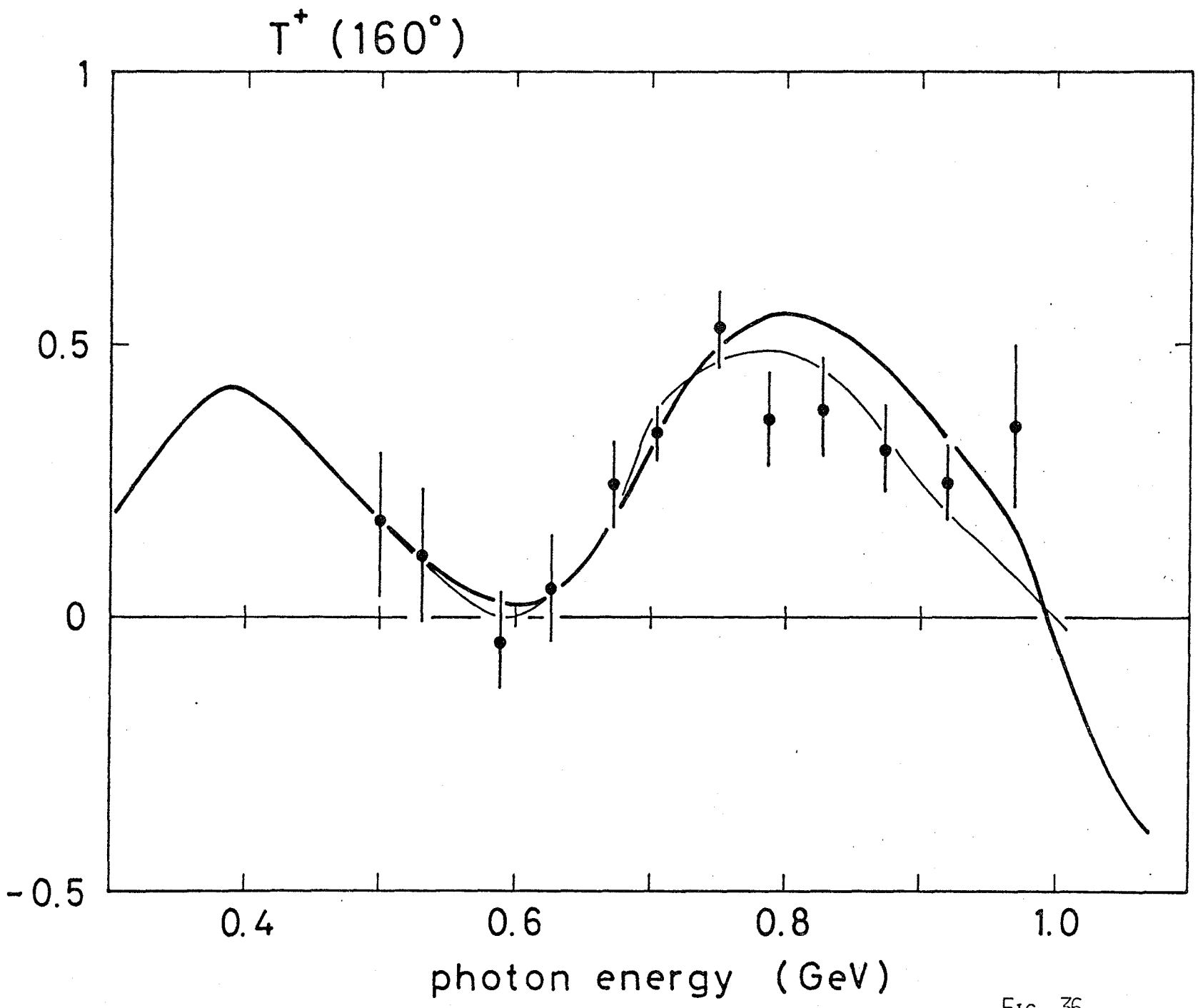

FIG. 36

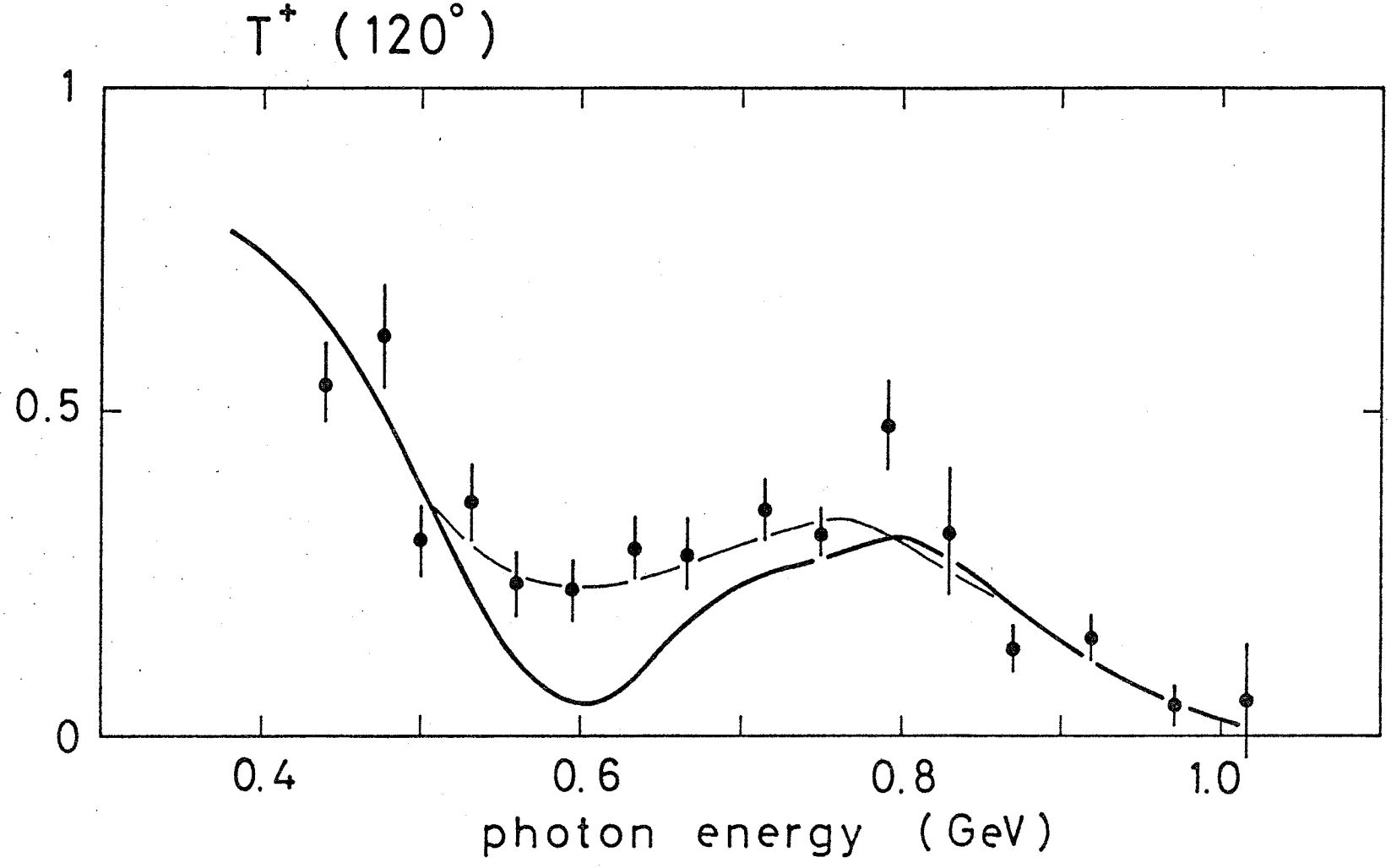

FIG. 37

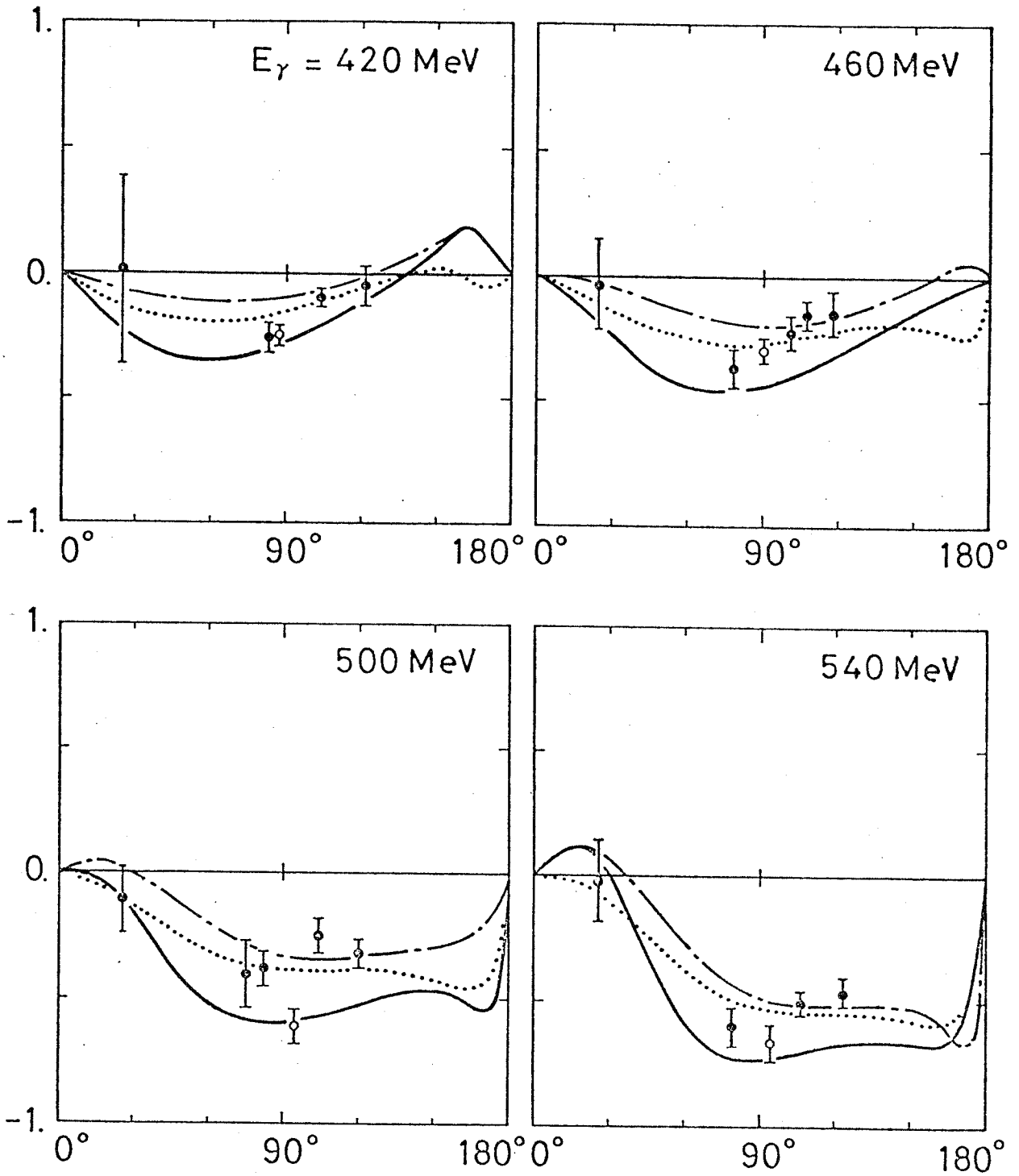

FIG. 38(A) - (D)

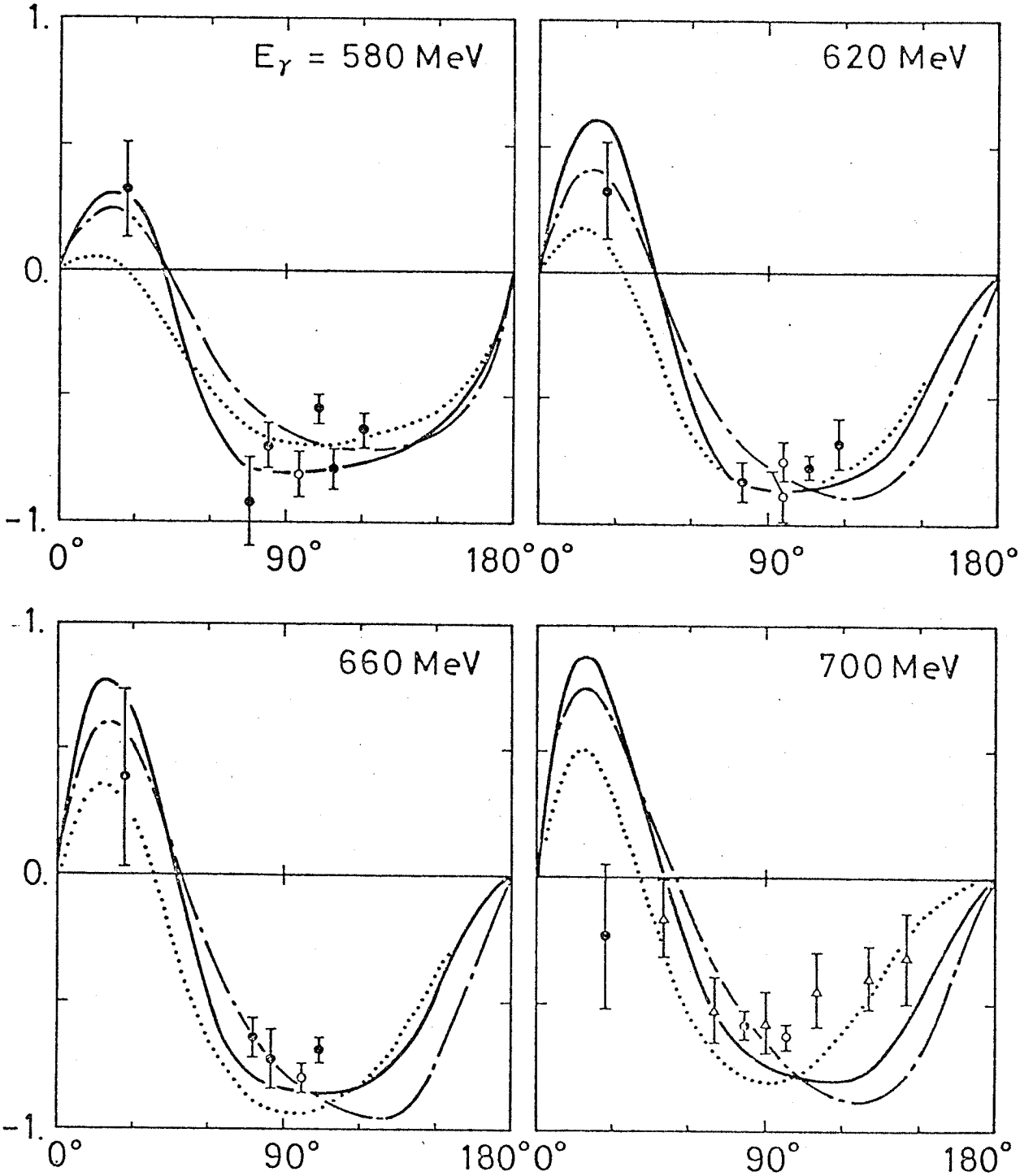

FIG. 38(E) - (H)

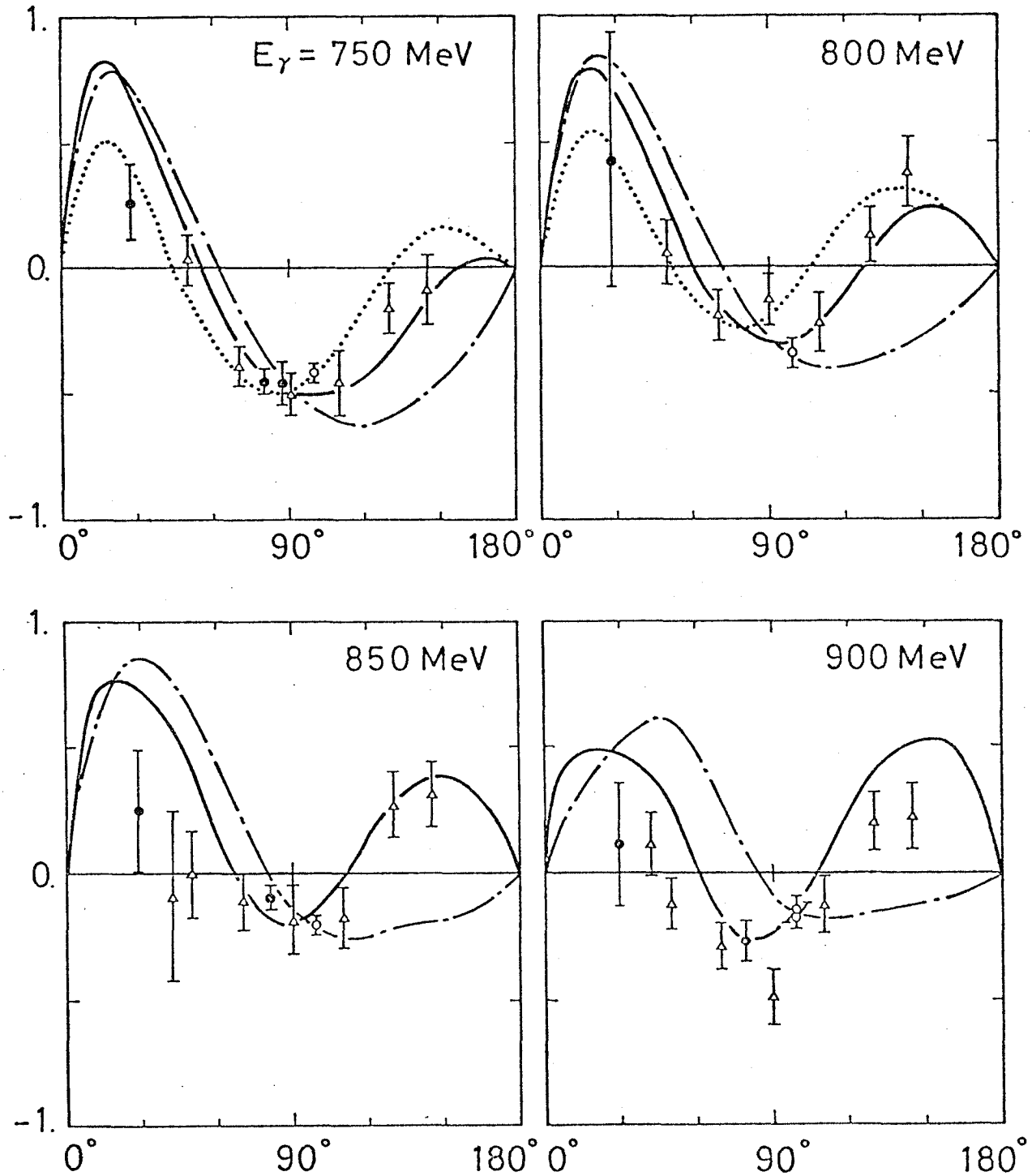

FIG. 38(I) - (L)

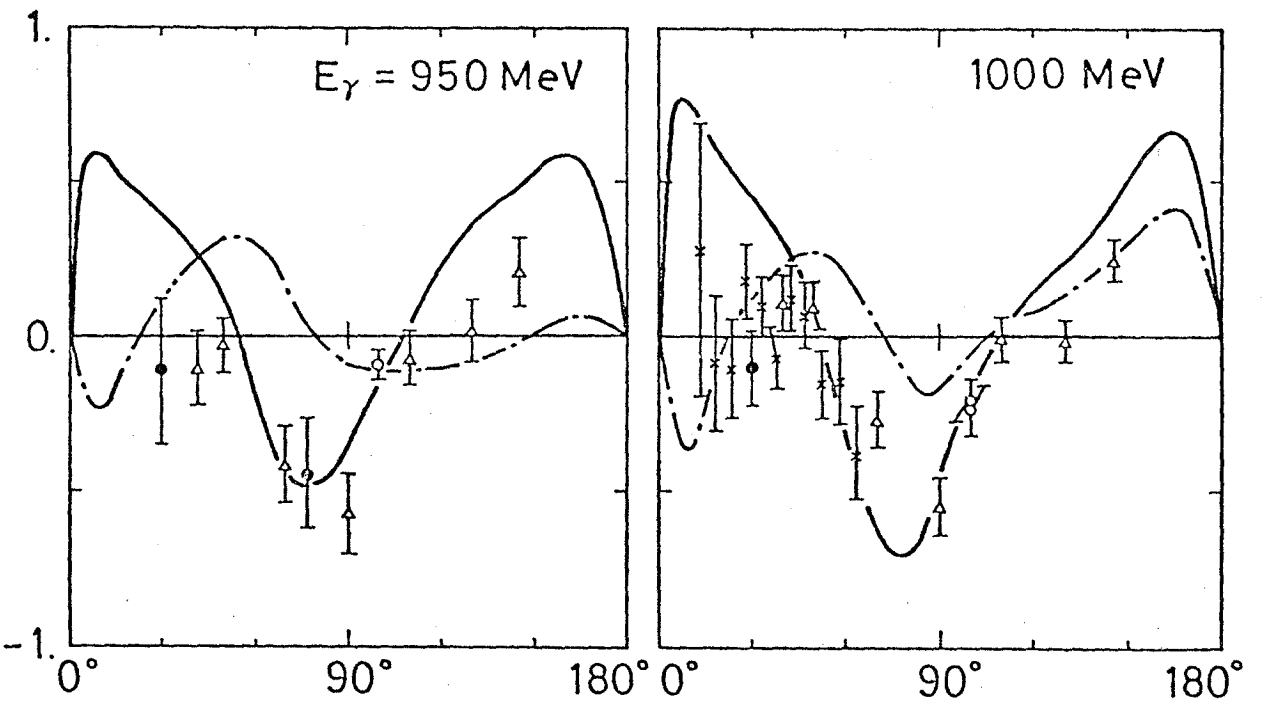
1.
0.
-1.
E_γ = 950 MeV
1000 MeV
0°
90°
180°
0°
90°
180°

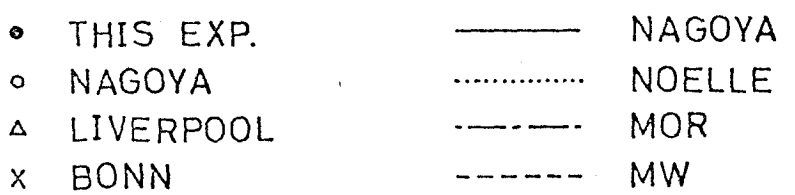
THIS EXP.
NAGOYA
LIVERPOOL
BONN
NAGOYA
NOELLE
MOR
MW

FIG. 38(M), (N)

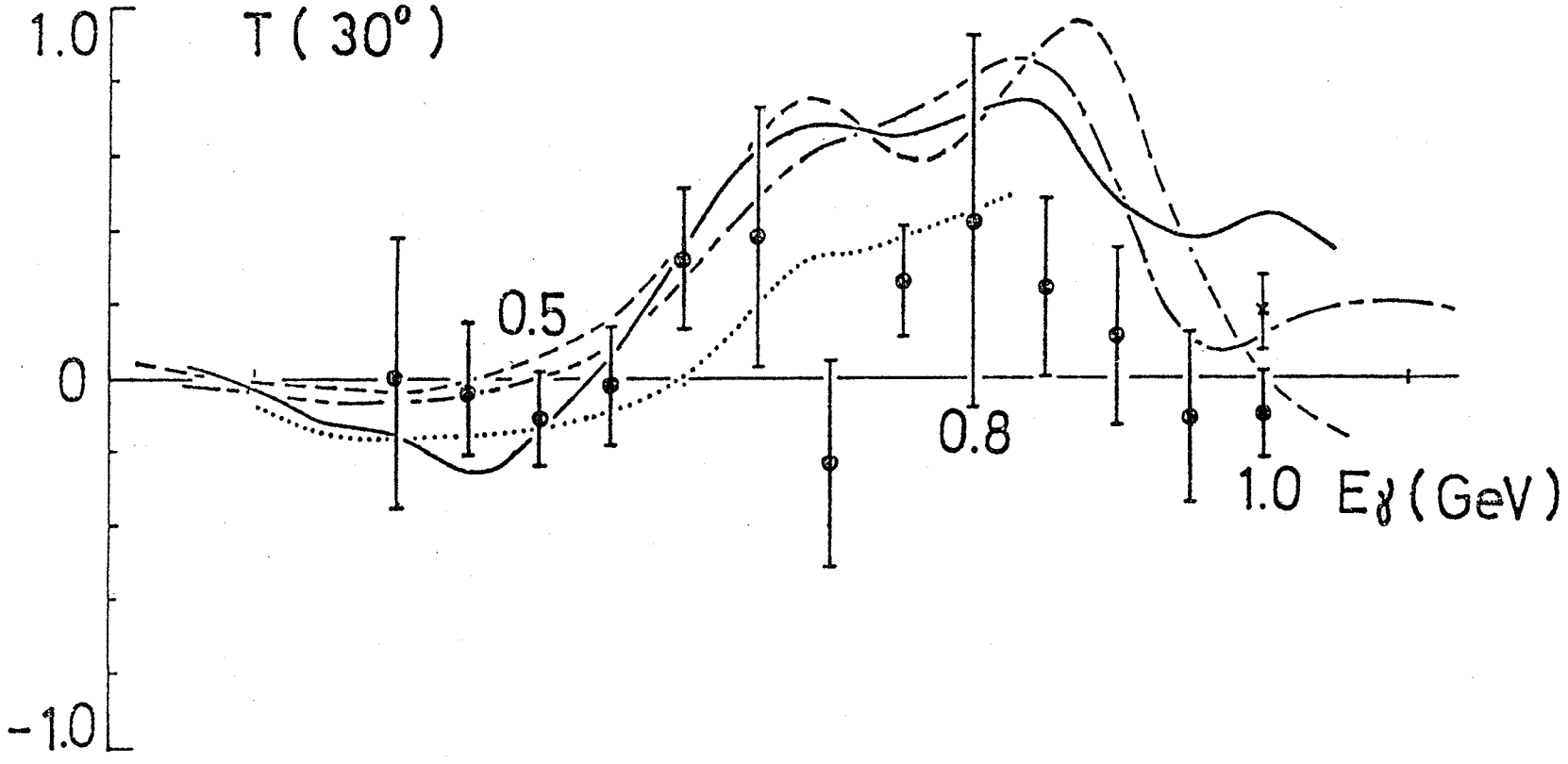

FIG. 39(A)

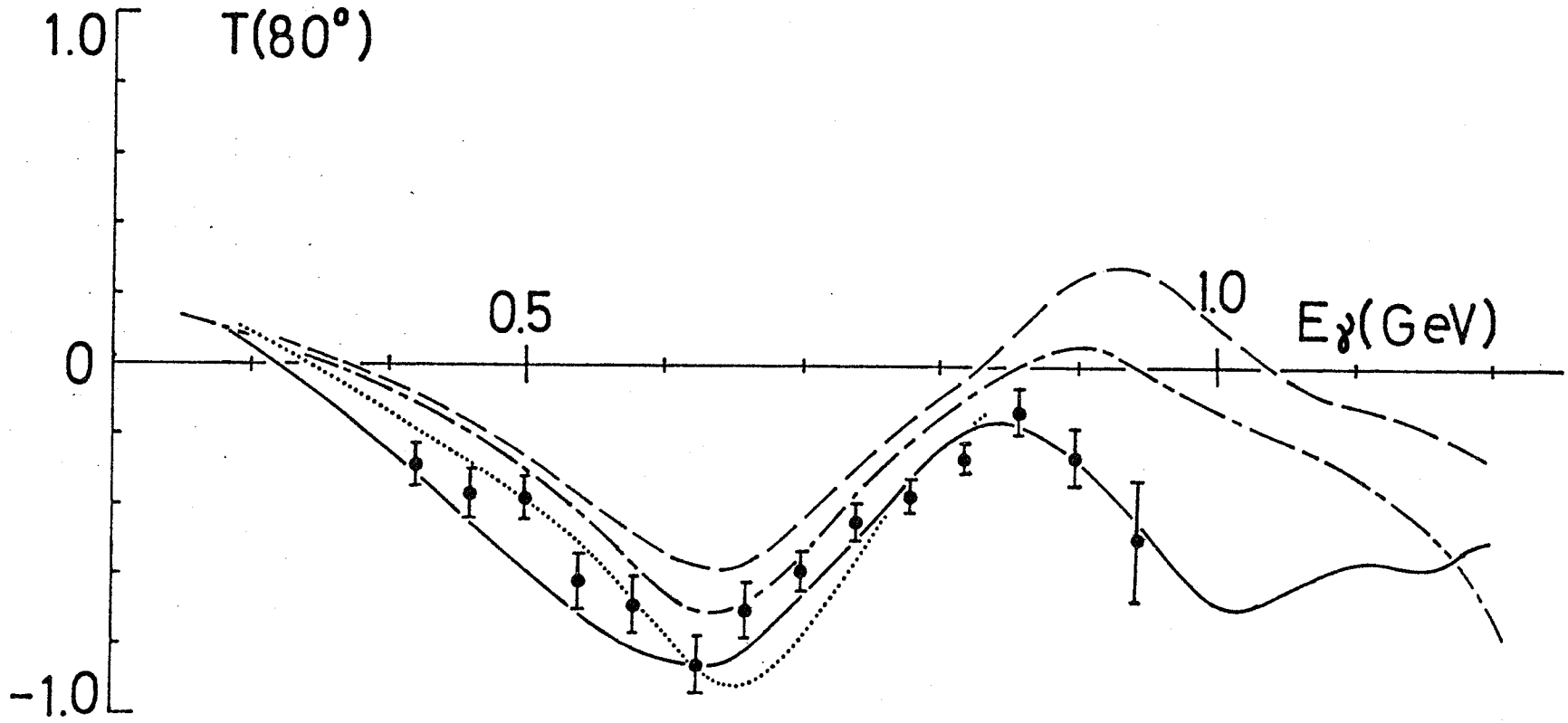

FIG. 39(B)

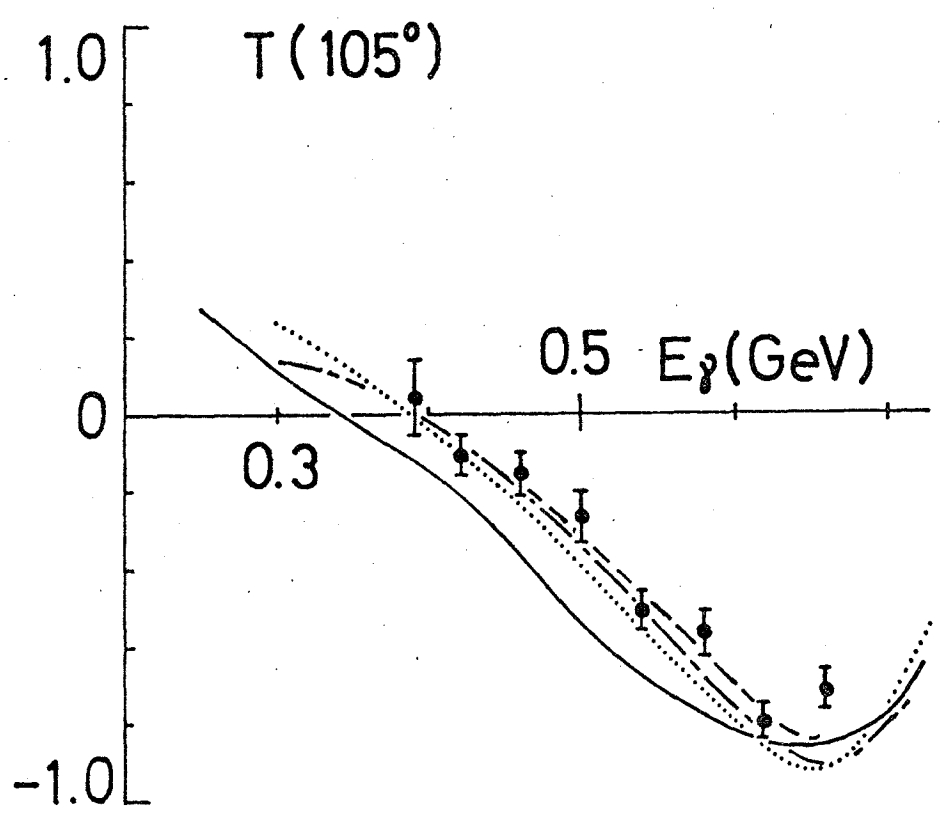

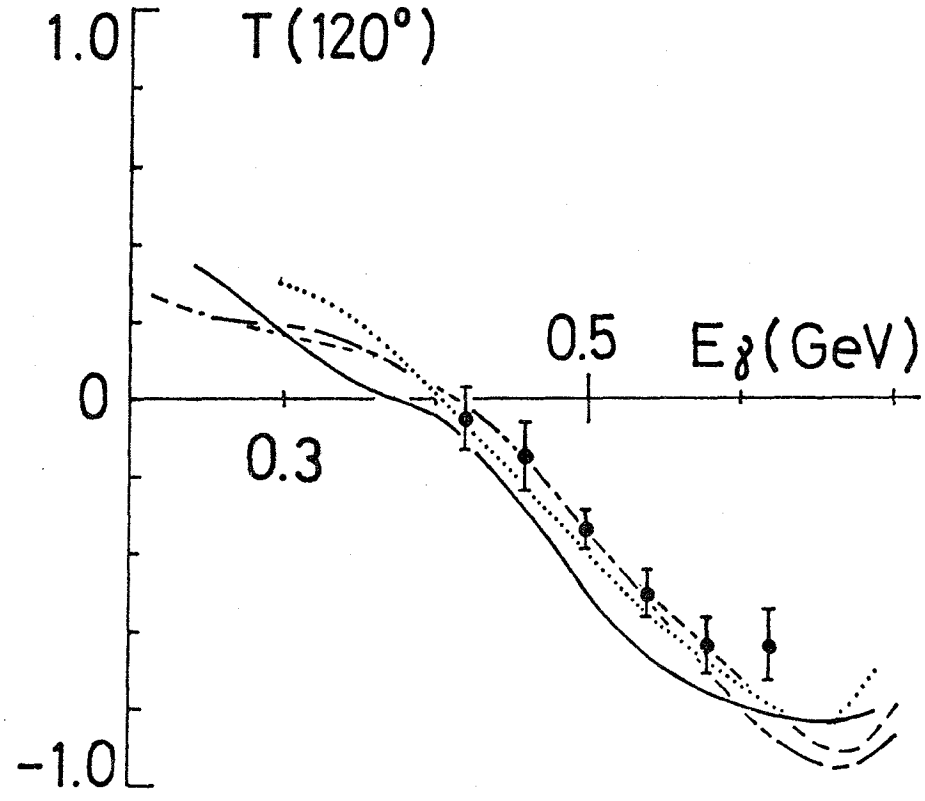

FIG. 39(C), (D)

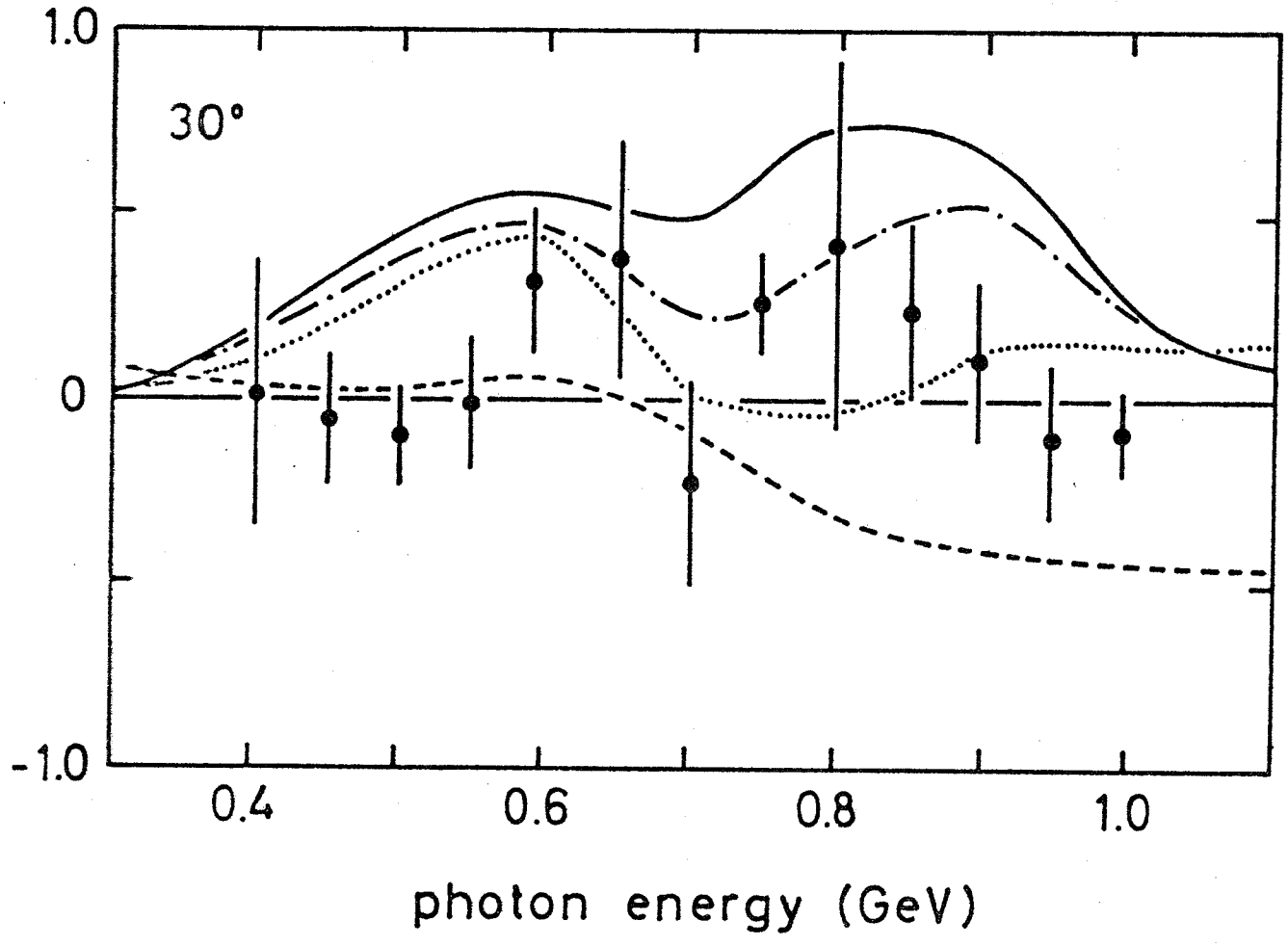

FIG. 40

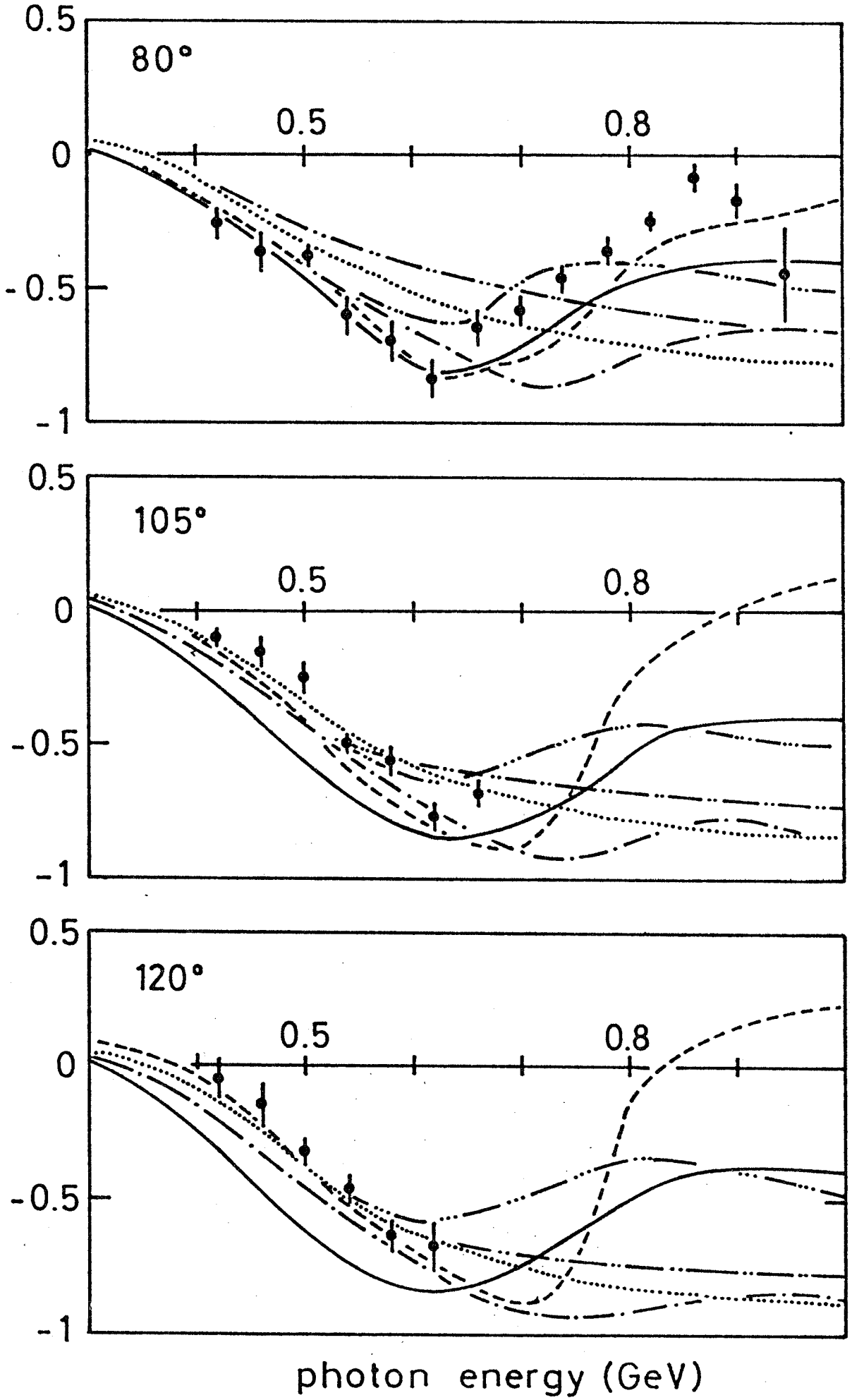
0.5
80°
0.5
0.8
0
-0.5
-1
0.5
105°
0.5
0.8
0
-0.5
-1
0.5
120°
0.5
0.8
0
-0.5
-1
photon energy (GeV)

FIG. 41

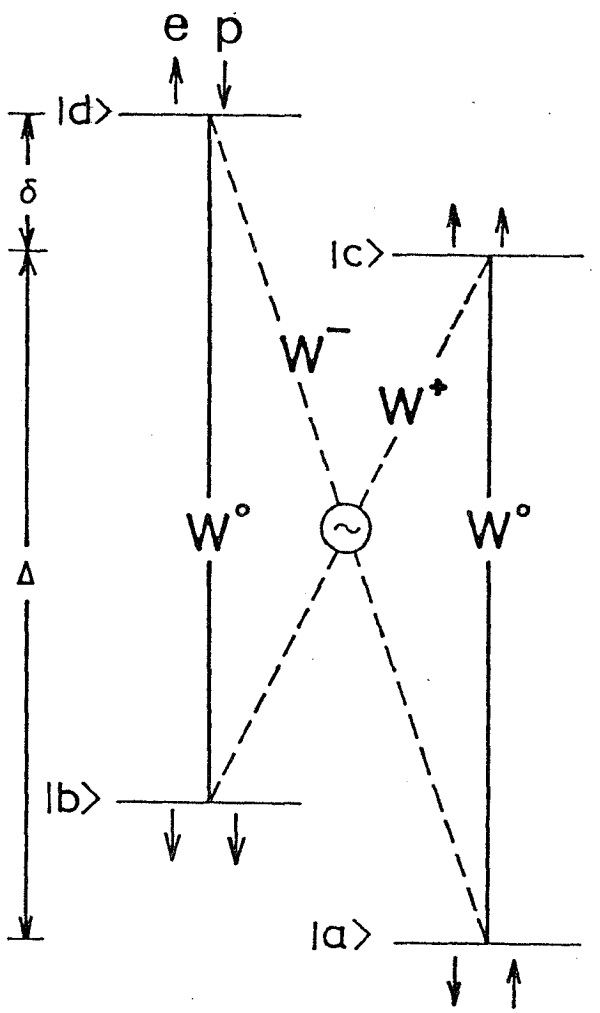

	sat.w^-	sat.w^+
$e^{-\delta-\Delta}$	1	$e^{-\Delta}$
$e^{-\Delta}$	$e^{-\Delta}$	1
$e^{-\delta}$	e^{Δ}	1
1	1	e^{Δ}
pol. $\tanh\frac{\delta}{2}$	$-\tanh\frac{\Delta}{2}$	$\tanh\frac{\Delta}{2}$

$\Delta = 2\mu_e H/kT$

$\delta = 2\mu_p H/kT$

FIG. 42

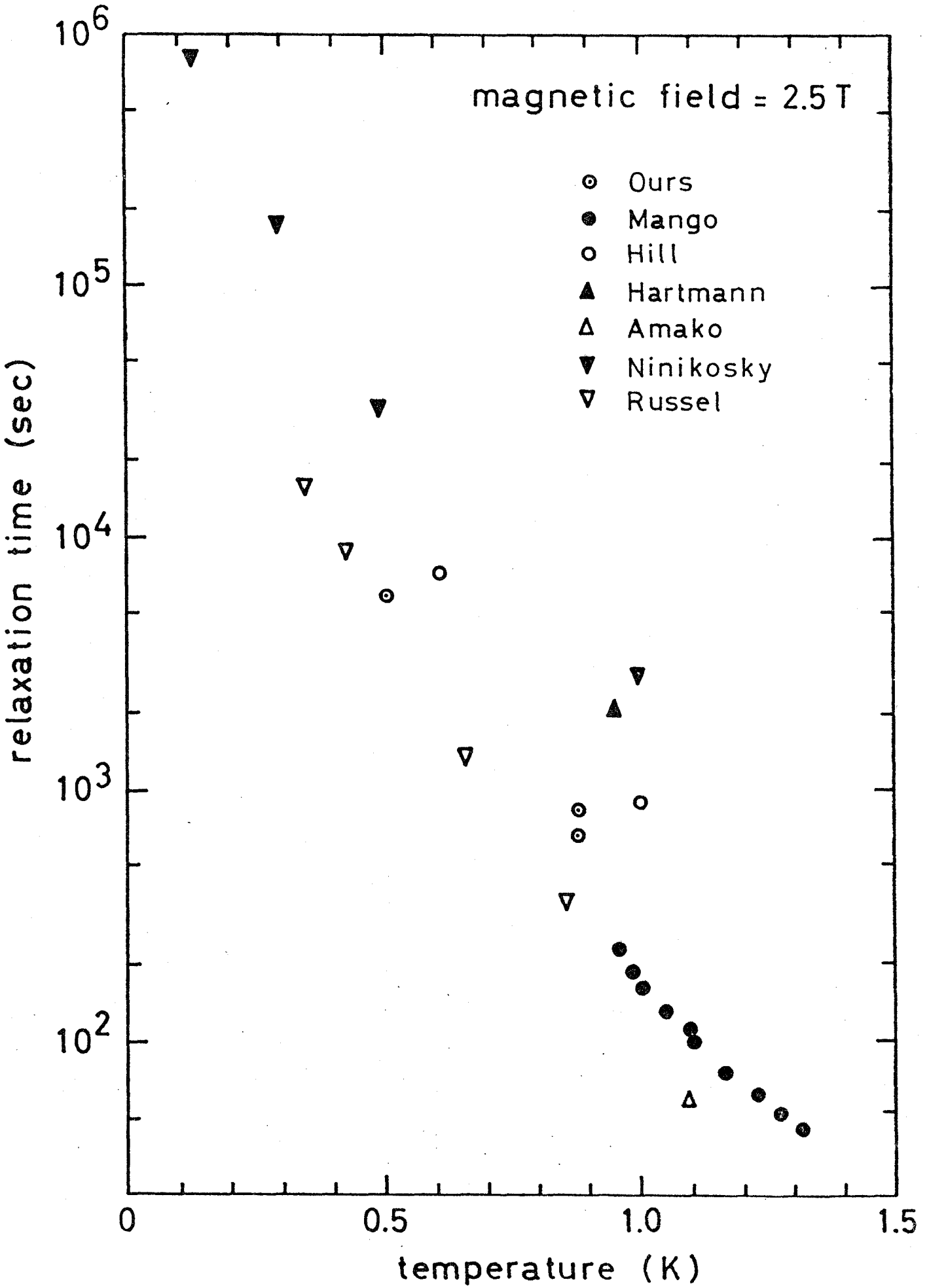
magnetic field = 2.5 T
Ours
Mango
Hill
Hartmann
Amako
Ninikosky
Russel
relaxation time (sec)
10^6
10^5
10^4
10^3
10^2
0
0.5
1.0
1.5
temperature (K)

FIG. 43

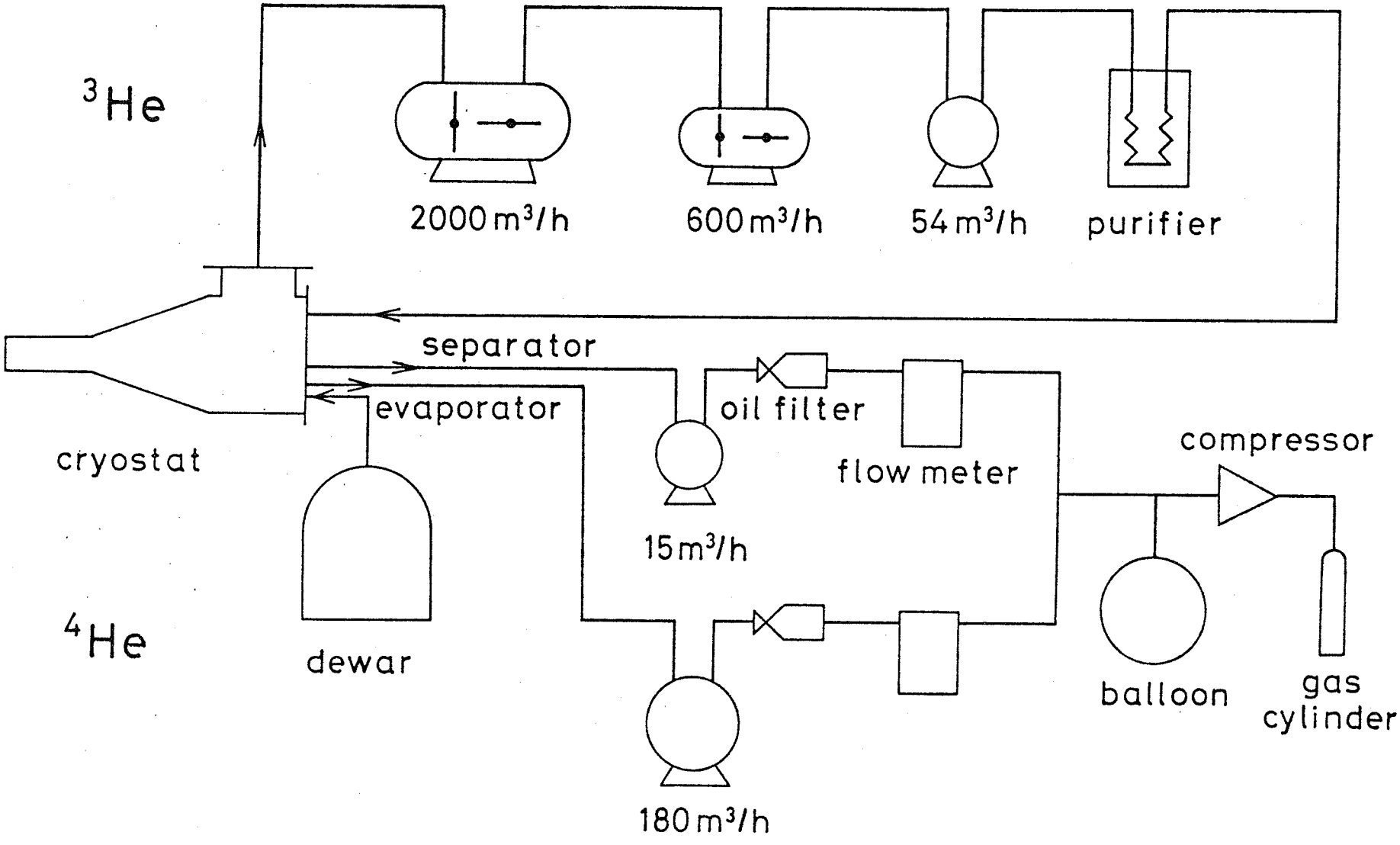
^{3}He
2000 m^3/h
600 m^3/h
54 m^3/h
purifier
separator
evaporator
oil filter
flow meter
compressor
cryostat
15 m^3/h
^{4}He
dewar
balloon
gas cylinder
180 m^3/h

FIG. 44

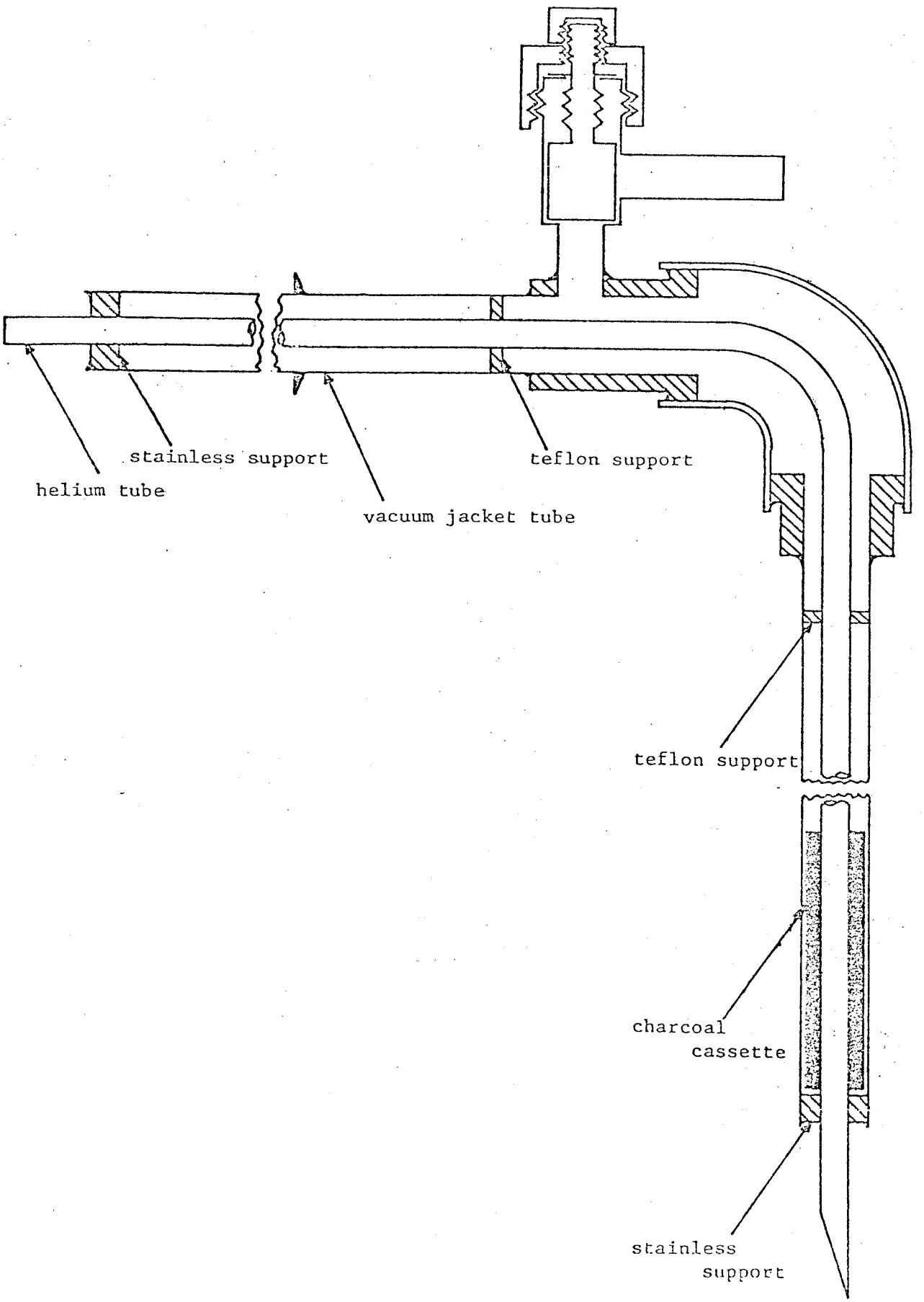
helium tube
stainless support
vacuum jacket tube
teflon support
teflon support
charcoal
cassette
stainless
support

FIG. 45

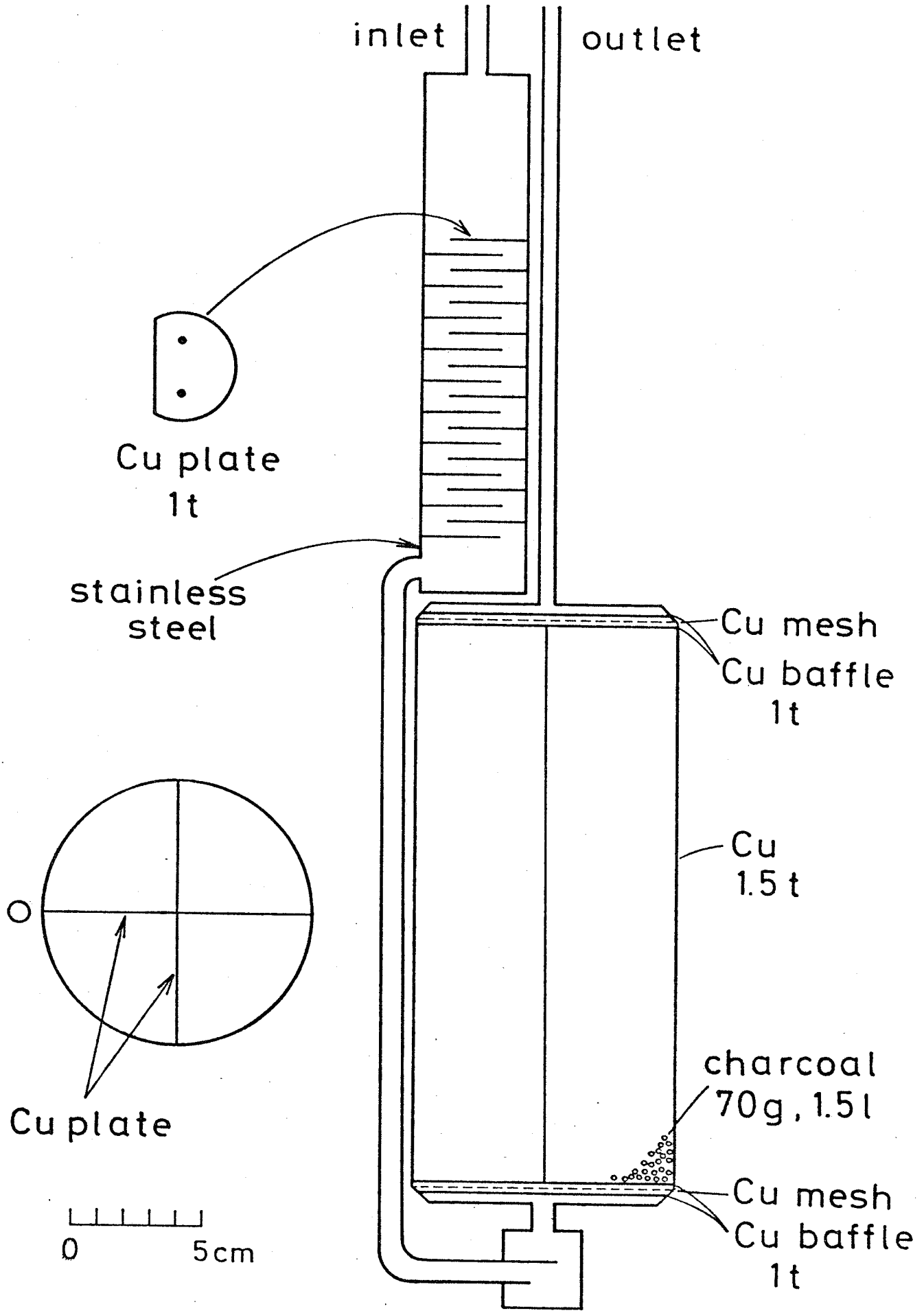
inlet
outlet
Cu plate
1t
stainless
steel
Cu mesh
Cu baffle
1t
Cu
1.5 t
charcoal
70g, 1.5l
Cu mesh
Cu baffle
1t
Cu plate
0
5cm

FIG. 46

Heat exchanger I

(in mm)

No.	D	d	l
1	108.0	2.5	5
2	112.2	2.5	5
3	116.4	2.5	5
4	120.5	3	6
5	124.7	3	6

Heat exchanger II

(in mm)

No.	D	d	l
1	68.0	1	2
2	69.6	1	2
3	71.3	1	2
4	73.0	1.5	3
5	74.6	1.5	3
6	76.3	1.5	3
7	78.0	1.5	3
8	79.7	2	4
9	83.0	2	4
10	86.3	2	4

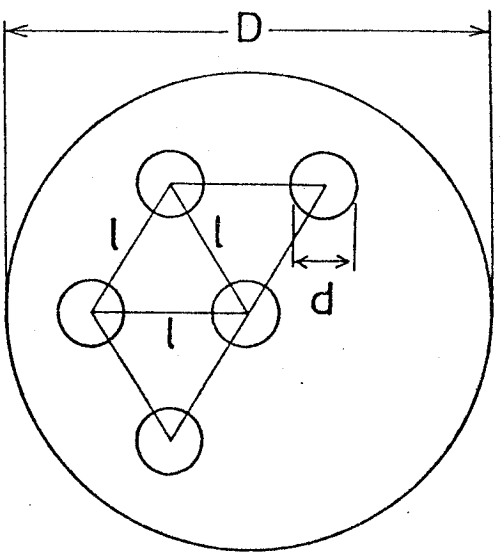

FIG. 47

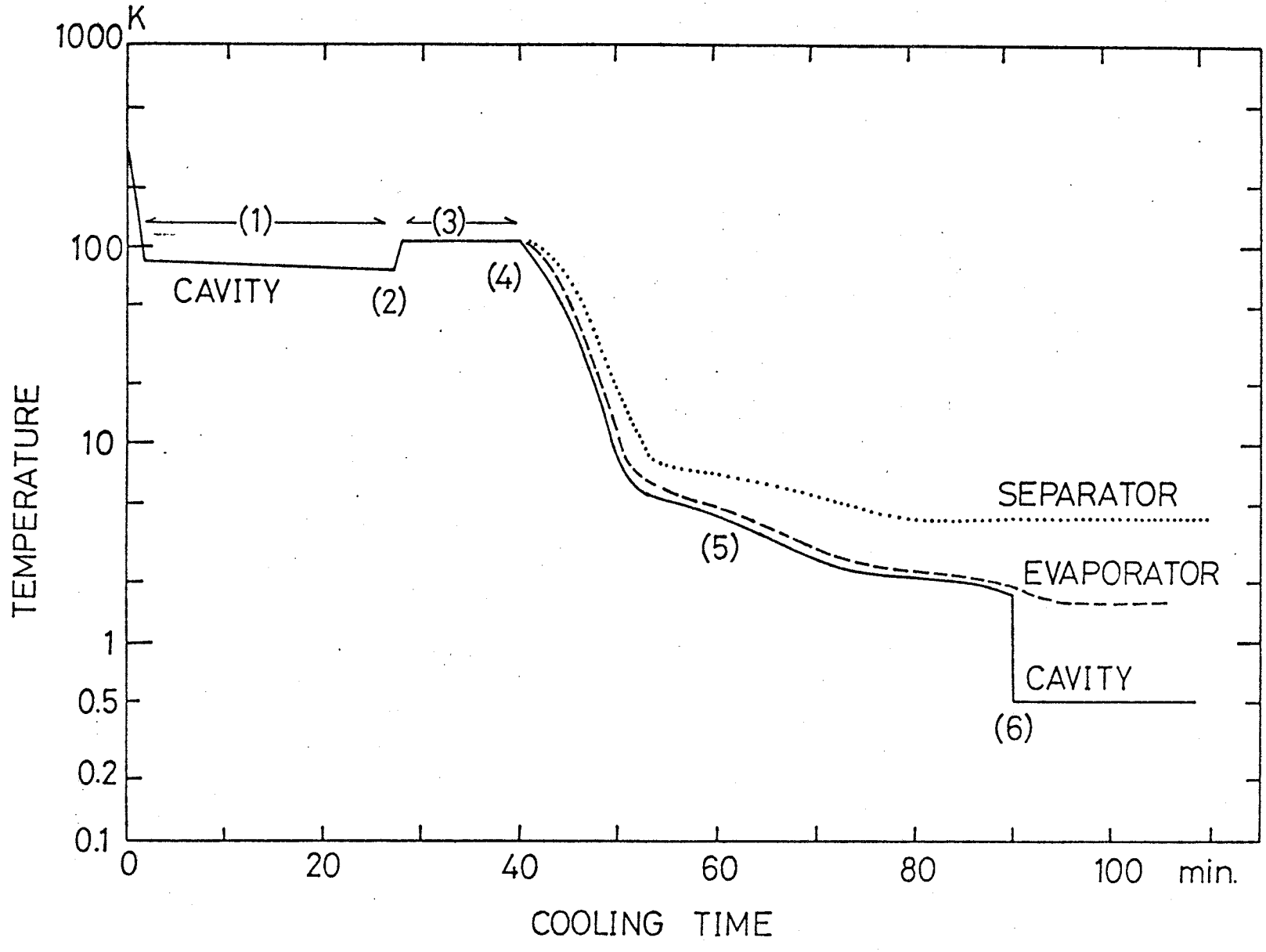
1000 K
100
10
1
0.5
0.2
0.1
TEMPERATURE
(1)
(3)
CAVITY
(2)
(4)
SEPARATOR
(5)
EVAPORATOR
CAVITY
(6)
0
20
40
60
80
100 min.
COOLING TIME

FIG. 48

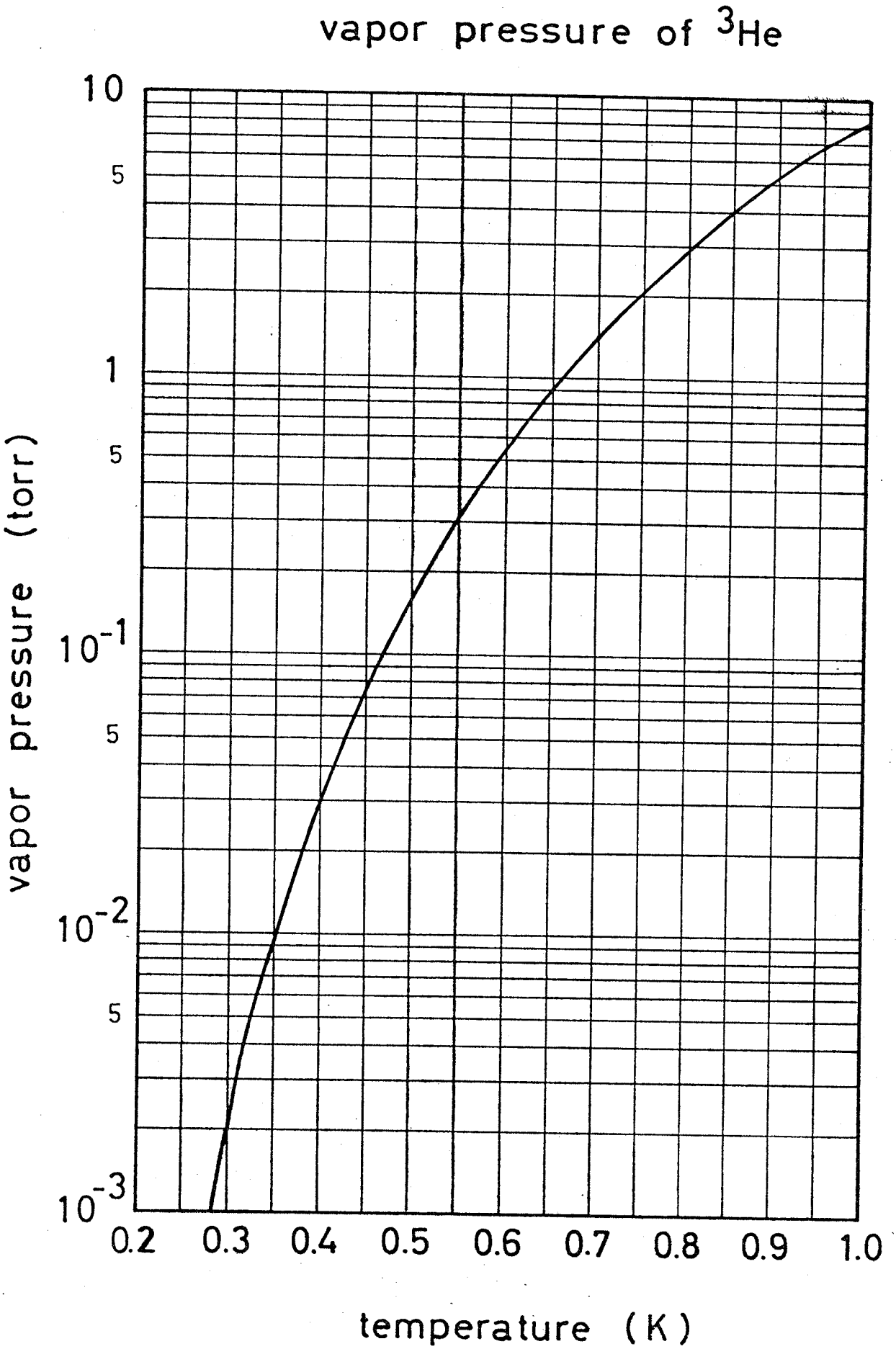
vapor pressure of ^{3}He
10
5
1
5
10^{-1}
5
10^{-2}
5
10^{-3}
vapor pressure (torr)
0.2
0.3
0.4
0.5
0.6
0.7
0.8
0.9
1.0
temperature (K)

FIG. 49

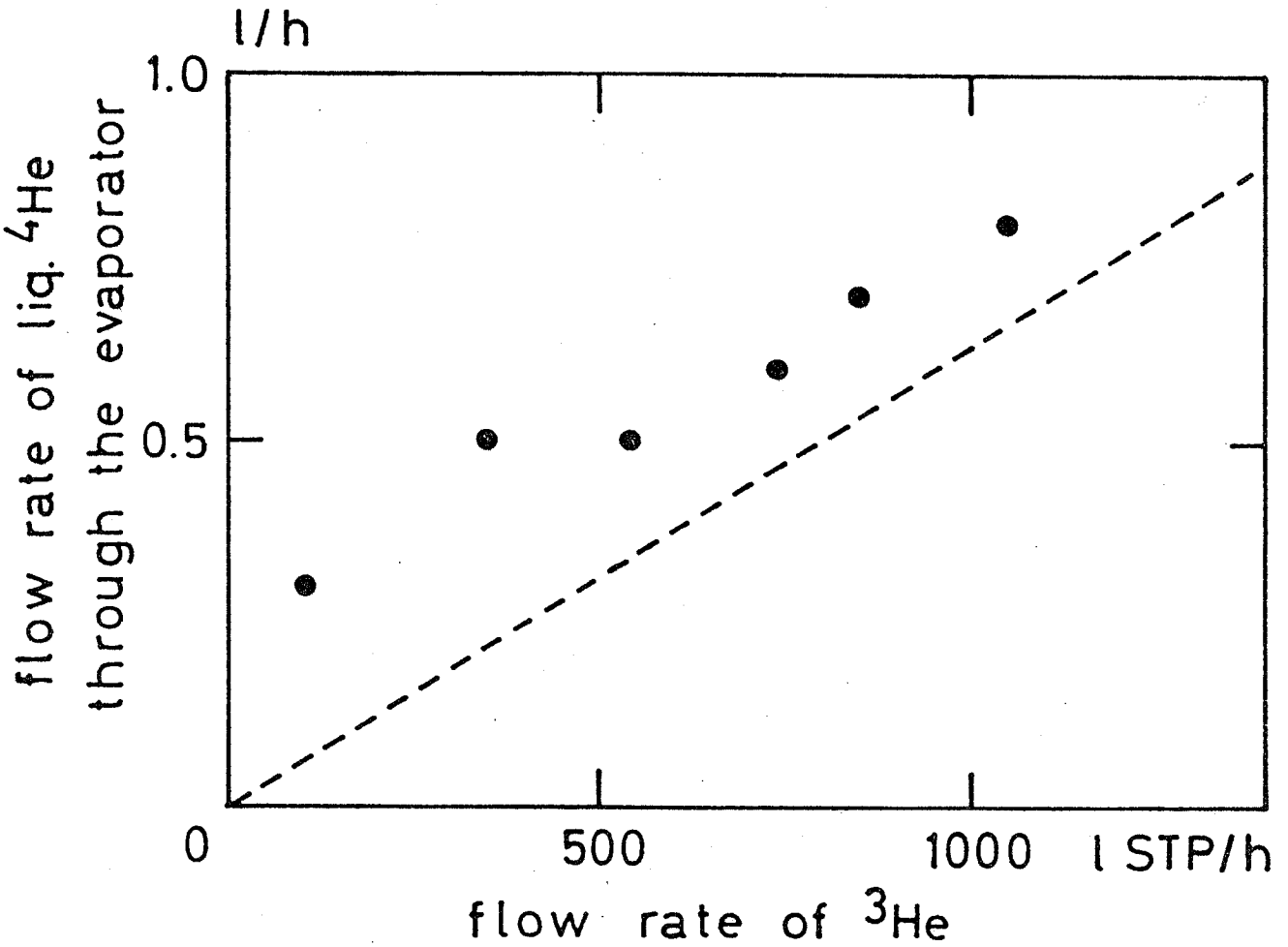
l/h
1.0
0.5
0
500
1000
l STP/h
flow rate of liq. 4He through the evaporator
flow rate of 3He

FIG. 50

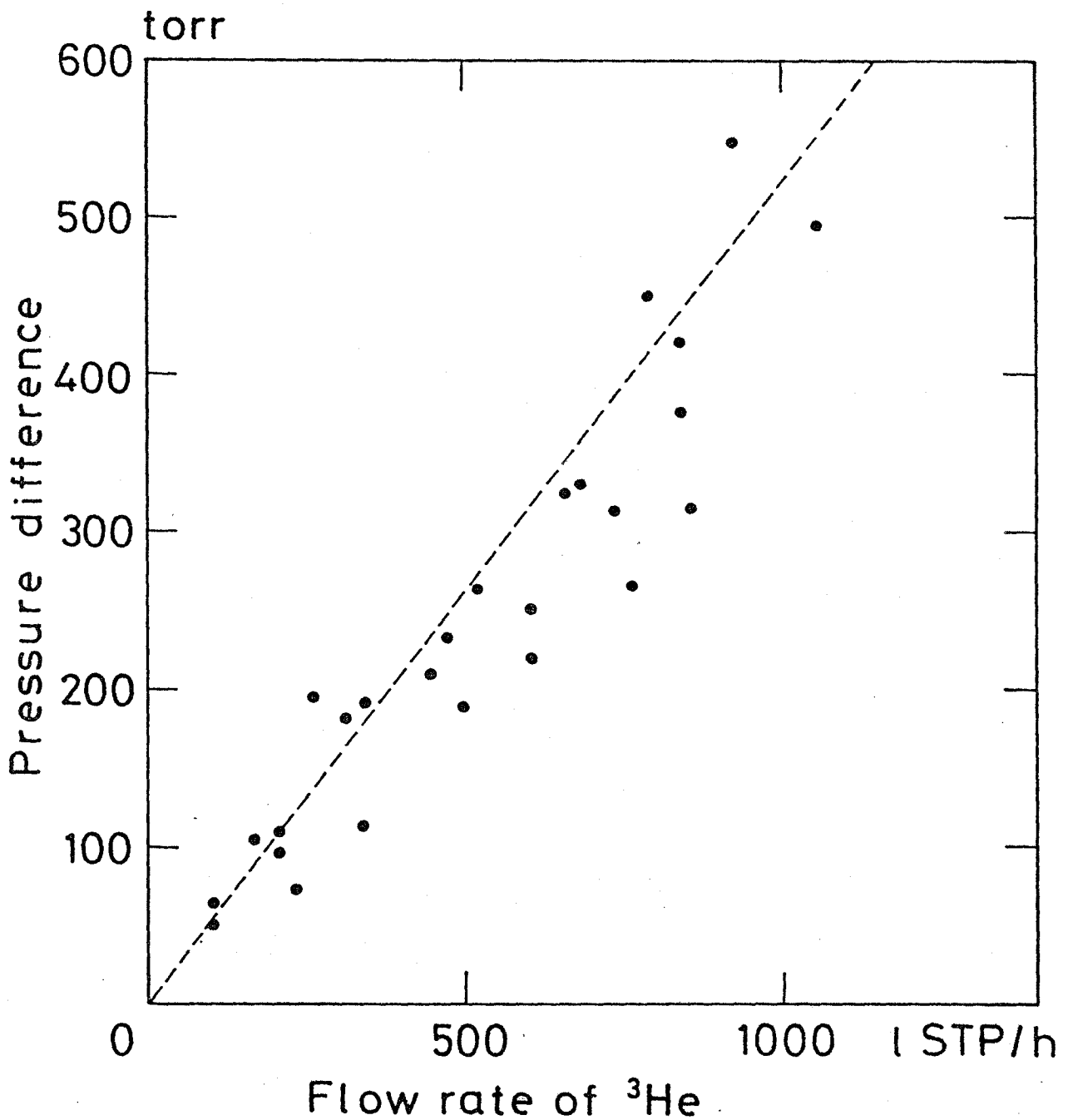
torr
600
500
400
300
200
100
0
Pressure difference
500
1000
l STP/h
Flow rate of ³He

FIG. 51

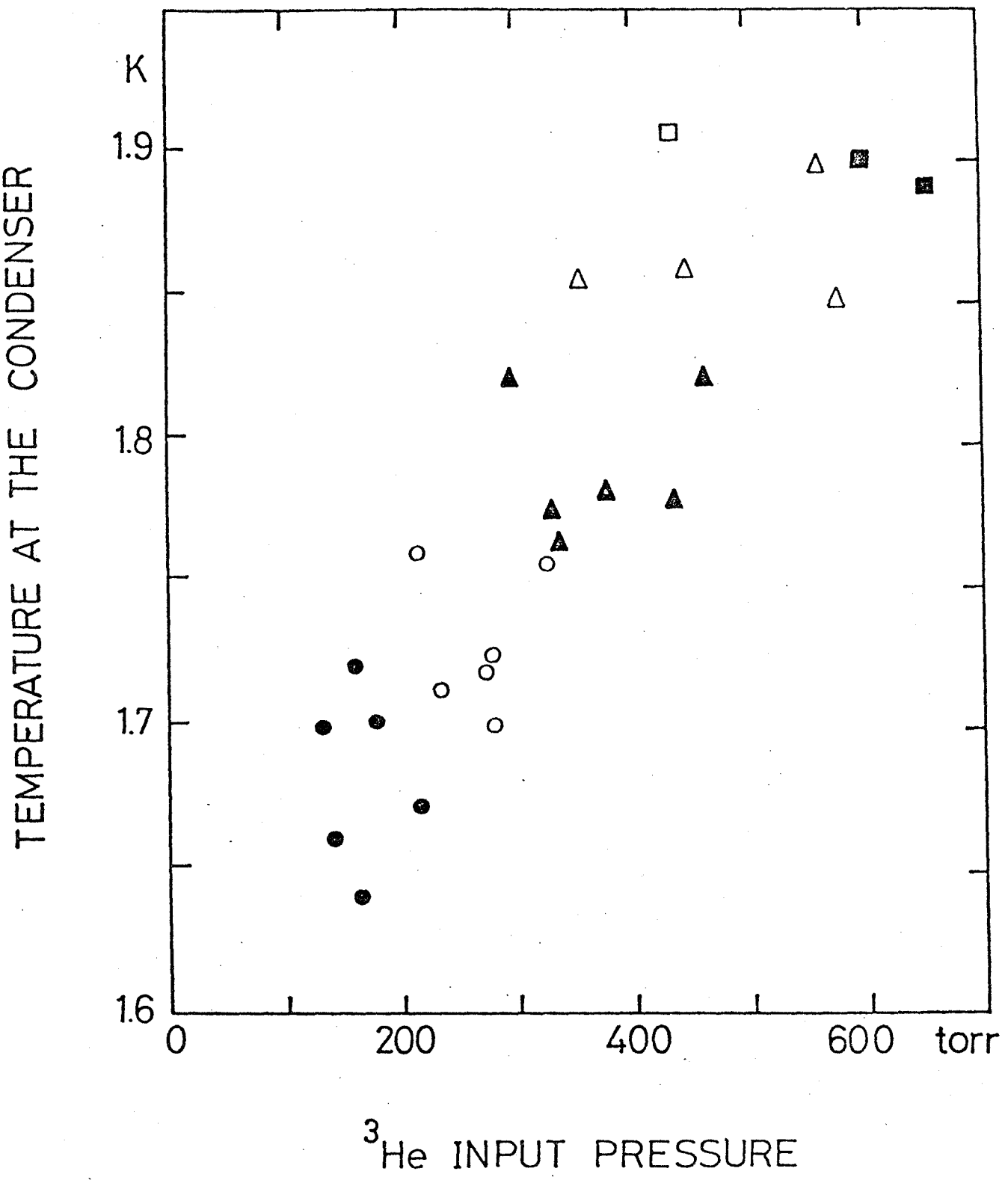
TEMPERATURE AT THE CONDENSER
K
1.9
1.8
1.7
1.6
0
200
400
600
torr
^{3}He INPUT PRESSURE

FIG. 52

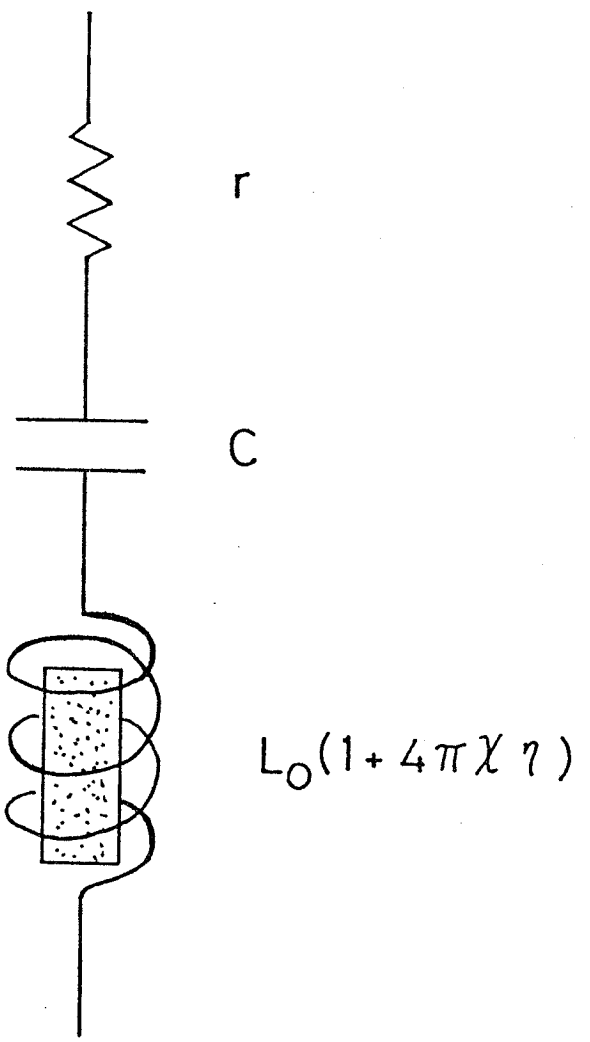

FIG. 53

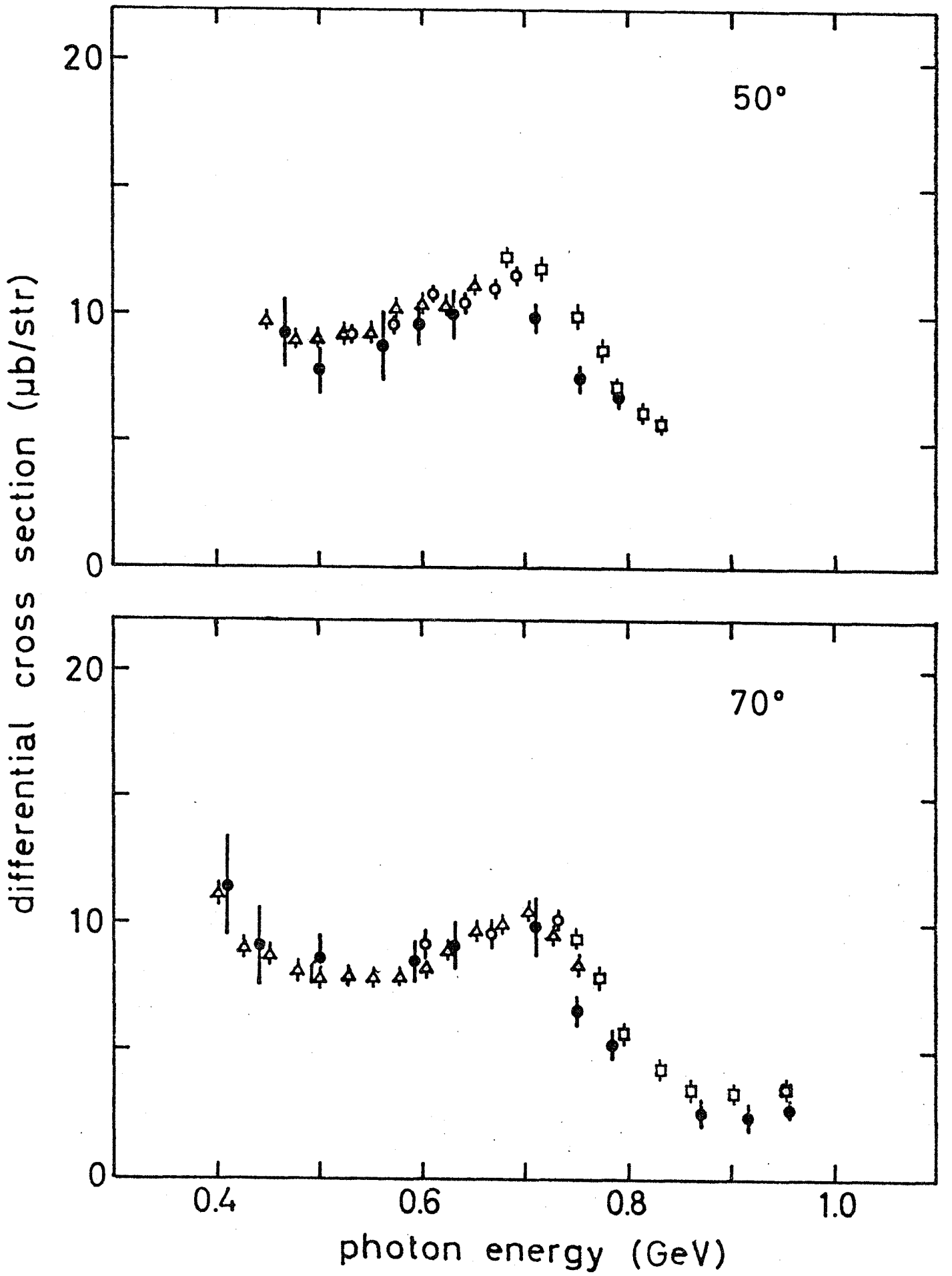
20
10
0
50°
20
10
0
70°
differential cross section (μb/str)
0.4
0.6
0.8
1.0
photon energy (GeV)

FIG. 54(A), (B)

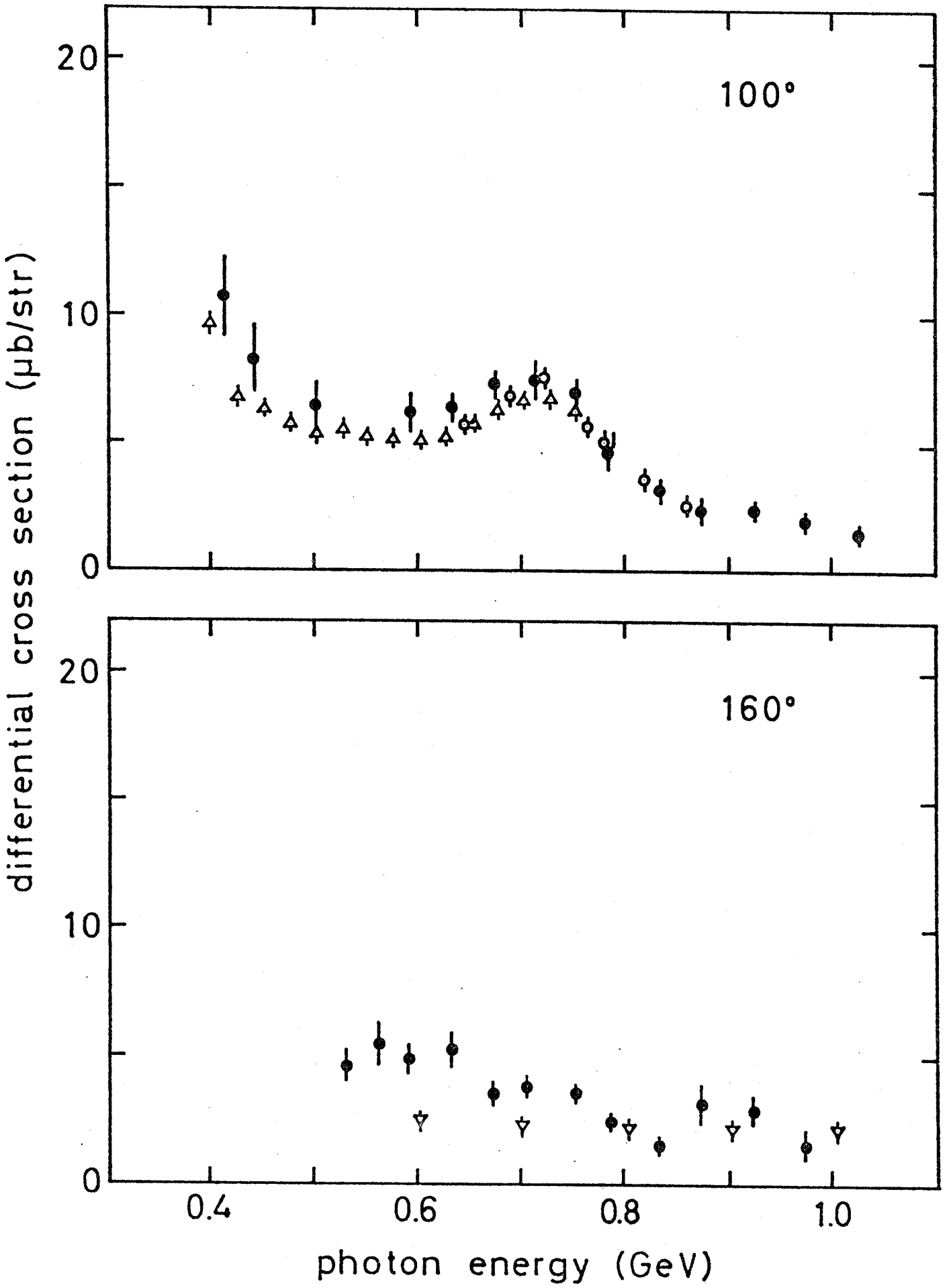
20
10
0
100°
20
10
0
160°
differential cross section (μb/str)
0.4
0.6
0.8
1.0
photon energy (GeV)

FIG. 54(C), (D)

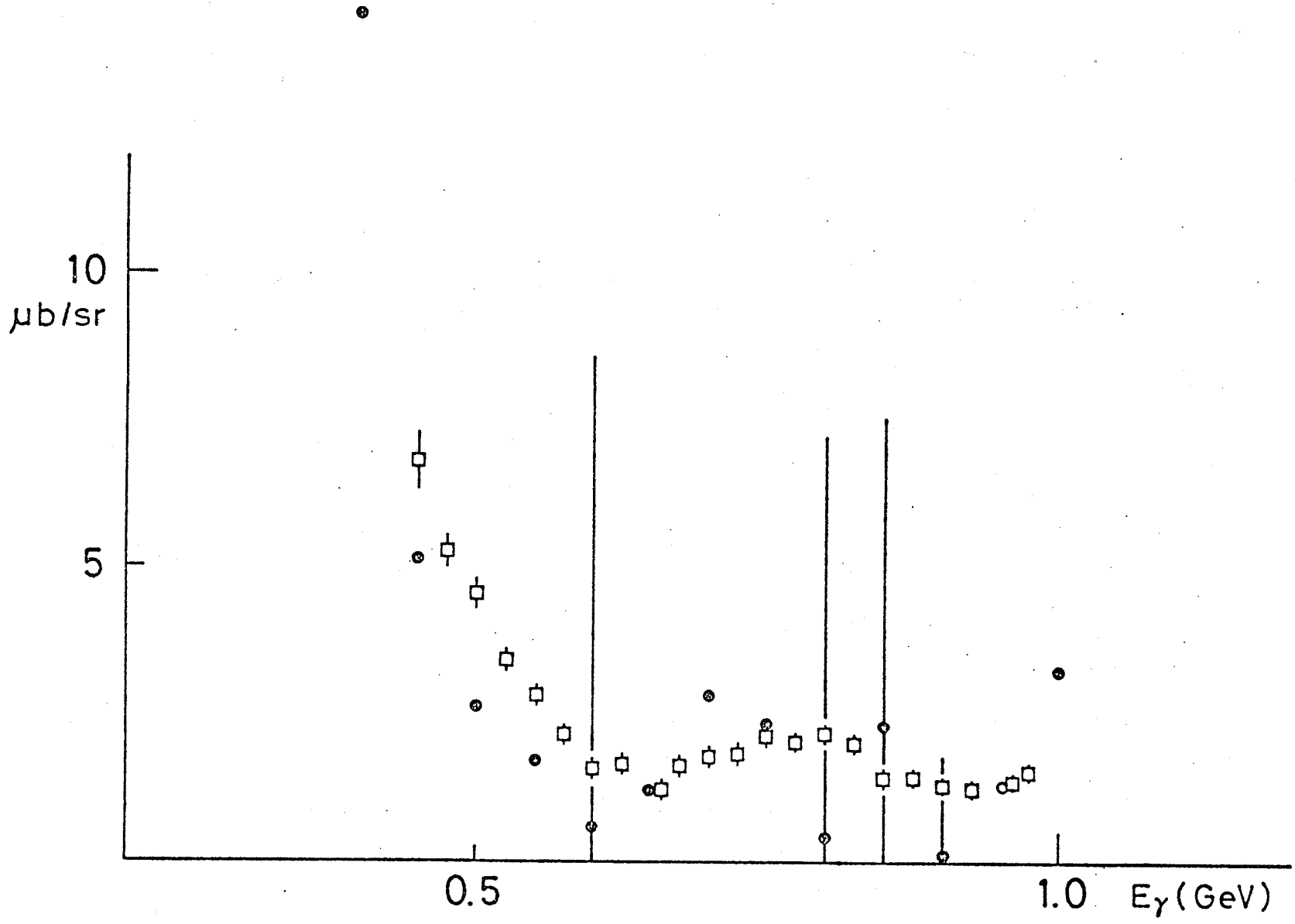

FIG. 55

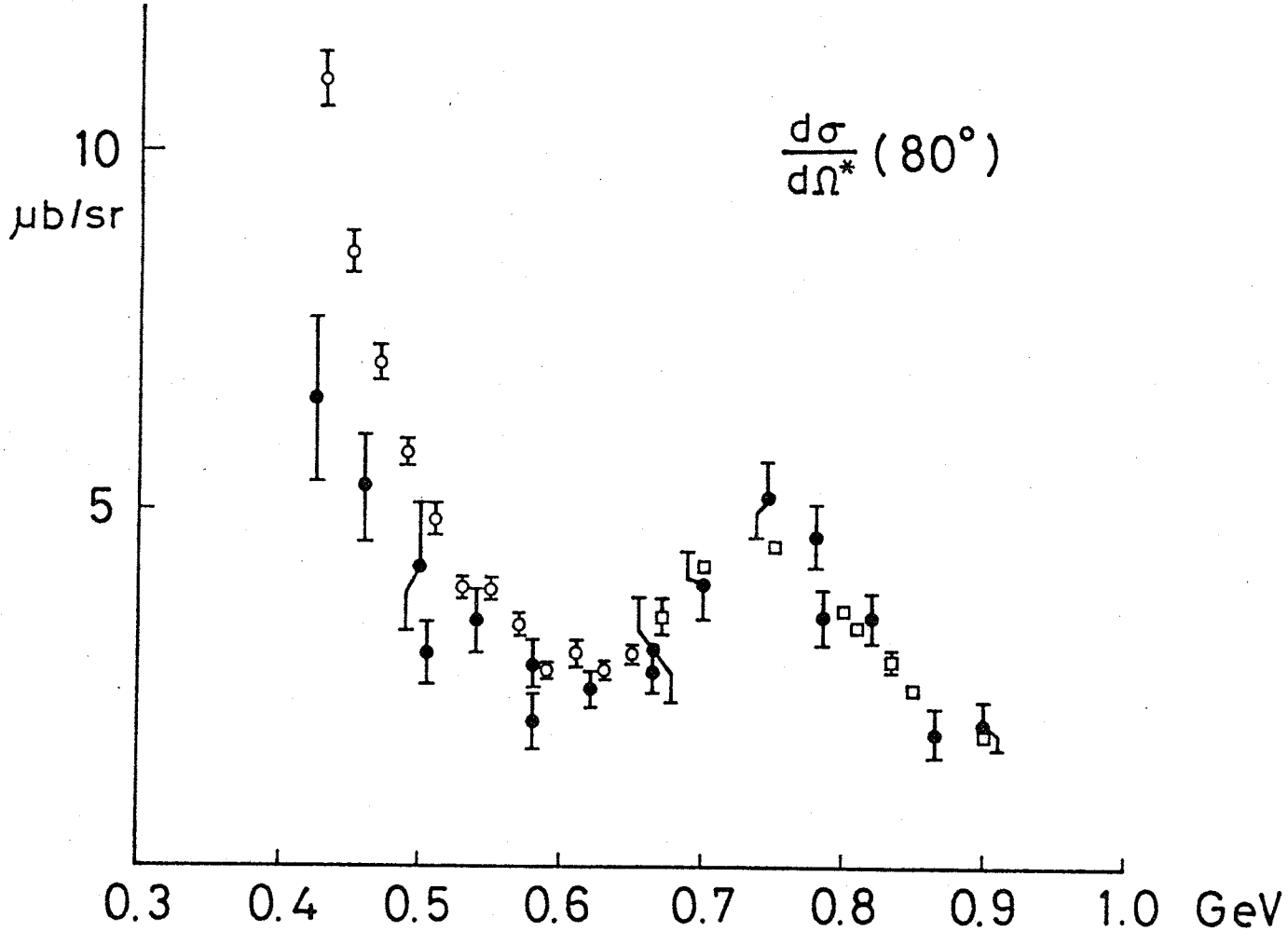

FIG. 56(A)

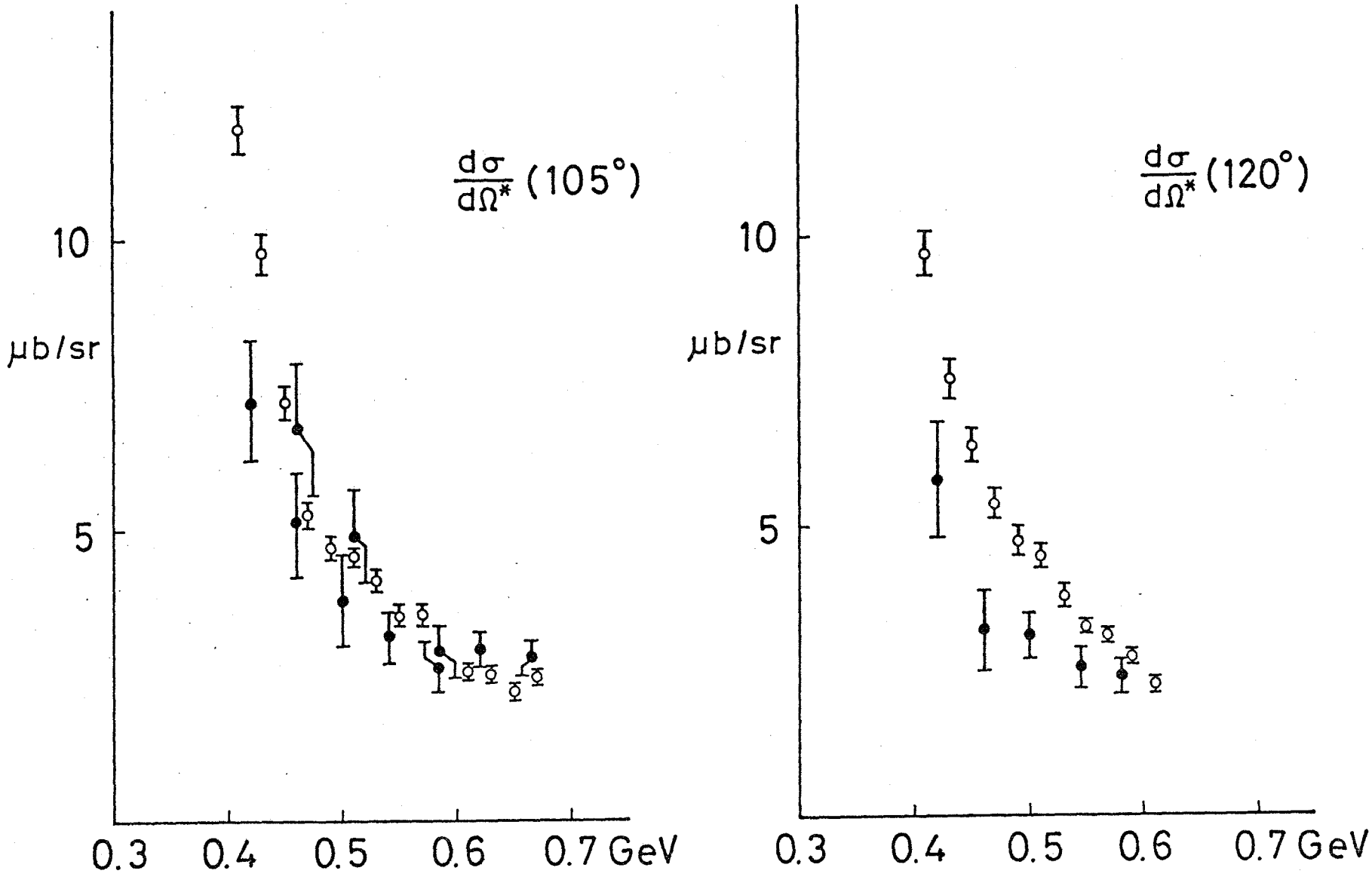
$\frac{d\sigma}{d\Omega^*}$ (105°)
10
μb/sr
5
0.3
0.4
0.5
0.6
0.7 GeV
$\frac{d\sigma}{d\Omega^*}$ (120°)
10
μb/sr
5
0.3
0.4
0.5
0.6
0.7 GeV

FIG. 56(B), (C)

Errata

On page 3 of Contents, line 3: Read "the measurement" instead of "themeasurement".

On page 1, line 5: Read "mechanisms" instead of "machanisms".

On page 3, line 10: Read "phase" instead of "pahse".

On page 5, line 16: Read "enabled" instead of "enables".

On page 21, line 7: Read "constructed" instead of "constucted".

On page 21, line 8: Read "production" instead of "productin".

On page 25, line 20: Read "fluctuations" instead of "flactuations".

On page 33, line 2: Read "measured" instead of "measureed".

On page 33, line 15: Read "subscripts" instead of "subscipts".

On page 36, line 11: Read "quantities" instead of "quantitites".

On page 41, line 3: Read "energies" instead of "enrgies".

On page 41, line 17: Read "trajectories" instead of "trajectires".

On page 42, line 18: Read "Additions" isntead of "Additons".

On page 49, line 2: Read "calculated" instead of "caluculated".

On page 51, line 17: Read "an assumed" instead of "a assumed".

On page 62, line 17: Read "$S_{11}(1535)$" instead of "$S_{11}(k535)$".

On page 66, line 4: Read "according" instead of "accoring".

On page 71, line 14: Read "polarization" instead of "poalrization".

On page 71, line 16: Read "temperature" instead of "temperaure".

On page 74, line 23: Read "consisting" instead of "consiting".

On page 76, line 5: Read "baffles" instead of "baffeles".

On page 80, line 5: Read "means" instead of "menas".

On page 81, line 11: Read "measuring" instead of "measureing".

On page 81, line 15: Read "constant" instead of "constat".

On page 83, line 9: Read "multiple" instead of "mutiple".

On page 84, line 4: Read "calculated" instead of "caculated".

On page 86, line 2: Read "thanks" instead of "tanks".

On page 95, line 10: Read "fig. 34" instead of "fig. 35".

On page 95, line 11: Read "$S_{11}(1535)$" instead of "$S_{11}(1700)$".

Figure 2 contains several errors. The correct version of the figure is

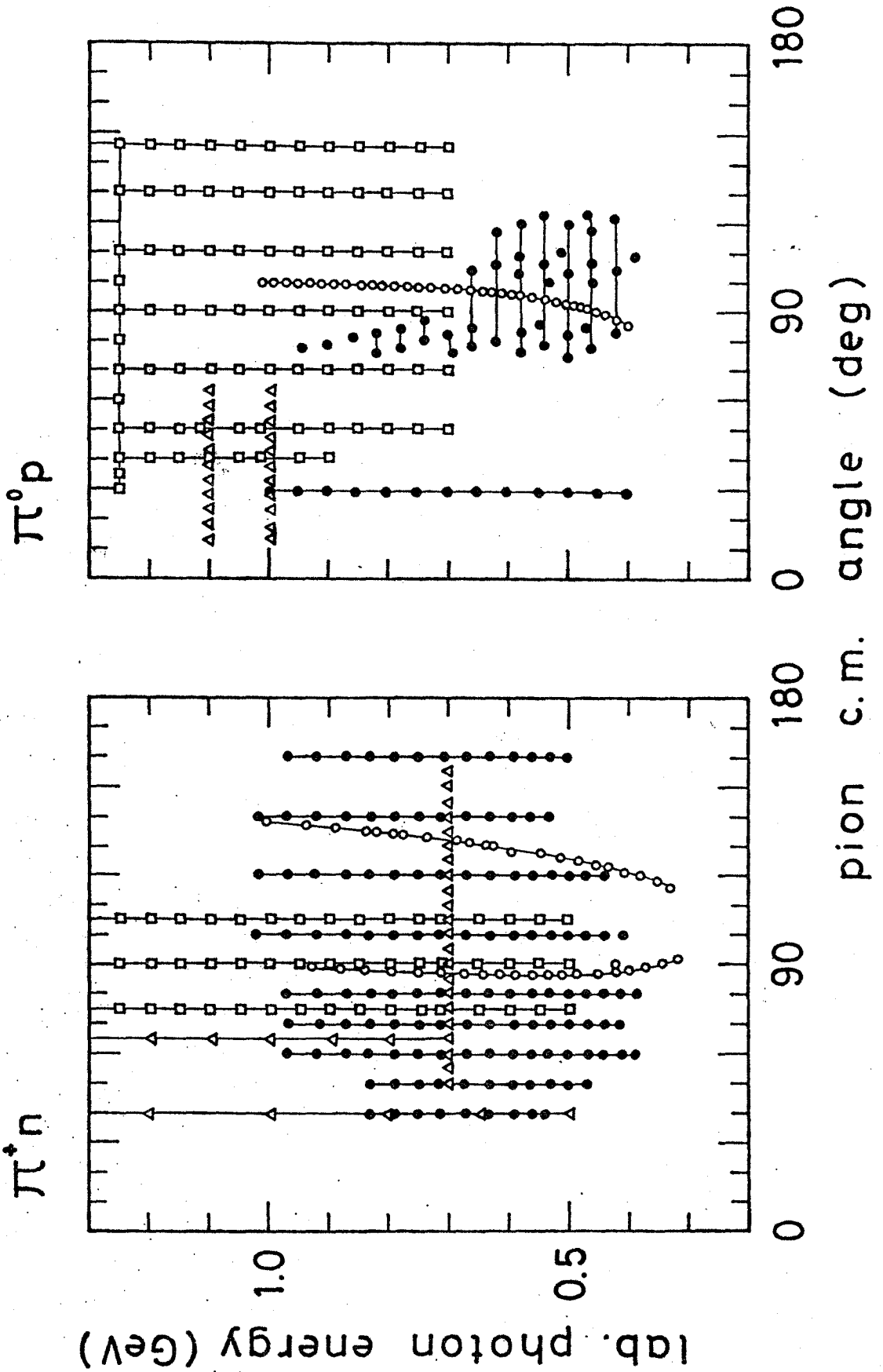

FIG. 2